

# AGARD

ADVISORY GROUP FOR AEROSPACE RESEARCH & DEVELOPMENT  
BP 25, 7 RUE ANCELLE, F-92201 NEUILLY-SUR-SEINE CEDEX, FRANCE

---

**AGARD ADVISORY REPORT 319**

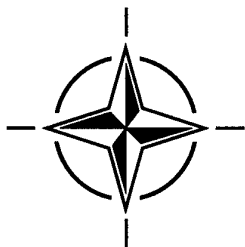
## **Hypersonic Experimental and Computational Capability, Improvement and Validation**

(l'Hypersonique expérimentale et de calcul – capacité,  
amélioration et validation)

**Volume II**

*This Advisory Report was prepared at the request of the Fluid Dynamics Panel.*

19990315 068



**NORTH ATLANTIC TREATY ORGANIZATION**

DISTRIBUTION STATEMENT A:  
Approved for Public Release -  
Distribution Unlimited

---

Published December 1998

*Distribution and Availability on Back Cover*

# AGARD

ADVISORY GROUP FOR AEROSPACE RESEARCH & DEVELOPMENT

BP 25, 7 RUE ANCELLE, F-92201 NEUILLY-SUR-SEINE CEDEX, FRANCE

---

## AGARD ADVISORY REPORT 319

### Hypersonic Experimental and Computational Capability, Improvement and Validation

(l'Hypersonique expérimentale et de calcul – capacité, amélioration et validation)

#### Volume II

##### Editors

Jean Muylaert  
ESTEC  
Aerothermodynamics Section  
Postbus 299  
2200 AG Noordwijk  
THE NETHERLANDS

Ajay Kumar  
NASA Langley Research Center  
M/S 285  
Hampton, VA 23681-0001  
USA

Christian Dujarric  
ESA, D/LAU-F  
8-10, rue Mario Nikis  
75015 Paris  
FRANCE

*This Advisory Report was prepared at the request of the Fluid Dynamics Panel.*



North Atlantic Treaty Organization  
Organisation du Traité de l'Atlantique Nord

---

AQF99-06-1174

# The Mission of AGARD\*

According to its Charter, the mission of AGARD is to bring together the leading personalities of the NATO nations in the fields of science and technology relating to aerospace for the following purposes:

- Recommending effective ways for the member nations to use their research and development capabilities for the common benefit of the NATO community;
- Providing scientific and technical advice and assistance to the Military Committee in the field of aerospace research and development (with particular regard to its military application);
- Continuously stimulating advances in the aerospace sciences relevant to strengthening the common defence posture;
- Improving the co-operation among member nations in aerospace research and development;
- Exchange of scientific and technical information;
- Providing assistance to member nations for the purpose of increasing their scientific and technical potential;
- Rendering scientific and technical assistance, as requested, to other NATO bodies and to member nations in connection with research and development problems in the aerospace field.

The highest authority within AGARD is the National Delegates Board consisting of officially appointed senior representatives from each member nation. The mission of AGARD is carried out through the Panels which are composed of experts appointed by the National Delegates, the Consultant and Exchange Programme and the Aerospace Applications Studies Programme. The results of AGARD work are reported to the member nations and the NATO Authorities through the AGARD series of publications of which this is one.

Participation in AGARD activities is by invitation only and is normally limited to citizens of the NATO nations.

\* AGARD merged with the Defence Research Group of NATO (DRG) on 1 January 1998 to form the Research and Technology Organization (RTO) of NATO. However, both AGARD and DRG will continue to issue publications under their own names in respect of work performed in 1997.

The content of this publication has been reproduced  
directly from material supplied by AGARD or the authors.



*Printed on recycled paper*

Published December 1998

Copyright © RTO/NATO 1998  
All Rights Reserved

ISBN 92-836-1078-4



*Printed by Canada Communication Group Inc.  
(A St. Joseph Corporation Company)  
45 Sacré-Cœur Blvd., Hull (Québec), Canada K1A 0S7*

# **Hypersonic Experimental and Computational Capability, Improvement and Validation**

**(AGARD AR-319 Vol. II)**

## **Executive Summary**

The present report is a summary of four years of activity by the AGARD Fluid Dynamics Panel's Working Group WG-18. This Working Group was composed of a group of senior managers and researchers from the United States and Western Europe. An initial report, which summarized the first two years of the Working Group, was published in May 1996.

A series of experiments conducted on standard test models in a wide range of hypersonic facilities provided a unique opportunity for facility and computational fluid dynamics code development. In addition, the Working Group contributed to the success of the initial calibration and shake-out of four new real-gas facilities.

This work has resulted in a better focusing of the major issues remaining in hypersonic vehicle design, and to a wide range of recommendations to address these issues. Specifically, it is recommended that resources be allocated within the NATO nations to:

- Resolve facility, computational and modeling deficiencies with targeted research efforts
- Accelerate the multiple facility/multiple computational strategy with standard models

The need for sustained hypersonic flight has been expressed by a number of NATO member states. Support of the above recommendations and the definition of specific NATO-wide projects, which will serve as drivers for increased collaboration in the future, would greatly advance the state of the art for Hypersonic Vehicle Design.



# **L'hypersonique expérimentale et de calcul – capacité, amélioration et validation**

**(AGARD AR-319 Vol. II)**

## **Synthèse**

Ce rapport est un résumé de quatre années d'activités du groupe de travail WG-18 du Panel AGARD de la dynamique des fluides. Le groupe a été composé de cadres supérieurs et de chercheurs des Etats-Unis et de l'Europe occidentale. Un premier rapport, résumant les deux premières années de travaux, a été diffusé au mois de mai 1996.

Une série d'expériences, réalisées sur des maquettes normalisées, dans des installations hypersoniques très diverses, a permis le développement en parallèle des installations et des codes de calcul. En outre, le groupe de travail a contribué au succès de l'étalonnage initial et à la mise en service de 4 nouvelles installations à gaz réel.

Ces travaux ont permis une meilleure compréhension des principales difficultés qui restent à résoudre dans le domaine de la conception des véhicules hypersoniques, et ont donné lieu à des recommandations permettant de les aborder. En particulier, il est recommandé que des ressources soient affectées au sein des pays membres de l'OTAN, afin de :

- Suppléer les carences au niveau des installations, des maquettes et des codes de calcul par des efforts de recherche bien ciblés
- Accélérer le progrès de la stratégie « installations multiples/calculs multiples » par l'adoption de maquettes normalisées

La capacité de vol hypersonique soutenu a été demandée par bon nombre de pays membres de l'OTAN. L'approbation et l'appui de ces recommandations, ainsi que la définition de projets spécifiques tout-OTAN pourraient être le moteur d'une collaboration plus intensive à l'avenir, qui feraient progresser de façon considérable l'état actuel des connaissances dans le domaine de la conception des véhicules hypersoniques.

# Contents

	Page
<b>Executive Summary</b>	<b>iii</b>
<b>Synthèse</b>	<b>iv</b>
<b>Preface</b>	<b>vi</b>
<b>Recent Publications of the Former AGARD Fluid Dynamics Panel</b>	<b>vii</b>
	<b>Reference</b>
<b>Shock Wave Boundary Layer Interactions in High Mach Number Flows A Critical Survey of Current Numerical Prediction Capabilities</b> by D.D. Knight and G. Degrez	<b>1</b>
<b>Hypersonic Laminar-Turbulent Transition</b> by W.S. Saric, E. Reshotko and D. Arnal	<b>2</b>
<b>Rarefied Flow</b> by J.N. Moss and J.-C. Lengrand	<b>3</b>
<b>Real Gas / Blunt Cone Phase II Report</b> by G.S. Deiwert and G. Eitelberg	<b>4</b>
<b>Extrapolation from Wind Tunnel to Flight: Shuttle Orbiter Aerodynamics</b> by J. Muylaert, L. Walpot, P. Rostand, M. Rapuc, G. Brauckmann, J. Paulson, D. Trockmorton and K. Weilmuenster	<b>5</b>
<b>Real-Gas Aerothermodynamics Test Facilities</b> by J.O. Arnold and G.L. Seibert and J.F. Wendt	<b>6</b>
<b>Conclusions/Recommendations</b>	<b>7</b>

# Preface

The world-wide research and technology development activities in hypersonics seems to follow a cycle due to the programs linked with the appearance of a new generation of vehicles. A tremendous effort was made to develop hypersonic technology during the Apollo era. During this period, technology superiority was at stake and cost was not an issue. A second peak of activities occurred in the United States with the development of the Space Shuttle, followed by technology programs such as Hermes and NASP. Finally, the current hypersonic activities are emerging with a focus on the development of low cost reusable launch vehicles. This new generation of vehicles is totally driven by economic aspects, but it does have implications on military capabilities.

The scientific community adapts to these cyclic activities with great difficulty. It is hard to maintain the necessary skills and facilities when there are no approved hypersonic projects. It is even more difficult to re-create them when new projects do appear. Although it may not have been the original objective of this Working Group, which was under the auspices of the AGARD Fluid Dynamics Panel (FDP), the Working Group has contributed to maintain an interest in hypersonics within NATO during the period 1991-1997 when programs like NASP in the United States and Hermes in Europe were progressively abandoned, and the reusable launch vehicle projects were not yet firmly in place. This period was the right time to turn towards hypersonic capabilities, and look at what could be put together, within NATO, to enhance confidence in hypersonic analysis and design tools. The WG18 exploited the opportunity well, and significant advances have been made in understanding hypersonic physics and in validating hypersonic analysis and design tools. In addition, durable links have been established amongst participants from various countries.

The present AGARD Advisory Report is the second and final volume edited by the WG18. Whereas the first volume was mainly focused upon the design methodology, plans, and initial results of experiments conducted to serve as validation benchmarks, the current volume presents a detailed experimental data base and the corresponding computations.

The members of the working group who co-ordinated and contributed to the effort in the second phase are as follows:

## **Belgium**

G.DEGREZ  
J.MUYLAERT (Panel Member Secretary)  
J.WENDT

## **France**

J.ALLEGRE  
D.ARNAL  
B.CHANETZ  
J.DELERY  
C.DUJARRIC (Panel Member-Chairman)  
H.HOLLANDERS (Panel Member)  
J.LENGRAND  
P.ROSTAND

## **Germany**

K.KIENAPPEL (former Chairman)  
G.EITELBERG  
P.KROGMAN

## **Greece**

A.PANARAS (Panel Member)

## **Italy**

M.BORSI (Panel Member)  
C.GOLIA (Panel Member)  
G.RUSSO  
M.PANDOLFI

## **United States**

J.ARNOLD  
W.CALARESE  
G.DEIWERT  
M.HOLDEN  
D.KNIGHT  
A.KUMAR (Co-Chairman)  
J.MOSS  
W.SARIC  
G.SEIBERT  
L.WILLIAMS (Panel Member)

The Chairman and Co-Chairman would like to extend their special thanks to Mr Jean Muylaert, who served as secretary to the group for the entire period. Mr Muylaert was responsible for maintaining high technical quality of the output of WG18. He is also the principal editor for this final report.

# **Recent Publications of the Former AGARD Fluid Dynamics Panel**

## **AGARDOGRAPHS (AG)**

### **Turbulent Boundary Layers in Subsonic and Supersonic Flow**

AGARD AG-335, July 1996

### **Computational Aerodynamics Based on the Euler Equations**

AGARD AG-325, September 1994

### **Scale Effects on Aircraft and Weapon Aerodynamics**

AGARD AG-323 (E), July 1994

### **Design and Testing of High-Performance Parachutes**

AGARD AG-319, November 1991

### **Experimental Techniques in the Field of Low Density Aerodynamics**

AGARD AG-318 (E), April 1991

## **CONFERENCE PROCEEDINGS (CP) AND MEETING PROCEEDINGS (MP)**

### **Missile Aerodynamics**

RTO Report MP-5, November 1998

### **Advanced Aerodynamic Measurement Technology**

AGARD CP-601, May 1998

### **Aerodynamics of Wind Tunnel Circuits and Their Components**

AGARD CP-585, June 1997

### **The Characterization & Modification of Wakes from Lifting Vehicles in Fluids**

AGARD CP-584, November 1996

### **Progress and Challenges in CFD Methods and Algorithms**

AGARD CP-578, April 1996

### **Aerodynamics of Store Integration and Separation**

AGARD CP-570, February 1996

### **Aerodynamics and Aeroacoustics of Rotorcraft**

AGARD CP-552, August 1995

### **Application of Direct and Large Eddy Simulation to Transition and Turbulence**

AGARD CP-551, December 1994

### **Wall Interference, Support Interference, and Flow Field Measurements**

AGARD CP-535, July 1994

### **Computational and Experimental Assessment of Jets in Cross Flow**

AGARD CP-534, November 1993

### **High-Lift System Aerodynamics**

AGARD CP-515, September 1993

### **Theoretical and Experimental Methods in Hypersonic Flows**

AGARD CP-514, April 1993

### **Aerodynamic Engine/Airframe Integration for High Performance Aircraft and Missiles**

AGARD CP-498, September 1992

### **Effects of Adverse Weather on Aerodynamics**

AGARD CP-496, December 1991

### **Manoeuvring Aerodynamics**

AGARD CP-497, November 1991

### **Vortex Flow Aerodynamics**

AGARD CP-494, July 1991

## **ADVISORY REPORTS (AR)**

### **A Selection of Test Cases for the Validation of Large-Eddy Simulations of Turbulent Flows**

AGARD AR-345, April 1998

### **Ice Accretion Simulation**

AGARD AR-344, Report of WG-20, December 1997

### **Sonic Nozzles for Mass Flow Measurement and Reference Nozzles for Thrust Verification**

AGARD AR-321, Report of WG-19, June 1997

### **Cooperative Programme on Dynamic Wind Tunnel Experiments for Manoeuvring Aircraft**

AGARD AR-305, Report of WG-16, October 1996

### **Hypersonic Experimental and Computational Capability, Improvement and Validation**

AGARD AR-319, Vol. I, Report of WG-18, May 1996

### **Aerodynamics of 3-D Aircraft Afterbodies**

AGARD AR-318, Report of WG-17, September 1995

### **A Selection of Experimental Test Cases for the Validation of CFD Codes**

AGARD AR-303, Vols. I and II, Report of WG-14, August 1994

### **Quality Assessment for Wind Tunnel Testing**

AGARD AR-304, Report of WG-15, July 1994

### **Air Intakes of High Speed Vehicles**

AGARD AR-270, Report of WG-13, September 1991

### **Appraisal of the Suitability of Turbulence Models in Flow Calculations**

AGARD AR-291, Technical Status Review, July 1991

## **EDUCATIONAL NOTES (EN)**

### **Fluid Dynamic Research on Supersonic Aircraft**

RTO EN-4, Special Course Notes, November 1998

## **REPORTS (R)**

### **High Speed Body Motion in Water**

AGARD R-827, February 1998

### **Turbulence in Compressible Flows**

AGARD R-819, Special Course Notes, June 1997

### **Advances in Cryogenic Wind Tunnel Technology**

AGARD R-812, Special Course Notes, January 1997

### **Aerothermodynamics and Propulsion Integration for Hypersonic Vehicles**

AGARD R-813, Special Course Notes, October 1996

### **Parallel Computing in CFD**

AGARD R-807, Special Course Notes, October 1995

### **Optimum Design Methods for Aerodynamics**

AGARD R-803, Special Course Notes, November 1994

### **Missile Aerodynamics**

AGARD R-804, Special Course Notes, May 1994

### **Progress in Transition Modelling**

AGARD R-793, Special Course Notes, April 1994

### **Shock-Wave/Boundary-Layer Interactions in Supersonic and Hypersonic Flows**

AGARD R-792, Special Course Notes, August 1993

### **Unstructured Grid Methods for Advection Dominated Flows**

AGARD R-787, Special Course Notes, May 1992

### **Skin Friction Drag Reduction**

AGARD R-786, Special Course Notes, March 1992

### **Engineering Methods in Aerodynamic Analysis and Design of Aircraft**

AGARD R-783, Special Course Notes, January 1992

# Shock Wave Boundary Layer Interactions in High Mach Number Flows

## A Critical Survey of Current Numerical Prediction Capabilities

Doyle D. Knight

Department of Mechanical and Aerospace Engineering  
Rutgers – The State University of New Jersey  
98 Brett Road, Piscataway NJ 08854-8059  
USA

Gérard Degrez

Aerospace Department  
von Karman Institute for Fluid Dynamics  
Chaussée de Waterloo, 72 – B-1640 Rhode-Saint-Genèse  
Belgium

### Abstract

The report assesses the capability for numerical simulation of 2-D and 3-D shock wave laminar and turbulent boundary layer interactions. Three fundamental configurations are considered: single fin, double fin, and hollow cylinder flare. Thirteen separate cases were examined by a distinguished international group of researchers using the Reynolds-averaged Navier-Stokes (RANS) equations with a wide range of turbulence models from zero equation to full Reynolds Stress Equation formulations. The report presents an extensive comparison of computations and experimental data, summarizes the results, and makes recommendations for future research.

Numerous reviews have been published on shock wave boundary layer interaction. Examples include Greene [1], Korkegi [2], Peake and Tobak [3], Delery and Marvin [4], Settles and Dolling [5, 6], Stollery [7], Degrez *et al.* [8], Delery and Panaras [9], and Zheltovodov [10].

The objective of this paper is to assess the capability for simulation of 2-D and 3-D shock wave boundary layer interactions. A test matrix of configurations (Table 1), based on the report of Delery and Panaras [9], was established. An international group of researchers (Table 2) participated in computation of one or more of the cases by using a variety of turbulence models. The results are presented in this paper, and conclusions are drawn for future work.

## 1 Introduction

The interaction between shock waves and boundary layers is a common occurrence in aerodynamics and aeropropulsion. Examples include deflection of control surfaces, high speed inlets, rotorcraft, transonic compressors, and wing- and tail-fuselage junctures. The interactions can significantly affect the performance of aeronautical systems. For example, the interaction on a deflected control surface can cause significant changes in the surface pressure and hence control moments.

Table 1: Test Matrix

<i>Configuration</i>	<i>Type</i>	<i>No. Cases</i>
Single fin	Turbulent	7
Double fin	Turbulent	4
Hollow cylinder flare	Laminar	1
Hollow cylinder flare	Turbulent	1

The details of the numerical algorithms, turbulence models and grids are presented in the individual references of the participants. The computations were conducted in a careful manner

to ensure accurate results. In many instances, grid refinement studies were performed to firmly establish the uncertainties in the numerical solutions. The reader is referred to the individual participants for further information regarding the numerical methodology.

Table 2: Participants

Participant	Organization
Greg Alexopoulos	North Carolina State Univ
J.-M. Bousquet	ONERA
R. Bur	ONERA
G�rard Degrez	Von Karman Institute
Jack Edwards	North Carolina State Univ
Datta Gaitonde	Wright Labs, WPAFB, OH
Marianna Gnedin	Rutgers University
F. Grasso	Universit� di Roma
Hassan Hassan	North Carolina State Univ
C. C. Horstman	NASA Ames
Doyle Knight	Rutgers University
James Moss	NASA Langley
Natraj Narayanswami	Rutgers University
Argyris Panaras	Hellenic AF Academy
Patrick Rodi	Univ of Texas-Austin
Balu Sekar	Wright Labs, WPAFB, OH
Edwin Van der Weide	Von Karman Institute
Gecheng Zha	Rutgers University

## 2 Single Fin

The single fin geometry is a wedge of angle  $\alpha$  attached normal to a flat plate (Fig. 1) on which an equilibrium turbulent boundary layer has developed. The wedge generates an oblique shock wave which interacts with the boundary layer on the flat plate. The flow parameters are the Mach number  $M_\infty$ , Reynolds number  $Re_{\delta_\infty}$  based on the upstream boundary layer thickness  $\delta_\infty$ , fin angle  $\alpha$ , and wall temperature ratio  $T_w/T_\infty$ . The fin is assumed to be semi-infinite in height and length.

The flowfield structure of the single fin interaction is generally understood. Detailed descriptions are presented in Alvi and Settles [11] and Zheltovodov and Shilein [12]. Provided that the shock strength is sufficient to cause separation, the wave structure and mean streamline pattern are approximately conical (see, for example, [13, 11]). Conical flow is defined in Appendix A. Thus, for example, the surface pressure and sur-

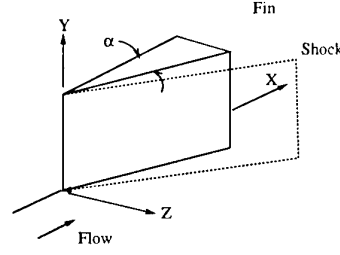


Figure 1: Single fin geometry

face flow visualization display conical behavior outside of an "inception zone" near the fin. An example (from [11]) is shown in Fig. 2 corresponding to case SF4 of this study. The wave structure includes a bifurcated shock ( $\lambda$ -shock) and slip line. The boundary layer separates to form a vortex whose center is approximately beneath the primary inviscid shock. Additional features may appear, depending on the shock strength including secondary separation of the boundary layer beneath the vortex, a normal shock in the impinging jet which turns back over the vortex, and supersonic reversed flow. Further discussion of these features is presented, for example, in Alvi and Settles [11], Zheltovodov *et al* [14] and Zubin and Ostapenko [15]. Other aspects of the single fin interaction flowfield do not display conical behavior, *e.g.*, the surface heat transfer [16]. Overall, therefore, the single fin interaction can be viewed as *quasi*-conical.

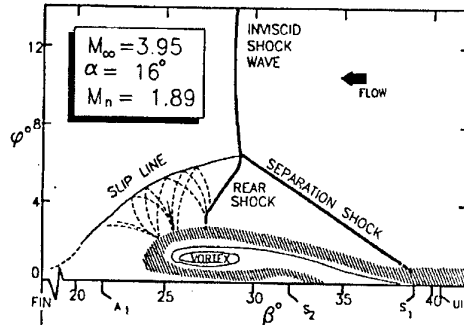


Figure 2: Flowfield structure (Case SF4) [11]

Seven configurations were computed by one or more of the participants. The flow conditions are shown in Table 3. The cases are ordered by the value of the normal Mach number  $M_n$  which determines the shock strength according to

$$\frac{p_2}{p_1} = \frac{2\gamma M_n^2 - (\gamma - 1)}{\gamma + 1} \quad (1)$$

There were five participants in the single fin studies (Table 4). Eleven computations employed the RANS equations, and two used the conical RANS equations. The turbulence models employed are shown in Table 5.

Table 3: Single Fin Cases

Case	Ref	$M_n$	$M_\infty$	$\alpha$	$Re_{\delta_\infty}$ ( $\times 10^5$ )	$T_w/T_{aw}$
SF1	[16]	1.50	4.9	8°	2.3	0.80
SF2	[17]	1.65	3.0	16°	1.9	1.06
SF3	[18]	1.82	2.9	20°	8.1	1.00
SF4	[17]	1.89	4.0	16°	2.1	1.06
SF5	[16]	2.12	4.9	16°	2.3	0.80
SF6	[17]	2.14	4.0	20°	2.1	1.06
SF7	[19]	2.90	8.2	15°	1.8	0.28

Note: Most experimental data tabulated in [20].

LEGEND			
$M_n$	$M_\infty \sin \theta$	$M_\infty$	Mach number
$\alpha$	Fin angle	$T_w$	Wall temperature
$\theta$	Shock angle	$T_{aw}$	Adiabatic $T_w$
$Re_{\delta_\infty}$	$\rho_\infty U_\infty \delta_\infty / \mu_\infty$		

Table 4: Participants for Single Fin Cases

Participant/SF	1	2	3	4	5	6	7
Jack Edwards						•	•
C. C. Horstman			•	•		•	
Doyle Knight			•	•		•	
Argyris Panaras		•		•		•	
Patrick Rodi	★				★		

LEGEND  
• RANS ★ Conical RANS

## 2.1 Case SF1

The computations solved the conical form of the Navier-Stokes equations using the Baldwin-Lomax turbulence model. A grid refinement study was performed using three separate grids which yielded a grid independent solution. Computations using conical Navier-Stokes equations must be viewed with some skepticism. As indicated previously, the surface pressure exhibits conical behavior, while the surface heat transfer does not.

Table 5: Turbulence Models for Single Fin

Participant	Model	Ref
J. Edwards	Spalart-Allmaras-Edwards	[21]
C. C. Horstman	$k - \epsilon$	[22]
D. Knight	Baldwin-Lomax	[23]
A. Panaras	Baldwin-Lomax-Panaras	[24]
P. Rodi	Baldwin-Lomax	[23]

The surface pressure is shown in Fig. 3. The abscissa is  $\beta$  (see Appendix A) measured from the virtual conical origin [16], and the ordinate is the wall pressure normalized by the freestream static pressure. There is general agreement. However, the computations underestimate the location of the beginning of the pressure rise which is typical for the Baldwin-Lomax model [25]. No experimental data are close to the fin, and therefore comparison of the computed and experimental results for the location and level of the maximum pressure is not possible [16].

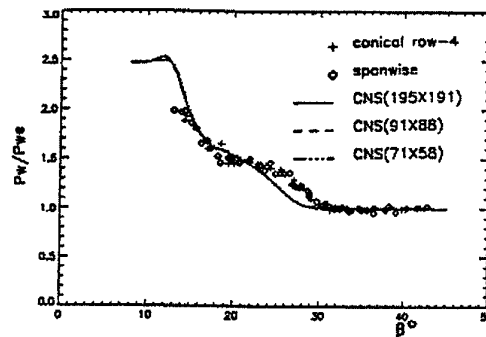


Figure 3: Surface pressure (Case SF1)

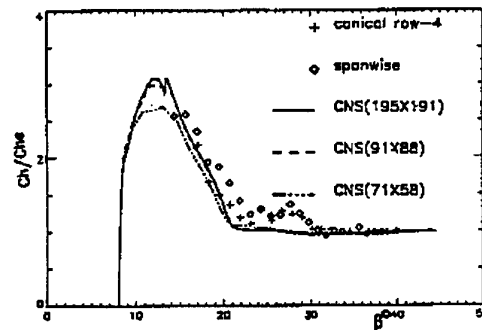


Figure 4: Heat transfer (Case SF1)

The heat transfer is shown in Fig. 4. The abscissa is  $\beta$ , and the ordinate is the heat transfer



coefficient normalized by its value immediately outside the interaction. Reasonable agreement is observed, except in the vicinity of the initial pressure rise ( $\beta \approx 30^\circ$ ). However, as noted previously, the experimental heat transfer does not behave in a conical manner, and thus the agreement may be somewhat fortuitous.

## 2.2 Case SF2

The surface pressure is shown in Fig. 5. The agreement between the Baldwin-Lomax-Panaras model and experiment is very good. The computation predicts both the plateau pressure, associated with the primary vortex (Fig. 2), and the peak pressure near the fin within 8%. The location of the beginning of the pressure rise is slightly underestimated.

The surface streamline angle  $\Phi$  on the flat plate, measured relative to the freestream direction  $x$ , is displayed in Fig. 6. The ordinate is  $\Phi - \beta$  in order to identify the separation and attachment lines which correspond to  $\Phi - \beta = 0$ . Good agreement is observed between the computation and experiment. The location of the primary separation line ( $\beta = 45^\circ$ ), secondary (incipient) separation line ( $\beta = 37^\circ$ ) and primary attachment line ( $\beta = 21^\circ$ ) are accurately predicted.

The skin friction coefficient  $c_f$  on the flat plate is shown in Fig. 7. The agreement is generally good. The computed skin friction displays a peak at  $\beta = 25^\circ$  which is not evident in the experiment. However, the number of experimental data points in this region is small, and thus a conclusive judgment on the accuracy of the  $c_f$  predictions cannot be made. For further discussion, see Panaras [24]. Minor discrepancies appear in the vicinity of the primary separation line at  $\beta = 45^\circ$ .

## 2.3 Case SF3

The surface pressure at a fixed spanwise location  $z/\delta_\infty = 6.8$  are shown in Fig. 8. The agreement is very good. There is very little difference between the predictions using the Baldwin-Lomax ("Theory-Knight") and  $k-\epsilon$  ("Theory-Horstman") models.

The locations of selected streamwise stations for comparison of computed and experimental pitot

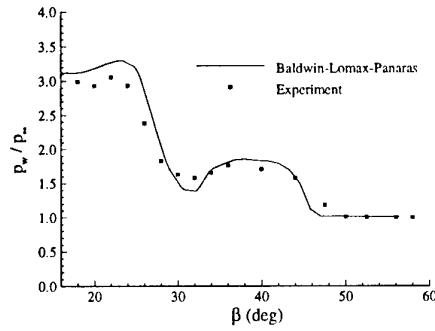


Figure 5: Surface pressure (Case SF2)

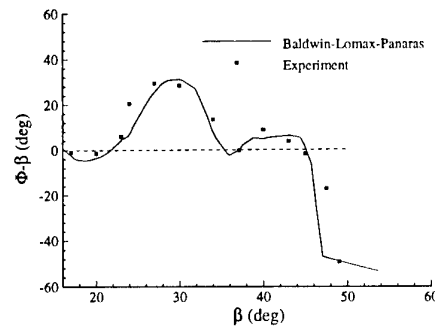


Figure 6: Surface streamline angle (Case SF2)

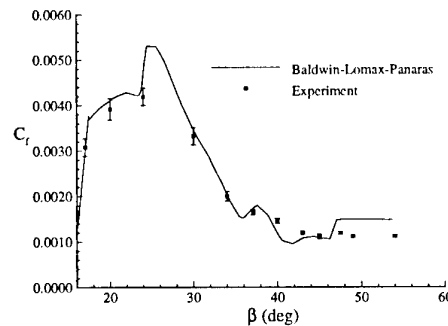


Figure 7: Skin friction coefficient (Case SF2)

pressure and yaw angle are shown in Fig. 9. The yaw angle is defined as  $\tan^{-1}(w/u)$  where  $u$  and  $w$  are the mean velocity components in the  $x$ - and  $z$ - directions, respectively. Location 5 is downstream of the separation line (line of coalescence) and upstream of the inviscid shock. Location 7 is close to the inviscid shock. Location 8 is downstream of the inviscid shock. Pitot pressure profiles are displayed in Figs. 10 to 12. The agreement is good<sup>1</sup>. In particular, the pitot pressure deficit associated with the primary vortex (at  $y/\delta_\infty = 0.5$  in Fig. 11) is accurately predicted. Yaw angle profiles are shown in Figs. 13 to 15. Close agreement is again observed, except in the immediate vicinity of the surface (at  $y/\delta_\infty < 0.5$  in Fig. 14). Overall, there are small differences between the predictions using the Baldwin-Lomax and  $k-\epsilon$  models.

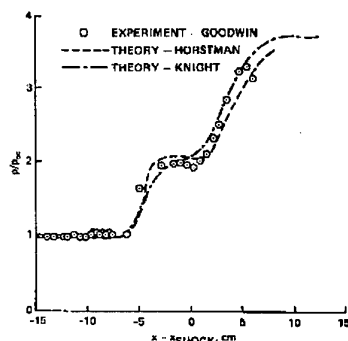


Figure 8: Surface pressure (Case SF3)

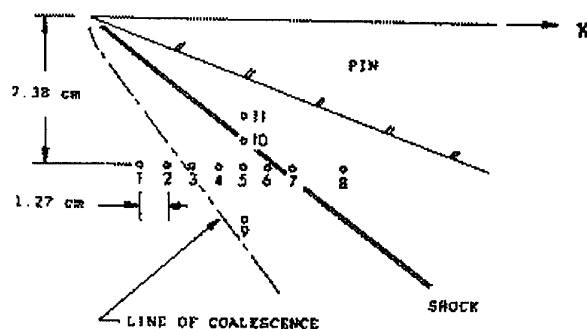


Figure 9: Location of surveys (Case SF3)

<sup>1</sup>The region  $y/\delta_\infty > 2$  in Fig. 11 is within the computed inviscid shock which is diffused over two to three grid cells, and therefore the differences in computed freestream pitot pressures are not significant.

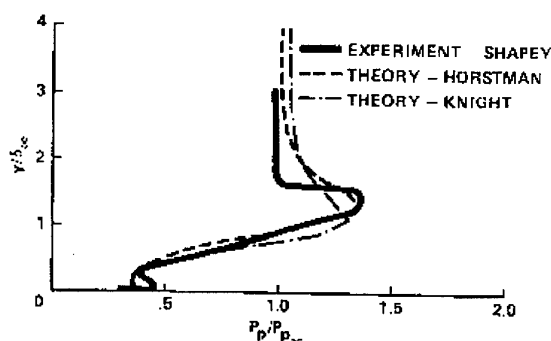


Figure 10: Pitot pressure at station 5 (Case SF3)

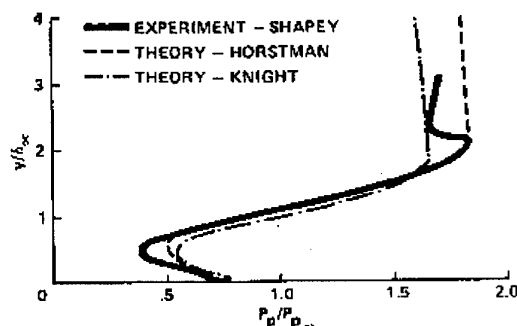


Figure 11: Pitot pressure at station 7 (Case SF3)

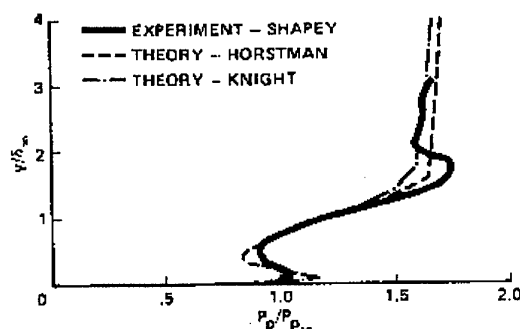


Figure 12: Pitot pressure at station 8 (Case SF3)

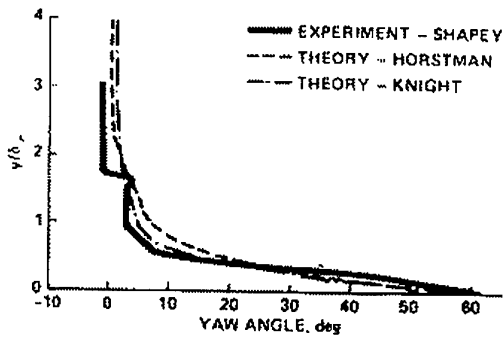


Figure 13: Yaw angle at station 5 (Case SF3)

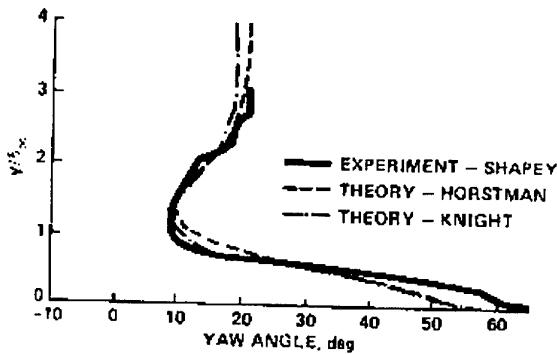


Figure 14: Yaw angle at station 7 (Case SF3)

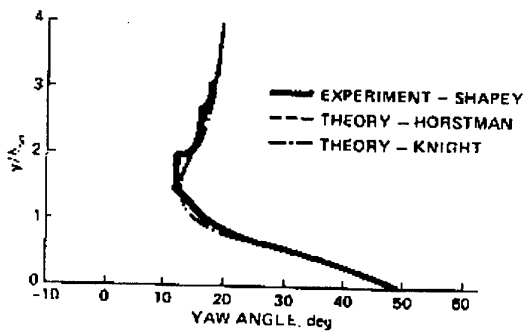


Figure 15: Yaw angle at station 8 (Case SF3)

## 2.4 Case SF4

The surface pressure is shown in Fig. 16. The Baldwin-Lomax-Panaras model is the most accurate. It predicts the plateau pressure within 5%, and the pressure trough (at  $\beta = 27^\circ$ ) within 13%. However, the peak pressure in the vicinity of the corner is overpredicted by 9%. The Baldwin-Lomax model underestimates slightly the location of the beginning of the pressure rise and fails to predict the pressure trough. However, it predicts the peak pressure at the corner within 4%. The  $k-\epsilon$  model is the least accurate.

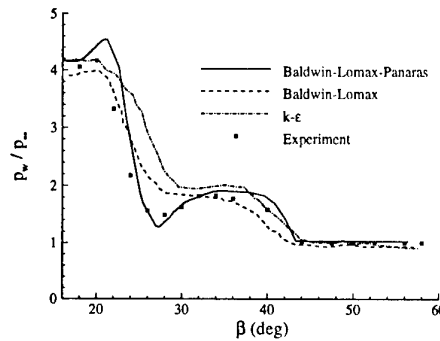


Figure 16: Surface pressure (Case SF4)

The surface streamline angle on the flat plate is displayed in Fig. 17. The ordinate is  $\Phi - \beta$ . The Baldwin-Lomax-Panaras is again the most accurate. It predicts the primary separation angle ( $\beta = 41^\circ$ ) within 4%, and the (incipient) secondary separation ( $\beta = 33^\circ$ ) within 9%. The Baldwin-Lomax and  $k-\epsilon$  models also predict the primary angle within 4%; however, both fail to predict the secondary separation.

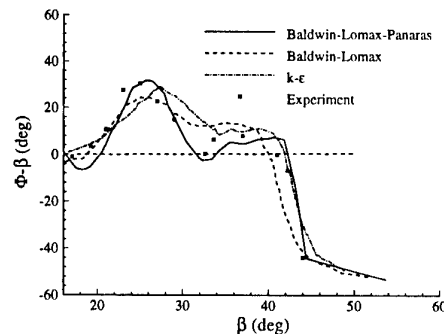


Figure 17: Surface streamline angle (Case SF4)

The skin friction coefficient is displayed in Fig. 18. The Baldwin-Lomax-Panaras model is more accurate, generally providing accurate prediction over the entire range of the interaction. The Baldwin-Lomax and  $k-\epsilon$  models display the general trends of the experiment, but underestimate the peak skin friction by 30% to 35%.

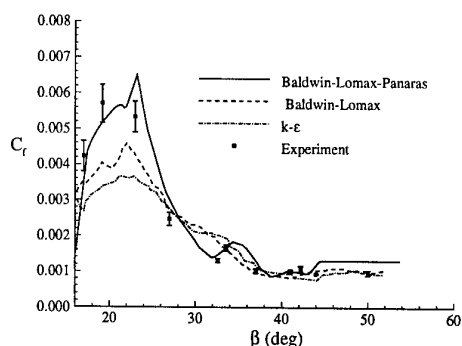


Figure 18: Skin friction coefficient (Case SF4)

## 2.5 Case SF5

The surface pressure is shown in Fig. 19. There is general agreement between the predictions using the Baldwin-Lomax model and the experiment. However, as observed in Case SF1, the computation underestimates the location of the beginning of the pressure rise. Since there are no experimental data close to the fin, comparison of the computed and experimental results for the location and level of the maximum pressure is not possible [16].

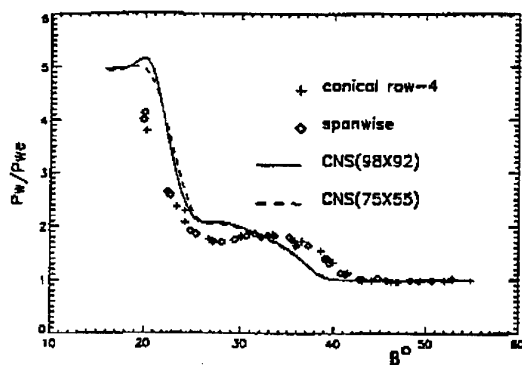


Figure 19: Surface pressure (Case SF5)

The heat transfer is shown in Fig. 20. Reasonable agreement is again observed, similar to Case SF1, except in the vicinity of the initial

pressure rise ( $\beta \approx 40^\circ$ ). However, the experimental heat transfer does not behave in a conical manner, and thus the good agreement may be fortuitous.

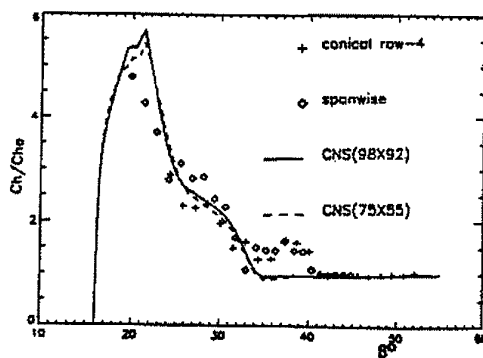


Figure 20: Heat transfer (Case SF5)

## 2.6 Case SF6

The surface pressure is shown in Fig. 21. The Baldwin-Lomax-Panaras and Spalart-Allmaras-Edwards models are the most accurate. Both models predict the surface pressure in the plateau region ( $36^\circ \leq \beta \leq 47^\circ$ ) within 5% to 10%. Also, both models display a pressure trough at  $\beta = 32^\circ$ , in agreement with the experiment, although the predictions differ from the experimental value by 30%. Both models overestimate the peak pressure in the vicinity of the corner by 11%. The predictions of the Baldwin-Lomax and  $k-\epsilon$  models exhibit the general trends of the experiment but are less accurate.

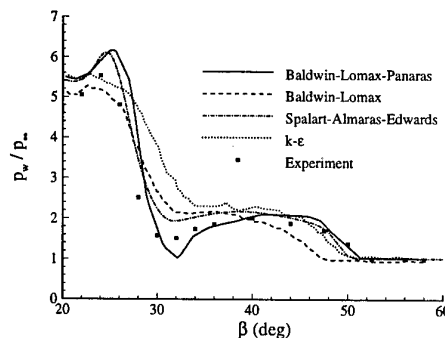


Figure 21: Surface pressure (Case SF6)

The surface streamline angle on the flat plate is displayed in Fig. 22. The Baldwin-

Lomax-Panaras is again the most accurate, with the Spalart-Allmaras-Edwards model providing nearly comparable results. The principal difference between the two predictions is in the region of the secondary separation at  $\beta = 40^\circ$ . Again, the Baldwin-Lomax and  $k-\epsilon$  models show general agreement with experiment, but are less accurate.

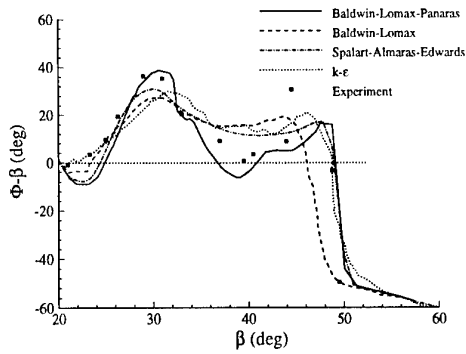


Figure 22: Surface streamline angle (Case SF6)

The skin friction coefficient is displayed in Fig. 23. The Baldwin-Lomax-Panaras and Spalart-Allmaras-Edwards models predict a peak in the vicinity of the corner which is not evident in the experiment<sup>2</sup>; in particular, their computed values at the experimental location  $\beta = 26.5^\circ$  are substantially above the experiment. Additional measurements in the region  $22^\circ < \beta < 26^\circ$  would be helpful in determining whether a peak appears<sup>3</sup>. Elsewhere, all four models provide generally good agreement with the experiment.

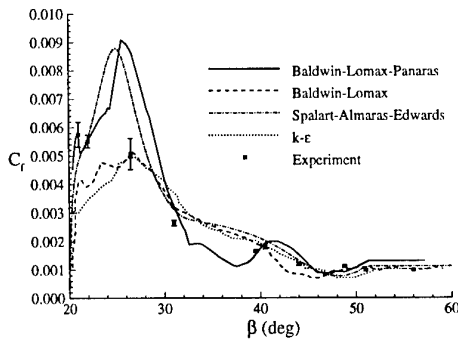


Figure 23: Skin friction coefficient (Case SF6)

<sup>2</sup>Corrected data for  $\beta = 22^\circ$  and  $26.5^\circ$ , provided by Prof. G. Settles, is included in Fig. 23.

<sup>3</sup>Note that the attachment line is  $\beta = 26^\circ$  [11].

## 2.7 Case SF7

The surface pressure on the flat plate at  $x/\delta_\infty = 4.9$  is displayed in Fig. 24. The agreement is very good. The Spalart-Allmaras-Edwards model provides an accurate prediction of the pressure distribution over the entire region. The peak pressure in the corner is predicted within 10%. The surface pressure on the fin at  $x/\delta_\infty = 4.8$  is shown in Fig. 25. Similar close agreement is observed.

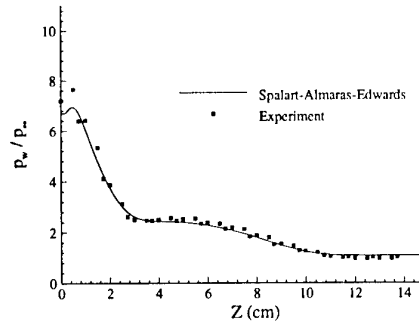


Figure 24: Surface pressure on plate (Case SF7)

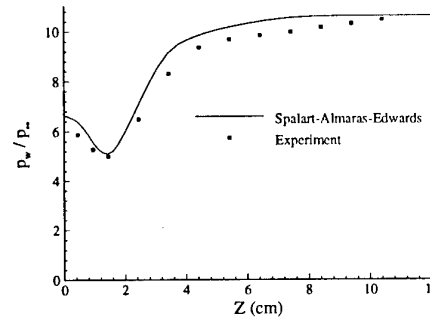


Figure 25: Surface pressure on fin (Case SF7)

The skin friction coefficient  $c_f$  is presented in Fig. 26. The agreement is very good. The peak  $c_f$  in the vicinity of the corner is predicted within the experimental uncertainty.

The heat transfer  $Q_w$ , normalized by the corresponding value in the upstream boundary layer  $Q_\infty$ , is displayed in Figs. 27 and 28 for the flat plate and fin surfaces, respectively, at  $x/\delta_\infty = 4.4$ . The agreement is reasonably good. On the flat plate, the peak heat transfer in the vicinity of the corner is overpredicted by 35%, and underestimated in the plateau region typically

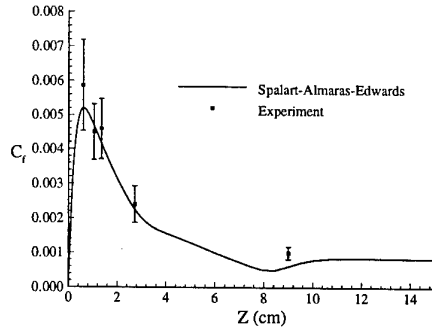


Figure 26: Skin friction on plate (Case SF7)

by 30%. A significant difference is evident on the fin surface away from the corner which is attributable to the assumption of fully turbulent flow from the leading edge in the computation. In the experiment, the boundary layer at this location and outside of the corner interaction was laminar.

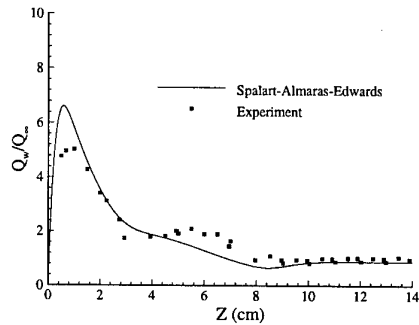


Figure 27: Heat transfer on plate (Case SF7)

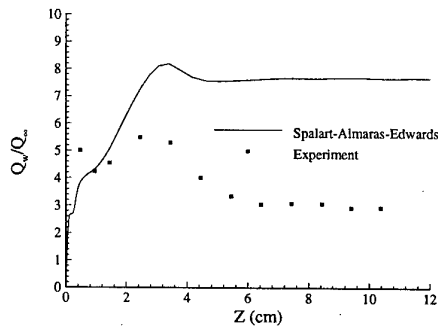


Figure 28: Heat transfer on fin (Case SF7)

### 3 Double Fin

The double fin ("crossing shock") geometry consists of two wedges of angles  $\alpha_1$  and  $\alpha_2$  affixed normal to a flat plate (Fig. 29) on which an equilibrium turbulent boundary layer has developed. The wedges generate intersecting oblique shock waves which interact with the boundary layers on the flat plate and inner fin surfaces. The flow parameters are the Mach number  $M_\infty$ , Reynolds number  $Re_{\delta_\infty}$ , fin angles  $\alpha_1$  and  $\alpha_2$ , contraction ratio  $L_2/L_1$ , throat middle line offset  $L_3/L_1$ , boundary layer to throat width ratio  $\delta_\infty/L_2$ , and wall temperature ratio  $T_w/T_{aw}$ . The fins are assumed semi-infinite in height. For the symmetric double fin,  $L_3 = 0$ .

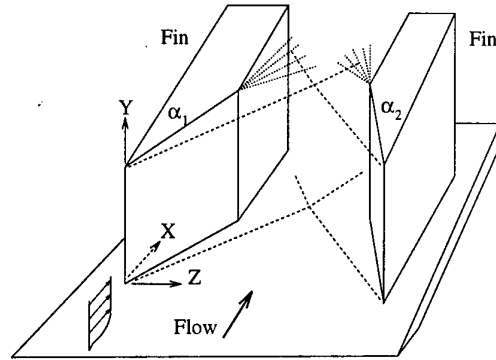


Figure 29: Double fin geometry

The flowfield structure of the double fin interaction is only partially understood. The interaction of the incident  $\lambda$ -shocks, generated by the initial single fin interactions, forms a complex wave system which is described in [26, 27, 28, 29, 30, 31] for the symmetric case, and in [32] for the asymmetric case. The principal mean streamline structure is a pair of counter-rotating vortices, generated by the initial single fin interactions, which merge to form a vortex pair which is associated with a region of low total pressure. A detailed discussion of the streamline structure for the symmetric case is presented in [33, 34, 35, 26, 27, 28] and for an asymmetric case in [32]. An example is shown in Fig. 30.

Four configurations were computed by one or more of the participants. The flow conditions are shown in Table 6. The cases are ordered in terms of magnitude of the pressure rise<sup>4</sup>  $p_4/p_1$

<sup>4</sup>This particular choice of ordering, though obvious, is arbitrary. Unlike the single fin configuration, no param-

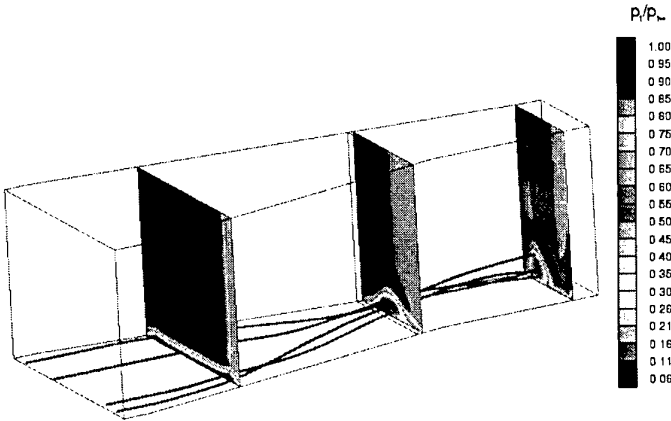


Figure 30: Computed streamlines and total pressure contours (Case DF2) using  $k-\epsilon$  Chien model

Table 6: Double Fin Cases

<i>Case</i>	<i>Ref</i>	$p_4/p_1$	$M_\infty$	$\alpha_1$	$\alpha_2$	$Re_{\delta_\infty}$ ( $\times 10^5$ )	$L_2/L_1$	$L_3/L_1$	$\delta_\infty/L_2$	$T_w/T_{aw}$
DF1	[36]	3.4	4.0	7°	7°	3.1	0.45	0	0.11	1.11
DF2	[36]	4.6	4.0	7°	11°	3.0	0.44	0.014	0.11	1.11
DF3	[37]	10.2	3.9	15°	15°	2.6	0.32	0	0.11	1.06
DF4	[38]	45.0	8.3	15°	15°	1.6	0.28	0	0.75	0.28

LEGEND			
$M_\infty$	Freestream Mach number	$\alpha_1, \alpha_2$	Fin angles
$Re_{\delta_\infty}$	$\rho_\infty U_\infty \delta_\infty / \mu_\infty$	$L_1$	Distance between fins at entrance
$L_2$	Distance between fins at throat	$L_3$	Offset of TML
TML	Throat Middle Line	$T_w$	Wall temperature
$T_{aw}$	Adiabatic wall temperature		

across the intersecting shocks.

There were eleven participants in the double fin studies (Table 7). All computations employed the Reynolds-averaged compressible Navier-Stokes equations. The turbulence models employed are shown in Table 8.

Table 7: Participants for Double Fin Cases

<i>Participant/DF</i>	1	2	3	4
Jack Edwards		•	•	•
Datta Gaitonde			•	•
Mariana Gnedin	•	•		
Hassan Hassan & Greg Alexopoulos		•		•
C. C. Horstman				•
Doyle Knight		•		
Natraj Narayanswami			•	•
Argyris Panaras			•	
Balu Sekar		•		•
GeCheng Zha		•		

### 3.1 Case DF1

The computed skin friction lines using the  $k-\epsilon$  Knight model and experimental surface flow visualization are shown in Figs. 31 and 32. The incident separation lines 1 and 2 which originate at the fin leading edges are visible. The computed and experimental separation line angles agree within 7%. The computed skin friction lines do not intersect. Rather, the lines slowly converge towards each other. Two weak divergence lines 3 and 4 are evident near the fin surfaces.

The surface pressure is shown in Figs. 33 and 34 along the Throat Middle Line<sup>5</sup> (TML) and at the three streamwise locations. The accuracy of the surface pressure measurements is  $\pm 0.5\%$ . The computed surface pressure displays excellent agreement with experiment.

The surface heat transfer coefficient  $c_h$  is displayed in Figs. 35 to 38. The accuracy of the measurements is  $\pm 10\%$  to  $\pm 15\%$ . Reasonable

eter(s) have been demonstrated to appropriately categorize the double fin configuration.

<sup>5</sup>The Throat Middle Line is the streamwise plane which bisects the throat (*i.e.*, the region of minimum cross section).

Table 8: Turbulence Models for Double Fin

<i>Participant</i>	<i>Model</i>	<i>Ref</i>
J. Edwards	Spalart-Allmaras-Edwards	[21]
D. Gaitonde	Baldwin-Lomax (BI,IB)	[26]
	$k-\epsilon$	[28]
	$k-\epsilon$ (CC)	[27, 28]
	$k-\epsilon$ (VC)	[28]
	$k-\epsilon$ (RH)	[28]
M. Gnedin	$k-\epsilon$ Knight	[39]
H. Hassan	$k-\omega$	[40]
C. C. Horstman	$k-\epsilon$ Rodi	[35]
D. Knight	$k-\epsilon$ Chien	[41]
N. Narayanswami	Baldwin-Lomax	[23]
A. Panaras	Baldwin-Lomax-Panaras	[24]
B. Sekar	Baldwin-Lomax	[42]
G. Zha	Reynolds Stress Equation	[43]

#### LEGEND

- BI Buleev Integral
- CC Compressibility correction
- IB Inverse blending
- RH Rodi-Horstman length scale modification
- VC Vuong-Coakley length scale modification

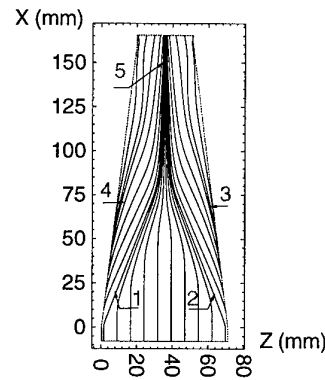


Figure 31: Computed skin friction lines (Case DF1):

- 1 Left incident separation line
- 2 Right incident separation line
- 3, 4 Lines of divergence
- 5 Downstream coalescence line



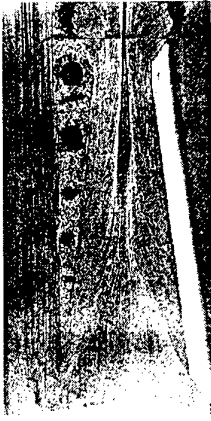


Figure 32: Experimental surface flow (Case DF1)

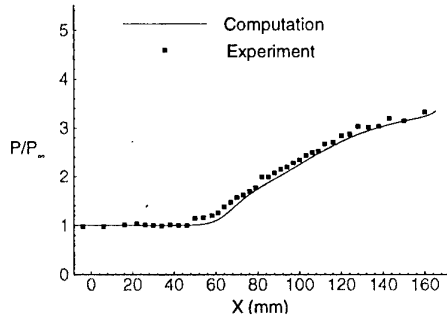


Figure 33: Wall pressure on TML (Case DF1)

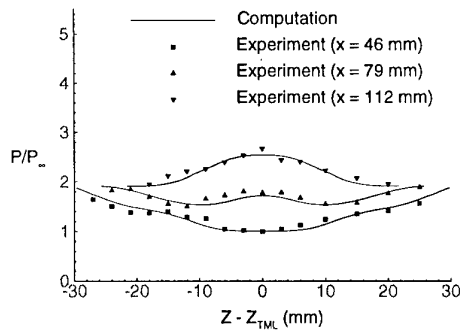


Figure 34: Wall pressure at  $x = 46$  mm,  $x = 79$  mm and  $x = 112$  mm (Case DF1)

agreement with the experiment is observed. On the TML, the heat transfer coefficient is predicted typically within 25% in the 3-D interaction region.

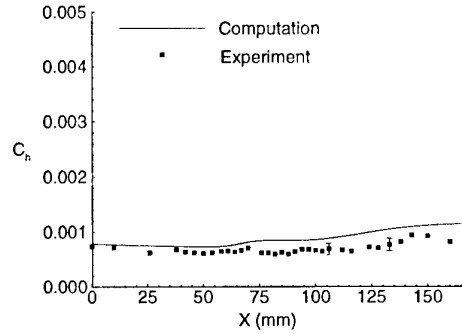


Figure 35:  $C_h$  on TML (Case DF1)

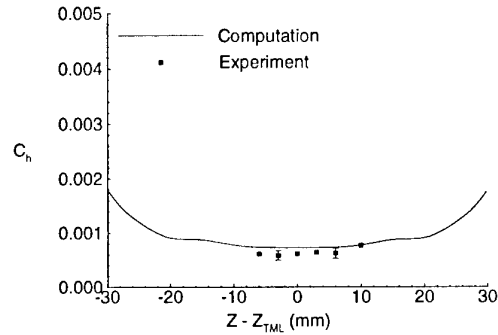


Figure 36:  $C_h$  at  $x = 46$  mm (Case DF1)

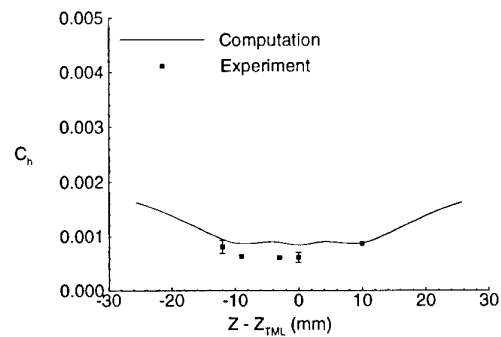
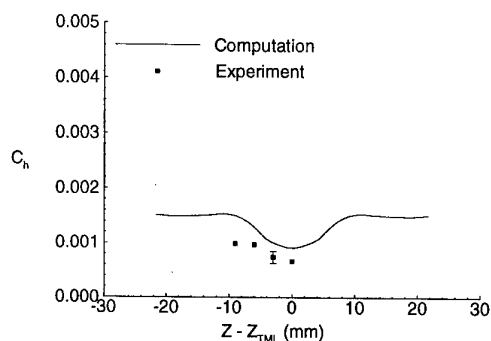
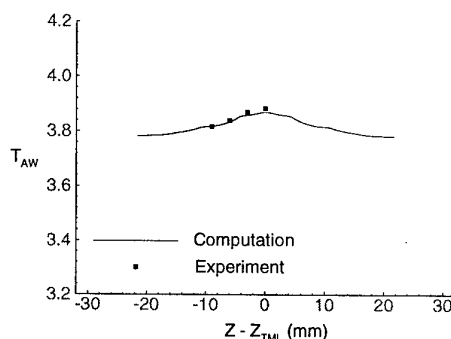
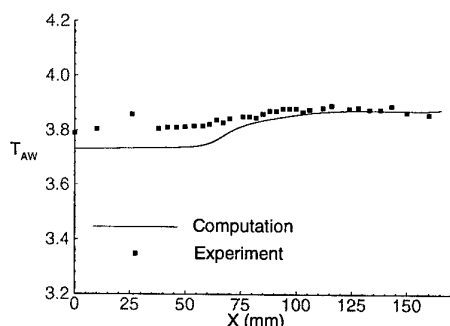
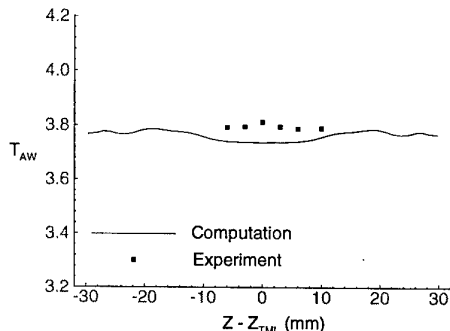
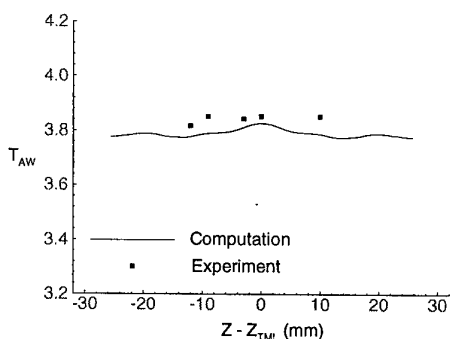


Figure 37:  $C_h$  at  $x = 79$  mm (Case DF1)

The adiabatic wall temperature  $T_{aw}/T_\infty$  is displayed in Figs. 39 to 42. The accuracy of the measurements is less than 0.2%. Close agreement is observed. The maximum difference between the predicted and measured  $T_{aw}$  is less than 2%.

Figure 38:  $C_h$  at  $x = 112$  mm (Case DF1)Figure 42:  $T_{aw}$  at  $x = 112$  mm (Case DF1)Figure 39:  $T_{aw}$  on TML (Case DF1)Figure 40:  $T_{aw}$  at  $x = 46$  mm (Case DF1)Figure 41:  $T_{aw}$  at  $x = 79$  mm (Case DF1)

### 3.2 Case DF2

The computed surface skin friction lines using the  $k-\epsilon$  Chien model and  $k-\epsilon$  Knight model are shown in Figs. 43 and 44, respectively, and the experimental surface visualization is shown in Fig. 45. The incident separation lines emanating from the fin leading edges (1 and 2) are evident in both computations and experiment. The computed separation line angles, measured relative to the  $x$ -axis, agree with the experiment to within 10% for the  $k-\epsilon$  Chien model and to within 9% for the  $k-\epsilon$  Knight model. The  $k-\epsilon$  Chien results display a coalescence of the incident separation lines into a narrow band (3) offset to the left side, in agreement with the experiment. This line represents the surface image of the boundary between the left and right vortices generated by the incident single fin interactions. The  $k-\epsilon$  Chien results also show a second line of coalescence form alongside on the right and farther downstream (4) associated with a secondary separation underneath the left side of the right vortex [32], and a line of divergence alongside the right fin (5). A similar line of divergence (unmarked) is near the left fin.

For the  $k-\epsilon$  Knight model (Fig. 44), the incident separation lines do not coalesce near the center of the region, but rather continue farther downstream almost in parallel until they converge at  $x \approx 110$  mm to form a narrow band of skin friction lines (3), which are offset to the left side of the channel. The band represents the surface image of the boundary between the left and right vortices generated by the incident single fin interactions. Lines of divergence are also apparent near the right fin (4) and left fin (5) associated with the incident single fin inter-

action. The second line of coalescence observed in the  $k-\epsilon$  Chien results (4 in Fig. 43) is not present in this computation. Consequently, the  $k-\epsilon$  Knight model does not predict a secondary separation underneath the left side of the right vortex. The difference is due to deviation in the predictions of the pressure distribution in the spanwise direction, obtained with each turbulence model as described below.

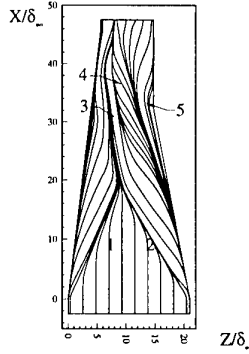


Figure 43: Computed skin friction lines  $k-\epsilon$  Chien model (Case DF2)

- 1 Left incident separation line
- 2 Right incident separation line
- 3 Left downstream coalescence line
- 4 Right downstream coalescence line
- 5 Line of divergence (similar line near left fin)

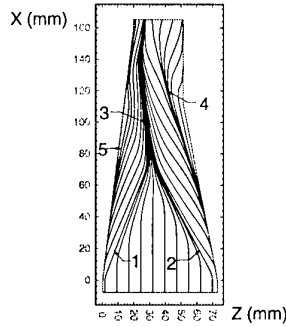


Figure 44: Computed skin friction lines  $k-\epsilon$  Knight model (Case DF2)

- 1 Left incident separation line
- 2 Right incident separation line
- 3 Left downstream coalescence line
- 4,5 Lines of divergence

The surface pressure distribution in the spanwise direction at  $x = 112$  mm is displayed in Figs. 46 and 47. The abscissa  $z - z_{TML}$  represents the spanwise distance measured from the TML (Throat Middle Line). The computations



Figure 45: Experimental surface flow for  $7^\circ \times 11^\circ$  (Case DF2)

using the  $k-\epsilon$  Chien,  $k-\epsilon$  Knight ("Present  $k-\epsilon$ "), and RSE models are in general agreement with the experiment, while the Spalart-Allmaras-Edwards, Baldwin-Lomax, and  $k-\omega$  models overpredict the pressure by 16% to 21%. The  $k-\epsilon$  Chien model predicts a local adverse pressure gradient in spanwise direction in the region  $-10 \text{ mm} < z - z_{TML} < -4 \text{ mm}$ . Since the flow near the surface at this location is moving towards the left fin, this adverse pressure gradient causes the secondary separation and the appearance of the right downstream coalescence line (4 in Fig. 43). The  $k-\epsilon$  Knight model does not predict a significant adverse pressure gradient in this region, and hence a secondary separation line does not appear.

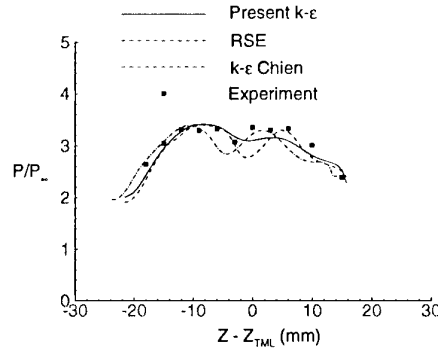


Figure 46: Wall pressure at  $x = 112$  mm (Case DF2)

The surface pressure along the Throat Middle Line is displayed in Figs. 48 and 49. The computed and experimental surface pressure on TML are in good agreement for  $x < 135$  mm for all models, although the computations slightly underestimate the extent of the upstream influ-

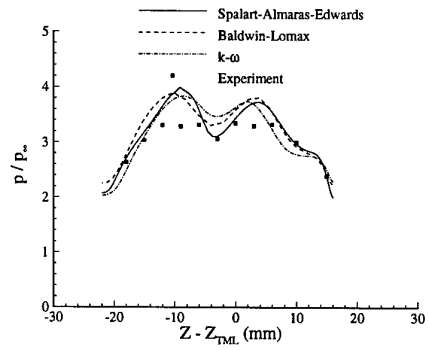


Figure 47: Wall pressure at  $x = 112$  mm (Case DF2)

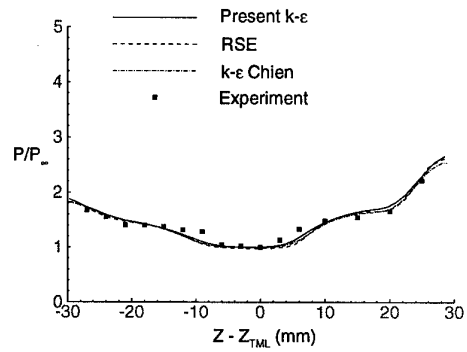


Figure 50: Wall pressure at  $x = 46$  mm (Case DF2)

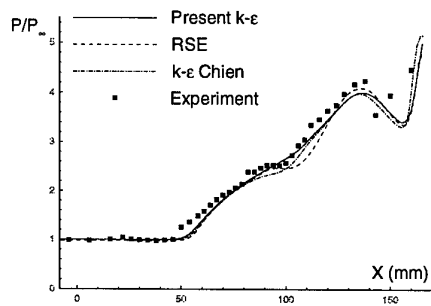


Figure 48: Wall pressure on TML (Case DF2)

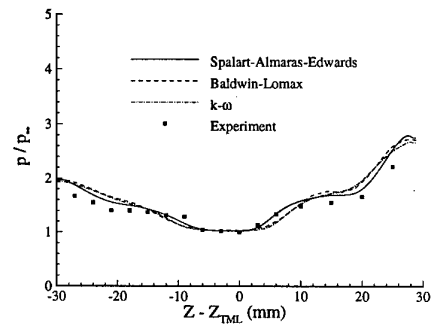


Figure 51: Wall pressure at  $x = 46$  mm (Case DF2)

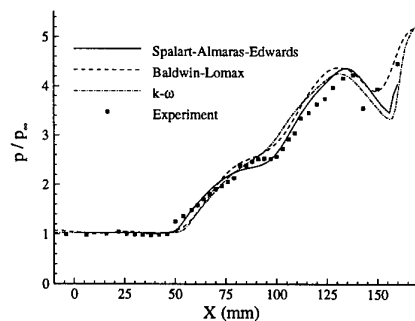


Figure 49: Wall pressure on TML (Case DF2)

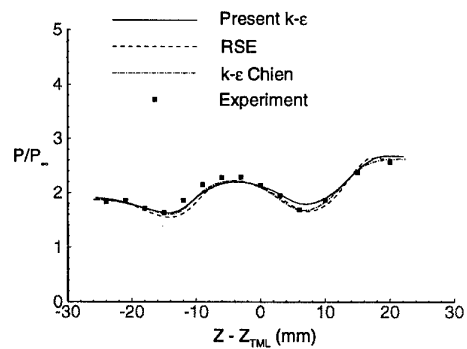


Figure 52: Wall pressure at  $x = 79$  mm (Case DF2)

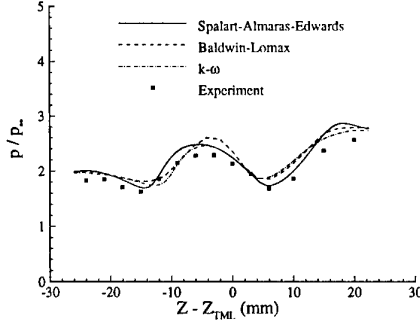


Figure 53: Wall pressure at  $x = 79$  mm (Case DF2)

ence. The computed results in Fig. 48 do not accurately predict the pressure rise (beginning at  $x = 145$  mm) associated with the shock reflection from the  $7^\circ$  fin, since the computations omit the boundary layers on the fin surfaces. The computed and experimental surface pressure at  $x = 46$  and  $79$  mm are displayed in Figs. 50 to 53. Close agreement is again observed between the predictions of all models and experiment.

The surface heat transfer coefficient  $C_h$  is shown in Figs. 54 to 61. The heat transfer coefficient is defined by

$$C_h = \frac{Q_w(x, z)}{\rho_\infty U_\infty c_p (T_w(x, z) - T_{aw}(x, z))} \quad (2)$$

On the Throat Middle Line (Figs. 54 and 55), all turbulence models overpredict the heat transfer by approximately a factor of two downstream of the intersection of the shocks (which occurs at  $x = 93.7$  mm). At  $x = 46$  mm (Fig. 56 and 57), there is close agreement between the experiment and the  $k-\epsilon$  Knight,  $k-\epsilon$  Chien, and RSE models, while the Spalart-Allmaras-Edwards, Baldwin-Lomax and  $k-\omega$  models show some discrepancies with the experiment. Note, however, that nearly all the experimental data at this location are situated in the nominally 2-D incoming boundary layer. A similar conclusion holds at  $x = 79$  mm (Fig. 58 and 59), where again most of the experimental data are within the nominally 2-D boundary layer. At  $x = 112$  mm (Figs. 60 and 61), located within the strongly 3-D region of the flow, all models show significant disagreement with the experiment.

The overprediction in  $C_h$  represents an overestimate in  $Q_w$ , since a series of studies [44, 45] have

demonstrated that the computed  $Q_w$  is proportional to the computed  $T_w - T_{aw}$ . A possible explanation [46] is that the turbulence models overestimate the effects of the shock-boundary layer interaction on the turbulence production, thereby generating excessive turbulence kinetic energy and turbulent eddy viscosity, and thus overestimating the turbulent thermal conductivity.

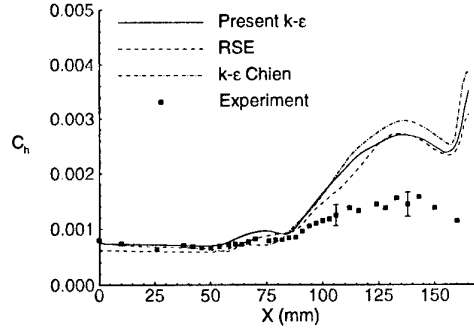


Figure 54:  $C_h$  on TML (Case DF2)

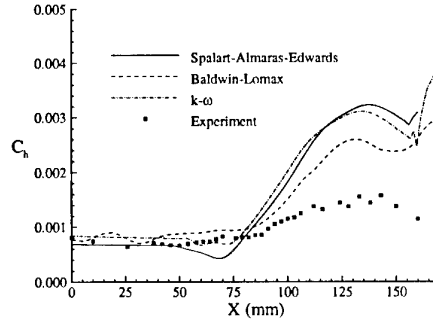


Figure 55:  $C_h$  on TML (Case DF2)

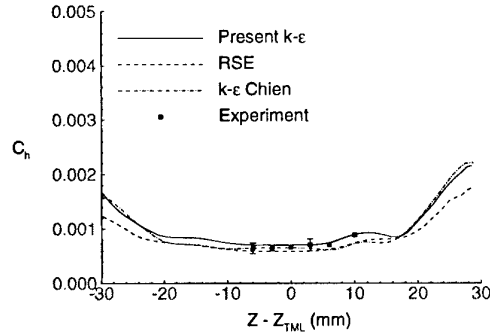
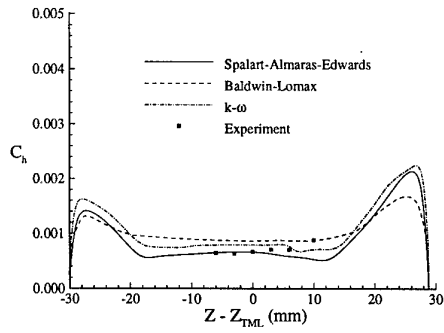
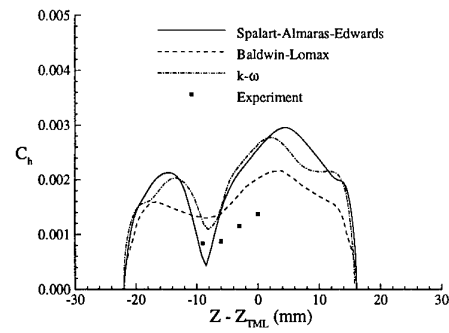
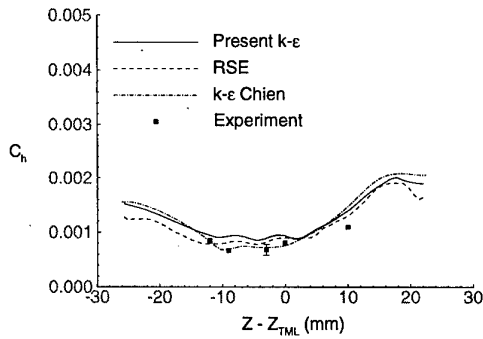
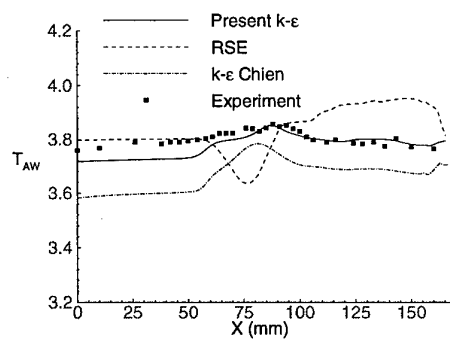
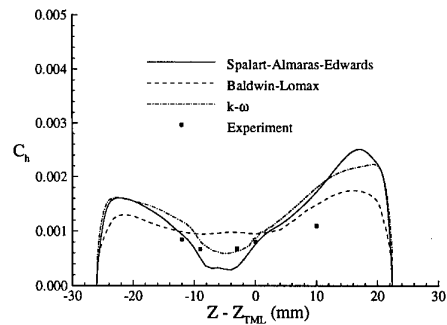
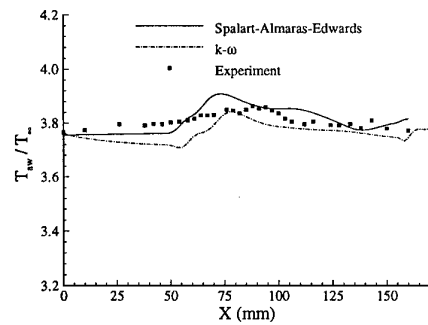
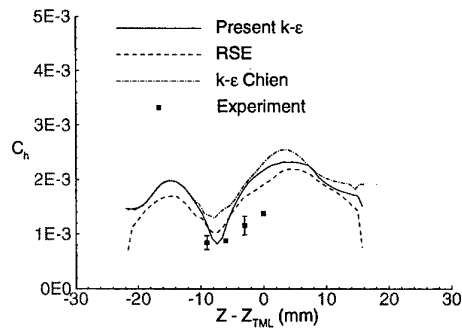
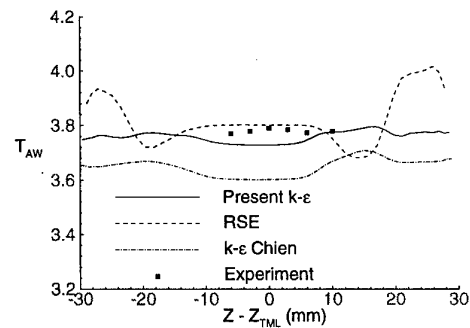
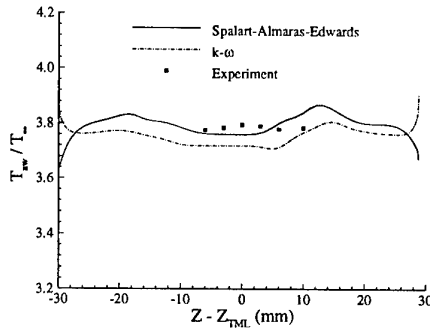
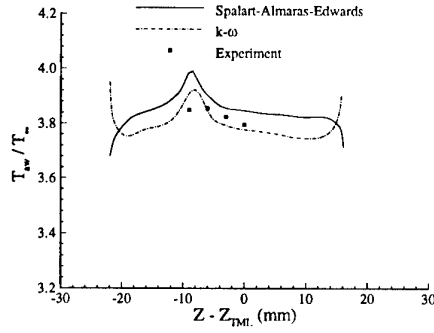
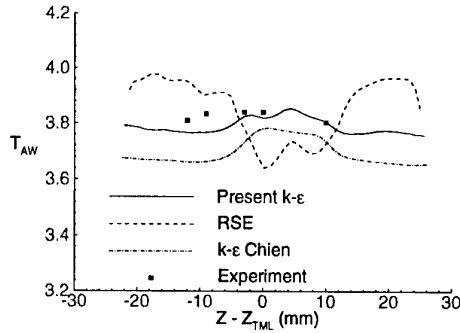
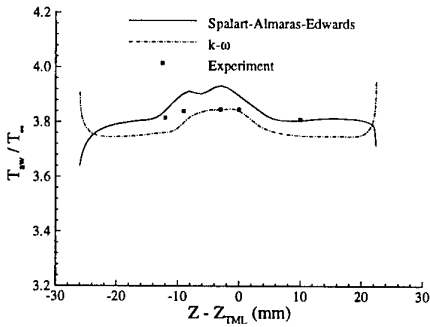
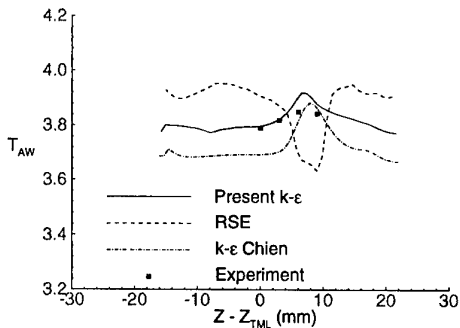


Figure 56:  $C_h$  at  $x = 46$  mm (Case DF2)

The adiabatic wall temperature  $T_{aw}/T_\infty$  is shown in Figs. 62 to 69, respectively. The  $k-\epsilon$

Figure 57:  $C_h$  at  $x = 46$  mm (Case DF2)Figure 61:  $C_h$  at  $x = 112$  mm (Case DF2)Figure 58:  $C_h$  at  $x = 79$  mm (Case DF2)Figure 62:  $T_{aw}$  on TML (Case DF2)Figure 59:  $C_h$  at  $x = 79$  mm (Case DF2)Figure 63:  $T_{aw}$  on TML (Case DF2)Figure 60:  $C_h$  at  $x = 112$  mm (Case DF2)Figure 64:  $T_{aw}$  at  $x = 46$  mm (Case DF2)

Figure 65:  $T_{aw}$  at  $x = 46$  mm (Case DF2)Figure 69:  $T_{aw}$  at  $x = 112$  mm (Case DF2)Figure 66:  $T_{aw}$  at  $x = 79$  mm (Case DF2)Figure 67:  $T_{aw}$  at  $x = 79$  mm (Case DF2)Figure 68:  $T_{aw}$  at  $x = 112$  mm (Case DF2)

Knight and  $k-\omega$  models display closest agreement with experiment.

### 3.3 Case DF3

The surface pressure on the centerline is shown in Fig. 70. The Baldwin-Lomax (IB) model displays virtually identical results for the second-order accurate [R2] and third-order accurate [R3] implementations of the inviscid flux using Roe's method [47]. The location of the beginning of the pressure rise (the "upstream influence") is underestimated, and the pressure downstream of the plateau region is overestimated. The Baldwin-Lomax-Panaras model provides the best prediction of surface pressure, although underestimating the peak pressure by 16%. The Spalart-Allmaras-Edwards model accurately predicts the upstream influence, but overestimates the pressure downstream of the plateau region, and underestimates the peak pressure. The  $k-\epsilon$  model accurately predicts the upstream influence, but overestimates the surface pressure elsewhere.

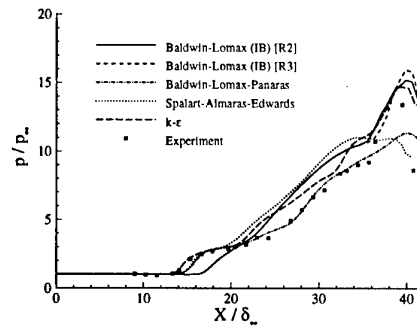


Figure 70: Surface pressure (Case DF3)

The skin friction coefficient  $c_f$  on the centerline is displayed in Fig. 71. Several turbulence models accurately predict the onset of separation, namely, Baldwin-Lomax-Panaras,  $k-\epsilon$  (with compressibility correction),  $k-\epsilon$  (Rodi-Horstman) and  $k-\epsilon$  (Vuong-Coakley). However, all turbulence models fail to accurately predict the skin friction downstream. The wide range of the predictions is reminiscent of the scatter in 2-D turbulent compression corner simulations [48].

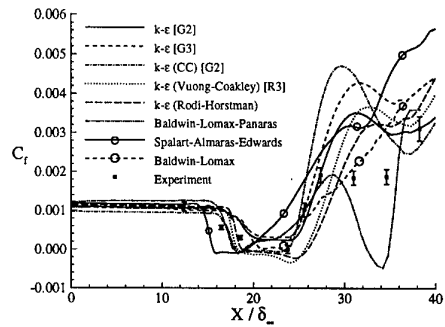


Figure 71: Skin friction on centerline (Case DF3)

The skin friction results at  $x = 25.3\delta_\infty$  are shown in Fig. 72. The computations again display generally poor agreement with experiment. The Baldwin-Lomax-Panaras model displays the smallest error.

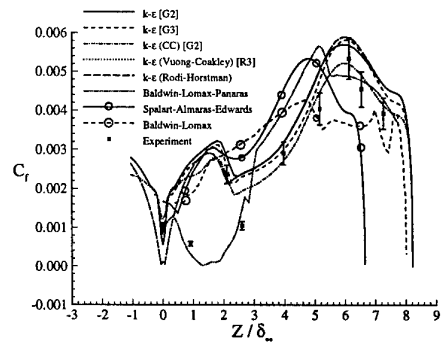


Figure 72: Skin friction at  $x = 25.3\delta_\infty$  (Case DF3)

The experimental pitot pressure  $p_p/p_{p_\infty}$  contours at  $x = 32.33\delta_\infty$  are presented in Fig. 73. One half of the cross section is shown, as experimental surveys demonstrated the symmetry of the flowfield [49]. The principal features include the low pitot pressure region near the centerline

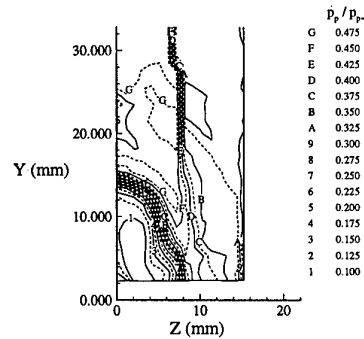


Figure 73: Experimental  $p_p$  at  $x = 32.33\delta_\infty$  (Case DF3)

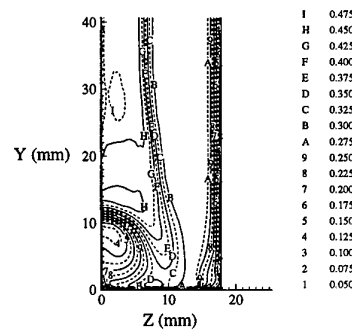


Figure 74: Computed  $p_p$  at  $x = 32.33\delta_\infty$  using Baldwin-Lomax [IB] (Case DF3)

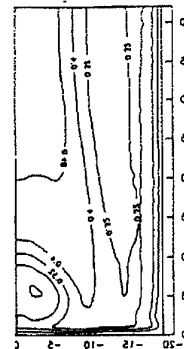


Figure 75: Computed  $p_p$  at  $x = 32.33\delta_\infty$  using Baldwin-Lomax model (Case DF3)



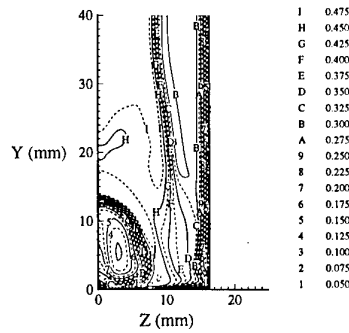


Figure 76: Computed  $p_p$  at  $x = 32.3\delta_\infty$  using Spalart-Allmaras-Edwards model (Case DF3)

and the inviscid shock.

The computed pitot pressure using the Baldwin-Lomax model is shown in Figs. 74 and 75. The computed width of the low  $p_p$  region is in reasonable agreement with the experiment, although the height is somewhat greater. Closer agreement is observed with the Spalart-Allmaras-Edwards model (Fig. 76).

### 3.4 Case DF4

The surface pressure on the centerline is presented in Figs. 77 and 78. The agreement is good. All turbulence models accurately predict the location of the beginning of the pressure rise (the upstream influence). The Baldwin-Lomax model using the Buleev Integral length scale overestimates the peak pressure by 30%. The expansion fan ( $7 \leq x/\delta_\infty \leq 8.5$ ) and subsequent second interaction ( $8.5 \leq x/\delta_\infty \leq 10$ ) are accurately predicted by all models except the  $k-\epsilon$  Rodi model<sup>6</sup>.

Figs. 79 and 82 display surface pressure at  $x = 5.6\delta_\infty$ . The pressure is overestimated typically by 30% at the centerline (see Figs. 77 and 78) and underestimated by at most a comparable amount off centerline. The results of all turbulence models are similar, with the exception of Baldwin-Lomax (Fig. 79). Figs. 80 and 82 display surface pressure at  $x = 6.9\delta_\infty$ . The re-

<sup>6</sup>In the experiment, the boundary layers on the fins separate at  $x \approx 6.5\delta_\infty$  due to the impingement of the shock waves. The  $k-\epsilon$  Rodi model does not predict separation on the fins. Consequently, the computed reflected shocks are stronger, thereby leading to higher pressure at  $x \approx 10\delta_\infty$ .

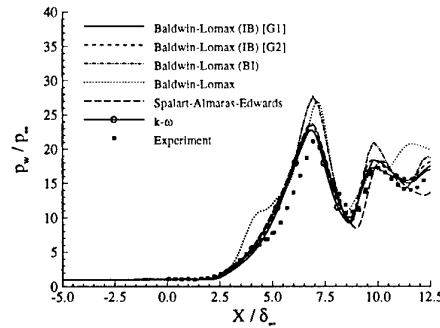


Figure 77: Surface pressure on centerline (Case DF4)

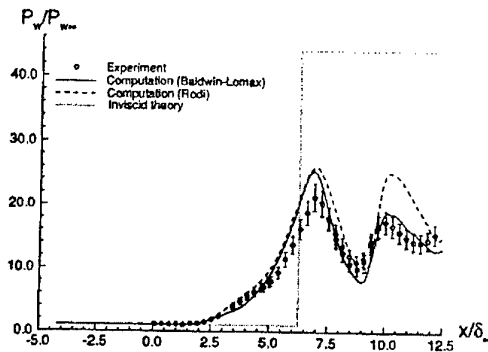


Figure 78: Surface pressure on centerline (Case DF4)

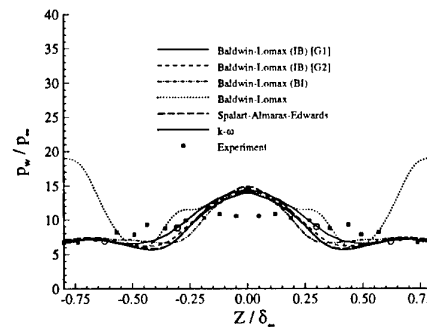


Figure 79: Surface pressure at  $x = 5.6\delta_\infty$  (Case DF4)

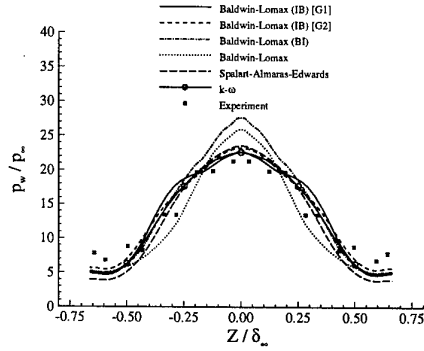


Figure 80: Surface pressure at  $x = 6.9\delta_\infty$  (Case DF4)

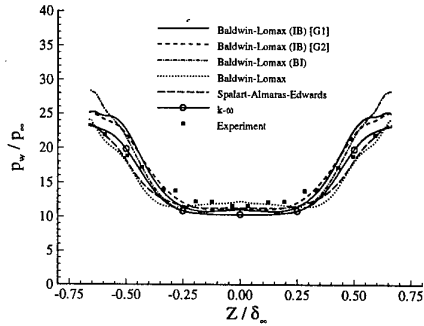


Figure 81: Surface pressure at  $x = 8.3\delta_\infty$  (Case DF4)

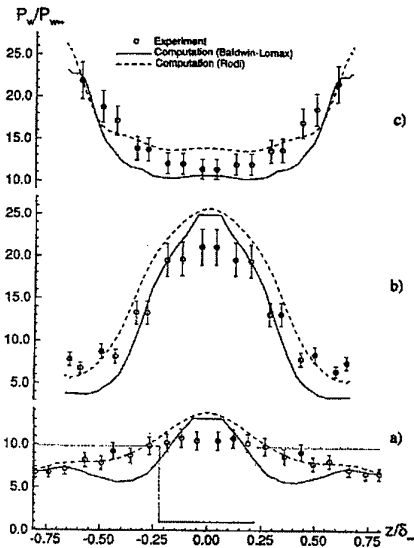


Figure 82: Surface pressure at  $x = 5.6, 6.9$  and  $8.3\delta_\infty$  (Case DF4)

sults of most turbulence models are similar, and in good agreement with the experiment. The Baldwin-Lomax model (Buleev Integral) overestimates the centerline pressure by 30%. Figs. 81 and 82 display surface pressure at  $x = 8.3\delta_\infty$ . All turbulence models are in good agreement with the experiment.

The surface heat transfer  $Q_w$  on the centerline is displayed in Figs. 83 and 84. With the exception of the Baldwin-Lomax model with the Buleev Integral length scale, there is generally good agreement with the experiment. However, away from the centerline, the agreement becomes increasingly poor with distance downstream, as shown at  $x = 5.08\delta_\infty$  (Figs. 85 and 86), at  $x = 6.4\delta_\infty$  (Figs. 87 and 88), and at  $x = 7.78\delta_\infty$  (Figs. 89 and 90) where the maximum deviation from experiment ranges from 40% to 150%.

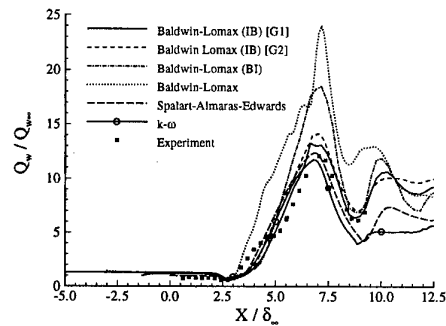


Figure 83: Surface heat transfer on centerline (Case DF4)

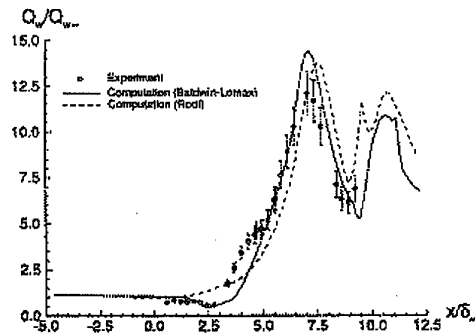


Figure 84: Surface heat transfer on centerline (Case DF4)

The surface streamline angle  $\Phi$ , measured relative to the freestream direction  $x$ , is presented at  $x = 5.6\delta_\infty$  (Fig. 91),  $6.9\delta_\infty$  (Fig. 92) and

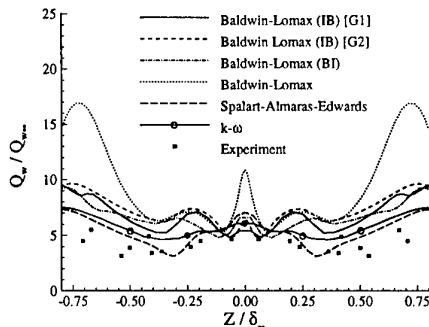


Figure 85: Surface heat transfer at  $x = 5.08\delta_\infty$  (Case DF4)

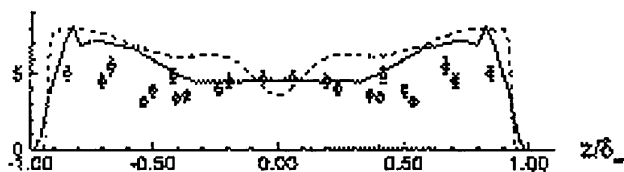


Figure 86: Surface heat transfer at  $x = 5.08\delta_\infty$  (Case DF4). See Fig. 84 for legend.

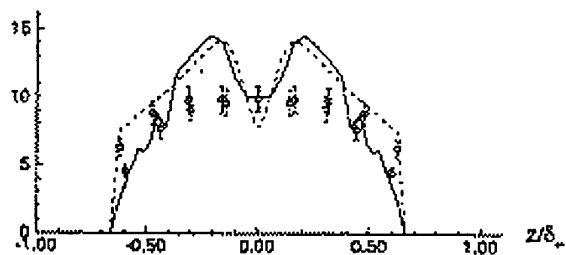


Figure 88: Surface heat transfer at  $x = 6.4\delta_\infty$  (Case DF4). See Fig. 84 for legend.

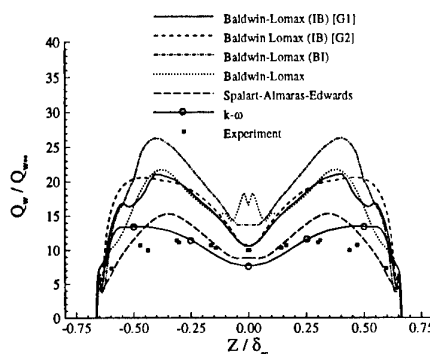


Figure 89: Surface heat transfer at  $x = 7.78\delta_\infty$  (Case DF4)

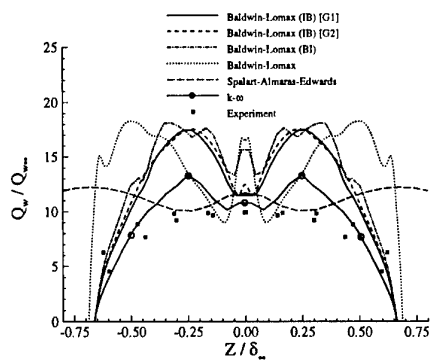


Figure 87: Surface heat transfer at  $x = 6.4\delta_\infty$  (Case DF4)

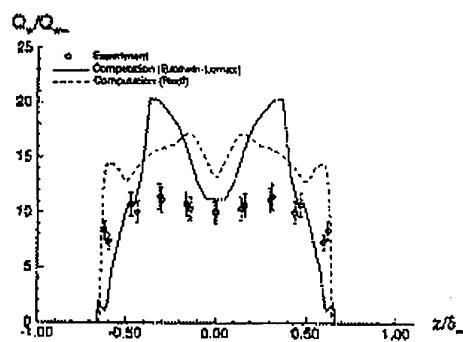


Figure 90: Surface heat transfer at  $x = 7.78\delta_\infty$  (Case DF4). See Fig. 84 for legend.

$8.3\delta_\infty$  (Fig. 93) for the Baldwin-Lomax model by using Inverse Blending and Buleev Integral length scales. The agreement is poor.

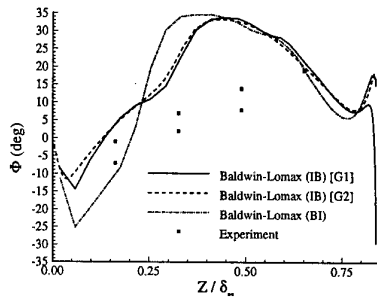


Figure 91: Surface streamline angle at  $x = 5.6\delta_\infty$  (Case DF4)

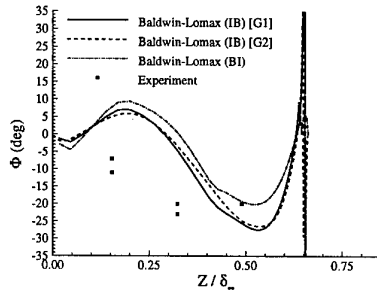


Figure 92: Surface streamline angle at  $x = 6.9\delta_\infty$  (Case DF4)

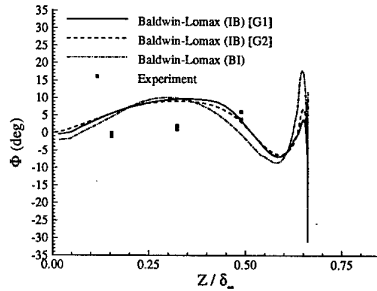


Figure 93: Surface streamline angle at  $x = 8.3\delta_\infty$  (Case DF4)

Yaw angle profiles at  $x = 5.6\delta_\infty$  and  $z/\delta_\infty = 0.16, 0.33, 0.49$ , and  $0.65$  are shown in Figs. 94 to 97, and pitot pressure profiles at the same locations (plus  $z = 0$ ) in Figs. 98 to 102, respectively. The principal features of both the yaw angle and pitot pressure profiles are generally predicted by all turbulence models.

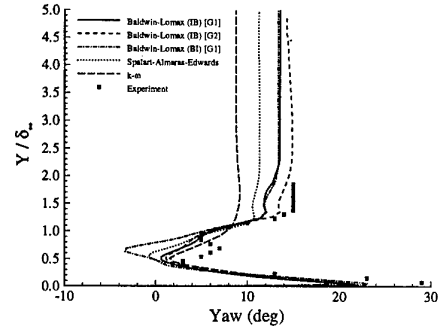


Figure 94: Yaw angle at  $x = 5.6\delta_\infty$  and  $z = 0.16\delta_\infty$  (Case DF4)

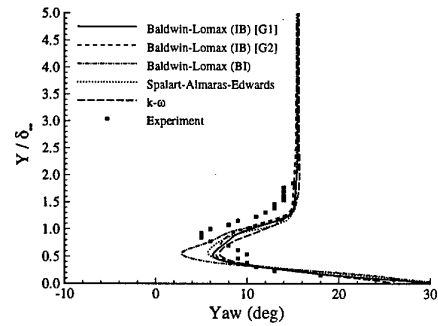


Figure 95: Yaw angle at  $x = 5.6\delta_\infty$  and  $z = 0.33\delta_\infty$  (Case DF4)

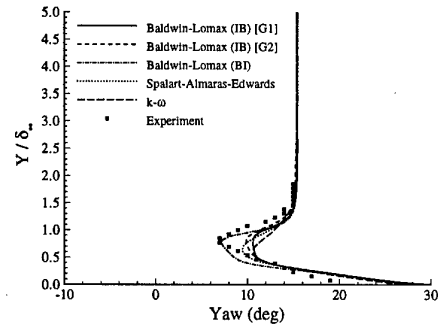


Figure 96: Yaw angle at  $x = 5.6\delta_\infty$  and  $z = 0.49\delta_\infty$  (Case DF4)

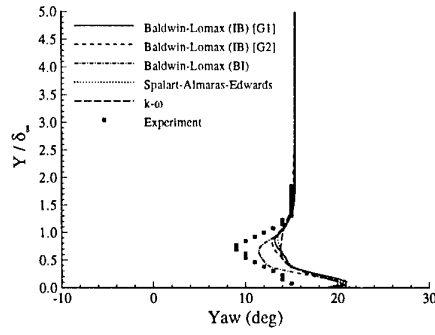


Figure 97: Yaw angle at  $x = 5.6\delta_\infty$  and  $z = 0.65\delta_\infty$  (Case DF4)

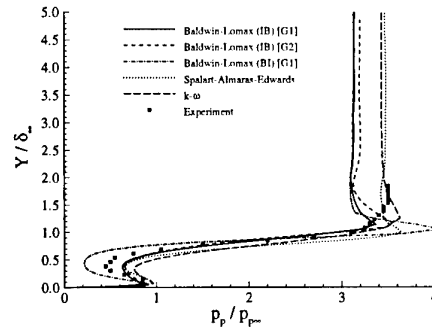


Figure 100:  $p_p$  at  $x = 5.6\delta_\infty$  and  $z = 0.33\delta_\infty$  (Case DF4)

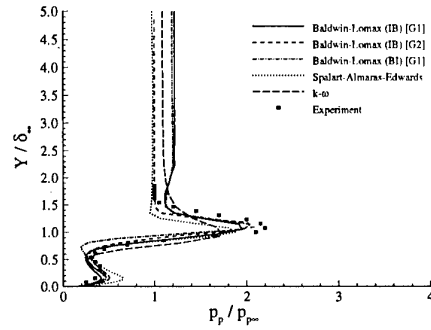


Figure 98:  $p_p$  at  $x = 5.6\delta_\infty$  and  $z = 0$  (Case DF4)

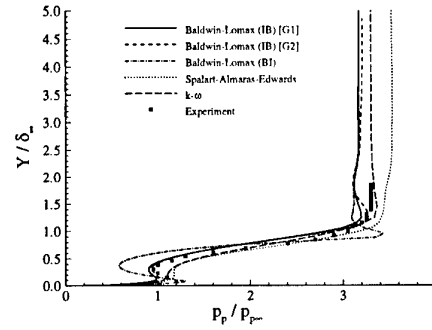


Figure 101:  $p_p$  at  $x = 5.6\delta_\infty$  and  $z = 0.49\delta_\infty$  (Case DF4)

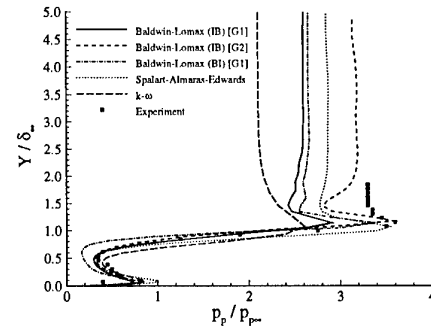


Figure 99:  $p_p$  at  $x = 5.6\delta_\infty$  and  $z = 0.16\delta_\infty$  (Case DF4)

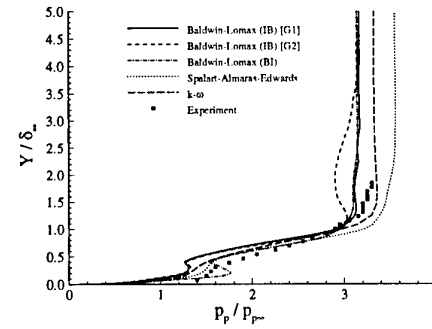


Figure 102:  $p_p$  at  $x = 5.6\delta_\infty$  and  $z = 0.65\delta_\infty$  (Case DF4)

## 4 Hollow-cylinder flare

The hollow-cylinder flare geometry is shown in Fig. 103. It is the axisymmetric counterpart

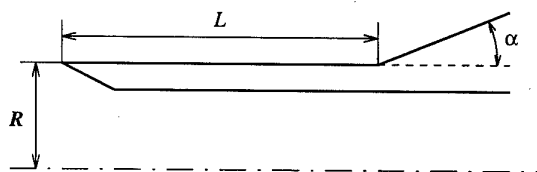


Figure 103: Hollow-cylinder flare model geometry

of the well-known compression ramp geometry. The flare generates a conical shock wave which interacts with the boundary layer developing on the cylinder. The flow parameters are the Mach number  $M_\infty$ , the Reynolds number  $Re_\infty$  based on the leading-edge-to-flare-hinge distance  $L$ , the flare angle  $\alpha$  and the wall temperature ration  $T_w/T_\infty$ <sup>7</sup>. The Reynolds number determines, in particular, the state of the boundary layer upstream of the interaction and therefore the nature of the interaction.

The flowfield structure of the hollow cylinder flare interaction is similar to that of the compression ramp flow which has been described in detail in several review reports [50, 4], in particular in the article by Détery and Panaras in the first report of this Working Group [9]. It is schematically represented on Fig. 104 for the

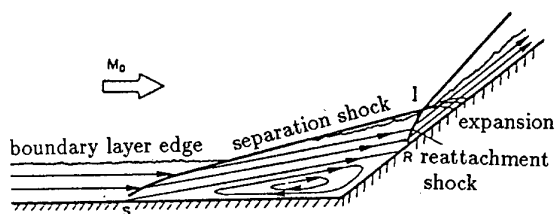


Figure 104: Hypersonic ramp flow. Sketch of the flowfield

case of a separated turbulent hypersonic interaction. At the beginning of the interaction, the

<sup>7</sup>For completeness, one should add the Reynolds number based on the cylinder outer radius, which controls the axisymmetry effects on the incoming boundary layer itself (transverse curvature effect). This effect is negligible for large Reynolds numbers, for which the boundary layer develops exactly as on a flat plate.

boundary layer starts thickening and eventually separates at point S. The thickening is responsible for the generation of compression waves which rapidly coalesce into a separation shock. The separated shear layer eventually reattaches on the wedge (flare for the axisymmetric configuration) where it produces a strong reattachment shock. The reattachment shock intersects the separation shock at the triple point I leading to the formation of the transmitted global compression shock and of a reflected expansion fan. Since for hypersonic flows the separation shock makes a small angle with the flat plate (or cylinder), the triple point I is quite close to the wall so that the reflected expansion reaches the wall only slightly downstream of reattachment. Laminar interactions are characterized by much more extended separation zones as well as by a smoother compression upstream of separation. The axisymmetric interaction differs from the 2-D interaction by weaker shock angles for a given deviation and by the non-uniformity of the flow downstream of a conical shock, although this latter effect is hardly noticeable for the cases under consideration.

Two configurations (a laminar configuration referred to as HCFL and a turbulent one referred to as HCFT) were computed by one or more participants. The flow conditions are shown in Table 9. The laminar case was

Table 9: Hollow-cylinder flare cases

Case	Ref	$M_\infty$	$\alpha$	$Re_\infty$	$T_w/T_{t\infty}$
				( $\times 10^3$ )	
HCFL	[51]	9.90	30°	18.9	0.276
HCFT	[52]	5.01	35°	11025	0.60

computed by six participants, four computations using a cell-centered finite volume Navier-Stokes (FVNS) solver, one using an unstructured grid residual distribution Navier-Stokes (RDNS) solver [53] and one a direct simulation Monte Carlo (DSMC) solver [54]. A detailed comparison of a subset of these computations with the experimental data by Chanetz [51] is presented in [55]. The turbulent case was computed by one participant using a Reynolds averaged Navier-Stokes solver with the Spalart-Allmaras turbulence model [56]. The simulations are summarized in Table 10.

Table 10: Participants for the hollow cylinder-flare cases

Participant (code)/case	HCFL	HCFT
J.-M. Bousquet (FLU3M)	FVNS	
R. Bur (NASCA)	FVNS	
G. Degrez et al. (VKI-MB)	FVNS	FVRANS
F. Grasso (HIG-2XP)	FVNS	
J. Moss (DSMC)	DSMC	
E. Van der Weide (IcARus)	RDNS	

#### 4.1 Case HCFL

Grid refinement studies have been performed both by Bousquet, who used a sequence of grids containing  $101 \times 39$ ,  $201 \times 77$  and  $401 \times 153$  points in the longitudinal and normal directions respectively, and by Tombarel and Degrez, who used a sequence of grids containing  $101 \times 26$ ,  $201 \times 51$  and  $401 \times 101$  points. The sensitivity of the results to the grid density is illustrated in Fig. 105, which shows Stanton number dis-

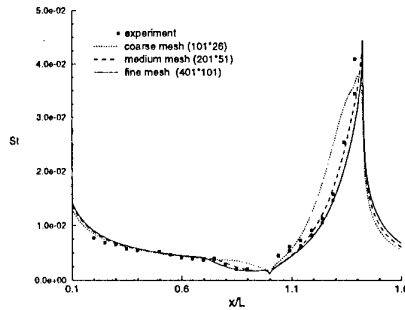
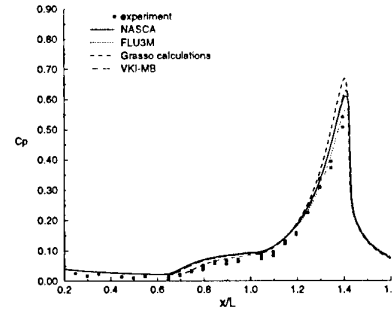


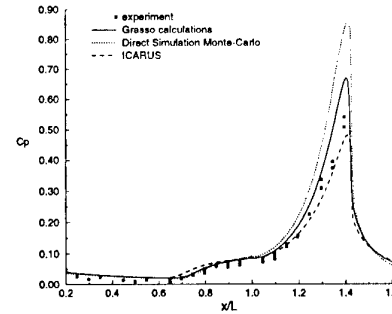
Figure 105: Stanton number distribution, grid sensitivity study (HCFL)

tributions as computed by Tombarel and Degrez. One sees that grid independence is not proven even for the finest mesh, since the finest mesh results are still noticeably different from the medium mesh results. As far as the calculations by Bousquet are concerned, only the fine grid results have been provided, but the author reports an excellent spatial convergence. Note that the latter grids are finer in the normal direction than those used by Tombarel and Degrez, which could explain a better grid convergence.

Surface pressure coefficient distributions computed by all six participants are shown on Fig. 106. First, one notices that all codes agree on the cylinder upstream of the interaction, but



(a) Finite volume Navier-Stokes computations



(b) IcARus, DSMC and HIG-2XP computations

Figure 106: Surface pressure coefficient distributions (HCFL)

the computed pressure coefficients are higher than the measured values, possibly due to some offset in the experimental values. One notices that the FLU3M, NASCA and VKI-MB results are nearly identical. The starting location of the pressure rise is seen to be slightly upstream of the experimental one (slightly overevaluated upstream influence) for these computations and for the IcARus unstructured grid computation while it is about at the experimental position for the HIP-2XP (Grasso) computation and slightly downstream for the DSMC computation.

At this stage, it should be noticed that slightly different freestream conditions were imposed by the various participants. Whereas the incoming freestream Mach number was set at 9.90 for the NASCA, VKI-MB, IcARus and DSMC computations as specified in [9], a value of 9.95 was used for the FLU3M computation which was performed before the experiment and a value of 9.91, closest to the real experimental one, for the HIP-2XP (Grasso) computation. Other slight differences concern the stagnation temperature (1070°K for the NASCA computation, 1050°K

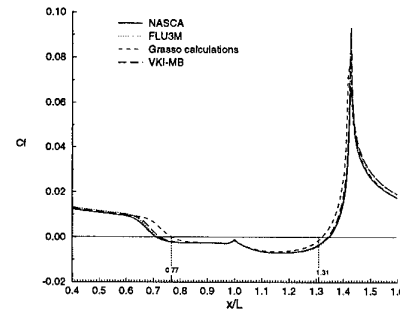
for all others) and the wall temperature (295°K for the DSMC computation, and 290°K for all others). These small variations in freestream conditions however are not deemed to have a significant impact on the computational results.

More substantial differences between computed pressure distributions are observed on the flare. In particular, the DSMC computation strongly overevaluates the pressure on the flare while the IcARus computation underevaluates it, possibly indicating an insufficient grid resolution on the flare for this computation. Finite volume Navier-Stokes computations are in closer agreement between themselves and with the experiment, the HIP-2XP computation giving the highest values, followed by the NASCA and VKI-MB computations, which give essentially identical results, and finally by the FLU3M computation, which gives the lowest values<sup>8</sup>. The latter computation appears to be in closest agreement with the experiment, but one should keep in mind the possible pressure offset in the experiments mentioned earlier.

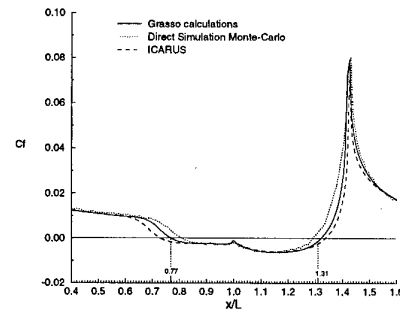
Computed skin friction distributions are shown on Fig. 107. Important differences are observed in the separation and reattachment regions. Just as for the pressure distributions, the FLU3M, NASCA, and VKI-MB computations give essentially identical results with a separation point at a reduced abscissa  $x/L = 0.72$  and a reattachment point at  $x/L = 1.34$ , to be compared with the experimental values obtained by an oil flow visualization  $x_{sep}/L = 0.77$  and  $x_{rea}/L = 1.31$ . The IcARus unstructured grid computation also gives very similar results. The HIP-2XP (Grasso) results are seen to be in better agreement with the experimental values while the DSMC computation underpredicts the size of the separation bubble. Experimental and computed separation and reattachment point locations are summarized in Table 11.

Finally, experimental and computed Stanton number distributions are shown on Fig. 108. The trends observed for the pressure coefficient and skin friction distributions are confirmed, *i.e.*, the underprediction of the size of the separation bubble by the DSMC computation, the better match with the experimental results given by the HIP-2XP (Grasso) computation, and

<sup>8</sup>The slightly higher freestream Mach number value used in this computation may play a role here.



(a) Finite volume Navier-Stokes computations



(b) IcARus, DSMC and HIP-2XP computations

Figure 107: Skin friction coefficient distributions (HCFL)

Table 11: Separation-reattachment point locations (HCFL)

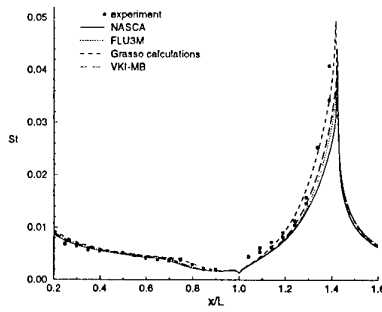
code/abscissa	sep.	reatt.
J.-M. Bousquet (FLU3M)	0.72	1.34
R. Bur (NASCA)	0.72	1.34
G. Degrez et al. (VKI-MB)	0.73	1.34
F. Grasso (HIP-2XP)	0.77	1.32
J. Moss (DSMC)	0.81	1.29
E. Van der Weide (IcARus)	0.73	1.34
experiment [51]	0.77	1.31

the close agreement between the remaining four computations (FLU3M, NASCA, VKI-MB and IcARus) which predict a slightly oversized separation bubble.

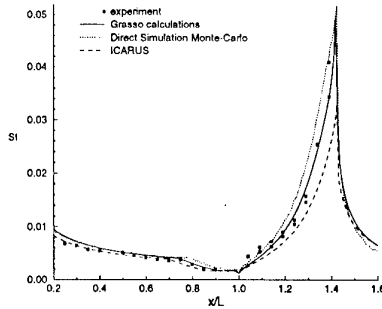
## 4.2 Case HCFT

This test case was computed by Paciorri et al. [57] on different grids. The initial coarse grid contained  $100 \times 50$  points and used a uniform stretching in the normal direction. A second adapted  $100 \times 50$  grid was then produced





(a) Finite volume Navier-Stokes computations

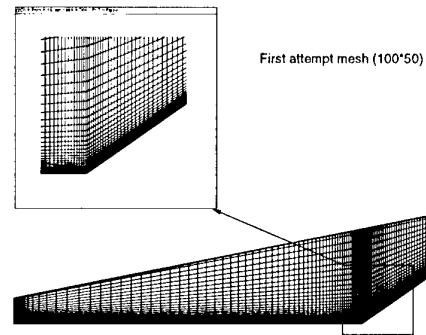


(b) IcARus, DSMC, and HIG-2XP computations

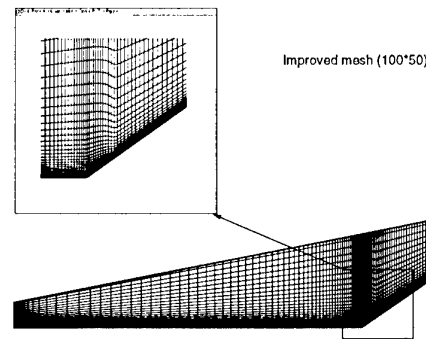
Figure 108: Stanton number distributions (HCFL)

in which the normal stretching was made variable along the wall to cluster grid lines closer to the wall in the vicinity and downstream of reattachment where the boundary layer is very thin. This clustering is illustrated in Fig. 109 which compares both grids. The corresponding first grid line  $y^+$  distributions are shown in Fig. 110, where one observes that, thanks to the increased clustering normal to the wall in the reattachment region, the wall coordinate  $y^+$  never exceeds 2 for the adapted grid, whereas it reaches a value of 6 in the reattachment region for the initial grid. Finally, a fine  $200 \times 100$  grid was obtained by refining the adapted grid by a factor of two in each direction.

Surface pressure distributions are shown on Fig. 111. Although there is a good agreement between computed results, the extent of the separated zone is seen to be strongly underestimated. In particular, the computed pressure rise at separation is well downstream of the experimental position. One also notices a slight disagreement between computed and experimental values downstream of reattachment.

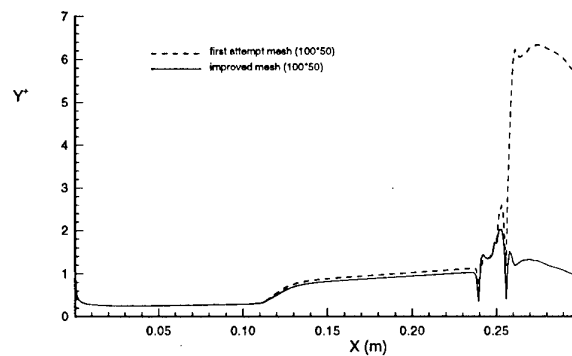


(a) Initial grid



(b) Adapted grid

Figure 109: Coarse grids for HCFT test case

Figure 110: First grid line  $y^+$  distributions on coarse meshes (HCFT)

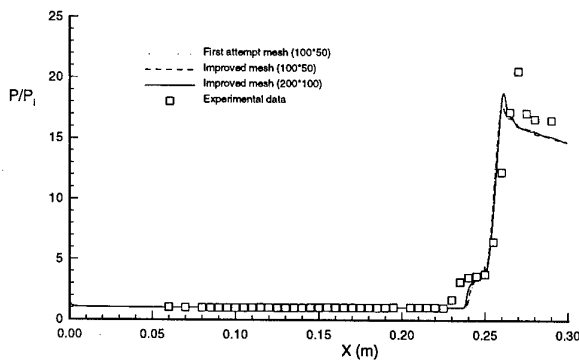


Figure 111: Surface pressure coefficient distributions (HCFT)

Stanton number distributions are shown on Fig. 112. Here, the effect of grid adaption is clearly visible. While the initial grid fails completely to predict the Stanton number at reattachment and downstream, the adapted grid results are in reasonable agreement with the experimental data both in terms of the peak value and of the distribution downstream of reattachment. The computed peak heat transfer location, however, is upstream of the experimental position because of the underestimation of the separated bubble size. The discrepancy between the computed and experimental separation bubble size is also the reason for the disagreement between computed and experimental values near the separation point.

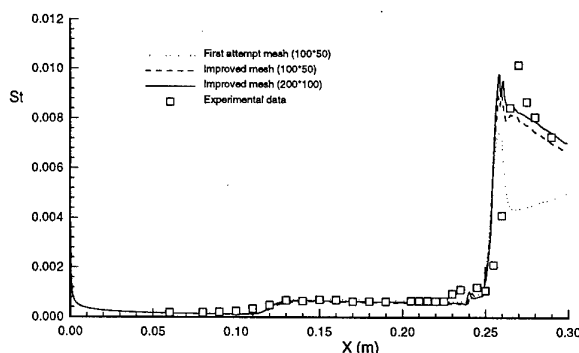


Figure 112: Stanton number distributions (HCFT)

## 5 Conclusions

The objective of the present study was to review the capabilities of current CFD solvers to predict quantities of interest for designers of high-speed vehicles, namely mean and fluctuating (RMS) aerodynamic (pressure, skin friction) and thermal (heat transfer) loads as well as flowfield structure (occurrence of separation and of vortical flow structures). Laminar and turbulent interactions are examined successively.

### 5.1 Laminar interactions

For laminar interactions, present CFD technology allows accurate prediction of both aerodynamic and thermal loads. For strong interactions at relatively high Reynolds numbers, though, extremely fine and carefully generated grids are necessary to obtain accurate results (at least  $200 \times 75$  points for nominally 2-D interactions and therefore, by extrapolations, at least 1.5 million points for 3-D interactions) because of the extremely high aspect ratio of laminar separated flow regions. Adaptivity thus appears essential to accurately calculate 3-D interactions at an affordable cost.

### 5.2 Turbulent interactions

For 3-D interactions, mean pressure distributions are generally predicted satisfactorily, with little variation between computations using different turbulence models. The satisfactory pressure predictions may be attributable to an approximate triple-deck structure of the flowfield [25] (see, for example, Inger [58, 59, 60] who extended the original work of Stewartson [61] to nonseparated 3-D shock wave turbulent boundary layer interactions). In the first layer ("deck"), located immediately adjacent to the surface, the flow is controlled by both viscous (*i.e.*, laminar and turbulent stresses and heat transfer) and inviscid effects. In the second layer, immediately above the first deck, the flow is rotational and inviscid to a first approximation; *i.e.*, turbulent stresses and heat transfer are higher order effects. This region comprises most of the boundary layer in the interaction. The third region is the inviscid, irrotational flow outside the boundary layer. The surface

pressure distribution is, to a first approximation, determined by the interaction of the second and third layers and is therefore insensitive to the turbulence model. In effect, the turbulence model provides the proper vorticity distribution in the incoming boundary layer, but does not otherwise significantly affect the surface pressure. Since all turbulence models provide the appropriate flat plate boundary layer profile as inflow, there is little difference in the prediction of surface pressure.

For nominally 2-D interactions, however, satisfactory prediction of mean pressure distributions is achieved typically only for weak interactions. For strong interactions, computed pressure distributions are generally in poor agreement with the experiment<sup>9</sup> for two reasons. First, the flow exhibits a high level of unsteadiness, which is not captured by any of the RANS computations [65] (see below). Second, eddy viscosity models use a single length scale to characterize the turbulence characteristics which, while valid for attached boundary layer flow, ceases to be correct in the presence of separation bubbles. In addition, many eddy viscosity models use wall functions which lose their validity in the neighbourhood of 2-D separation and reattachment points.

As far as the 3-D flowfield structure is concerned, primary separation is generally well predicted whereas secondary separation appears to be very sensitive to the turbulence model and is not predicted accurately in most cases.

For 3-D interactions, boundary layer profiles of pitot pressure and yaw angle are reasonably predicted for weak interactions but accuracy degrades as interaction strength increases. The concept of a triple-deck structure (described above) would explain the general insensitivity of the computed profiles to the turbulence model, since the middle deck occupies most of the boundary layer.

Skin friction and heat transfer distribution predictions are generally poor, except for weak interactions, and significant differences are evident between turbulence models. Differences of up to

100% between experimental and numerical results were obtained for strong interactions.

None of the RANS computations captured the flowfield unsteadiness associated with shock wave motions observed in experimental studies, in particular for nominally 2-D interactions, and therefore no RANS computation was able to predict the fluctuating aerodynamic and thermal loads.

Ad hoc modifications of turbulence models such as proposed by Panaras improve the accuracy of numerical predictions, but the practical usefulness of such approaches is limited because the modifications required are strongly model dependent. Nevertheless, such studies are useful insofar as they are physically based (*e.g.*, the model of Panaras is based on the observation of a low turbulence region beneath the main vortex) and point out the deficiencies of standard models.

The previous conclusions lead to the following recommendations for further study.

- For turbulent interactions, it appears necessary to develop large eddy simulation solvers, as only LES models will allow us to predict the fluctuating pressure and heat transfer loads which can be very significant in shock wave/boundary layer interactions.
- Grid adaptivity strategies based on reliable error estimates are essential to allow accurate and affordable shock wave/boundary layer interaction computations.
- In order to continue making progress in turbulence modeling for shock wave / boundary layer interactions, it is essential to obtain accurate experimental data for
  - flowfield Reynolds stresses,
  - flowfield turbulent heat flux
  - wall pressure and heat transfer fluctuations.

<sup>9</sup>A notable exception are the predictions of Borisov *et al.* [62] and Bedarev *et al.* [63] for the 2-D compression corner using the  $k - \omega$  model of Wilcox [64] which are in close agreement with the experiments of Zheltovodov.

## 6 Acknowledgments

The authors express their sincere appreciation to the participants whose contributions have provided and formed the basis for this study. The study has been supported by the Air Force Office of Scientific Research under grant F49620-93-1-0005 (monitored by Dr. Len Sakell). The experimental data for cases DF1 and DF2 was obtained by Dr. Alexander Zheltovodov and his colleagues through support of the Russian Foundation for Basic Research (Project Code 96-01-01777) and United Technologies Research Center (monitored by Dr. Michael Werle). The second author also gratefully acknowledges the help of B. Chanetz for the preparation of the hollow-cylinder flare computational data from ONERA, U. Rome, and NASA Langley, and of Christophe Tombarel for the preparation of the figures of section 4.

## References

- [1] J. E. Greene. Interactions between Shock Waves and Turbulent Boundary Layers. In *Progress in Aerospace Science*, volume 11, pages 235–340. Pergamon Press, 1970.
- [2] R. Korkegi. Survey of Viscous Interactions Associated with High Mach Number Flight. *AIAA Journal*, 9:771–784, May 1971.
- [3] D. Peake and M. Tobak. Three-Dimensional Interactions and Vortical Flows with Emphasis on High Speed. Technical Report TM 81169, NASA, March 1980.
- [4] J. Delery and J. Marvin. Shock-Wave Boundary-Layer Interactions. AGARDograph No. 280, February 1986.
- [5] G. Settles and D. Dolling. Swept Shock Wave Boundary Layer Interactions. In *Tactical Missile Aerodynamics*, pages 297–379. AIAA, 1986.
- [6] G. Settles and D. Dolling. Swept Shock / Boundary-Layer Interactions – Tutorial and Update. AIAA Paper 90-0375, 1990.
- [7] J. Stollery. AGARD Special Course on Three-Dimensional Supersonic and Hypersonic Flows Including Separation. Advisory Group for Aerospace Research and Development, May 1989.
- [8] G. Degrez, editor. *AGARD Special Course on Shock-Wave/Turbulent Boundary-Layer Interactions in Supersonic and Hypersonic Flow*. Advisory Group for Aerospace Research and Development, August 1993. AGARD Report 792.
- [9] J. Delery and A. Panaras. Shock-Wave Boundary-Layer Interactions in High Mach Number Flows. AGARD AR-319, Volume 1, May 1996.
- [10] A. Zheltovodov. Shock Waves / Turbulent Boundary Layer Interactions – Fundamental Studies and Applications. AIAA Paper No. 96-1977, 1996.
- [11] F. Alvi and G. Settles. Physical Model of the Swept Shock / Boundary Layer Interaction Flowfield. *AIAA Journal*, 30:2252–2258, September 1992.
- [12] A. Zheltovodov and E. Shilein. 3-D Swept Shock Waves / Turbulent Boundary Layer Interaction in Angles Configuration. Institute of Theoretical and Applied Mechanics, Russian Academy of Sciences, Siberian Division, Preprint No. 34-86, 1986.
- [13] A. Zheltovodov. Physical Features and Some Properties of Two and Three-Dimensional Separated Flows at Supersonic Velocities. *Izvestiya AN SSSR, Mekhanika Zhidkosti i Gaza*, 3:42–50, 1979.
- [14] A. Zheltovodov, A. Maksimov, and E. Shilein. Development of Turbulent Separated Flows in the Vicinity of Swept Shock Waves. In *The Interaction of Complex 3-D Flows*, pages 67–91. Institute of Theoretical and Applied Mechanics, USSR Academy of Sciences, Novosibirsk, Russia, 1987.
- [15] M. Zubin and N. Ostapenko. Structure of the Flow in the Separation Region Resulting from Interaction of a Normal Shock Wave with a Boundary Layer in a Corner. *Izvestiya AN SSSR, Mekhanika Zhidkosti i Gaza*, 3:51–85, May-June 1979.
- [16] P. Rodi, D. Dolling, and D. Knight. An Experimental/Computational Study of Heat

Transfer in Sharp Fin Induced Turbulent Interactions at Mach 5. AIAA Paper 91-1764, 1991.

- [17] K. Kim, Y. Lee, F. Alvi, G. Settles, and C. Horstman. Laser Skin Friction Measurements and CFD Comparison of Weak-to-Strong Swept Shock / Boundary Layer Interactions, 1990. AIAA Paper No. 90-0378.
- [18] D. Knight, C. Horstman, B. Shapey, and S. Bogdonoff. Structure of Supersonic Turbulent Flow Past a Sharp Fin. *AIAA Journal*, 25:1331-1337, 1987.
- [19] M. Kussoy and K. Horstman. Documentation of Two- and Three Dimensional Shock-Wave/Turbulent Boundary Layer Interaction Flows at Mach 8.2. Technical Report NASA TM 103838, NASA Ames Research Center, May 1991.
- [20] G. Settles and L. Dodson. Hypersonic Shock / Boundary Layer Interaction Database. Technical Report PSU-ME-90/91-003, Gas Dynamics Laboratory, Department of Mechanical Engineering, Penn State University, December 1990.
- [21] J. Edwards and S. Chandra. Comparison of Eddy Viscosity-Transport Turbulence Models for Three-Dimensional, Shock-Separated Flowfields. *AIAA Journal*, 34:756-763, 1996.
- [22] W. Jones and B. Launder. The Prediction of Laminarization with a Two-Equation Model of Turbulence. *Int. Journal of Heat and Mass Transfer*, 15:301-304, 1972.
- [23] B. Baldwin and H. Lomax. Thin Layer Approximation and Algebraic Model for Separated Flows. AIAA Paper 78-257, 1978.
- [24] A. Panaras. Algebraic Turbulence Modeling for Swept Shock Wave / Turbulent Boundary Layer Interactions. Technical Report IB 223-96 A 22, Deutsche Forschungsanstalt für Luft- und Raumfahrt e.V., March 1996.
- [25] D. Knight. Numerical Simulation of 3-D Shock Wave Turbulent Boundary Layer Interactions. In *AGARD/VKI Special Course on Shock-Wave Boundary-Layer Interactions in Supersonic and Hypersonic Flows*, pages 3-1 to 3-32. Von Karman Institute for Fluid Dynamics, May 1993. AGARD R-792.
- [26] D. Gaitonde, J. Shang, and M. Visbal. Structure of a Double-Fin Interaction at High Speed. *AIAA Journal*, 33(2):193-200, February 1995.
- [27] D. Gaitonde and J. Shang. Structure of a Turbulent Double-Fin Interaction at Mach 4. *AIAA Journal*, 33(12):2250-2258, December 1995.
- [28] D. Gaitonde and J. Shang. On 3-D Shock Wave Turbulent Boundary Layer Interactions at Mach 4. AIAA Paper 96-0043, 1996.
- [29] T. Garrison and G. Settles. Flowfield Visualization of Crossing Shock-Wave / Boundary Layer Interactions. AIAA Paper 92-0750, January 1992.
- [30] T. Garrison, G. Settles, N. Narayanswami, and D. Knight. Structure of Crossing-Shock Wave/Turbulent Boundary Layer Interactions. *AIAA Journal*, 31:2204-2211, December 1993.
- [31] T. Garrison and G. Settles. Interaction Strength and Model Geometry Effects on the Structure of Crossing - Shock Wave / Turbulent Boundary - Layer Interactions. AIAA Paper 93-0780, January 1993.
- [32] D. Knight, T. Garrison, G. Settles, A. Zheltovodov, A. Maksimov, A. Shevchenko, and S. Vorontsov. Asymmetric Crossing-Shock Wave / Turbulent Boundary Layer Interaction. *AIAA Journal*, 33(12):2241-2249, Dec 1995.
- [33] N. Narayanswami, D. Knight, S. Bogdonoff, and C. Horstman. Interaction Between Crossing Oblique Shocks and a Turbulent Boundary Layer. *AIAA Journal*, 30:1945-1952, August 1992.
- [34] N. Narayanswami, D. Knight, and C. C. Horstman. Investigation of a Hypersonic Crossing Shock Wave / Turbulent Boundary Layer Interaction. *Shock Waves*, 3(1):35-48, 1993.

- [35] N. Narayanswami, C. C. Horstman, and D. Knight. Computation of Crossing Shock Turbulent Boundary Layer Interaction at Mach 8.3. *AIAA Journal*, 31:1369-1376, August 1993.
- [36] A. Zheltovodov, A. Maksimov, A. Shevchenko, S. Vorontsov, and D. Knight. Experimental Study and Computational Comparison of Crossing Shock Wave - Turbulent Boundary Layer Interaction. In *Proceedings of the International Conference on Methods of Aerophysical Research - Part 1*, pages 221-230, August 1994. Russian Academy of Sciences, Siberian Division.
- [37] T. Garrison, G. Settles, N. Narayanswami, D. Knight, and C. Horstman. Flowfield Surveys and Computations of a Crossing Shock Wave / Boundary Layer Interaction. *AIAA Journal*, 34:50-56, Jan 1996.
- [38] M. Kussoy and K. Horstman. Intersecting Shock-Wave/Turbulent Boundary-Layer Interactions at Mach 8.3. Technical Report NASA TM 103909, NASA Ames Research Center, Feb 1992.
- [39] C. Becht and D. Knight. A Simple Low Reynolds Number Modification for the Compressible  $k-\epsilon$  Model. Part I. Boundary Layer Flows. AIAA Paper 95-2218, 1995.
- [40] G. Alexopoulos and H. Hassan. Computation of Crossing Shock Flows Using the  $k$ - $\epsilon$  Turbulence Model. AIAA Paper No. 97-0206, 1997.
- [41] K.-Y. Chien. Predictions of Channel and Boundary Layer Flows with a Low Reynolds Number Turbulence Model. *AIAA Journal*, 20:33-38, January 1982.
- [42] B. Sekar. Three Dimensional Computations of Parallel and Non-Parallel Injection in Supersonic Flow. AIAA Paper No. 95-0886, 1995.
- [43] G. Zha and D. Knight. Three-Dimensional Shock / Boundary-Layer Interaction Using Reynolds Stress Equation Turbulence Model. *AIAA Journal*, 34:1313-1320, July 1996.
- [44] G. Zha, D. Smith, M. Schwabacher, A. Gelsey, and D. Knight. High performance supersonic missile inlet design using automated optimization. AIAA Paper No. 96-4142, 1996.
- [45] M. Gnedin. *Numerical Simulation of 3-D Shock Wave Turbulent Boundary Layer Interaction Using a Two Equation Model of Turbulence*. PhD thesis, Rutgers University, May 1996.
- [46] M. Gnedin, D. Knight, A. Zheltovodov, A. Maksimov, A. Shevchenko, and S. Vorontsov. 3-D Crossing Shock Wave Turbulent Boundary Layer Interaction. AIAA Paper No. 96-2001, 1996.
- [47] P. Roe. Approximate Riemann Solvers, Parameter Vectors, and Difference Schemes. *Journal of Computational Physics*, 43:357-372, 1981.
- [48] D. Dolling. Problems in the Validation of CFD Codes through Comparison with Experiment. AGARD Symposium on Theoretical and Experimental Methods in Hypersonic Flows, Turin, Italy, 1992.
- [49] T. Garrison, G. Settles, N. Narayanswami, and D. Knight. Comparison of Flowfield Surveys and Computations of a Crossing - Shock Wave / Boundary - Layer Interaction. AIAA Paper 94-2273, June 1994.
- [50] W. L. Hankey and M. S. Holden. Two-dimensional shock wave-boundary layer interactions in high speed flows. AGARDograph 203, 1975.
- [51] B. Chanetz. Study of an axisymmetric shock wave/boundary layer interaction in hypersonic laminar flow. TR 42/4362 AN, ONERA, 1995.
- [52] A. Joulot. *Contribution à l'étude de l'interaction onde de choc-couche limite sur rampe bidimensionnelle en régime hypersonique*. PhD thesis, Université Pierre et Marie Curie, Paris, 1992.
- [53] E. Issman, G. Degrez, and H. Deconinck. Implicit upwind residual-distribution Euler and Navier-Stokes solver on unstructured meshes. *AIAA Journal*, 34(10):2021-2029, 1996.

- [54] J. N. Moss, V. K. Dogra, and J. M. Price. DSMC simulations of viscous interactions for a hollow cylinder-flare configuration. AIAA Paper 94-2015.
- [55] B. Chanetz, R. Benay, J.-M. Bousquet, R. Bur, T. Pot, F. Grasso, and J. Moss. Experimental and Numerical Study of the Laminar Separation in Hypersonic Flow. *Aerospace Science and Technology*, 1997. to be published.
- [56] P. R. Spalart and S. R. Allmaras. A one-equation turbulence model for aerodynamic flows. *La Recherche Aéronautique*, (1):5-21, 1994.
- [57] R. Paciorri, H. Deconinck, and G. Degrez. Implementation and validation of the Spalart-Allmaras turbulence model for application in hypersonic flows. Technical Note 190, von Karman Institute, 1996.
- [58] G. Inger. Supersonic Viscous-Inviscid Interaction of a Swept Ramp with a Turbulent Boundary Layer. AIAA Paper 85-1669, 1985.
- [59] G. Inger. Incipient Separation and Similitude Properties of Swept Shock/Turbulent Boundary Layer Interactions. AIAA Paper 86-0345, 1986.
- [60] G. Inger. Spanwise Propagation of Upstream Influence in Conical Swept Shock / Boundary Layer Interactions. *AIAA Journal*, 25:287-293, 1987.
- [61] K. Stewartson. Some Recent Studies in Triple-Deck Theory. In T. Cebeci, editor, *Numerical and Physical Aspects of Aerodynamic Flows*, page 142. Springer-Verlag, 1981.
- [62] A. Borisov, A. Zheltovodov, A. Maksimov, N. Fedorova, and S. Shpak. Verification of Turbulence Models and Computational Methods of Supersonic Separated Flows. In *Proceedings of the International Conference on Methods of Aerophysical Research*, pages 54-61, September 1996. Russian Academy of Sciences, Siberian Division.
- [63] I. Bedarev, A. Zheltovodov, and N. Fedorova. Supersonic Turbulent Separated Flows Numerical Model Verification. In *Proceedings of the International Conference on Methods of Aerophysical Research*, pages 30-35, June 1998. Russian Academy of Sciences, Siberian Division.
- [64] D. C. Wilcox. *Turbulence Modelling for CFD*. DCW Industries, 1993.
- [65] D. Dolling. Unsteady Phenomena in Shock - Wave / Boundary Layer Interaction. In *AGARD/VKI Special Course on Shock-Wave Boundary-Layer Interactions in Supersonic and Hypersonic Flows*, pages 4-1 to 4-46. Von Karman Institute for Fluid Dynamics, May 1993. AGARD R-792.
- [66] F. Alvi and G. Settles. Structure of Swept Shock Wave / Boundary Layer Interactions Using Conical Shadowgraphy. AIAA Paper 90-1644, 1990.
- [67] R. Courant and K. Friedrichs. *Supersonic Flow and Shock Waves*. Springer-Verlag, New York, 1948.

## A Conical Flow

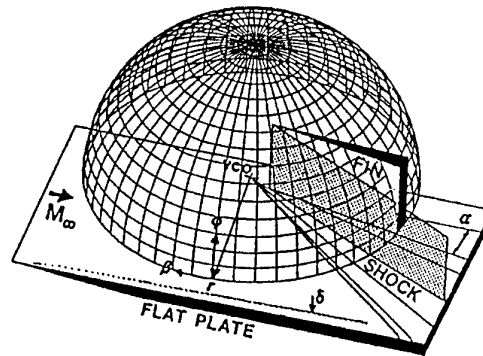


Figure 113: Spherical polar coordinates (from [66])

A conical flow is a steady flowfield whose Cartesian velocity components  $u_i$ , static pressure  $p$  and static temperature  $T$  are invariant with radial distance from a common vertex [67]. Consider the spherical polar coordinate system  $(R, \beta, \phi)$  shown in Fig. 113. Thus,

$$\begin{aligned}\frac{\partial u_i}{\partial R} &= 0 \\ \frac{\partial p}{\partial R} &= 0\end{aligned}$$

$$\frac{\partial T}{\partial R} = 0$$

where  $R$  is the spherical polar radius

$$R = \sqrt{(x-x_0)^2 + (y-y_0)^2 + (z-z_0)^2}$$

where  $(x_0, y_0, z_0)$  is the Virtual Conical Origin. For the single fin, the VCO is close to the intersection of the fin with the flat plate. The velocity, pressure and temperature are functions of the spherical polar coordinates

$$\beta = \tan^{-1}((z-z_0)/(x-x_0))$$

$$\phi = \tan^{-1}\left((y-y_0)/\sqrt{(x-x_0)^2 + (z-z_0)^2}\right)$$



# HYPersonic LAMINAR-TURBULENT TRANSITION

**WILLIAM S. SARIC**

Mechanical and Aerospace Engineering  
Arizona State University  
Tempe AZ 85287-6106 USA

**ELI RESHOTKO**

Mechanical and Aerospace Engineering  
Case-Western Reserve University  
Cleveland OH 44106 USA

**DANIEL ARNAL**

Département Aérodynamique  
ONERA / CERT  
31055 Toulouse, FRANCE

## ABSTRACT

The computational and experimental progress covering the four basic instability mechanisms that contribute to laminar-turbulent transition is reviewed. Streamwise, crossflow, centrifugal, and attachment-line instabilities and their principal means for initiating transition in hypersonic boundary layers are discussed. Comparisons between computations and experiments are given. Issues relating to how freestream disturbances influence the initial amplitudes of disturbances are also documented. Particular attention is paid to prediction schemes based on linear theory although other techniques are reviewed. This discussion is used to review the capabilities of present and future transition prediction methods as well as flow-quality requirements for hypersonic experimental facilities.

## 1 INTRODUCTION

The reliable computation of flowfields over hypersonic vehicles including skin friction and heat transfer information involves the determination of the location and extent of the region of laminar-turbulent transition. The rational estimation of transition location is generally not a part of any contemporary flowfield computational code. This report discusses some of the factors that would have to be considered in the estimation of transition behavior for hypersonic flight.

The evolution to turbulence in compressible boundary layers follows the generally accepted view that laminar-turbulent transition is a consequence of the nonlinear response of the laminar boundary layer to forcing disturbances. These distur-

bances are part of the environment within which the laminar flow develops and could include freestream turbulence, entropy disturbances, radiated sound, surface roughness, surface vibrations, etc., or any combination of these. These freestream disturbances enter the boundary layer as steady and/or unsteady fluctuations of the basic state. This part of the process is called *receptivity* (Morkovin, 1969) and although it is still not well understood, it provides the vital initial conditions of amplitude, frequency, and phase for the breakdown of laminar flow. Initially these disturbances may be too small to measure and they are observed only after the onset of an instability. A variety of different instabilities can occur independently or together and the appearance of any particular type of instability depends on Reynolds number, wall curvature, sweep, roughness, and initial conditions. The initial growth of these disturbances is described by *linear* stability theory (i.e. linearized, unsteady, Navier-Stokes). This growth is weak, occurs over a viscous length scale, and can be modulated by pressure gradients, surface mass transfer, temperature gradients, etc. As the amplitude grows, three-dimensional and nonlinear interactions occur in the form of *secondary* instabilities. Disturbance growth is very rapid in the case (now over a convective length scale) and breakdown to turbulence occurs.

Since the linear stability behavior can be calculated, transition prediction schemes are usually based on linear theory. However, since the initial conditions (receptivity) are not generally known, only correlations are possible and, most importantly, these corrections must be between two systems with similar environmental conditions.

At times, the initial instability can be so strong that the growth of linear disturbances is *by-passed* (Morkovin, 1969) and turbulent spots or secondary instabilities occur and the flow quickly becomes turbulent. This phenomenon is not well understood but has been documented in cases of roughness and high freestream turbulence (Reshotko, 1986). In this case, transition prediction schemes based on linear theory fail completely.

In the flight environment without large surface roughness, the most successful of the transition estimation techniques are those based on the results of linear stability calculations. Presently we have only developing knowledge of the nonlinear phenomena and breakdowns at supersonic and hypersonic speeds. Thus, much of what is discussed herein relies on linear theory.

This paper has benefited from other recent reviews of the important issues, principally those of Morkovin (1987, 1988), Morkovin and Reshotko (1990), Reed and Saric (1989), Reshotko (1994), and Reed et al. (1996, 1997). In particular, the work of Reed et al. (1997) directly complements this report.

## 2 GENERAL BACKGROUND

### 2.1 Linear Stability Theory

Linear theory addresses the first stage of boundary-layer eigenmode development, both for two-dimensional (2D) and three-dimensional flows (3D). The most thorough review of the details of the theory is given by Mack (1984). The principle is to introduce small sinusoidal disturbances into the Navier-Stokes equations in order to compute the range of unstable frequencies. Linear stability theory can be used either in its *local* or in its *nonlocal* formulation.

#### 2.1.1 Local Formulation

Any fluctuating quantity  $r'$  (velocity, pressure, density or temperature) is expressed by:

$$r' = r(y) \exp[i(\alpha x + \beta z - \omega t)] \quad (1)$$

where  $x, y, z$  is an orthogonal coordinate system, which can be either Cartesian or curvilinear,  $y$  being normal to the surface. The complex amplitude function  $r$  depends on  $y$  only. In the general case,  $\alpha, \beta$ , and  $\omega$  are complex numbers.

The fluctuating quantities are very small, so that the quadratic terms of the disturbances can be neglected in the Navier-Stokes equations. It is also assumed that the mean flow quantities do not vary significantly over a wavelength of the disturbances; therefore  $U$  and  $W$  (mean flow components in the  $x$  and  $z$  directions) as well as the mean temperature  $T$  are functions of  $y$  alone, and the normal velocity  $V$  is equal to zero.

The implication of this *parallel flow approximation* is that the stability of the flow at a particular station ( $x, z$ ) is determined by the local conditions at that station independently of all others.

This leads to a system of homogeneous, ordinary differential equations for the amplitude functions  $r(y)$ . The homogeneous boundary conditions (the disturbances must vanish in the freestream and the velocity fluctuations are zero at the wall), establish an eigenvalue problem: when the mean flow is specified, nontrivial solutions exist only for certain combinations of the parameters  $\alpha, \beta, \omega$  and  $R$ , where  $R$  is the Reynolds number. This constitutes the *dispersion relation*.

In this paper, the discussion will be restricted to the *spatial theory*, which is more relevant than the temporal theory for boundary-layer flows. Thus,  $\omega$  is real,  $\alpha$  and  $\beta$  are complex:  $\alpha = \alpha_r + i\alpha_i$  and  $\beta = \beta_r + i\beta_i$ . Then  $r'$  is expressed by:

$$r' = r(y) \exp(-\alpha_i x - \beta_i z) \exp[i(\alpha_r x + \beta_r z - \omega t)] \quad (2)$$

It is possible to define a wavenumber vector  $\vec{k} = (\alpha_r, \beta_r)$  and an amplification vector  $\vec{A} = (-\alpha_i, -\beta_i)$  with angles  $\varphi$  and  $\bar{\varphi}$  with respect to the  $x$  direction:

$$\varphi = \tan^{-1}(\beta_r / \alpha_r) \quad (3)$$

$$\bar{\varphi} = \tan^{-1}(\beta_i / \alpha_i) \quad (4)$$

From these definitions, it is now clear that any eigenvalue problem involves six real parameters  $(\alpha_r, \alpha_i, \beta_r, \beta_i, \omega, R)$  which are often replaced by  $(\alpha_r, \alpha_i, \varphi, \bar{\varphi}, \omega, R)$ . The input data are the mean velocity and mean temperature profiles and four of the six parameters listed above. The computation gives the values of the two remaining parameters (eigenvalues) as well as the disturbance amplitude profiles (eigenfunctions).

#### 2.1.2 Nonlocal Formulation

A new formulation for the stability analysis was recently proposed by Herbert (see overview in Herbert 1994) and by DLR Göttingen (see Simen and Dallmann 1992 and Dallmann et al. 1996). In this approach, the general expression of the disturbances is:

$$r' = r(x, y) \exp[i(\theta(x) + \beta z - \omega t)] \text{ with } \frac{d\theta}{dx} = \alpha(x) \quad (5)$$

$\alpha$  is complex,  $\beta$  and  $\omega$  are real and constant. In contrast to the local approach expressed by relation (1), the amplitude functions depend on  $y$  and  $x$ , and  $\alpha$  depends on  $x$ . Substituting the previous expression into the stability equations, neglecting  $\partial^2 r / \partial x^2$  and linearizing in  $r$  yield a partial differential equation of the form:

$$Lr + M \frac{\partial r}{\partial x} + \frac{d\alpha}{dx} Nr = 0 \quad (6)$$

where  $L$ ,  $M$ , and  $N$  are operators in  $y$  with coefficients that depend on  $x$  and  $y$  through the appearance of the basic flow profiles and of the wavenumber  $\alpha$ . When  $d\alpha/dx$  is computed from a so-called normalization condition, the previous equation can be solved using a marching procedure in  $x$  with prescribed initial conditions: this constitutes the PSE (Parabolized Stability Equations) approach. The interest of this procedure is that the nonparallel effects are taken into account. As it will be discussed in section 2.2, it is also possible to introduce the *nonlinear* terms.

## 2.2 Nonlinear Approaches

Today, several approaches are available to analyze the behavior of the disturbances when they begin to deviate from the linear amplification regime. These numerical tools include, for instance, the method of multiple scales or the secondary instability theories (Herbert 1988). DNS are of course particularly helpful for improving the understanding of the nonlinear mechanisms. For practical applications, nonlinear PSE are particularly attractive; although they only describe *weakly nonlinear phenomena*, they are less time-consuming than DNS and they can be used for rather complex geometries.

The basic ideas of the nonlinear PSE have been explained in many papers, see for instance Herbert (1994) and Reed et al. (1998). The disturbances are written as double Fourier expansions containing two- and three-dimensional discrete normal modes denoted as  $(n, m)$  modes:

$$r' = \sum_{n=-\infty}^{\infty} \sum_{m=-\infty}^{\infty} r_{n,m}(x, y) F_{n,m} \quad (7)$$

with

$$F_{n,m} = \exp \left[ i \left[ \int_{x_0}^x \alpha_{n,m}(\xi) d\xi + m\beta z - n\alpha x/2 \right] \right]$$

$\alpha_{n,m}$  is complex,  $\beta$  and  $\omega$  are real and constant. Introducing (7) into the Navier-Stokes equations leads to a system of coupled partial differential equations which are solved by a marching procedure in the  $x$  direction. This method makes it possible to treat nonlinear mode interactions with a numerical effort which is much less than that required by DNS.

## 3 STATE-OF-THE-ART CONSIDERATIONS

### 3.1 Streamwise Instability

Theoretical studies have concentrated principally on determining the character and properties of the growing normal modes. In their pioneering study, Lees and Lin (1946) introduced the generalized inflection criterion (maximum of the local angular momentum  $\rho \partial U / \partial y$ ), and the classification of

disturbances as subsonic or supersonic with respect to the local external flow. Subsonic disturbances whether neutral, growing, or decaying all display exponential drop-off of amplitude at large distances from the wall. The neutral stability curves of the subsonic modes in the inviscid limit for insulated, flat-plate compressible boundary layers are described in Fig. 1 (Mack 1969). The lowest mode ( $n = 1$ ) is the vortical mode which corresponds to the TS modes of the subsonic boundary layer. The higher subsonic modes ( $n \geq 2$ ), discovered by Mack (1965a), are trapped acoustic modes that occur when additionally the wall is supersonic relative to the phase velocity ( $c_r/a_w > 1$ ). For insulated surfaces, these higher "Mack" modes appear for  $M > 2.2$ ; however it is not until the Mach number is of the order of 4 or greater that the second mode is at a low enough frequency to have experimental consequences as shown in Fig. 2. Once the second mode sets in, it becomes the dominant instability since its growth rate tends to exceed that of the first mode. For insulated surfaces this occurs for  $M > 4$  as shown in Fig. 3. For cooled surfaces, second-mode dominance can occur at even lower Mach number. In contrast to the first or TS mode, the higher subsonic modes are destabilized by cooling (Mack 1969). Indications are that the second-mode subsonic disturbances can be somewhat stabilized by favorable pressure gradient or by suction (Malik 1988, Malik 1989, Mack 1990a).

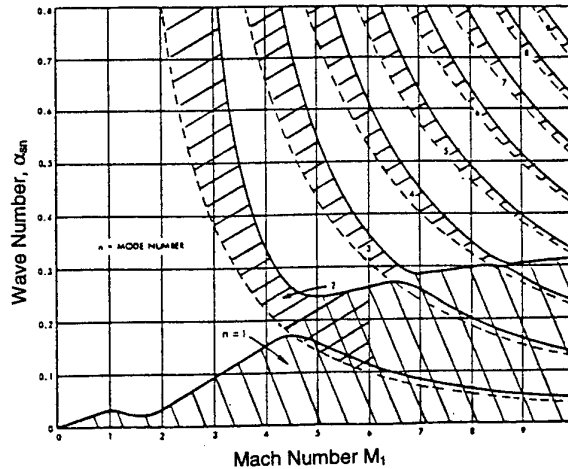


Figure 1. Wave numbers  $2\pi/\lambda^*$  corresponding to inviscid compressible instabilities in insulated flat-plate boundary layers. (2D Waves). Solid lines are subsonic waves. Dashed lines are supersonic waves. (Mack 1969).

Supersonic disturbances ( $c_r < 1 - 1/M_e$ ) were long considered irrelevant since supersonic neutral disturbances have non-vanishing amplitudes at infinite distances from the wall. Mack (1969) has shown, however, that amplifying outgoing supersonic disturbance amplitudes do decay exponentially for large  $y$ , albeit slowly, and are therefore acceptable normal modes.

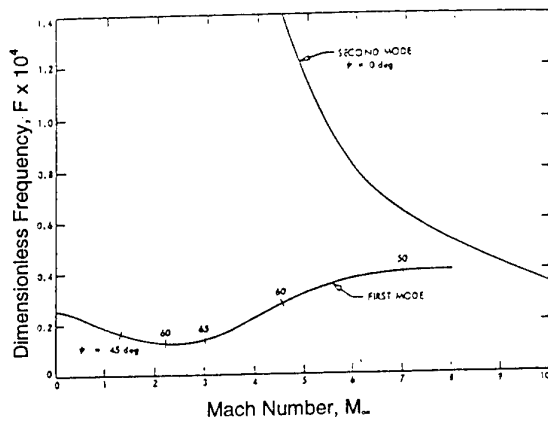


Figure 2. Effect of Mach number on first-and second-mode most unstable frequencies  $Re=1500$ , insulated wall; wind tunnel temperatures (Mack 1969).

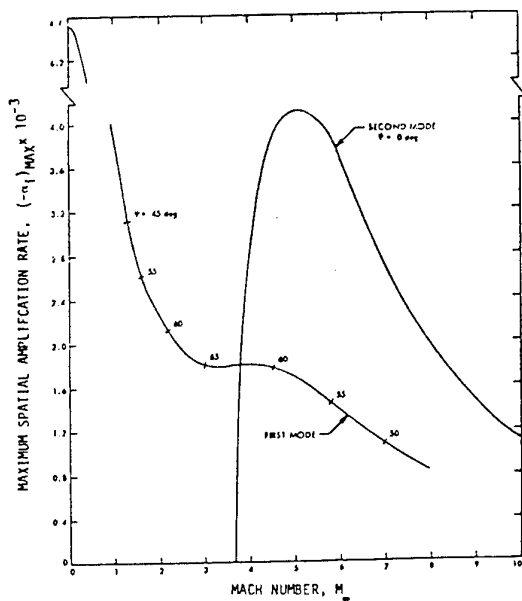


Figure 3. Effect of Mach number on spatial amplification rate of most unstable first-and second-mode disturbances  $Re=1500$ . Insulated wall; wind tunnel temperatures (Mack 1969).

Mack (1969) found second-mode supersonic disturbances at  $M = 5.8$  for highly-cooled walls ( $T_w/T_{aw} < 0.15$ ) in the inviscid limit. Their growth rates however were found to be much lower than those of the subsonic disturbances and their

wavenumbers (frequencies) noticeably larger. Mack (1990a) has also calculated cases of highly-cooled boundary layers at  $M = 3$  and  $M = 4.5$ , again in the inviscid limit, and found second-mode supersonic disturbances that are destabilized by suction. Although the growth rates of these latter disturbances approach the levels associated with subsonic disturbances, the disturbance wavenumbers and corresponding frequencies are very large. The significance of these disturbances to the transition process is likely to be negligible since Mack (1990b) further indicates that they are strongly damped at finite Reynolds number.

### 3.1.1 Description of Mack Modes

As stated above, the Mack modes are trapped acoustic modes whose phase velocities are subsonic with respect to the freestream but supersonic with respect to the wall. Their geometry was clarified by Morkovin (1987). Referring to Fig. 4, harmonic vorticity and entropy perturbations traveling along  $y_1$  (the height of the sonic speed relative to  $y_s$ ) are shown to be phase-tuned to coupled trapped acoustic perturbations traveling to the wall and back along Mach lines, stationary in this frame of reference. The reflection at the sonic streamline changes compression to expansion and vice-versa (the essence of the trapping). As a geometrical consequence, perfect phase coincidences at any Mach number occur only for wave number  $\alpha_{1n}$  in the exact ratios to  $\alpha_{11}$  of 1, 3, 5, ...  $2n-1$ . This is the property of Mack's noninflectional neutral-mode families as shown as dotted lines in Fig. 1.

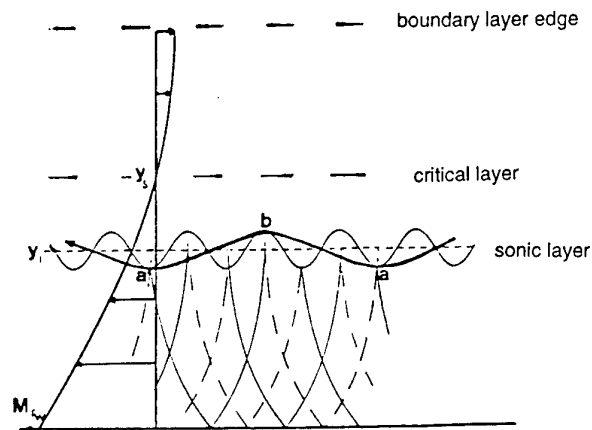


Figure 4. View of the mean flow and of vorticity-entropy-pressure disturbance interactions along characteristic curves in higher instability modes, (Mack modes) as seen when traveling with the flow at the height of the generalized inflection point.

### 3.1.2 $e^N$ Method

The so-called  $e^N$  method is widely used by people who are assigned the job of making transition prediction. It was first developed by Smith and Gamberoni (1956) and by van Ingen

(1956) for low-speed flows and then extended to compressible and/or three-dimensional flows.

The  $e^N$  method is based on linear theory only, so that many fundamental aspects of the transition process are not accounted for. However, one has to keep in mind that there is no other practical method presently available for industrial applications. Caveats regarding the use and application of this method are found in Morkovin and Reshotko (1990).

**Incompressible flows.** In this case, only 2D waves ( $\beta = 0$ ) are considered. The disturbances are amplified or damped according to the sign of the spatial growth rate  $-\alpha_i$ .

For a given mean flow, it is possible to compute the total amplification rate of a spatially growing wave by integrating the local growth rate in the streamwise direction:

$$\ln(A/A_0) = \int_{x_0}^x -\alpha_i dx \quad (8)$$

where  $A$  is the wave amplitude and the index 0 refers to the streamwise position where the wave becomes unstable. The envelope of the total amplification curves is:

$$N = \max_f [\ln(A/A_0)] \quad (9)$$

In incompressible flow, with a low disturbance environment, experiments show that transition occurs when the  $N$ -factor reaches a critical value in the range 7–10, i.e., when the most unstable wave is amplified by a factor  $e^7$  to  $e^{10}$ .

**Compressible flows.** When compressibility begins to play a role, the problem becomes more complex, because the most unstable waves are often oblique waves. As a consequence, a new parameter enters the dispersion relation: the angle  $\varphi$  between the streamwise direction and the wavenumber vector. It is still assumed that the amplification takes place in the  $x$ -direction only, i.e.,  $\beta = 0$  or  $\bar{\varphi} = 0$ , but  $\beta_r$  (or  $\varphi$ ) needs to be specified.

For *second-mode disturbances*, the problem is rather simple, because the most unstable direction is  $\varphi = 0^\circ$  i.e.,  $\beta_r = 0$ . As  $\beta_i$  is also zero, it is sufficient to drop  $\beta_r$  in the exponential term of equation (1).

For *first-mode disturbances*, the most unstable direction is no longer the  $x$ -direction; in addition, this direction varies when the computation proceeds downstream. Two strategies are essentially used for two-dimensional flows:

- At each streamwise location, one finds the direction,  $\varphi_M$ , of the wave which gives the maximum value  $-\alpha_{iM}$  of  $\alpha_i$ . The  $N$ -factor is then defined by:

$$N = \max_f \int_{x_0}^x -\alpha_{iM} dx \quad (10)$$

This is the so-called *envelope method*.

- The integrations are performed by following waves having a given dimensional frequency  $f$  and a constant value of the dimensional component  $\beta_r$  of the wavenumber vector in the spanwise direction. The  $N$ -factor is then computed by maximizing the total growth rate with respect to both  $f$  and  $\beta_r$ . The interest of this *fixed-frequency/fixed-spanwise-wavenumber method* is that it is congruent with the expression of the disturbances in the nonlocal theory.

**Examples of application.** The results presented in this section have been obtained with the local approach. Additional details are given in Reed et al. (1996, 1997). Comparison between local and nonlocal results will be discussed later on.

In supersonic and hypersonic wind tunnels, the main factor affecting transition on the models is noise, the origin of which lies in the pressure disturbances radiated by the turbulent boundary layers developing along the nozzle walls. This leads to low transition Reynolds numbers, i.e., small values of the  $N$ -factor at transition; typical values are in the range between 1 and 4.

Since the radiated noise is inherent in the presence of walls around the model, there is little doubt concerning the incapacity of conventional ground facilities to properly simulate free-flight conditions. In order to reduce this noise level, it is necessary to delay transition on the nozzle walls because a laminar boundary layer is less noisy than a turbulent one. This was done in the *quiet tunnel* built at NASA Langley with a freestream Mach number  $M_\infty = 3.5$  (see description in Beckwith 1983). Notable features are the use of boundary-layer bleed slots upstream of the throat, a careful polishing and a careful design of the nozzle walls contour in order to minimize the development of Görtler vortices. With a laminar boundary layer on the nozzle walls, the measured pressure fluctuations can be one or two orders of magnitude below those measured in conventional facilities.

Several transition experiments were carried out in the quiet tunnel. On a flat plate, transition Reynolds numbers  $R_{XT}$  as high as  $12 \times 10^6$  were measured; this result corresponds to  $N$ -factors around 10 (Chen and Malik 1988). The flow on supersonic sharp cones constitutes a second case where the freestream Mach number is constant in the streamwise direction. Measurements performed in the quiet tunnel give values of  $R_{XT}$  close to 7 or  $8 \times 10^6$ . The predicted transition Reynolds number computed for  $N = 10$  is  $8 \times 10^6$ , in good agreement with experimental data (Chen and Malik 1988).

The problem is to know whether or not low-disturbance-level wind tunnels are representative of free-flight conditions. As

direct comparisons of the disturbance environment are difficult to perform, indirect comparisons are made by looking at the value of the  $N$ -factor at transition. In this respect, the flight experiments on the so-called AEDC cone (Fisher and Dougherty 1982) provided us with some interesting information. Malik (1984) computed the  $N$ -factor for four flight-test points corresponding to  $M_\infty = 1.2, 1.35, 1.6$  and  $1.95$ . He found transition Reynolds numbers at the onset of transition that were correlated by  $N$ -factors between 9 and 11.

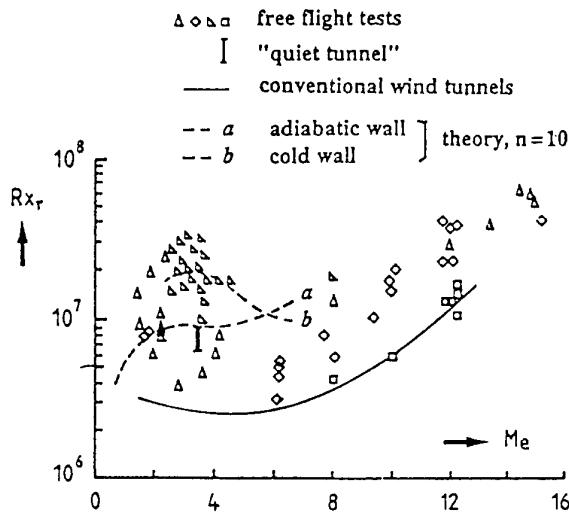


Figure 5. Comparison between measured and predicted transition Reynolds numbers on sharp cones

Unfortunately, reliable and accurate free flight data are scarce at higher, hypersonic Mach numbers. Figure 5 shows flight transition results collected for sharp cones by Beckwith (1975). The transition Reynolds numbers  $R_{XT}$  are plotted as function of the freestream Mach number. The figure also contains a correlation for wind tunnel transition data, which lies much below the flight results. The range of  $R_{XT}$  measured in the quiet tunnel are reported for comparison. The main reason for the large scatter in the free-flight results is that these data have been obtained for various conditions of wall temperatures, the distribution of which is not known in many cases. Malik (1989) calculated the values of  $R_{XT}$  corresponding to  $N = 10$  for a  $5^\circ$  half angle cone and for Mach numbers up to 7. He made two series of computations: one by assuming that the wall was adiabatic, and the other by assuming that the wall temperature decreased with increasing  $M_\infty$  according to a certain empirical relationship. The latter computations (curve  $b$  in Fig. 5) make it possible to reproduce the trends exhibited by the flight results.

The  $e^N$  method was also used by Malik et al. (1990b) for the rather complex reentry-F experiments. The reentry-F vehicle (Johnson et al. 1972) consisted of a  $5^\circ$  half angle cone with an initial nose radius of 2.54 mm. Computations were performed at an altitude corresponding to a freestream Mach number close to 20. The basic flow was calculated by equilibrium gas Navier-Stokes and PNS codes. At the measured transition location, the  $N$ -factor was around 7.5. Roughness effects probably affected the transition mechanisms, so that the value of  $N$  would be somewhat larger for a perfectly smooth surface.

The conclusion is that the  $e^N$  method with  $N \approx 10$  can be applied to predict transition in high-speed two-dimensional flows if the background disturbance level is low enough and if the wall is smooth.

Examples of parametric studies: Bluntness effects. Even if the exact value of the  $N$ -factor is not known for practical applications, the  $e^N$  method remains a very efficient tool for parametric studies: for a given test model and for a given disturbance environment, it is often able to predict the variation of the transition location as a function of the variation of a key parameter which governs the stability properties of the mean flow.

In hypersonic flows, the nose bluntness of a cone at zero angle of attack strongly affects the transition location. For instance, Malik et al. (1990a) performed a linear stability analysis for the experimental conditions studied by Stetson et al. (1984). In these experiments ( $M_\infty = 8$ ) the transition mechanisms were investigated on a cone which could be equipped with interchangeable spherically blunted noses of various radii. By using the  $e^N$  method, Malik et al. found that the predicted transition Reynolds number increased due to small nose bluntness, in qualitative agreement with experimental results. They also demonstrated that nose bluntness could explain the unit Reynolds number effect observed in the aeroballistic range data of Potter (1974).

Quite recently, ESA (European Space Agency) launched a TRP (Technological Research Programme) involving several research centers under the responsibility of Aerospatiale. The general objective was to analyze laminar-turbulent transition problems for hypersonic flow on slender lifting configurations. One of the experimental studies was devoted to the effect of nose bluntness for a cone placed at zero angle of attack in a wind tunnel at Mach 7 (unit Reynolds number  $= 25 \times 10^6 / \text{m}$ ). It was found that the  $e^N$  method was able to reproduce the rearward movement of the transition point when the nose radius increased from (nearly) 0 to 0.5 mm; the chosen value of the  $N$ -factor was that corresponding to the sharp cone case (Tran et al. 1995; Arnal et al. 1996).

### 3.1.3 Stability and Transition Experiments at Hypersonic Speeds

Meaningful stability and transition experiments at hypersonic speeds require facilities or techniques that are free of influence of the noise content of the facility. The stability experiments are best performed by inputting prescribed disturbances and measuring their growth properties. Of course, through astute signal analysis, the growth of tunnel disturbances can also be monitored and stability characteristics deduced, but there can be aliasing problems. Of the stability experiments performed before 1990, most notable are the  $M = 4.5$  flat-plate experiment of Kendall (1975) and the cone experiments of Stetson et al (1991) in AEDC Tunnel B summarized by Stetson and Kimmel (1992). By inputting 2D and oblique disturbances, Kendall mapped out the first- and second-mode stability characteristics of the adiabatic flat-plate boundary layer. Stetson et al. (1991) did not generate disturbances in the boundary layer but relied on an analysis of the response of the boundary layer to the disturbance content in the wind tunnel. Transition experiments on the other hand should be done in quiet tunnels, which hardly exist at hypersonic speeds. Conventional tunnels above Mach 8 or so tend to have very low noise levels at second mode and higher frequencies and so have been used to obtain transition data. But since such tunnels are not quiet at subharmonic and mode-mode interaction frequencies, the nonlinear interactions leading to transition can be different than in flight. The discussion in this section will emphasize work performed in the last five years.

**Experiments in the  $M = 5$  Ludwig Tube Facility at DLR.** A set of flat-plate and cone experiments have been performed in the  $M = 5$  Ludwig-tube facility at DLR (Wendt et al. 1993, Krogmann 1996). The authors claim that despite having turbulent nozzle-wall boundary layers, this facility is quieter than conventional supersonic tunnels but not as quiet as the  $M = 3.5$  quiet tunnel at NASA-Langley (Beckwith et al 1983) or the new quiet-flow Ludwig tube facility at Purdue University (Schneider and Haven 1995). Although not specified, the ratio  $T_w/T_{aw}$  is estimated to be about 0.9 for all these tests. Based on analysis of the response in the boundary layer to tunnel disturbances, the authors conclude that their signals are primarily from growing oblique first-mode disturbances. They could not find any significant second-mode response in their tests. They accordingly conclude that transition in their facility is first-mode dominated and are surprised by this result. They should however not have been surprised. In an  $e^N$  study of transition on sharp cones at zero angle-of-attack, Malik (1989) showed that for adiabatic walls, the transition is first-mode dominated up to  $M_\infty \approx 7$ , and second-mode dominated above that. Thus there is no inconsistency between the  $M_\infty = 5$  results at DLR and second-mode dominant experi-

ments of Stetson et al. (1991) at  $M_\infty = 8$ . The  $M_\infty = 5$  condition is not hypersonic enough for second-mode dominance. The transition Reynolds numbers (Krogmann 1996), are of course lower than the expected values from  $e^N$  calculations since the facility is not sufficiently quiet. But they are remarkably independent of unit Reynolds number.

**Experiments at  $M = 8$  in AEDC Tunnel B.** As a follow-on to the circular cone experiments at  $M_\infty = 7.93$  in AEDC Tunnel B reported by Stetson and Kimmel (1992), there have been recent measurements reported (Kimmel et al. 1996; Kimmel and Poggie 1997; Poggie and Kimmel 1997) that address the three-dimensional structure of the instability waves. It was earlier established that the initial instability is second mode and its growth is in accordance with linear theory. Using two hot-film probes, both located at the height in the boundary layer of maximum broadband rms signal, but with varying circumferential separation, the correlation of the signals (Fig. 6) indicates second-mode disturbances (streamwise wavelength  $\sim 2\delta$ ) that are essentially two-dimensional.

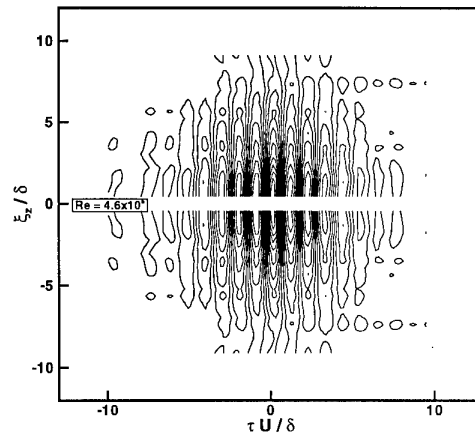


Figure 6. Circumferential correlations on the axisymmetric cone for  $Re_x = 2.3 \times 10^6$  (Kimmel and Poggie 1997).

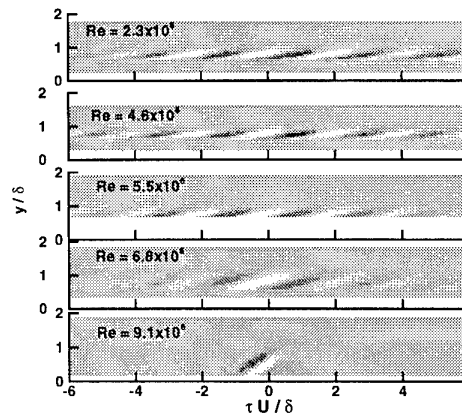


Figure 7. Vertical correlations on the axisymmetric cone.

Correlations in the vertical direction were obtained using two probes separated vertically by 1.47 mm and traversing them vertically through the boundary layer. With appropriate signal analysis (see Kimmel and Poggie 1997), the second-mode waves are shown to have a flattened structure (Fig. 7) that agrees qualitatively with shadowgraphs of the "rope waves" for the same configuration. These rope waves which appear before boundary-layer breakdown, seem to be a nonlinear manifestation of the second mode. With an increase in Reynolds number approaching transition, the waves become more erect approaching the angles of turbulent structures.

Cone experiments at  $M = 5$  in the Caltech T5 Hypervelocity Shock Tunnel. Boundary-layer transition experiments were performed on a 5° half-angle cone at zero angle-of-attack in air, nitrogen and carbon dioxide (Germain et al. 1993; Adam and Hornung 1997). With air and nitrogen as test gases, reservoir enthalpies varied from 4 MJ/kg to 27 MJ/kg at stagnation pressures from 10 MPa to 85 MPa. For carbon dioxide, reservoir enthalpies varied from 3 MJ/kg to 10 MJ/kg and reservoir pressures from 40 MPa to 95 MPa. Dissociative effects are clearly important. The wall temperature is not specified. However, assuming it to be about 300 K gives a wall enthalpy of just under 0.6 MJ/kg for air and nitrogen and just under 0.5 MJ/kg for carbon dioxide. So these tests are conducted under very cold-wall conditions where under linear stability arguments, the second mode should dominate.

However, while the disturbance environment is not quantitatively described, it is generally regarded as noisy. Therefore the relationship between the obtained results and linear stability arguments is not clear. Adam and Hornung (1997) state that no clear relationship is found to exist between the transition Reynolds number based on the boundary layer edge conditions and the reservoir enthalpy. However, when reference temperature conditions are used instead, the different test gases give distinguishable results which are ordered according to their dissociation energies. These authors also compare their T-5 results with Reentry-F flight data reported by Wright and Zoby (1977). The flight data are in a Mach number range from about 8 to 20 and are taken in a relatively quiescent environment. Nevertheless, Adam and Hornung (1997) show that the transition Reynolds numbers under reference temperature conditions are between 600,000 and 2,000,000 for both the T-5 and the Reentry-F flight data. This collapse of data is interesting and unexpected. More data are needed to show that this result is other than fortuitous.

Stability experiments on a flared cone model in the NASA-Langley Mach 6 Quiet Tunnel. Experiments were conducted on 5° half-angle cones followed by large-radius circle-arc flares. The experiments at adiabatic wall conditions with and without small bluntness are by Lachowitz et al. (1996). Those

on the sharp-tipped model at small angles of attack are by Doggett et al. (1997), while those on a slightly different sharp-tipped model with wall cooling are by Blanchard (1995). All three sets of experiments are summarized by Wilkinson (1997). In all cases, the cone portions of the models and a portion of the flare region were free from any tunnel noise. Only the aft portions of the flare were subject to low-level radiated noise from the part of the nozzle wall boundary layers that were undergoing some mild Görtler instability growth. The experiments included a detailed study of the mean flow and the stationary freestream disturbance patterns in the Mach 6 nozzle. The experiments documented the growth of the dominant second-mode disturbances with adverse pressure gradient, small nose bluntness, wall cooling and small angle of attack.

Under adiabatic wall conditions, the recovery temperature distributions on the sharp-tipped model showed transition occurring only at the very end of the flared section. Hot-wire spectra for this case taken at each streamwise measuring station showed a dominant second-mode peak at about 226 kHz corresponding to a linear stability prediction of 230 kHz (Balakumar and Malik 1994). There are however also harmonic peaks around 449 kHz and 670 kHz indicating some nonlinear behavior. Very small nose bluntness eliminated transition but still showed some growth of the second mode at around 230 kHz. With slightly larger nose bluntness there was neither transition nor evidence of second-mode growth. At two degrees angle of attack, the boundary layer on the windward side is stabilized and the dominant second-mode frequency increased, while on the leeward side the boundary layer is destabilized and the dominant frequency sharply decreased. Also on the leeward side, localized peaks over a range of low frequencies are observed upstream of the second-mode growth. These may be associated with crossflow instability.

Under cold wall conditions (sharp-tipped model at zero angle of attack), the second-mode frequency is at slightly higher frequency as expected theoretically (Balakumar and Malik 1994), the first harmonic (at just under 600 kHz) is comparable in amplitude to the fundamental and transition is advanced to mid-flare.

Transition studies on curved compression surfaces in the Calspan 48-inch Hypersonic Shock Tunnel. Pressure and heat transfer measurements were made on a curved compression ramp whose geometry is typical of an inlet to a scramjet engine (Holden and Chadwick 1995). The measurements were made at Mach numbers 10, 11 and 12 for a range of Reynolds numbers at each Mach number to place the beginning of transition at various stations along the ramp. Whereas the thin-film heat flux gauges were capable of obtaining transient data,



and these were used to more closely identify transition locations, only mean heat transfer data are presented. In the absence of spectral information, it is not possible to identify the dominant modes of the pre-transitional growth.

The transition results are not particularly sensitive to the small differences in Mach number in the  $M = 10 - 12$  range. At the highest unit Reynolds numbers, transition occurs on the 5° wedge preceding the curved portion of the ramp. As unit Reynolds number is lowered, transition moves downstream as expected until at the lowest unit Reynolds numbers tested, it occurs around the end of the curved ramp. Although transition Reynolds numbers are not computed, it appears that the highest transition Reynolds numbers are obtained at the highest unit Reynolds numbers. Some of the reduction in transition Reynolds number with unit Reynolds number is due to the influence of the adverse pressure gradient on the compression ramp, and in fact, the length of the transition zone is reduced when the transition occurs on the curved ramp. In these experiments the maximum end-of-transition Reynolds number is about  $3 \times 10^6$ , below what one expects in flight at these Mach numbers. The facility may not be "quiet" enough for flight-quality data for the reported tests.

### 3.1.4 Effects of Chemistry and Bow Shock (Reed et al. 1997)

Linear stability solutions for hypersonic flows are complicated for some of the following reasons. 1) At hypersonic speeds, the gas often cannot be modeled as perfect because the molecular species begin to dissociate due to aerodynamic heating. In fact, sometimes there are not enough intermolecular collisions to support local chemical equilibrium and a nonequilibrium-chemistry model must be used. 2) The bow shock is close to the edge of the boundary layer and must be included in studies of transition.

Malik (1987, 1989, 1990) investigated the stability of an equilibrium-air boundary layer on an adiabatic flat plate. Malik et al. (1990) used the  $e^N$  method for the reentry-F experiments; the basic state was calculated by equilibrium-gas Navier-Stokes and PNS. Gasperas (1990) studied stability for an imperfect gas. Stuckert and Reed (1994) analyzed the stability of a shock layer in chemical nonequilibrium and compared results with the flow assuming 1) local chemical equilibrium and 2) a perfect gas.

Stuckert and Reed's coordinate system for both the basic-state and stability analysis fit the body and bow shock as coordinate lines. This makes it easier to apply the linearized shock-jump conditions as the disturbance boundary conditions (e.g. Stuckert 1991). At the surface of the cone, for the nonequilibrium calculations, the species mass fluxes were set to zero (non-catalytic wall), whereas for the equilibrium calculations the disturbances were assumed to be in chemical equilibrium. It is

clear that the equilibrium and nonequilibrium solutions can differ significantly depending on the rates of the reactions relative to the time scales of convection and diffusion. For example, some of the equilibrium modes were determined to be supersonic modes, each of which was a superposition of incoming and outgoing amplified solutions in the inviscid region of the shock layer. (No similar solutions were found for the nonequilibrium shock layer.) The magnitudes of these modes oscillated with  $y$  in the inviscid region of the shock layer. This behavior is possible only because the shock layer has a finite thickness. They are also unlike Mack's higher modes (except for the second) in that the disturbance-pressure phase for all of these supersonic modes changed most across the inviscid region of the shock layer. (The disturbance-pressure phase change for Mack's higher modes occurs across the viscous region of the flow, i.e. the boundary layer.) In fact, the disturbance-pressure phase change for all of these supersonic modes through the boundary layer is comparable to that of Mack's second mode.

Another effect of the chemical reactions is to increase the size of the region of relative supersonic flow primarily by reducing the temperature in the boundary layer through endothermic reactions, increasing the density, and hence decreasing the speed of sound. This reduces the frequency of the higher modes; in particular, the most unstable one, the second mode. The higher modes in the reacting-gas cases are also more unstable relative to the corresponding perfect-gas modes. The first modes are, however, more stable.

Finally, the finite thickness of the shock layer has a significant effect on the first-mode solutions of all of the families. The effect on higher-mode, higher-frequency solutions does not seem to be as large as long as they are subsonic. This is perhaps what one would intuitively expect because the shock is likely "stiff" and hence difficult to perturb with smaller-wavelength, larger-wavenumber, higher-frequency disturbances. However, the nonparallel effects are known to be large for first-mode solutions, and so a complete quantitative description of the effects of the finite shock-layer thickness awaits either a PSE solution or a DNS analysis.

The inclusion of the bow shock is especially critical to studies of leading-edge receptivity as demonstrated by Zhong (1997). His DNS results over a blunt wedge show that the instability waves developed behind the bow shock consist of both first and second modes. His results also indicate that external disturbances, especially entropy and vorticity disturbances, enter the boundary layer to generate instability waves mainly in the leading-edge region.

### 3.1.5 Nonlocal Effects

It is now recognized that the growth rate of two-dimensional waves is only weakly affected by nonparallel effects. This was demonstrated for the Blasius flow by the computations of Gaster (1974) who used the method of multiple scales. This result was confirmed by PSE and DNS computations. PSE results were published by Bertolotti (1991) and by Chang et al. (1991) for supersonic Mach numbers. A good agreement was achieved with the multiple scale analysis of El-Hady (1991) at  $M_e = 1.6$ .

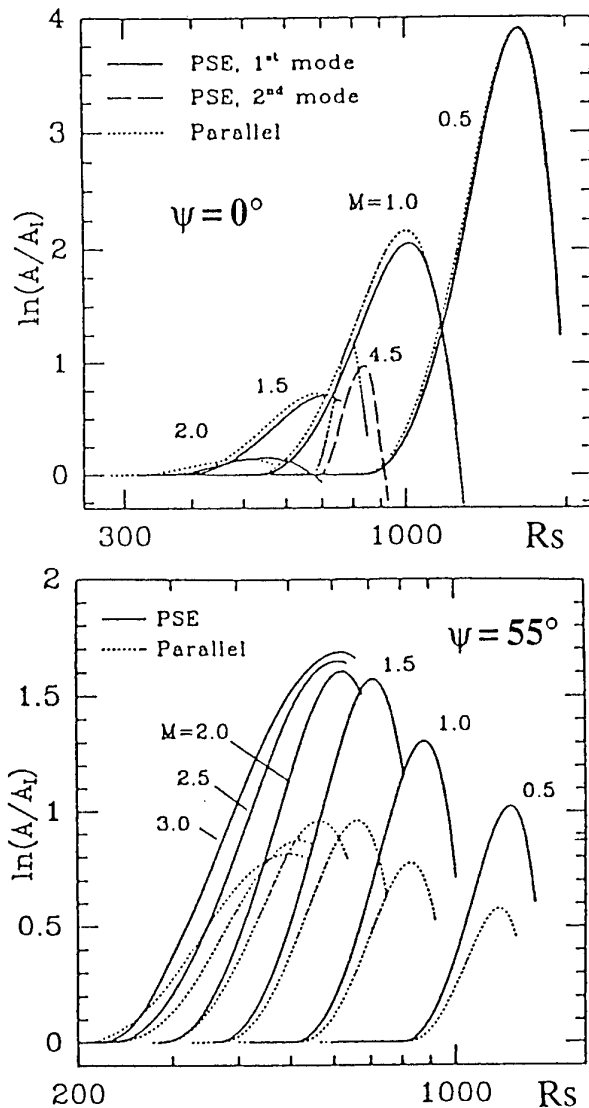


Figure 8. Integrated amplification rates for 2D waves,  $\psi = 0^\circ$ , and oblique waves,  $\psi = 55^\circ$ .

Figure 8 shows the integrated growth rates for a two-dimensional wave (the dimensionless frequency  $F = 2\pi f v_e / U_e^2$  is  $5 \times 10^{-5}$ ) at several Mach numbers. The streamwise Reynolds number  $R_s$  is defined as the square root of  $\rho_e U_e x / (\mu_e M_e)$ . The curves obtained under the parallel flow assumption are compared with the PSE results of Ber-

tolotti (1991) with the growth rate computed at the maximum of the mass flux. The nonparallel effects become appreciable at  $M_e = 4.5$  only.

This conclusion, however, is no longer valid for oblique waves, as it can be seen in Fig. 8 (Bertolotti 1991) which displays the evolution of the total growth rate for the same frequency, but with  $\psi = 55^\circ$ . The mean flow nonparallelism exerts a strong destabilizing effect, and this effect increases with increasing Mach number. The importance of this difference on the  $N$ -factor could be significant for supersonic flows since the oblique waves are the most unstable ones and for hypersonic Mach numbers when first mode disturbances are dominant.

A detailed study of the nonparallel effects using PSE was also performed by Chang and Malik (1993). Trends qualitatively similar with those described before were reported for Mach 1.6 and 4.5 flat-plate flows. In general, nonparallel effects appear to be less significant for oblique waves near the lower branch of the neutral curve but become more important at higher Reynolds numbers near the upper branch.

### 3.2 Crossflow Instability

In the leading-edge region of a swept wing, both the surface and flow streamlines are highly curved. The combination of pressure gradient and sweep deflects the inviscid streamlines inboard. Because of the lower momentum fluid near the wall, this deflection is made larger within the boundary layer and causes *crossflow*, i.e. the development of a velocity component within the boundary layer that is perpendicular to the local edge-velocity vector. This crossflow profile exhibits an inflection point causing an instability in the form of crossflow waves. Reed and Saric (1989) give a review of the instabilities associated with this flow.

#### 3.2.1 Transition correlation methods

The apparent complexity of the crossflow problem a few decades ago drove analysts to desperate measures in order to correlate transition. Owen and Randall (1952) introduced a *crossflow Reynolds number*  $R_{cf} = W_{\max} \delta_{10} / v_e$  (based on the maximum crossflow velocity and the boundary-layer height where the crossflow velocity is 10% of the maximum) as the governing parameter for crossflow-dominated transition. It was suggested that transition occurs when the crossflow Reynolds number becomes equal to about 150; a value for  $W_{\max}$  of order 3% of the local inviscid speed is typical for wind-tunnel and flight tests (Poll 1984 discusses the details of this correlation). Pfenninger (1977) used the crossflow Reynolds number and a *crossflow shape factor*  $H_{cf} = y_{\max} / \delta_{10}$  in the design of supercritical airfoils. Dagenhart (1981) then considered stationary crossflow vortices and, instead of solv-

ing the linear stability equations each time, he used a table lookup of growth rates based on the profile characteristics: crossflow shape factor and crossflow Reynolds number.

In supersonic flow, Chapman (1961) and Pate (1978) made similar conclusions that crossflow Reynolds number correlates well with transition location. On a yawed cone, King (1991) found that there was no correlation with the traditional crossflow Reynolds number. However, when he reformulated this parameter to include both compressibility and yawed-cone geometry effects, he found a correlation for both his and Stetson's (1982) data, but only as a function of azimuthal angle around the cone. Therefore, because this parameter depends on cone yaw angle, cone half-angle, and azimuthal angle, it is limited in its applicability to general geometries.

Reed and Haynes (1994) account for compressibility and cooling by introducing the *Howarth-Illingsworth-Stewartson* transformation (Howarth 1948; Illingsworth 1948, Stewartson 1949). They develop a new crossflow Reynolds number that correlates a rather wide range of data. The details are left to the original paper and the results are shown in Fig. 9.

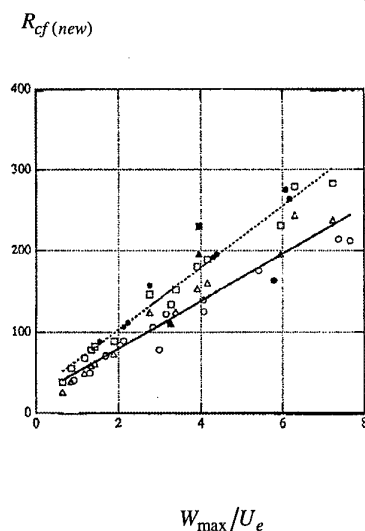


Figure 9. New crossflow Reynolds number (including compressibility and wall temperature) vs maximum crossflow velocity (solid line – noisy data; dashed line – quiet data) compared with experiments: King (1991) quiet  $\square$ ; King noisy  $\blacksquare$ ; Stetson (1982)  $\circ$ ; Holden et al. (1995)  $\bullet$

The results of Fig. 9 are calculated using only basic-state profiles. Although the results of Fig. 9 are very encouraging, Reed and Haynes caution that this sort of correlation should only be used in *conceptual* transition prediction, design, and the evaluation of parameter trends. Once an airfoil shape is selected, nonlinear parabolized stability calculations are strongly urged. The present authors echo these comments.

### 3.2.2 The $e^N$ Method in Three-Dimensional Flows

**Strategies of integration.** The extension of the  $e^N$  method to three-dimensional flows is not straightforward. The first reason is that the assumption  $\beta_i = 0$  is not necessarily correct. Hence  $\beta_i$  must be assigned or computed. Several solutions have been proposed to solve this problem, see review in Arnal (1994). For instance, it is possible to use the wave packet theory and to impose the ratio  $\partial\alpha/\partial\beta$  to be real. A simpler solution is to assume that the growth direction is the group velocity direction or the potential flow direction. In the case of delta wings, it can be assumed that there is no amplification in the spanwise direction.

After one of the previous assumptions for  $\beta_i$  has been adopted, one has to integrate the local growth rates in order to compute the  $N$ -factor. Several strategies are available:

- Envelope method: this strategy was previously described for two-dimensional, compressible flows.
- Fixed frequency/fixed spanwise wavenumber method: also used for first mode disturbances in two-dimensional, compressible flows.
- Fixed frequency/fixed wavelength method and fixed frequency/ fixed direction method: as a wave of fixed frequency moves downstream, the wavelength or the propagation direction of the disturbances are kept constant. These strategies resemble the previous one in this sense that they represent the envelope of several envelope curves.
- Streamwise  $N$ -factors/crossflow  $N$ -factors: the principle is to compute an  $N$ -factor for streamwise disturbances and another  $N$ -factor for crossflow disturbances. Transition is assumed to occur for particular combinations of these parameters.

As it can be expected, each strategy gives a different value of the  $N$ -factor at the onset of transition.

**Examples of Application.** Up to now there are only a few results dealing with the application of the  $e^N$  method for three-dimensional supersonic and hypersonic flows. The geometries which have been studied in these investigations are cones at angle of attack, swept (or delta) wings or rotating bodies without angle of attack.

Transition on a cone at incidence usually occurs earlier on the leeward line of symmetry than on the windward line. As there is no azimuthal mean velocity component along these lines, their stability properties are those of two-dimensional flows (at least in the framework of the classical stability theory).

Away from the windward and leeward rays, crossflow instability can dominate and cause transition.

Malik and Balakumar (1992) studied the linear stability of the three-dimensional flow field on a  $5^\circ$  half-angle cone at  $2^\circ$  incidence, for freestream conditions corresponding to those of King's experiments (King 1991) ( $M_\infty = 3.5$ , unit Reynolds number  $= 2.5 \times 10^6/\text{ft}$ ). As an example of result, Fig. 10 shows a comparison between measured and predicted transition fronts. The  $N$ -factor trajectories are plotted in the  $x$ - $\phi$  plane ( $\phi$  is the azimuthal angle, which is  $0^\circ$  for the windward ray), with each line ending at  $N=10$ . Along each line, the frequency is held constant, and the  $N$ -factor integration is carried out along the inviscid streamlines. The agreement is satisfactory, even if the predicted transition location is underestimated in the windward ray region. Early transition on the leeward ray is caused by the fact that the mean flow profiles are highly inflectional.

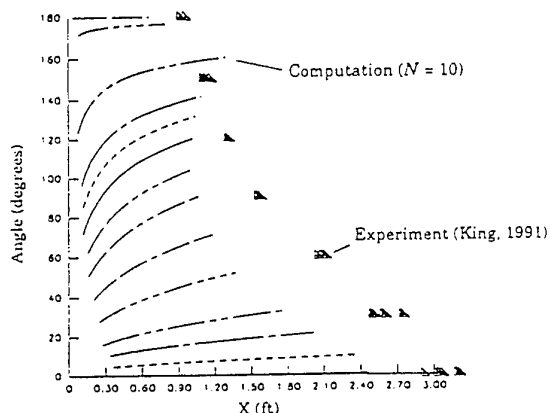


Figure 10. Comparison of experimental transition data with the computed ( $N = 10$ ) location of transition

The problem becomes more complicated at higher Mach numbers due to the appearance of second-mode disturbances. In the framework of the ESA TRP mentioned before (paragraph 3.1.2 experiments and computations (local theory) have been performed for a cone at Mach 7 and  $2^\circ$  angle of attack (Tran et al. 1995) (Arnal et al. 1996). Figure 11 shows the integrated growth rates of first and second-mode disturbances at the measured transition locations on the leeward ray (denoted as  $L$  in the figure) and on the windward ray (denoted as  $W$ ). Results at zero angle of attack are given for comparison. The most striking feature is that  $N$  increases from windward to leeward ray for first mode disturbances, whereas it decreases for second-mode disturbances. As a consequence, predicted transition occurs earlier on the leeward ray than on the windward ray (in agreement with the experiments) if one assumes that it is triggered by first mode disturbances. But transition would appear earlier on the windward ray if it were induced by second-mode disturbances. This could be an indication that second-mode, high frequency disturbances do not play any

major role in these experiments, even if their  $N$ -factors are much larger than those of first mode disturbances.

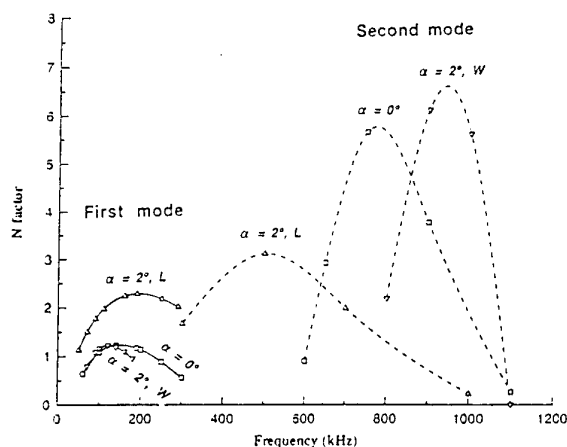


Figure 11.  $N$ -factors at transition on a cone at angle of attack (windward and leeward rays)

The stability characteristics along the leeward and windward rays of a cone at incidence were investigated by Hanifi (1995) using PSE approach (NOLOT code, developed at FFA/KTH in Sweden and DLR in Germany Hanifi et al. 1994). The computations were performed for conditions corresponding to King's experiments (King 1991) and to Krogmann's experiments Krogmann 1977). Due to the rather low values of  $M_\infty$  (3.5 and 5), only first mode disturbances were present. The movement of transition as a function of angle of attack was fairly well predicted by the  $e^N$  method. It was also observed that the nonlocal effects were larger on the windward meridian than on the leeward meridian.

Transition on a swept wing leading edge model at Mach-3.5 was investigated by Cattafesta et al. (1995). Numerical results obtained with the  $e^N$  method (local theory, envelope strategy) were compared to experimental transition location measured in the NASA Langley "quiet tunnel". It was found that traveling disturbances with  $N \approx 13$  provided a good correlation with experiments over a range of unit Reynolds numbers and angles of attack.

The transition process on a delta wing was investigated at Imperial College gun tunnel within ESA TRP Tran et al. (1995). A large number of parameters (angle of attack, angle of sweep, unit Reynolds number, leading edge bluntness) was investigated. Linear, local stability computations have then been performed for a few experimental configurations (Arnal et al. 1996). With sharp leading edges, the boundary layer development was nearly two-dimensional, and experimental

transition locations were correlated with  $N$ -factors between 1 and 2. As soon as the leading edge radius was increased, the boundary layer flow became highly three-dimensional, and transition was induced by crossflow instability at much larger values of the  $N$ -factor. From this (rather limited) series of computations, it appears that the  $N$ -factors at transition are likely to be very different depending on the type of dominant instability. Reed and Haynes (1994) investigated the local instability properties of a supersonic rotating cone at zero angle of attack, which was used as a model of a swept wing. The results were then used to develop a simple criterion which was applied to several experiments on cones at angle of attack.

**Shortcomings of the  $N$ -factor Method.** As the  $e^N$  method is based on linear stability only, receptivity and nonlinear mechanisms are not taken into account. In addition the nonparallel effects are neglected in the local procedure, and it has been shown that they could be important for oblique waves.

Several particular problems arise for three-dimensional flows. The first one is to choose the "best" strategy of integration of the  $N$ -factor. The envelope method is widely used, but its physical meaning is not clear in many cases. A classical problem occurs for swept wings, especially in transonic conditions: in the vicinity of the point of minimum pressure, rapid variations in  $\phi_M$  can be observed when the dominant instability suddenly changes from the crossflow to the streamwise type. The other strategies are often used in order to avoid these discontinuous (and probably unphysical) evolutions. In particular, this problem does not appear with PSE computations.

From a practical point of view, the most important issue is the value of the  $N$ -factor at the onset of transition. Concerning two-dimensional flows, it has been shown (paragraph 3.1.2) that the  $e^N$  method with  $N \cong 10$  can be applied to predict transition for a wide range of flows in a low background turbulence environment. In three-dimensional flows, the results depend, of course, on the strategy which is chosen to compute the  $N$ -factor, but, even with the same strategy, the results are not very clear. In fact, all the strategies produce a large scatter in the values of  $N$  at the onset of transition. A possible reason is that crossflow and streamwise instabilities are not initiated by the same type of forced disturbances. For instance, the crossflow disturbances are very sensitive to micron-sized roughness elements which have no effect on streamwise disturbances, see Radeztsky et al. (1993). Another reason is that there exists a multiplicity of nonlinear processes before the breakdown to turbulence, depending on the relative part of stationary and travelling unstable modes. In particular, it is now clear that the extent of the nonlinear regime is much

larger for three-dimensional flows than for two-dimensional flows, resulting in a larger scatter in the (linear)  $N$ -factor at transition.

In spite of these deficiencies, the  $e^N$  method can help to understand the physics of the transition phenomena. As for two-dimensional flows, it is useful for parametric studies, as soon as the  $N$ -factor for the different types of disturbances has been fixed from some reference case.

### 3.3 Görtler Instability

Boundary layers over concave surfaces are subject to a centrifugal instability that appears in the form of stationary streamwise-oriented, counter-rotating vortices usually called Görtler vortices. A description of the physical mechanisms and a recent review is given by Saric (1994b).

A graphic example of this mechanism can be observed as streamwise surface striations on reentry vehicle heat shields. The differential ablation between the nose cone and the heat shield of reentry vehicles produces a concave surface which induces a Görtler instability. The vortices then cause spanwise variations in the heat transfer.

#### 3.3.1 Swept-Wing Flows and Stagnation Flows

Hall (1985) has shown that beyond a very small sweep angle, the principal instability on a swept wing with concave curvature is a crossflow instability and not a Görtler instability. This analysis reduces the concern about Görtler problems in swept-wing flows. Bassom and Hall (1991) extend these ideas to the receptivity question.

Another issue that frequently comes up in the context of Görtler vortices concerns stagnation flows. The Rayleigh circulation criterion appears to be satisfied near the stagnation region of bluff bodies and a Görtler instability has been a suspect regarding the origin of streamwise vorticity in a boundary layer such as observed by Klebanoff et al. (1962). Stuart (1984) has shown conclusively that an instability does not exist.

#### 3.3.2 Compressibility Effects

A recent application for information regarding transition induced by Görtler vortices in a compressible flow is in the design of "quiet" supersonic wind tunnels. The major source of freestream noise is radiation from the turbulent boundary layers on the nozzle. Since the accelerating pressure gradient generally stabilizes Tollmien-Schlichting instabilities, transition is induced by Görtler vortices on the concave region of the nozzle (Beckwith et al. 1985, Chen et al. 1985). Efforts to calculate the growth of the instability with compressibility are given by Hämmerlin (1961), Kobayashi and Kohama (1977), El-Hady and Verma (1983a,b), Tumin and Chernov (1988),

and Jallade et al. (1990) using the separation-of-variables technique without the large spanwise wavenumber limit. Hall and Malik (1989) analyze the role of compressibility within the large wavenumber limit. As mentioned earlier, these results will have limited applicability. Recently Dando and Seddougui (1991) and Dando (1992) completed analyses for two-dimensional and three-dimensional boundary layers, respectively in the large Görtler number limit (inviscid flow). Both papers use unit Prandtl number and Chapman viscosity law approximations that have been shown to be grossly incorrect for other types of instabilities in high-speed flows. In the absence of an experiment, there is no telling whether these approximations are valid for Görtler vortices.

Spall and Malik (1989) integrate the linearized parabolic stability equations and show that compressibility is stabilizing but the stabilization is reduced as hypersonic speeds are approached. Hall and Fu (1989) and Fu et al. (1993) assess the role of Sutherland's viscosity law and real-gas effects on the linear stability of Görtler vortices and remove the restrictions of previous analyses. Fu and Hall (1991a, 1991b) then extend this work to nonlinear effects and secondary instabilities. Fu and Hall (1994) demonstrate how crossflow affects Görtler instabilities. These last five papers by Hall and his group have jumped so far ahead of the experimental capability and present knowledge base that it is difficult to assess their value. We know that some of the approximations made on the mean flow might not be appropriate for streamwise traveling instabilities. On the other hand, this body of work may offer some insight into operative mechanisms that a well-established experiment could examine. The initial experimental work by de Luca et al. (1993) is a step in the right direction.

### 3.4 Attachment-Line Problems

It is not easy to give an accurate definition of the attachment line of a three-dimensional body, except for simple geometries such as symmetrical bodies of constant chord and infinite span: it is the line along which the static pressure is maximum. More intuitively, the attachment line represents a particular streamline which separates the flow into one branch following the upper surface and one branch following the lower surface.

Let us consider the simplest case of a swept cylinder of constant radius  $R$ . In the coordinate system  $(X, Z, y)$  linked to the cylinder,  $Z$  coincides with the attachment line,  $X$  is normal to  $Z$  on the cylinder surface, and the  $y$  axis is normal to the wall.  $U$  and  $W$  are the projections of the mean velocity along  $X$  and  $Z$ .  $U_e$  depends linearly on  $X$  ( $U_e = kX$ ). If the infinite span assumption is used,  $W_e$  is constant. The Reynolds number  $\bar{R}$  and the reference length  $\mu$  are defined as:

$$\bar{R} = \frac{W_e \eta}{\nu_e} \text{ and } \eta = (\nu_e/k)^{1/2} \quad (11)$$

For low-speed flows,  $\eta$  is close to the displacement thickness  $\delta_1$ . For high-speed flows, Poll (1985) introduced a modified length scale  $\eta^*$  and a modified Reynolds number,  $\bar{R}^*$  which have the same definitions as  $\eta$  and  $\bar{R}$ , except that  $\nu_e$  is replaced by  $\nu^*$ . The latter quantity is the kinematic viscosity computed at a reference temperature  $T^*$  which may be estimated from the following empirical relationship (Poll 1985):

$$T^* = T_e [1 + 0.1(T_w/T_e - 1) + 0.6(T_{aw}/T_e - 1)] \quad (12)$$

$T_w$  and  $T_{aw}$  denote the wall temperature and the adiabatic wall temperature, respectively.

The equations for a yawed infinite cylinder are obtained from the 3D boundary-layer equations by imposing that all spanwise derivatives are identically zero. If the flow is laminar, self-similar equations can be obtained by using appropriate transformations. When the freestream Mach number is zero, solutions of these equations are also solutions of the exact Navier-Stokes equations. Solutions for compressible flows have been published, e.g. Reshotko and Beckwith (1958) who used Stewartson's transformation. It is also possible to introduce Levy-Lees variables, which lead to a system of ordinary differential equations with three parameters: the Mach number  $M_e$ , the temperature ratio  $T_w/T_{aw}$  and a suction parameter  $K$ .  $M_e$  is the spanwise Mach number based on the velocity and on the temperature at the boundary-layer edge. Only the case  $K = 0$  will be considered in this section.

Most of the transition problems which have been discussed so far take place some distance downstream of the attachment line. However, transition phenomena which are likely to occur along this streamline exhibit some peculiar features which will be summarized in this section. Distinction will be made between "natural" transition mechanisms (transition occurs through the selective amplification of boundary layer eigenmodes), leading-edge contamination (transition occurs through a "bypass" process induced by a source of large disturbances such as end plates parallel to the freestream) and boundary-layer tripping by roughness elements. In the latter case, distinction will be made between roughness elements on and slightly off the attachment line.

#### 3.4.1 "Natural" Transition on Attachment Line

Linear Stability Theories for Incompressible Flows. The simplest idea is to introduce small traveling disturbances similar to TS waves:

$$(u', v', w', p') = (u, v, w, p) \exp(\sigma Z) \exp[i(\alpha Z - \omega t)] \quad (13)$$

The parallel-flow approximation is then used. With the condition  $U = 0$ , the fourth-order differential equation is exactly the Orr-Sommerfeld equation written for the attachment-line profile  $\bar{W}$ .

It is possible to follow a more rigorous approach by considering a special class of small-amplitude disturbances, first introduced by Görtler (1955) and Hämmerlin (1955). These Görtler-Hämmerlin (GH) disturbances are of the form:

$$u' \sim xu \exp(\sigma Z) \exp[i(\alpha Z - \omega t)] \quad (14)$$

$$v', w', p' \sim (v, w, p) \exp(\sigma Z) \exp[i(\alpha Z - \omega t)] \quad (15)$$

As for the TS waves,  $u, v, w$  and  $p$  depend only on  $y$ . There is no real justification for the  $X$ -dependence of the  $u'$  fluctuation. Görtler chose it for reasons of "mathematical feasibility", but recent computations performed by Spalart (1988) supported this assumption.

Introducing (14) and (15) into the Navier-Stokes equations and linearizing in  $u, v, w$  create, of course, an eigenvalue problem. But, in contrast to the Orr-Sommerfeld approach (TS waves), the system of ordinary differential equations are obtained without using the parallel-flow approximation. In other words, the GH disturbances are exact solutions of the linearized Navier-Stokes equations. This system is sixth order, while the Orr-Sommerfeld equation is fourth order.

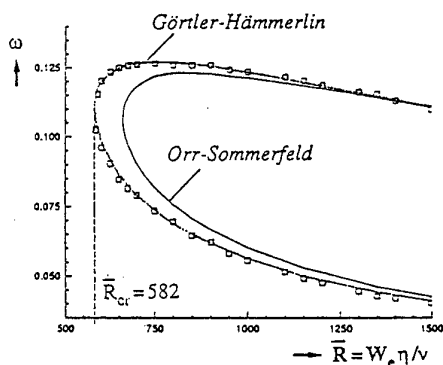


Figure 12. Neutral curves computed for TS disturbances and for GH disturbances. Symbols: Hall, Malik and Poll. Lines: ONERA/CERT

Figure 12 presents a comparison between the neutral curves computed for the TS-type disturbances (Orr-Sommerfeld equation) and for the GH disturbances. Two series of computations are presented for the GH disturbances: the first one was published by Hall et al. (1984), the second one was obtained at ONERA/CERT by Arnal (1993) with a completely different numerical technique. The critical Reynolds numbers  $\bar{R}_{cr}$  are 662 and 582 for the TS and for the GH disturbances,

respectively. In the unstable region, the growth rates of the latter are significantly larger than those of the former. Pfenninger and Bacon (1969) and Poll (1978) observed naturally occurring disturbances along the attachment line of different swept models at low speed. It was found that such disturbances existed above a critical value of  $R_\theta$  close to 230, in excellent agreement with the linear stability results for the GH disturbances.

Assuming that the mean flow is uniform in the spanwise direction, application of the  $e^N$  method along the attachment line is straightforward. For a given frequency,  $\sigma$  is constant in the  $Z$ -direction, and the transition location  $Z_T$  is given by:

$$Z_T = \frac{N}{\sigma_{\max}} \quad (16)$$

with  $Z = 0$  corresponding to the origin of the attachment line.  $\sigma_{\max}$  denotes the value of  $\sigma$  computed for the most unstable disturbances. Values of  $N$  around 10 correlate the available experimental data at low speed (Arnal 1993).

The important result is that "natural" transition on the attachment line will appear as soon as  $\bar{R}$  exceeds the critical Reynolds number  $\bar{R}_{cr}$  deduced from the linear theory. For  $\bar{R} > \bar{R}_{cr}$ , the value of  $\bar{R}$  determines the value of  $\sigma_{\max}$  and then the transition location  $Z_T$ .

**Extension to Compressible Flows.** Unfortunately, it is not possible to use the GH approach for oblique waves, because the stability problem becomes ill posed. This implies that this approach cannot be used for attachment-line problems at high speed, because oblique waves become dominant as soon as  $M_e$  exceeds a value close to 1. If one wants to follow a classical, linear stability approach, the only possibility is to consider TS-type disturbances having a chordwise wavenumber component; i.e. equation (13) is replaced by:

$$u' \sim Xu \exp(\sigma Z) \exp[i(\alpha Z + \beta X - \omega t)] \quad (17)$$

The stability problem is then reduced to the usual 2D stability problem on a flat plate, the three-dimensionality of the basic flow being taken into account by the particular shape of the attachment line mean velocity profile. Of course, there is no evidence that TS-type waves would be the most unstable disturbances along a compressible attachment-line flow.

Linear stability results based on the TS-type approach have been published, for instance, by Malik and Beckwith (1988), Arnal et al. (1991) and Da Costa (1990). The computations by Malik and Beckwith were performed for flow conditions corresponding to the experiments of Creel et al (1987) in the "quiet tunnel" at NASA Langley ( $M_\infty = 3.5$ ,  $M_e = 2.39$ ). It was found that the most unstable waves propagate with a

wavenumber angle  $\varphi$  close to  $50\text{--}60^\circ$ . For an adiabatic wall, the critical Reynolds number is  $\bar{R}_{cr} = 640$ , or  $\bar{R}_{cr}^* = 391$ . As for flat-plate flows, cooling the wall has a strong stabilizing effect. Similar results were obtained by Arnal et al. (1991). Da Costa (1990) performed computations related to his experiments on a swept cylinder ( $M_\infty = 7.1$ ,  $M_e = 5.13$ ). The critical Reynolds number for adiabatic conditions is  $\bar{R}_{cr} \approx 172$ . This surprising result means that “natural” transition is likely to occur at a Reynolds number which is smaller than that corresponding to leading-edge contamination ( $\bar{R}_{cr}^* \approx 250$  see next paragraph). For a wall temperature ratio  $T_w/T_{aw}$  around 0.4,  $\bar{R}_{cr}$  increases up to 13–500, i.e.  $\bar{R}_{cr}^* \approx 4500$ .

**Simple Criteria for “Natural” Transition.** Bushnell and Huffman (1967) observed that laminar flow on a smooth attachment line could exist up to at least  $R_{\infty,D} = 8 \times 10^5$ , where  $R_{\infty,D}$  is the Reynolds number based on freestream conditions and leading-edge diameter. This criterion is valid for Mach numbers  $M_\infty$  between 2 and 8, and for sweep angles larger than  $40^\circ$ . Another criterion proposed by Poll is  $\bar{R}^* \approx 660$  at transition. It will be discussed later on.

**Experimental Results.** There are only a few experimental results available for the problem of “natural” transition along the attachment line of swept models at high-speed conditions. Careful experiments were conducted by Creel et al. (1987) in the “quiet tunnel” at NASA Langley; under adiabatic conditions, transition was found to occur for  $\bar{R}$  close to 700, a value which is nearly twice the theoretical value computed by Malik and Beckwith (1988). However, it is interesting to note that the experimental value is close to that of the critical Reynolds number  $\bar{R}$  computed for incompressible flow. This observation led Poll to the conclusion that  $\bar{R}^* \approx 660$  could be a “universal” value for transition on smooth leading edges. The most interesting finding of Creel’s experiments is that the wind tunnel noise has no effect on the “natural” transition Reynolds number (see Fig. 16). This can be explained by a theory on the receptivity of supersonic laminar boundary layer to acoustic disturbances; calculations by Gaponov demonstrated that external noise cannot generate unstable waves when the boundary-layer thickness is constant, as it is the case along the attachment line.

The measurements by Gaillard (1993), shown in Fig. 13, have been performed on circular cylinders as well as on cylinders having a nearly flat surface around the attachment line (in order to reach large values of  $\bar{R}^*$ ). The experimental results for  $T_w/T_{aw} \approx 0.4$  are plotted in Fig. 13. It can be seen that the transition Reynolds number decreases when the spanwise Mach number increases. Gaillard also studied the influence of the wall temperature. He found that cooling has a small stabilizing effect for spanwise Mach numbers up to about 5, and

then a small destabilizing effects for larger values of  $M_e$ . All of these results completely disagree with the trends predicted by the linear stability theory when considering TS-type disturbances.

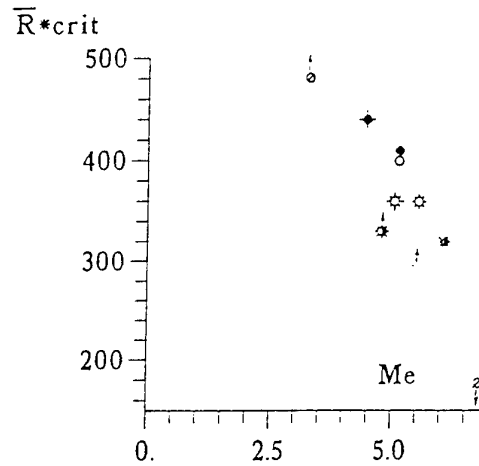


Figure 13. Transition Reynolds numbers as a function of  $M_e$  on a smooth leading edge without end plates ( $T_w/R_{aw} \approx 0.4$ ) From (Gaillard 1993).

Recent experiments were performed by Holden et al. (1994) in the Calspan 48-inch shock tunnel on a highly swept cylinder, at freestream Mach numbers from 10 to 12. Attachment line measurements with a smooth leading edge, with end plates and with roughness strips were reported. With a smooth leading edge, transition was observed for values of  $\bar{R}^*$  from 600 to 800. The corresponding freestream Reynolds numbers based on cylinder diameter were above  $8 \times 10^5$ . However, turbulent bursts were observed at  $\bar{R}^* \approx 550$ , which could be attributed to a misalignment of the nosetip with the freestream.

Experiments were conducted by Murakami et al. (1995), in the hypersonic Ludwig-tube wind tunnel of DLR at Mach numbers  $M_\infty = 5$  and 6.9 (spanwise Mach numbers  $M_e = 1.9$  and 2.9). Transition was detected on swept cylinders by liquid-crystal technique. In the absence of gross disturbance sources, the Reynolds numbers  $\bar{R}^*$  for “natural” transition were in the range 680–750, corresponding to values of  $R_{\infty,D}$  in the range  $0.9\text{--}1.2 \times 10^6$ . These values agree with Creel’s data.

#### 3.4.2 Attachment-Line Contamination by End Plates

**Empirical Criteria.** Leading edge contamination is likely to occur when a swept body is attached to a solid surface (fuselage, wind-tunnel wall, etc.). This problem has been widely studied for low-speed flows (see reviews in Poll 1978 and Arnal 1992 for instance), and a simple criterion, based on the value of  $\bar{R}$ , was developed by Pfenninger (1965). If  $\bar{R}$  is lower than 250, the bursts of turbulence convected along the



wall are damped and vanish as they travel along the attachment line. However, for  $\bar{R} > 250$ , these bursts are self-sustaining. They grow, overlap and the leading-edge region becomes turbulent.

Several series of experiments were devoted to the study of leading-edge contamination at high speeds. In most of the cases, end plates were used as sources of gross disturbances. The first attempt to quantify attachment-line contamination in these conditions is due to Bushnell and Huffman (1967), who observed that the boundary-layer flow on the leading edge became turbulent if  $R_{\infty,D} > 2 \times 10^5$  ( $M_\infty$  between 2 and 8, sweep angle larger than  $40^\circ$ ).

Poll (1985) analyzed available experimental data for  $0 < M_e < 6$  and showed that leading-edge contamination occurs for  $\bar{R}^* = 245 \pm 35$ , as illustrated in Fig. 14. There are no effects of Mach number, unit Reynolds number and wall temperature.

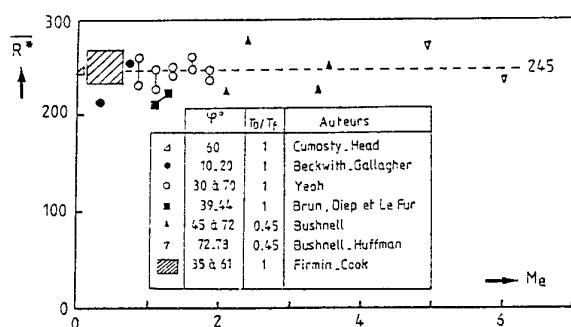


Figure 14. Leading edge contamination criterion at high speed. From (Poll 1985)

**Experimental Results.** In the experiments of Murakami et al. (1995), it was found that disturbances generated by end plates parallel to the incoming flow induced leading edge contamination at free stream Reynolds numbers  $R_{\infty,D}$  of approximately  $0.15$  to  $0.5 \times 10^6$ , in reasonable agreement with Bushnell's criterion. When expressed in term of  $\bar{R}^*$ , leading-edge contamination occurred for values which are significantly larger than those due to Pfenninger's criterion and other experimental data (mean value around 300-350). The explanation could be that the disturbances generated at the end-plate/cylinder junction were small because the boundary layer on the end plate was laminar.

The influence of the end-plate length was investigated in detail by Costa (1990) and Gaillard (1993) at CEAT Poitiers. For "long" end plates (i.e.  $L/D > 1$ , where  $L$  is the plate length), leading-edge contamination was observed for  $\bar{R}^* \approx 250$ . For  $L/D = 0.79$ , the attachment-line boundary layer became turbulent for  $\bar{R}^* \approx 330$ . This result is in agree-

ment with the findings of Murakami et al. (1995) and supports their explanation for the increase of  $\bar{R}_c^*$  in the case of "short" end plates. A more surprising observation was made in the case of a "very short" end plate ( $L/D = 0.53$ ); in this case, the Reynolds number at attachment-line contamination was reduced to about 200. The explanation proposed by Gaillard is that, for "long" and "short" end plates, the main source of gross disturbances is the boundary layer (either turbulent or laminar) at the end plate/cylinder junction. For "very short" end plates, the shock generated at the plate leading edge begins to play the dominant role, leading to a decrease in  $\bar{R}_c^*$ .

### 3.4.3 Boundary-Layer Tripping with Roughness Elements on the Attachment Line

**Low Speed Flows.** As far as low-speed flows are concerned, a detailed experimental study was carried out by Poll (1978), who investigated the response of the attachment line boundary layer to the presence of wires, the axis of which was normal to the leading edge direction. If the wire diameter,  $d$ , is made dimensionless with the length scale  $\eta$  defined previously, four  $d/\eta$  ranges have to be distinguished, as it is illustrated in Fig. 15:

- Region I: for  $0 < d/\eta < 0.7$ , the wire has no effect, and transition is triggered by linear mechanisms; the main parameter is the freestream disturbance level.
- Region II: for  $0.7 < d/\eta < 1.5$ , the wire begins to control transition. The location of the first turbulent spots moves closer to the wire when  $\bar{R}$  is increased.
- Region III: for  $1.5 < d/\eta < 1.9$ , the flow is either fully turbulent or fully laminar behind the wire. At a fixed value of  $d/\eta$  this change in the boundary layer structure occurs for a very small variation of  $\bar{R}$ . Gaster (1967) and Cumpsty and Head (1967) observed this phenomenon which Poll called "flashing".
- Region IV: for  $d/\eta > 1.9$ , turbulent bursts always appear immediately behind the wire. But, if  $\bar{R}$  is lower than about 250, they decay more or less rapidly as they are convected along the attachment line. If  $\bar{R}$  is greater than this critical value, the size of the burst increases and leading-edge contamination occurs. It is clear that there is a strong similarity with the leading-edge contamination induced by a wing-wall junction. One can deduce that there exists a minimum Reynolds number ( $\bar{R} \approx 250$ ) beyond which every turbulent structure generated by a gross disturbance source becomes self-sustaining, develops and makes the leading edge turbulent.

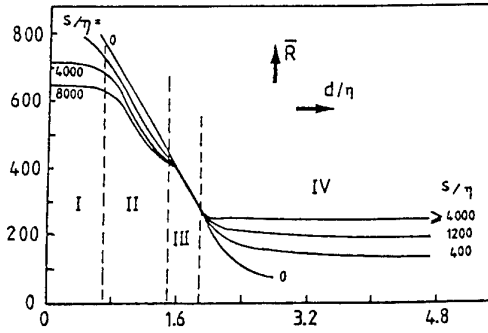


Figure 15. Location  $S$  where the first turbulent bursts are observed.  $S$  is measured from the wire along the attachment line. From (Poll 1978).

**High Speed Flow.** Region I was studied by Creel et al. (1987) in the “quiet tunnel” at NASA-Langley (freestream Mach number  $M_\infty = 3.5$ ). Transition was detected along the attachment line of a swept cylinder, without disturbance sources and with small roughness elements. By changing the operating conditions, the freestream noise levels were varied from very low values to much higher values approaching those in conventional wind tunnels. The main results are reported in Fig. 16, which shows the evolution of  $\bar{R}^*$  at transition as function of  $k/\eta^*$  ( $k$  is the roughness height). The following effects are observed:

- On smooth cylinders, “natural” transition occurs for  $\bar{R}^* = 650$  to  $700$ , in agreement with the lower limit of Fig. 16 for  $k = 0$ . As stated previously (section 3.4.1), the acoustic disturbances generated by the boundary layers developing along the nozzle walls have no effect on the transition Reynolds number.
- Small trips have no well-defined influence on transition Reynolds number until a “critical value” of  $k/\eta^*$  is reached. This value is around  $0.9$  for  $\phi = 60^\circ$  and around  $1.5$  for  $\phi = 45^\circ$ . As soon as this critical size is exceeded,  $\bar{R}^*$  at transition decreases rapidly, but a detailed comparison with Fig. 16 is not easy. For fixed values of  $\phi$  and  $k/\eta^*$ , an increase in the wind-tunnel noise decreases the transition Reynolds number. The interpretation by Creel et al. is that the external noise generates unstable disturbances at the location where the laminar

boundary layer is disturbed locally by the roughness element.

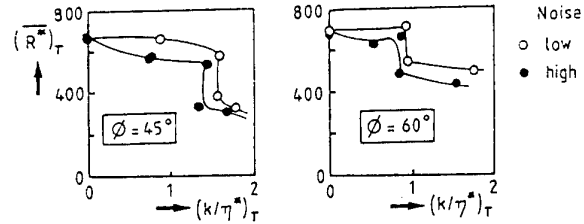


Figure 16. Transition Reynolds number along the attachment line with small roughness elements. From (Creel et al 1987).

Boundary-layer transition data with trip wires were obtained at DLR by Murakami et al. (1995) and at CEAT by Da Costa (1990) and Gaillard (1993). Trends in the dependence of the  $\bar{R}^*$  transition Reynolds number on the dimensionless roughness height were similar to those observed in other investigations, i.e. there exists a “critical” value of  $k/\eta^*$  for which transition Reynolds number starts to decrease when the trip diameter increases; in region II, the behavior of  $\bar{R}^*$  at transition strongly depends on the spanwise Mach number.

Transition phenomena with roughness elements located on the attachment line of a swept cylinder were investigated at ITAM Novosibirsk by Skuratov and Fedorov (1991) at  $M_\infty = 6$ . The tripping devices were small steel elements of rectangular section. Runs were performed at fixed roughness height and different unit Reynolds number values. Values of  $\bar{R}^*$  at “natural” transition (region I) have not been reported. When  $k/\eta^*$  increases, the transition Reynolds number in regions II and III exhibit a behavior which is qualitatively similar to that of Fig. 16. For large values of  $k/\eta^*$ , the region of self-sustaining turbulence (region IV) is observed at a constant Reynolds number  $\bar{R}^*$  around  $240$ . The same value was found to correlate data with sand roughness strips.

Boundary layer tripping experiments on swept cylinders have been carried out at ONERA at Mach 10 (Arnal et al. 1991). The tripping elements consisted of small steel cylinders (height = diameter) fixed on the attachment line with their axis normal to the wall. As the maximum value of  $\bar{R}^*$  was

around 400, only little information was obtained in regions I, II and III. For  $k/\eta^*$  larger than 2, turbulent flow developed as soon as  $\bar{R}_*$  exceeded a critical value of 250.

In the experiments performed by Holden et al. (1994) on a swept cylinder with roughness strips, two series of results have been reported. One corresponds to values of  $k/\eta^*$  between 0.8 and 2 (regions II and III); in this case, the transition Reynolds numbers were in satisfactory agreement with the correlation of Fig. 15. Other results were obtained for highly tripped configurations ( $k/\eta^*$  between 2 and 3), leading to transition Reynolds numbers  $\bar{R}^*$  around 330, a value which is significantly larger than the usual limit  $\bar{R}^* = 250$ .

#### 3.4.4 Boundary-Layer Tripping with Roughness Elements off the Attachment Line

The effect of roughness element chordwise location was studied at ONERA on a swept cylinder at Mach 10 (Arnal et al. 1991). The tripping devices (small cylinders as before) were placed at non-zero values of  $\theta_k$ , where  $\theta_k$  denotes the azimuthal angle of the roughness location,  $\theta_k = 0^\circ$  corresponding to the attachment line.

The results are summarized in Fig. 17 for two sweep angles. The full circles correspond to configurations for which the wall heat flux distribution was of the turbulent type downstream of the roughness element. The open circles correspond to configurations for which the roughness height was not sufficient to trigger transition. The circles with a cross refer to "intermediate cases": the wall heat flux distribution was neither laminar nor turbulent.

It is clear that the minimum roughness height which is necessary to trigger transition increases with  $\theta_k$ . As previously stated by Morrisette (1976) and Poll (1985), the attachment line is the location where a laminar boundary layer is the most sensitive to roughness elements.

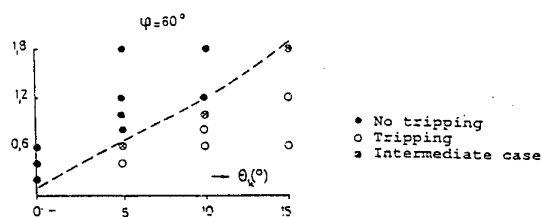


Figure 17. Effect of roughness location on boundary layer tripping. From (Arnal et al 1991).

#### 3.4.5 Blunt-Body Problem

Using a multiple-scales analysis, Reshotko and Khan (1980) showed that for a blunted flat plate, upstream of the location

where the boundary layer swallows the entropy layer (layer of air coming through the strong part of the bow shock wave), both the boundary layer and the shock layer can become unstable in a generalized inflectional sense. After the boundary layer swallows the entropy layer, the boundary-layer profiles asymptote to those for a sharp leading edge and their stability characteristics follow suit. Within the swallowing region, the stability characteristics are also affected by the fact that the shock-layer flow at the edge of the boundary layer is non-uniform in  $y$ . This seems to be stabilizing for the first mode but destabilizing for the second mode. Equivalent studies for blunted cones had been hampered by the unavailability of reliable laminar flowfield calculations particularly over the first 20 or so nose radii. Computational results by Malik (1988) for the blunted cone of the experiment of Stetson et al. (1984) ( $M_\infty = 8, \theta_c = 7^\circ$ ) qualitatively resemble experimental features including presence of the second-mode frequency band. But, they significantly underestimate  $Re_{min,crit}$  for both the sharp and blunted cones. For the sharp cone, this may be due to the very small bluntness of the experimental cone. For the blunted cone, the discrepancy may stem from an inadequate calculation of the basic flow in the vicinity of the nose. Malik et al. (1990) point out further that their computations did not detect the instability in the shock layer as observed by Stetson et al. (1984). No theory has offered explanation for the observed growth at a frequency band above the second mode but below the third. Stetson speculatively identified this feature as a nonlinearity, possibly a harmonic of the second mode.

In the light of these uncertainties, Herbert et al. (1992) concentrated on a correct calculation of the basic laminar flow over a blunted cone as prerequisite for the subsequent stability calculations. Since PNS methods are not reliable in the nose region, they use a Navier-Stokes method out to  $s/R = 5$  and a PNS method downstream of that location. Care is also given to the accuracy of the derivatives of the flow profiles since stability calculations are sensitive to these derivatives. Early stability calculations showed good agreement with Malik et al. (1990) but were only qualitatively reminiscent of the Stetson et al. (1984) data. Not addressed by Malik et al. (1990) or Herbert et al. (1992) is the relationship between the stability characteristics to features of the swallowing phenomenon. A recent work by Johnson et al. (1997) obtains the flowfield over a spherically blunted cone-like body using a Navier-Stokes method. They showed the existence of a generalized inflection point in the shock layer outside the boundary layer that progressed from midway in the shock layer at  $s/R \approx 2$  to near the outer edge of the boundary layer at  $s/R \approx 7$ . Their stability calculations for their assumed flight conditions however found no growing disturbances in this portion of the

flowfield. Clearly, the effects of nose blunting on stability and transition are not resolved.

### 3.5 Receptivity and roughness

#### 3.5.1 Use of Ground Based Facilities

Transition experiments done into the 1960's and the transition Reynolds number correlations developed from them included among the factors affecting transition a so-called "unit Reynolds number effect," which usually showed itself as an increase in transition Reynolds number with increase in wind-tunnel total pressure. Reshotko (1969) pointed out that this is in fact due to the spectral character of the disturbance environment. To that point, the disturbance environment had not been specifically considered among the experimental factors affecting transition. Morkovin (1969) enlarged upon this by pointing out that one must determine the means by which the disturbance environment generates growing disturbances in a boundary layer, a process that he called "receptivity." Also in this time frame, Pate and Schueler (1969) showed convincingly that transition behavior in conventional supersonic tunnels was dominated by the sound radiated onto wind-tunnel models by the turbulent boundary layers on the tunnel walls - an artifact of wind-tunnel testing with no flight counterpart. This was confirmed by the important flight experiments of Dougherty and Fisher (1980). Their transition cone had already been run in many transonic and supersonic wind tunnels throughout the world. In wind tunnels for  $M > 2$  they consistently obtained the familiar transition "bucket" with a  $Re_{\tau\tau}$  minimum between Mach numbers 4 and 5. However, in flight experiments with the cone model mounted ahead of the fuselage of an F-15 aircraft, the transition Reynolds number corrected to adiabatic wall conditions showed consistent increase with Mach number over the entire flight speed range whereas the values for  $Re_{\tau\tau}$  obtained in conventional wind tunnels started falling at  $M > 1.6$ .

The Pate and Schueler (1969) work led directly to the development of "quiet" supersonic wind tunnels. A "conventional" quiet supersonic tunnel is one where laminar boundary layers are maintained over as much of the nozzle and test section walls as possible. The character, limitations and accomplishments of the NASA-Langley  $M = 3.5$  pilot quiet tunnel are described by Beckwith et al. (1990). Quiet supersonic tunnels have been developed further and shown to give flight-quality transition data (Wilkinson 1997). At  $M > 8$ , even conventional tunnels with turbulent tunnel-wall boundary layers display an essentially quiet behavior as the primary instability frequency bands tend to be above the tunnel noise spectrum. However if the path to transition involves subharmonic frequencies, then those tunnels may not be sufficiently quiet. Conventional supersonic and hypersonic tunnels may still be used to study

TS, swept attachment-line and crossflow instability and transition provided that it is ascertained that the results are not affected by tunnel noise. Reed et al. (1997) contain additional discussions on this topic.

#### 3.5.2 What is Known About Supersonic Receptivity

The disturbance environment affecting boundary layers on vehicles in flight can come from two sources: a) atmospheric disturbances or particulate effects as modified by passage through the inevitable shock waves, and b) mechanical and acoustic disturbances coming from other parts of the vehicle. Bushnell (1990) supplies background, references and speculations on the triggering mechanisms associated with such disturbances.

Receptivity phenomena for supersonic and hypersonic boundary layers are just now beginning to receive serious attention. Whatever the receptivity mechanisms, the receptivity considerations are altered considerably by the presence of attached or bow shock waves and the fact that while vorticity and entropy disturbances are convected along streamlines, acoustic disturbances propagate along (relative) Mach lines (Morkovin 1987). Any freestream disturbance field is altered in passage through a shock wave. When entropy or vorticity disturbances on streamlines remote from the boundary layer pass through the shock wave, they are modified and are partially converted to pressure waves that impinge on the boundary layer along (relative) Mach lines (Mack 1975). Sound waves change amplitude and refract through shock waves and give rise to vorticity and entropy disturbances. Furthermore, irregularities on the vehicle surface generate pressure waves that are modified by the shock and reflected back toward the body. Once the disturbances are internalized in the boundary layer, the problem of matching wavenumbers and frequencies of amplified normal modes remains conceptually similar to that at low speeds. Very recently, Zhong (1997, 1998) calculated by DNS methods the receptivity of two-dimensional and axisymmetric hypersonic ( $M = 15$ ) blunted configurations to freestream acoustic disturbances (upstream of the bow shock wave). He was able to show the processing of the incoming disturbances by the bow shock wave leading to vorticity, entropy as well as acoustic disturbances downstream of the shock wave, and the subsequent development of first- and second-mode disturbances in the boundary layer.

#### 3.5.3 Roughness

While surface roughness can have a profound effect on transition, the mechanisms associated with single roughness elements are only partially understood while those responsible for transition with distributed roughness are not yet known. This has led to a large body of empirical information in the literature that is not fully consistent. These correlations are

generally based on 2D parameters such as  $Re_k$ ,  $k/\delta^*$ ,  $k/\delta$  whereas the distributed roughness is inherently 3D. The three dimensionality is introduced into the correlations by providing separate curves for each 3D shape and distribution. Nevertheless, these correlations are still the operative database for dealing with distributed roughness. The  $Re_\theta/M_e$  correlations that are so prevalent in reentry vehicle transition work are now understood to be primarily a reflection of surface roughness effects.

The bulk of applicable roughness data for hypersonic vehicles comes from wind-tunnel and flight tests of the Shuttle orbiter vehicle. The roughness on this vehicle is principally from the gaps and grooves between the tiles of the thermal protection system (TPS). The prime applicable correlations are due to Bertin et al. (1982). These correlations have been recently reviewed and revised (Bouslog et al. 1997). The latest versions show good collapse of the wind-tunnel data. The flight data follow the trends of the wind-tunnel data but are about 60% higher. It is suggested that this is due to the reduced noise level in flight.

#### 4 IMPORTANT QUESTIONS AND PRESENT POSITION OF RESEARCH

##### 4.1 Facility and Flow-Quality Issues

Quantitative flow quality criteria for obtaining flight quality transition data in wind tunnels have only recently been enunciated (Reshotko et al. 1997) and then only for subsonic and transonic facilities. Separate criteria are given for turbulence level and for acoustic intensity.

However, transition behavior in conventional supersonic wind tunnels above  $M = 2$  is dominantly due to the noise radiated onto the model from the turbulent boundary layers on the tunnel walls (Pate and Schueler 1969). This was confirmed by the important flight experiments of Dougherty and Fisher (1980). Their transition cone model had already been run in many transonic and supersonic wind tunnels throughout the world. In wind tunnels for  $M > 2$  they consistently obtained the familiar "transition bucket" with a minimum  $Re_{tr}$  between Mach numbers 4 and 5. However, in flight experiments with the cone model mounted ahead of the fuselage of an F-15 aircraft, the transition Reynolds number corrected to adiabatic wall conditions showed consistent increase with Mach number over the entire flight speed range, whereas the values for  $Re_{tr}$  obtained in conventional wind tunnels started falling at  $M > 1.6$ . This further accentuates the need for further flight experiments and for studies in "quiet" supersonic wind tunnels.

How does one define a "quiet" tunnel? Seemingly it should be one where the frequency bands of unstable modes are not excited by acoustic radiation from the turbulent boundary

layers on the tunnel walls. "Conventional" quiet tunnels do this by maintaining laminar boundary layers on the tunnel walls (see Beckwith and Chen 1989). At  $M > 8$ , even conventional tunnels with turbulent sidewalls display some quiet behavior as the instability bands tend to be separated from the tunnel noise spectrum (Fig. 18). However, while the primary instability may be noise free, subharmonics may not be, and so the transition process beyond primary instability can be affected by the tunnel noise. This issue merits further study. Conventional supersonic tunnels may still be used for TS, swept attachment-line and crossflow instability studies, provided that it is ascertained that the results are not affected by tunnel noise. Additional material on this topic is contained in Reed et al. (1997).

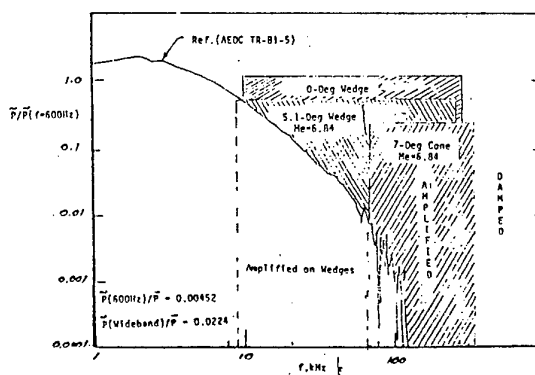


Figure 18. Tunnel B Turbulence (Acoustic) Spectrum for Mach No. 8 Nozzle,  $Re/ft = 3 \times 10^9$ .

##### 4.2 Guidelines for conducting experiments

The standards for research quality experiments on stability and transition are the "guidelines" as formulated by the U.S. Boundary Layer Transition Study Group (Reshotko 1976):

- 1 Any effects specifically and only associated with the test facility characteristics must be identified and if possible avoided.
- 2 Attention must be given to disturbances introduced by the model surface, model material and internal structure. Experimental studies should include documentation of these various factors.
- 3 Details of coupling of disturbances of various kinds to the boundary layer must be understood theoretically and experimentally, so that the sensitivity of the transition process to the flight environment might be determined.

- 4 Whenever possible, tests should involve more than one facility. Tests should have ranges of overlapping parameters, and whenever possible, experiments should have redundancy in transition measurements.

Morkovin has suggested strongly that Guideline Number Four be applied also to computational studies.

The above guidelines apply as well to flight experiments. Their implementation for flight experiments requires special attention to a number of factors:

- 1 The measurement of disturbance environment must be incorporated into the model design and in fact must be part of the model.
- 2 Attention has to be given to the maintenance and monitoring of test conditions such as Mach number, Reynolds number, angle of attack, yaw angle and surface temperature for the duration of the measurement period.
- 3 Attention has to be given to the maintenance and monitoring of model surface conditions for each flight. This includes protection of the model surface before launch, and recovery of the vehicle for inspection and reconditioning of the surface prior to the succeeding flight.
- 4 Because stability phenomena at supersonic and hypersonic speeds occur at frequencies of hundreds of kHz and even to MHz levels, there is a need for very high data sampling rates, especially when monitoring multiple channels. This poses special problems in data acquisition and data reduction. Reliable digital telemetering of data from the vehicle may also be necessary in order to minimize weight and volume of the data acquisition equipment.

#### 4.3 Transition prediction or estimation

One can dream about an eventual capability of computing the full flowfield about a vehicle or vehicle component including the transition process. Since transition is the result of unsteady phenomena as discussed in this article, the computation through transition requires time-accurate solutions of the compressible, three-dimensional, unsteady Navier-Stokes equations in a domain large enough to contain the complete phenomenon, and with a grid that is fine enough over the extended boundary layer to capture the detailed linear eigenfunctions and the subsequent nonlinearities. In addition, initial and boundary conditions must be properly specified and enforced. The initial and upstream boundary conditions should represent properly the physical disturbance environment to which the flow is subjected. Truncation error and round-off introduce disturbances whose spectrum is non-physical. The

downstream boundary condition should be non-reflecting in order that spurious feedback phenomena be absent. Herbert (1994), Reed (1994), and Reed et al. (1998) present critical discussions of the relevant issues.

At present, these requirements are marginally attainable only for small portions of simple flows. The calculation of a full vehicle is still a number of computer generations ahead of us. Parallelization of the codes and running them in parallel on multiprocessors can enable the implementation of such calculations. But until the overall capability is available, the estimation of transition locations will probably have to depend on linear stability properties of the calculated laminar flows and their synthesis into an  $e^N$  procedure that properly accounts for the three-dimensionality of the flow and the disturbances as well as for surface curvature effects.

#### 4.4 Design considerations for hypersonic flight

Vehicle design often starts by choosing a configuration based on inviscid reasoning and then fine tuning that configuration to optimize its features. For flight up to  $M = 3$ , this generally means reducing form drag, wave drag, and friction drag as well as improving the low-speed high-lift properties of the configuration. Above  $M = 3$ , as flight Mach numbers increase, reducing aerodynamic heating loads becomes the primary consideration. Every attempt is made to minimize the need for active cooling. This means giving very definite attention to delaying transition and taking advantage of passive cooling through radiation from the aerodynamically heated surfaces to the surroundings. Rarely does this alter the original general shape of the configuration.

An exception is the recent experience with NASP - the U.S. National AeroSpace Plane (Eiswirth and Lau 1997). This is a case where the baseline configuration was axisymmetric. The forebody served as the compression surface of the inlet and was subject to adverse pressure gradient, Görtler instability and crossflow instability when the body was at angle of attack. Because of the axial symmetry, the entropy layer became successively thinner with distance downstream so that the boundary layer edge conditions were beyond swallowing and subject to second and higher mode instabilities. All of these factors promote earlier transition. In this situation, the TS as well as the Görtler and crossflow instabilities are not ameliorated by surface cooling. By the time of the configuration development, it had already been established in the NASA-Langley Quiet Pilot Tunnel that flat plates (2D) had higher transition Reynolds numbers than cones at the same freestream conditions (Chen and Malik 1988). This had also been verified by  $e^N$  calculations (Mack 1987, Elias and Eiswirth 1990).

This prompted a reconsideration of the geometry of the vehicle. The forebody was replaced by a wedge-like configuration with rounded corners at its spanwise edges. The lower surface was again a compression surface but the upper surface had a slightly favorable pressure gradient. The leading edge of course had to be blunted for its own protection. The blunting was sufficient so that the boundary layers on both the lower and upper surfaces are within the entropy layer where the edge Mach numbers are low enough that first mode TS instabilities, which can be controlled by surface cooling, are dominant. The upper surface could be radiation cooled over the flight range while the lower surface required active cooling through heat exchange with the cryofuel. Crossflow instabilities were confined to the rounded edge regions and did not add greatly to the cooling requirements. The transition behavior was verified by  $e^N$  type calculations using a 3D code known as the " $e^{\text{Malik}}$ " code (Malik 1989, Malik and Balakumar 1992, Schwoerke 1993).

This case is instructive for future configuration development in that it shows that transition considerations could constructively alter the basic configurational shape of a vehicle.

#### ACKNOWLEDGEMENT

The authors would like to acknowledge the discussions and helpful suggestions of Professor Helen Reed on much of the content of this report.

#### REFERENCES

- Adam, P.H., Hornung, H.G. 1997 Enthalpy effects on hypervelocity boundary layer transition: experiments and free flight data. *AIAA Paper 97-0764*.
- Arnal, D. 1992 Boundary-layer transition: Prediction, application to drag reduction. *AGARD Rep. 786* (Special course on skin friction drag reduction).
- Arnal, D. 1994 Predictions based on linear theory. *In Progress in Transition Modelling. AGARD Rep. 793*.
- Arnal, D., Kufner, E., Oye, I., Tran, P. 1996 *PROGRAMME TRP TRANSITION*: Computational results for transition prediction. Study Note 7.
- Arnal, D., Vignau, F., and Laburthe, F. 1991 Recent supersonic transition studies with emphasis on the swept cylinder case. *Conf. on Boundary Layer Transition and Control*, Cambridge.
- Balakumar, P., Malik, M.R. 1994 Effect of adverse pressure gradient and wall cooling on instability of hypersonic boundary layers. *High Technology Corporation, Hampton, VA Rep. HTC-9404*.
- Bassom, A.P., Hall, P. 1991 Vortex instabilities in three-dimensional boundary layers: the relationship between Görtler and crossflow vortices. *J. Fluid Mech.* 232 pp. 647-80.
- Beckwith, I.E. 1975 Development of a high-Reynolds-number quiet tunnel for transition research. *AIAA J. 13*(3) pp. 300-6.
- Beckwith, I.E. Chen, F.J., Malik, M.R. 1990 Transition research in low-disturbance high-speed wind tunnels, *Laminar-Turbulent Transition III*, pp. 227-38. Eds. D. Arnal, R. Michel. Springer-Verlag.
- Beckwith, I.E., Creel, T.R., Jr., Chen, F.J., Kendall, J.M. 1983 Freestream noise and transition measurements on a cone in a Mach 3.5 pilot low-disturbance tunnel. *NASA TP 2180*.
- Beckwith, I.E., Malik, M.R., Chen, F.J., Bushnell, D.M. 1985 Effects of nozzle design parameters on the extent of quiet test flow at Mach 3.5. In *Laminar-Turbulent Transition*. Ed. V.V. Kozlov. New York: Springer-Verlag pp. 589-600.
- Bertin, J.J., Hayden, T.E., Goodrich, W.D. 1982 Shuttle Boundary Layer Transition due to Distributed Roughness and Surface Cooling. *J. Spacecraft and Rockets. 19*(5) pp. 389-96.
- Bertolotti, F.P. 1991 Compressible boundary layer stability analyzed with the PSE equations. *AIAA Paper 91-1637*.
- Blanchard, A.E. 1995 *An investigation of wall-cooling effects on hypersonic boundary-layer stability in a quiet wind tunnel*. PhD Dissertation, Old Dominion University, Dept. of Mechanical Engineering, Norfolk VA.
- Bouslog, S.A., Bertin, J.J., Berry, S.A., Caram, J.M. 1997 Isolated Roughness Induced Boundary Layer Transition: Shuttle Orbiter Ground Tests and Flight Experience. *AIAA Paper 97-0274*.
- Bushnell, D.M. 1990 Notes on Initial Disturbance Fields for the Transition Problem. *In Instability and Transition Vol I*. Eds. Hussaini, Voight., Springer-Verlag, pp. 217-32.
- Bushnell, D.M., Huffman, J.K. 1967 Investigation of heat transfer to leading edge of a 76° swept fin with and without chordwise slots and correlations of swept-leading-edge transition data for Mach 2 to 8. *NASA-TM-X-1475*.
- Cattafesta, III, L.N., Iyer, V., Masad, J., King, R., Dagenhart, J. 1995 Three-dimensional boundary-layer transition on a swept wing at mach 3.5. *AIAA J. 33* (11).
- Chang, C.-L., Malik, M., Erlebacher, G., Hussaini, M. 1991 Compressible stability of growing boundary layers using parabolized stability equations. *AIAA Paper 91-1636*.
- Chang, C.-L., Malik, M.R. 1993 Non-parallel stability of compressible boundary layers. *AIAA Paper 93-2912*.
- Chapman, G.T. 1961 Some effects of leading edge sweep on boundary-layer transition at supersonic speeds. *NASA-TN-D-1075*.

- Chen, F. and Malik, M. 1988 Comparison of boundary layer transition on a cone and flat plate at Mach 3.5. *AIAA Paper 88-0411*.
- Chen, F.J., Malik, M.R., Beckwith, I.E. 1985 Instabilities and transition in the wall boundary layers of low-disturbance supersonic nozzles. *AIAA Paper 85-1573*.
- Chen, F.-J., Malik, M.R., Beckwith, I.E. 1989 Comparison of Boundary Layer Transition on a Cone and Flat Plate at Mach 3.5. *AIAA J.* 27(6) pp. 687-93.
- Creel, T.R., Beckwith I.E. and Chen, F.J. 1987 Transition on swept leading edges at Mach 3.5. *J. Aircraft* 25(10).
- Cumpsty, N. and Head, M. 1967. The calculation of three-dimensional turbulent boundary layers. Part II: attachment line flow on an infinite swept wing. *Aeron. Quart.*, XVIII, Part 2.
- Da Costa, J.D. 1990 *Contribution à l'étude de la transition de bord d'attaque par contamination en écoulement hypersonique*. Master's thesis, Poitiers University, France.
- Dagenhart, J.R. 1981 Amplified crossflow disturbances in the laminar boundary layer on swept wings with suction. *NASA TP 1902*.
- Dallmann, U., Hein, S., Koch, W., Bertolotti, F., Simen, M., Stolte, A., Gordner, A., and Nies, J. 1996 Status of the theoretical work within DLR's non empirical transition prediction project. 2<sup>nd</sup> *European forum on Laminar Flow Technology*, Bordeaux.
- Dando, A. 1992 The inviscid compressible Görtler problem in three-dimensional boundary layers. *Theoret. Comput. Fluid Dyn.* 3 pp. 253-65.
- Dando, A., Seddougui, S.O. 1991 The inviscid compressible Görtler problem. *ICASE Rep.* 91-54.
- de Luca, L., Cardone, D. Aymer de la Chevalerie, D. Fonteneau, A. 1993 Görtler instability of a hypersonic boundary layer. *Exp. Fluids* 6 10-6.
- Doggett, G.P., Chokani, N., Wilkinson, S.P. 1997 Effect of angle of attack on hypersonic boundary-layer stability. *AIAA J.* 35(3) pp. 464-70.
- Dougherty, N.S., Fisher, D.F. 1980 Boundary layer transition on a 10-degree cone: Wind tunnel/flight data correlation. *AIAA Paper 80-0154*.
- Eiswirth, E., Lau, K. 1997 Boundary Layer Transition on Hypersonic Configurations-Lessons Learned from NASP. *Private communication to E. Reshotko*.
- Eiswirth, E., Lau, K. 1997 Boundary Layer Transition on Hypersonic Configurations -Lessons Learned from NASP. *AIAA Paper 97-1909*.
- El-Hady, N.M. 1991 Nonparallel instability of supersonic and hypersonic boundary layers. *Phys. Fluids A* 3(9) pp. 2164.
- El-Hady, N.M., Verma, A.K. 1983a Growth of Görtler vortices in compressible boundary layers along curved surfaces. *J. Eng. Appl. Sci* 2 pp. 213-38.
- El-Hady, N.M., Verma, A.K. 1983b. Görtler instability of compressible boundary layers. *AIAA J.* 22 pp. 1354-55.
- Elias, T.I., Eiswirth, E.A. 1990 Stability Studies of Planar Transition in Supersonic Flows. *AIAA Paper 90-5233*.
- Fisher, D. and Dougherty, N. 1982 Inflight transition measurements on a 10 deg. Cone at Mach numbers from 0.5 to 2. *NASA TP 1971*.
- Fu, Y.B., Hall, P. 1991a Nonlinear development and secondary instability of Görtler vortices in hypersonic flows. *ICASE Rep.* 91-39.
- Fu, Y.B., Hall, P. 1991b Effect of Görtler vortices, wall cooling and gas dissociation of the Rayleigh Instability in a hypersonic boundary layer. *ICASE Rep.* 91-87.
- Fu, Y.B., Hall, P. 1994 Crossflow effects on the growth rate of inviscid Görtler vortices in a hypersonic boundary layer. *J. Fluid Mech.* 276 343-67.
- Fu, Y.B., Hall, P. Blackaby, N. 1993 On the Görtler instability in hypersonic flows: Sutherland law fluids and real gas effects. *Phil. Trans. R. Soc. Lond. A* 342 325-77.
- Gaillard, L. 1993 *Etude de la transition de bord d'attaque sur un cylindre en flèche en écoulement hypersonique*. Master's thesis, Poitiers University, France.
- Gasperas, G. 1990 Stability of the laminar boundary layer for an imperfect gas. *Laminar-Turbulent Transition II*. Eds. D. Arnal, R. Michel. Berlin: Springer-Verlag. pp. 291-302.
- Gaster, M. 1967 On the flow along leading edges. *Aeron. Quart.* XVIII Part 2.
- Gaster, M. 1974 On the effects of boundary-layer growth on flow stability. *J. Fluid Mech.* 66 pp. 465-80.
- Germain, P., Cummings, E. and Hornung, H. 1993 Transition on a sharp cone at high enthalpy; new measurements in the Shock Tunnel T5 at GALCIT. *AIAA Paper 93-0343*.
- Görtler, H. 1955 Dreidimensionale Instabilität der ebenen Staupunktströmung gegenüber wirbelartigen Störungen. In *Fifty Years of Boundary Layer Research*. Eds. Görtler and Tollmien. Vieweg and Sohn, Braunschweig.
- Hall, P. 1985 The Görtler vortex instability mechanism in three-dimensional layers. *Proc. R. Soc. London Ser. A* 399 pp. 135-52.
- Hall, P., Fu, Y.B. 1989 On the Görtler vortex instability mechanism at hypersonic speeds. *Theoret. Comput. Fluid Dyn.* 1 pp. 125-34.
- Hall, P., Malik, M.R. 1989 The growth of Görtler vortices in compressible boundary layers. *J. Eng. Math.* 23 pp. 239-45.
- Hall, P., Malik, M.R., Poll, D.I.A. 1984 On the stability of an infinite swept attachment-line boundary layer. *Proc. Roy. Soc. Lond. A.* 395 pp. 229-45.



- Hämmerlin, G. 1955 Zur Instabilitätstheorie der ebenen Stau-punktströmung. In *Fifty Years of Boundary Layer Research*. Eds. Görtler and Tollmien. Vieweg and Sohn, Braunschweig.
- Hämmerlin, G. 1961 Über die Stabilität einer kompressiblen Störung längs einer konkaven Wand bei verschiedenen Wand-temperaturverhältnissen. *Deutsche Versuchsanstalt für Luftfahrt*, Bericht 175.
- Hanifi, A. 1995 *Nonlocal stability analysis of the compressible boundary layer on a yawed cone*. Ph.D. diss., KTH, Stockholm.
- Hanifi, A., Henningson, D., Hein, S., Bertolotti, F., and Simen, M. 1994 Linear nonlocal instability analysis the linear NOLOT code. *FFA Rep.* 1994-54.
- Herbert, Th. 1988 Secondary instability of boundary layers. *Ann. Rev. Fluid Mech.* 20 pp. 487-526.
- Herbert, Th. 1994 Parabolized stability equations. In *Progress in Transition Modelling. AGARD-FDP VKI Course. Rep.* 793. Ed. W. S. Saric.
- Herbert, Th., Esfahanian, V. 1992 Stability of hypersonic flow over a blunt body. *AGARD CP 514 Theoretical and Experimental Methods in Hypersonic Flows*.
- Holden, M.S., Bower, D.R., Chadwick, K.M. 1995 Measurements of boundary layer transition on cones at angle of attack for Mach numbers from 11 to 13. *AIAA Paper No.* 95-2294.
- Holden, M.S., Chadwick, K.M. 1995 Studies of laminar, transitional, and turbulent hypersonic flows over curved compression surfaces. *AIAA Paper* 95-0093.
- Holden, M.S., Kolly, J.M. 1995 Attachment-line transition studies on swept cylindrical leading edges at Mach numbers from 10-12. *AIAA Paper* 95-2279.
- Holden, M.S., Kolly, J.M., Bower, D. 1994 Attachment-line transition studies on swept cylindrical leading edges at Mach numbers from 10-12. *CALSPAN Tech. Rep.* 26106.
- Howarth, L. 1948 Concerning the effect of compressibility on laminar boundary layers and their separation. *Proceedings of the Royal Society of London A. Vol.* 194.
- Illingworth, C.R. Steady flow in the laminar boundary layer of a gas. *Proc. R. Soc. London Ser. A Vo.* 199.
- Jallade, S., Arnal, D., Ha Minh, H. 1990 Theoretical study of Görtler vortices; linear stability approach. In *Laminar-Turbulent Transition*. Eds. D. Arnal, R. Michel. Berlin: Springer-Verlag. pp. 563-72.
- Johnson, C., Stainback, P., Wiker, K., and Bony, L. 1972 Boundary layer edge conditions and transition Reynolds number data for a flight test at Mach 20 (Reentry-F). *NASA TM X2584*.
- Johnson, H.B., Candler, G.V., Hudson, M.L. 1997 Numerical Study of Hypersonic Boundary Layer Transition on a Blunt Body. *AIAA Paper* 97-0554.
- Kendall, J.M. 1975 Wind tunnel experiments relating to supersonic and hypersonic boundary-layer transition. *AIAA J.* 13(3) pp. 290-9.
- Kimmel R.L., Demetriades, A., Donaldson, J. 1996 Space-time correlation measurements in a hypersonic transitional boundary layer. *AIAA J.* 34(12) pp. 2484-9.
- Kimmel, R.L., Poggie, J. 1997 Disturbance evolution and breakdown to turbulence in a hypersonic boundary layer: ensemble-averaged structure. *AIAA Paper* 97-0555.
- King, R.A. 1991 Mach 3.5 boundary layer transition on a cone at angle of attack. *AIAA Paper* 91-1804.
- Klebanoff, P.S., Tidstrom, K.D., Sargent, L.M. 1962 Three-dimensional nature of boundary layer instability. *J. Fluid Mech.* 12 pp. 1-34.
- Kobayashi, R., Kohama, Y. 1977 Taylor-Görtler instability of compressible boundary layers. *AIAA J.* 15 pp. 1723-7.
- Krogmann, P. 1977 An experimental study of boundary layer transition on a slender cone at Mach 5. *AGARD-CP-224*.
- Krogmann, P. 1996 *Private communication to W.S. Saric*, 26 Nov. 1996.
- Lachowitz, J.T., Chokani, N., Wilkinson, S.P. 1996 Boundary-layer stability measurements in a hypersonic quiet tunnel. *AIAA J.* 34(12) pp. 2496-500.
- Lees, L., Lin, C.C. 1946 Investigation of the stability of the laminar boundary layer in a compressible fluid. *NACA TN* 1115.
- Mack, L.M. 1965a Computation of the stability of the laminar compressible boundary layer. In *Methods in Comp. Phys. Vol. 4* pp. 247-99. Ed. B. Alder. Academic Press, New York.
- Mack, L.M. 1965b The stability of the compressible laminar boundary layer according to a direct numerical solution. *AGARDograph* 97, pt.1 pp. 329-62.
- Mack, L.M. 1969 Boundary layer stability theory. *JPL Rep.* 900-277, Rev. A.
- Mack, L.M. 1975 Linear stability theory and the problem of supersonic boundary-layer transition. *AIAA J.* 3 pp. 278-89.
- Mack, L.M. 1984 Boundary-layer linear stability theory. *AGARD Rep.* 709 (Special course on stability and transition of laminar flows).
- Mack, L.M. 1987 Stability of Axisymmetric Boundary Layers on sharp Cones at Hypersonic Mach Numbers. *AIAA Paper* 87-1413.
- Mack, L.M. 1990a On the inviscid acoustic-mode instability of supersonic shear flows, Part 1: two-dimensional waves. *J. Theor. and Comp. Fluid Dyn.* 2 pp. 97-123.
- Mack, L.M. 1990b *Private communication to E. Reshotko*.
- Malik, M. 1990a Numerical methods for hypersonic boundary layer stability. *J. Comp. Phys.* 86 pp.376-423.

- Malik, M., Balakumar, P. 1992 Instability and transition in threedimensional supersonic boundary layers. *AIAA Paper* 92-5049.
- Malik, M.R. 1984 Instability and transition in supersonic boundary layers. In *Laminar Turbulent Boundary Layers*. Energy Sources Technology Conference, New Orleans.
- Malik, M.R. 1988 Stability theory for NASP transition prediction. *Fifth National Aero-Space Plane Symposium*, Paper 57.
- Malik, M.R. 1989a Prediction and control of transition in supersonic and hypersonic boundary layers. *AIAA J.* 27(11) pp. 1487-93.
- Malik, M.R. 1989b  $e^{M_{alik}}$ : A New Spatial Stability Analysis Program for Transition Prediction Using the  $e^n$  Method. *High Technology Rep. HTC-8902*.
- Malik, M.R., Beckwith, I.E. 1988 Stability of a supersonic boundary layer along a swept leading edge. *AGARD CP 438*.
- Malik, M.R., Spall, R.E., Chang, C.L. 1990a Effect of nose bluntness on boundary layer stability and transition. *AIAA Paper* 90-0112.
- Malik, M.R., Zang, T., Bushnell, D.M. 1990b Boundary layer transition in hypersonic flows. *AIAA Paper* 90-5232.
- Morkovin, M.V. 1969 Critical evaluation of transition from laminar to turbulent shear layers with emphasis on hypersonically traveling bodies. *Air Force Flight Dynamics Laboratory Rep. AFFDL-TR-68-149*.
- Morkovin, M.V. 1969 On the many faces of transition. *Viscous Drag Reduction*. Ed. C.S. Wells, Plenum.
- Morkovin, M.V. 1987 Transition at hypersonic speeds. *ICASE Interim Report 1 (NASA Contractor Rep. 178315)*.
- Morkovin, M.V. 1988 Recent insights into instability and transition to turbulence in open-flow systems. *AIM Paper* 88-3675. Also *ICASE Report No. 88-44, (NASA Contractor Report 181693)*.
- Morkovin, M.V., Reshotko, E. 1990 Dialogue on progress and issues in stability and transition research. *Laminar-Turbulent Transition III*. Eds. D. Arnal, R. Michel. pp. 3-30. Berlin: Springer-Verlag.
- Morrisette, E. 1976 Roughness induced transition criteria for space shuttle-type vehicles. *J. Aircraft*, 13(2).
- Murakami, A., Stanewsky, E., Krogmann, P. 1995 Boundary layer transition on swept cylinders at hypersonic speeds. *AIAA Paper* 95-2276.
- Pate, S.R. 1978 Dominance of radiated aerodynamic noise on boundary-layer transition in supersonic-hypersonic wind tunnels: theory and application. *AEDC-TR-77-107*.
- Pate, S.R., Schueler, C.J. 1969 Radiated aerodynamics noise effects on boundary-layer transition in supersonic and hypersonic wind tunnels. *AIAA J.* 7 pp. 450-7.
- Pfenninger, W. 1965 Some results from the X-21 program. Part I. Flow phenomenon at the leading edge of swept wings. *AGARDograph No. 97*.
- Pfenninger, W. 1977 Laminar Flow control Laminarization.. *AGARD Rep. R-654*. (Special course: concepts in drag reduction).
- Pfenninger, W. and Bacon, Jr, J.W. 1969. Amplified laminar boundary layer oscillations and transition at the front attachment line of a 45 deg. swept flat\_nosed wing with and without boundary-layer suction. In *Viscous Drag Reduction*. Ed. C. Wells. Plenum Press.
- Poggie, J., Kimmel, R.L. 1997 Disturbance evolution and breakdown to turbulence in a hypersonic boundary layer: instantaneous structure. *AIAA Paper* 97-0556.
- Poll, D. 1978 Some aspects of the flow near a swept attachment line with particular reference to boundary layer transition. *Cranfield College of Aeronautics Tech. Rep. 7805*.
- Poll, D. 1985 Boundary layer transtion on the windward face of space shuttle during reentry. *AIAA Paper* 85-0899.
- Poll, D.I.A. 1984 Transition Description and Prediction in Three-Dimensional Flows, *AGARD Rep. 709*. (Special course: stability and transition of laminar flows).
- Poll, D.I.A. 1985 Some observations of the transition process on the windward face of a long yawed cylinder. *J. Fluid Mech.* 150.
- Poll, D.I.A. 1986 A new hypothesis for transition on the windward face of space shuttle. *J. Space. Rockets*, 23(6).
- Potter, J.L. 1974 *The unit Reynolds number effect on boundary layer transition*. Ph.D. Dissert. Vanderbilt Univ.
- Potter, J.L. 1980 Review of the influence of cooled walls on boundary-layer transition. *AIAA J.* 18(8) pp. 1010-2.
- Radeztsky, R.H. Jr., Reibert, M.S., Saric, W.S., Takagi, S. 1993 Effect of micron-sized roughness on transition in swept-wing flows. *AIAA Paper* 93-0076.
- Reed, H.L. 1994 Direct Numerical Simulation of Transition: The Spatial Approach. In *Progress in Transition Modeling. AGARD-FDP VKI Course. Rep. 793*. Ed. W.S. Saric.
- Reed, H.L., Haynes, T.S. 1994 Transition correlations in three-dimensional boundary layers. *AIAA J.* 32(5) pp. 923-9.
- Reed, H.L., Haynes, T.S., Saric, W.S. 1998 Computational Fluid Dynamics Validation Issues in Transition Modeling. *AIAA J.* 36(5) pp. 742-51.
- Reed, H.L., Kimmel, R.L., Schneider, S.P., Arnal, D. 1997 Drag prediction and transition in hypersonic flow. *AIAA Paper* 97-1818 (also *AGARD-CP-600, Vol. 3* pp. C15-1-17).
- Reed, H.L., Saric W.S. 1989 Stability of three-dimensional boundary layers. *Ann. Rev. Fluid Mech.* 21 pp. 235-84.

- Reed, H.L., Saric, W.S., Arnal, D. 1996 Linear stability theory applied to boundary layers. *Annu. Rev. Fluid Mech.* 28 pp. 389-428.
- Reshotko, E., Saric, W.S., Nagib, H.M. 1997 Flow Quality Issues for Large Wind Tunnels. *AIAA Paper 97-0225*.
- Reshotko, E. 1969 Stability Theory as a Guide to the Evaluation of Transition Data. *AIAA J.* 7(6) pp. 1086-91.
- Reshotko, E. 1986 Stability and Transition: what do we know? *Proc. U.S. Nat'l. Congress Appl. Mech.* Austin, TX. ASME, 421.
- Reshotko, E. 1994 Boundary layer instability, transition, and control. *AIAA Paper 94-0001*.
- Reshotko, E., Khan, M.M.S. 1980 Stability of the laminar boundary layer on a blunted plate in supersonic flow. In *Laminar Turbulent Transition I*, Springer-Verlag.
- Reshotko, E., Beckwith, I. 1958 Compressible laminar boundary layer over a yawed infinite cylinder with heat transfer and arbitrary Prandtl number. *NACA Tech. Rep.* 1379.
- Saric, W.S. 1994a Physical description of boundary-layer transition: experimental evidence. In *Progress in Transition Modelling. AGARD-FDP VKI Course. Rep.* 793. Ed. W.S. Saric
- Saric, W.S. 1994b Görtler vortices. *Ann. Rev. Fluid Mech.* 26 pp. 379-409.
- Schneider, S.P., Haven, C.E. 1995 Quiet flow Ludwig tube for high-speed transition research. *AIAA J.* 33(4) pp. 688-93.
- Schwoerke, S. 1993 Quiet Tunnel Results and Analysis for Various Forebody Shapes at Mach 3.5. *National Aerospace Plane Technology Review, Paper No.* 158.
- Simen, M., Dallmann, U. 1992 On the instability of hypersonic flow past a pointed cone: Comparison of theoretical and experimental results at Mach 8. *DLR-FB 92-02. AGARD CP 514 Theoretical and Experimental Methods in Hypersonic Flows*.
- Skuratov, A., Fedorov, A. 1991 The laminar-turbulent transition past roughness at the attachment line of a swept cylinder in supersonic flow. *Izv. AN SSSR, Mekh. Zhidk. I Gasa (translated in english)*, (6) pp. 2835.
- Smith, A.M.O., Gamberoni, N. 1956 Transition, pressure gradient and stability theory. *DAC Report No.* ES 26388.
- Spalart, P.R. 1989 Direct numerical study of leading-edge contamination. *AGARD-CP 438*.
- Spall, R.E., Malik, M.R. 1989 Görtler vortices in supersonic and hypersonic boundary layers. *Phys. Fluids A* 1 pp. 1822-35.
- Stetson, K.F. 1982 Mach 6 experiments of transition on a cone at angle of attack. *J. Spacecraft Rockets* 19 (5) pp. 397-403.
- Stetson, K.F., Kimmel, R.L. 1992 On hypersonic boundary-layer stability. *AIAA Paper 92-0737*.
- Stetson, K.F., Kimmel, R.L., Thompson, E.R., Donaldson, J.C., Siler, L.G., 1991 A Comparison of planar and conical boundary layer stability and transition at a Mach number of 8. *AIAA Paper 91-1639*.
- Stetson, K.F., Thompson, E.R., Donaldson, J.C., Siler, L.G. 1984 Laminar boundary layer stability experiments on a cone at Mach 8, Part 2: blunt cone. *AIAA Paper 84-0006*.
- Stewartson, K. Correlated Compressible and Incompressible boundary Layers. *Proc. R. Soc. London Ser. A Vol.* 200 pp. 84-100.
- Stuart, J.T. 1984 Instability of laminar flows, nonlinear growth of fluctuations and transition to turbulence. In *Turbulence and Chaotic Phenomena in Fluids*, Ed. T. Tatsumi. Amsterdam: North-Holland pp. 17-26.
- Stuckert, G.K. 1991 *Linear stability theory of hypersonic, chemically reacting viscous flows*. Ph.D. Dissert., Ariz. State Univ., Tempe.
- Stuckert, G.K., Reed, H.L. 1994 Linear disturbances in hypersonic, chemically reacting shock layers. *AIAA J.* 32(7) pp. 1384-93.
- Tran, P., Seraudie, A., Wendt, V., and Poll, D.I.A. 1995 *PROGRAMME TRP TRANSITION* : Experimental results for transition prediction. Study Note 6.
- Tumin, A.M., Chernov, Yu. P. 1988 Asymptotic analysis of flow instability in a compressible boundary layer on curved surface. *Ah. Prikl. Mekh. Tekh. Fiz.* 3 pp. 84-9.
- Van Ingen, J.L. 1956 A suggested semi-empirical method for the calculation of the boundary-layer transition region. *Rep. No. VTH 71 and 74*, Dept. Aero. Eng., Tech. Univ. Delft, Neth.
- Wendt, V., Kreplin, H., Höhler, G., Grosche, F., Krogmann, P., Simen, M. 1993 Planar and conical boundary layer stability experiments at Mach 5. *AIAA Paper 93-5112*.
- Wendt, V., Simen, M., Hanifi, A. 1995 An experimental and theoretical investigation of instabilities in hypersonic flat plate boundary layer flow. *Phys. Fluids* 7(4) pp. 877-87.
- Wilkinson, S. 1997 A Review of Hypersonic Boundary Layer Stability Experiments in a Quiet Mach 6 Wind Tunnel. *AIAA Paper 97-1819*.
- Wright, R.L., Zoby, E.V. 1977 Flight boundary layer transition measurements on a slender cone at Mach 20. *AIAA Paper 77-719*.
- Zhong, X. 1997 Direct Numerical Simulation of Hypersonic Boundary-Layer Transition over Blunt Leading Edges Part II: Receptivity to Sound. *AIAA Paper 97-0756*.
- Zhong, X. 1998 Direct Numerical Simulation of 3-D Hypersonic boundary Layer Receptivity to Freestream Disturbances. *AIAA Paper 98-0533*.

## RAREFIED FLOW

**James N. Moss**

Aerothermodynamics Branch  
Aerodynamics and Gas Dynamics Division  
NASA Langley Research Center  
Hampton, VA 23681-0001  
USA

and

**Jean-Claude Lengrand**

Laboratoire d'Aérodynamique du  
CNRS  
4 ter, route des gardes  
92190 Meudon  
FRANCE

### CONTENTS

		5.4 Flight Entry Test Conditions	1xx
1 INTRODUCTION	1xx	6 FINDINGS AND RECOMMENDATIONS	1xx
2 TEST-CASE DEFINITION	1xx	6.1 Corner-Flow/Jet Interaction	1xx
2.1 Experimental	1xx	6.2 Blunt-Body/Wake-Closure	1xx
2.2 Atmospheric Entry	1xx	REFERENCES	
3 SCOPE OF EXPERIMENTS	1xx	1 INTRODUCTION	
3.1 Rarefaction	1xx	Rarefaction effects are important for hypersonic applications for a wide spectrum of conditions ranging from low-density (high altitude) situations to relatively high-density flows where the characteristic dimension is small. The present chapter concentrates on two hypersonic flow problems at flow conditions that produce a significant range of rarefaction effects: corner flow with jet interaction and blunt body flow with special emphasis on the near wake. These problems were chosen because they involve complex flow interactions that have significant implications for both spacecraft and re-entry vehicles. In an effort to clarify issues associated with these two general flow problems and to enhance their respective databases, both experimental and computational contributions were executed by an international group of researchers. In some cases, multiple data sources for both experimental and computational contributions are achieved. The Phase I report of WG 18 <sup>1</sup> (Chapter IV) provides an overview of the accomplishments and plans of this activity as of early 1994.	
3.2 Enthalpy	1xx	The corner flow jet interaction problem was incorporated to provide data to enhance our understanding of the forces	
4 CORNER-FLOW/JET INTERACTION RESULTS	1xx		
4.1 Experiments and Results	1xx		
4.2 Computations and Comparisons	1xx		
4.3 Discussion	1xx		
5 BLUNT-BODY/WAKE-CLOSURE RESULTS	1xx		
5.1 CNRS Tests (SR3)	1xx		
5.2 DLR Tests (V3G, V2G, HEG)	1xx		
5.3 Calspan Tests (LENS)	1xx		

generated on surfaces as a result of the interaction between reaction control system (RCS) exhaust plumes and the flow field surrounding a vehicle. Most space vehicles are controlled with reaction thrusters during atmospheric entry. These RCS jets can be used independently or in conjunction with movable aerodynamic surfaces, depending on the specific vehicle configuration and flight conditions. The exhaust plumes of the control jets act as barriers to the external flow, creating an effect that can change the pressure distribution along the vehicle surface containing the jet, as well as on surfaces surrounding the exhaust plume. The surface pressure perturbations from the jet interaction must be accurately predicted in order to obtain the desired vehicle aerodynamic performance.

The use of RCS jets becomes vital at higher altitudes where the density is low enough to render the control surfaces ineffective. As the altitude increases and the free-stream flow becomes more rarefied, the level of interaction between the control jet and the free stream diminishes and is practically nonexistent when the free-stream mean free path is very large. Therefore, it is crucial to accurately model RCS firings at intermediate altitudes where reaction controls are needed and significant control jet interactions are expected.

In an effort to gain further insight into the control jet interaction problem, an experimental<sup>2-4</sup> study was conducted by the European Space Agency (ESA) at the SR3 low-density wind tunnel of CNRS in Meudon, France. The principal measurements were surface pressure for a matrix of free-stream and jet flow conditions with nitrogen as the test gas for the free stream and jet.

Subsequent to the SR3 experiment, numerical studies were conducted at Aerospatiale<sup>5</sup>, CNRS<sup>6</sup>, and NASA Langley<sup>7-9</sup> using both direct simulation Monte Carlo (DSMC) and Navier-Stokes computational tools. These are believed to be the first computational studies for this type of complex three-dimensional problem with both rarefied and continuum components, i.e., the rarefied external flow interaction with a jet whose central core is at continuum conditions.

The second problem concerns blunt body flows and their wake closure, which is important for planetary probes and aerobrake configurations. Wake closure is a critical issue for aerobrakes because the low lift-to-drag ratio aeroshell designs impose constraints on payload configuration/spacecraft design. The issue is that the payload must fit into the wake flow to minimize heating because high heating rates are generally associated with reattachment of the separated near-wake flows.

A number of fundamental questions exist concerning such flows: How does the wake structure change as a function of rarefaction? What role does thermochemical nonequilibrium play in the near-wake structure? To what limits are

continuum models realistic as rarefaction in the wake is progressively increased? Answers to these fundamental questions are needed because the potential for rarefaction effects on wake structure exists for much of an aerobraking maneuver. Note that the expansion of even continuum forebody flow into the near wake can result in relatively large local Knudsen numbers.

The experimental test plan for this problem consisted of two parts: one is the high-enthalpy tests obtained with impulse facilities complemented with perfect gas wind tunnel data (discussed in Chapter IV) and the second is tests at intermediate- to high-Knudsen-number conditions. The rarefied tests were performed primarily in low-enthalpy facilities with chemically inert conditions. In addition, tests were conducted in two impulse facilities at either low pressure conditions or with very small models to capture both real gas and rarefaction effects. The same forebody model configuration was used for all tests—a 70° spherically blunted cone—and is the same as that for the Mars Pathfinder Probe<sup>10</sup>. Mars Pathfinder was launched in December 1996 and made a successful entry, descent, and landing July 4, 1997.

The rarefied experiments were performed in five facilities: four in Europe and one in the U.S. For all of the tests performed, the Knudsen number based on free-stream mean free path and model base diameter was of the order of 0.001 or larger. The database from these studies includes aerodynamics ( $C_L$ ,  $C_D$ ,  $C_m$ , and the center of pressure); local surface heating rate along the forebody, base plane, and sting; and wake structure as inferred from density and velocity measurements in the near wake. The model was supported either by sting or wires.

Extensive calculations at these experimental test conditions have been performed using DSMC and Navier-Stokes solvers. The computational results are compared with selected experimental results and code-to-code comparisons are made for a few test cases. Computational findings help clarify the boundaries for realistic application of Navier-Stokes algorithms with respect to rarefaction effects. Also, the potential for application of hybrid DSMC/Navier Stokes solvers to the blunt body wake problem was explored. By expanding the computational problems to include high altitude flight conditions, an assessment of the combined effects of rarefaction and thermochemical nonequilibrium on wake structure is made. Two flight conditions are examined: one in the Earth's atmosphere and one in the Mars atmosphere, both at the same free-stream velocity (7 km/s) and number density ( $1.654 \times 10^{20} \text{m}^{-3}$ ) and for the same forebody configuration with a base diameter of 2 meters.

## 2 TEST-CASE DEFINITION

Two experimental test cases have been investigated. The corner-flow/jet interaction test model is used to analyze

transverse flows interacting with walls and with external rarefied hypersonic flows. The blunt-body/wake closure test model is investigated to characterize the wake structure and aerothermal loads at different rarefaction levels of the external hypersonic flow.

The corner-flow/jet interaction problem is complicated because it combines the corner flow problem (often studied as a simplification of the wing-fuselage junction problem) with jet interaction. A bibliographic study of this problem reveals that

- it has been widely studied in the past with a major application to space vehicles and missiles;
- the approach was based on a combination of experimental results and similarity considerations;
- co-flowing and counter-flowing configurations have been studied more than transverse injection; however transverse injection has been studied for application to SCRAMJET engines (low external Mach number, no rarefaction, important role of turbulence);
- predictive methods adapted to the problem of jet/flow interaction require validation for each particular case, and generally they do not account for rarefaction effects;
- general methods (solving Navier-Stokes equations, DSMC, and hybrid DSMC/Navier-Stokes) are candidates for solving the problem but face difficulties due to severe gradients and to the simultaneous presence of dense and rarefied zones.

The blunt-body wake-closure problem involves complex flow interactions resulting from the compressive forebody flow undergoing a rapid expansion into the wake and its associated shear layer reattachment process. Existing data bases for the rarefied flow regime were quite sparse from both the experimental and computational perspectives at the outset of the WG 18 activity.

## 2.1 Experimental

### 2.1.1 Corner-Flow / Jet Interaction

As shown in Fig. 1, the corner-flow model is made of two perpendicular flat plates with sharp leading edges. The intersection of the two plates is oriented in the direction of the external free stream. A transverse jet is issued from a supersonic nozzle located in the horizontal plate. This jet interacts with the external flow (part (a) of Table 1) and with the surrounding surfaces.

### 2.1.2 Blunt-Body / Wake-Closure Test Model

The blunt body is an axisymmetric ASTV (Aeroassist Space Transfer Vehicle) type model. Depending upon the test facility and the type of measurement, models were supported by either stings or wires. For the sting-mounted models, the

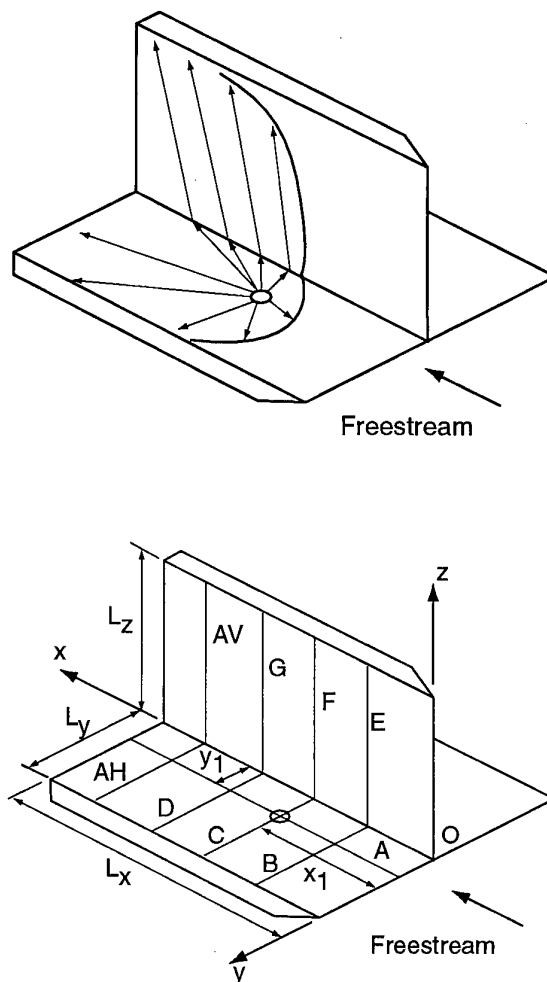


Fig. 1 Schematic of corner-flow/jet interaction test model.

sting radius was  $R_b/4$  and the length was  $6R_b$  or less since some of the test facilities were not able to accommodate stings of this length. Blunt body and rear sting dimensions are indicated in Fig. 2 where the base radius ranged from 2.5 to 76.2 mm.

## 2.2 Atmospheric Entry

The flight test cases consist of four individual cases to provide code-to-code comparisons for a  $70^\circ$  spherically blunted cone with a 2 m base diameter. No experimental results are available for these test cases. The test cases are for both Earth and Mars entry using both reacting and nonreacting gas models. The free-stream and surface boundary conditions are listed in Table 2. These conditions correspond to altitudes of approximately 85 and 68 km in the Earth and Mars atmospheres, respectively.

Table 1. Experimental test conditions

Test Case	$T_0$ (K)	$P_0$ (bars)	$M_\infty$	$Re_\infty$ /cm	$\rho_\infty \times 10^{-5}$ (kg/m <sup>3</sup> )	$V_\infty$ (m/s)	$T_\infty$ (K)	$\lambda_\infty$ (mm)	$T_w$ (K)	Gas
(a) SR3 Wind Tunnel, CNRS Meudon; d = 5 cm										
1	1100	3.5	20.2	284	1.73	1503	13.3	0.671	300	N2
2	1100	10.0	20.0	835	5.19	1502	13.6	0.226	300	N2
3	1300	120.0	20.5	7253	46.62	1634	15.3	0.027	300	N2
(b) V2G Wind Tunnel, DLR Göttingen; d = 5, 2.5, and 0.5 cm										
1	575	2	15.6	719	6.70	1082	11.6	0.163	490	N2
2	675	5	16.5	1233	11.02	1173	12.2	0.103	565	N2
3	775	10	16.8	1935	17.25	1257	13.4	0.069	635	N2
(c) V3G Wind Tunnel, DLR Göttingen, d = 0.5 cm										
1	295	0.163	9.0	859	14.22	759	17.2	0.093	variable	N2
2	295	0.0549	9.0	286	4.74	759	17.2	0.278	variable	N2
3	295	0.0163	9.0	86	1.42	759	17.2	0.929	variable	N2
4	295	0.0054	9.0	29	0.47	759	17.2	2.808	variable	N2
(d) HEG, DLR Göttingen; d = 0.5 cm										
1	6713	576.0	10.1	7043	408.5	4539	489.9	0.017	300	Air
2	9244	385.0	9.5	2498	156.4	6075	856.4	0.044	300	Air
(e) LENS, Calspan Buffalo; d = 15.24 cm										
1	4351	74.1	15.6	578	13.06	3246	103.7	0.35	294	N2

Table 2. Flight test conditions<sup>a</sup>

Quantity	Earth Reentry	Mars Entry
Number density, m <sup>-3</sup>	$1.654 \times 10^{20}$	$1.654 \times 10^{20}$
Temperature, K	180.65	141
Velocity, km/s	7.0	7.0
Mole fraction N <sub>2</sub>	0.7628	0.05
Mole fraction O <sub>2</sub>	0.2372	-----
Mole fraction CO <sub>2</sub>	-----	0.95

<sup>a</sup>70° blunted cone with base diameter of 2 m and a noncatalytic surface with a wall temperature of 1000 K.

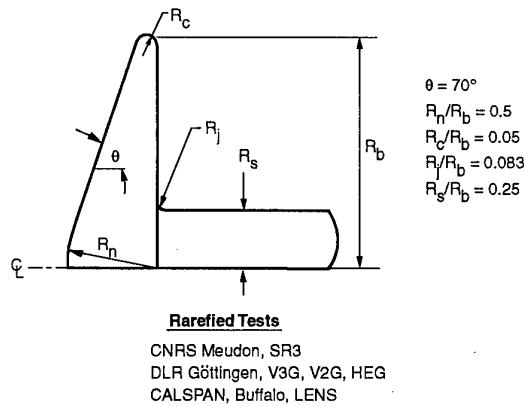


Fig. 2 Blunt-body/wake-closure test model.

### 3 SCOPE OF EXPERIMENTS

#### 3.1 Rarefaction

The manifestation of rarefaction is the existence of local nonequilibrium in the gas. This can be discussed by considering the scale length of flow gradients,  $L$ , where  $L = |Q/\nabla Q|$  (where  $Q$  is any macroscopic flow parameter) and by comparing  $L$  with the mean distance traveled by molecules between successive collisions. In a subsonic flow, the molecular velocity is essentially the (randomly oriented) thermal velocity, and  $L$  is equal to the mean free path,  $\lambda$ . In a supersonic flow, the molecular velocity is essentially the (oriented) stream velocity  $\vec{V}$ , and  $L$  is equal to  $\vec{V}/\nu$  where  $\nu$  is the collision frequency. In a subsonic flow, a local rarefaction parameter (or local Knudsen number) is defined as

$$\mathcal{P} = \lambda \times \left| \frac{\nabla Q}{Q} \right| \quad (1)$$

In a supersonic flow, the gradient must be projected on the direction of the flow and the rarefaction parameter is defined as

$$\begin{aligned} \mathcal{P} &= \frac{1}{v} \times \left| \frac{\vec{V} \cdot \nabla Q}{Q} \right| = \frac{v}{v} \times \left| \frac{\vec{V} \cdot \nabla Q}{VQ} \right| = \frac{s\sqrt{\pi}}{2} \times \lambda \times \left| \frac{\vec{V} \cdot \nabla Q}{VQ} \right| \\ &= M \sqrt{\frac{\gamma\pi}{8}} \times \lambda \times \left| \frac{\vec{V} \cdot \nabla Q}{VQ} \right| \end{aligned} \quad (2)$$

where  $s$  is the molecular speed ratio and  $\gamma$  the specific heat ratio.  $\mathcal{P}$  can be interpreted as  $(1/v) \times |D \ln Q / Dt|$ , a parameter that was first introduced by Bird<sup>11</sup>. Bird found a breakdown of translational equilibrium for  $\mathcal{P} \approx 0.02$  when  $Q$  represents the density.

Some quantities require more collisions than others to reach equilibrium. The number of collisions required is usually

characterized by a collisional number  $Z$  that ranges from a few units (for translation and rotation) to a few thousands (for vibration and chemistry). Equilibrium requires that  $\mathcal{P} \ll 1/Z_Q$ , where  $Z_Q$  is relative to the process considered.

When the flow gradients are governed by the collisional process rather than by the geometry (e.g., in a shock wave, in a Knudsen layer, etc.), we have  $\mathcal{P} \approx 1/Z_Q$ ,  $\mathcal{P} \approx 1$  for the most rapidly changing parameter. The gradient scale length is then

$$L \approx \lambda \quad \text{or} \quad L \approx \lambda_s \frac{\sqrt{\pi} \cos(\vec{V}, \nabla Q)}{2}, \quad (3)$$

whichever is larger.

Although they have usually less physical meaning, global rarefaction parameters can also be defined by regarding  $L$  as a characteristic length defined by the geometry and flow conditions in some location in the flow field (e.g., in the free stream). In a subsonic flow,  $\mathcal{P}$  is the usual Knudsen number  $Kn = \lambda/L$ , while in a supersonic flow, the adequate parameter  $\mathcal{P}$  is  $s(\sqrt{\pi}/2) \times Kn \approx s \times Kn$ . An estimation of the mean free path,  $\lambda$ , is given by Bird<sup>12</sup>

$$\lambda = \frac{\mu}{p\sqrt{2RT}} \times \frac{2(7-2\omega)(5-2\omega)}{15\sqrt{\pi}} \quad (4)$$

for a Variable Hard Sphere (VHS) gas characterized by a power-law viscosity-temperature relationship  $\mu \propto T^\omega$ . In practice, this expression can be used to calculate the mean free path for given flow conditions of an arbitrary gas by using "local VHS properties"  $\omega = \omega_L = (d\mu/\mu) \times (T/dT)$ . The mean free path of nitrogen has been plotted in Fig. 3 as a function of pressure and temperature in a wide range that covers the experiments reported in the present chapter. The viscosity used in Eq. 4 to generate the results in Fig. 3 was that given by Sutherland's expression for temperatures above 100 K and a linear  $\mu(T)$  function below 100 K. Values at the lower free-stream temperatures common to the low density

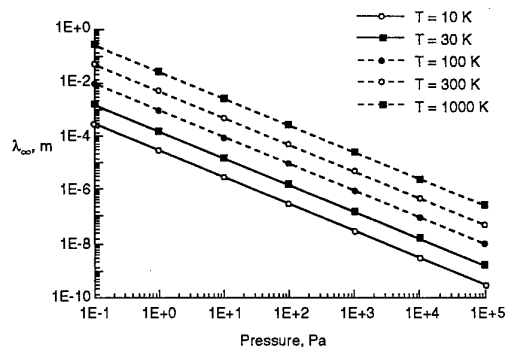


Fig. 3 Mean free path in nitrogen.



wind tunnel tests (Table 1) are problematic because of uncertainties associated with the low temperature gas properties.

### 3.2 Enthalpy

The experimental measurements for both test problems were made predominately at low enthalpy conditions, with free-stream enthalpy of the order of 1 MJ/kg. For these conditions, nonequilibrium effects are confined primarily to the translational and rotational modes. For the blunt body tests that were conducted in the impulse facilities, free-stream enthalpy was varied from 5 to 23 MJ/kg. These higher enthalpy conditions introduce additional complexities associated with vibrational and chemical nonequilibrium. The same is true of the two generic flight test conditions with enthalpy levels of approximately 25 MJ/kg.

## 4 CORNER-FLOW/JET INTERACTION RESULTS

### 4.1 Experiments and Results

Experiments were carried out at the Laboratoire d'Aérodynamique du CNRS, Meudon, in facility SR3. They consisted essentially of wall pressure measurements. The experimental procedure and the results have been presented exhaustively by Allègre and Raffin<sup>3</sup>. Partial results have also been presented by Allègre and Raffin<sup>2,4</sup> and in the AGARD WG18 Phase I report<sup>1</sup>.

#### 4.1.1 Flow Conditions and Procedure

The experimental model consisted of two perpendicular flat plates oriented as shown in Fig. 1. Both plates were aligned parallel to the external flow direction. A hypersonic conical nozzle was embedded in the horizontal plate. The nozzle axis was vertical and the nozzle exit was flush with the plate surface. The nozzle was located at a distance  $x_1 = 60$  mm downstream from the leading edge. Its geometry was characterized by throat and exit diameters of 0.213 and 1.53 mm, respectively, with a divergence half-angle of  $9^\circ$ .

The other plate was vertical, 60 mm high, and parallel to the external flow direction. Two configurations were investigated corresponding to the two distances  $y_1$  of 15 mm and 30 mm between the nozzle and the vertical plate. The width  $L_y$  of the horizontal plate was equal to 40 and 55 mm in configurations 1 and 2, respectively. Both plates had sharp leading edges with bevel angles of  $20^\circ$ . The plates were equipped with 38 wall pressure orifices with diameters of 1 mm. Wall pressure distributions could be obtained along some arbitrary lines:  $y = y_1$  on the horizontal plate (line A), and lines of constant abscissa  $x$  (B at  $x = 40$  mm, C at  $x = 60$  mm, D at  $x = 80$  mm, AH at  $x = 100$  mm on the horizontal plate and lines E, F, G, AV at the same values of  $x$  on the vertical plate). Lines A and C passed through the center of the exit section of the nozzle. The first measurements were obtained on a model 100 mm long and the other measurements on a model 120 mm long. The regions investigated on the two models overlap each

other and the pressures coincide within experimental uncertainty in the overlapping region.

The gas used for both the external free-stream flow and the jet was nitrogen. Three conditions for the free-stream flow could be realized (subscript  $\infty$ ). The corresponding nominal values of the flow parameters are listed as part (a) of Table 1. Additional free-stream parameters are given in Table 3: pressure  $P_\infty$ , stagnation pressure behind a normal shock  $P_{i2}$  and unit Reynolds number  $Re_w = \rho_\infty V_\infty / \mu(T_w)$  based on viscosity at wall temperature  $T_w = 300$  K.

The nozzles used to generate the external free-stream flow had a conical divergent (continued by a cylindrical part for Conditions 1 and 2) and the free-stream flow was not uniform. Mach number distributions in the free-stream flow are given by Allègre<sup>3</sup> et al.

The jet flow was generated from a stagnation temperature of 300 K and stagnation pressures  $P_{0j}$  of 4, 12, and 20 bars. The nominal exit Mach number based on the nozzle geometry was 5.96. The jet flow rate  $q_{m,j}$  and the jet exit conditions (subscript  $e$ ) are given in Table 4. They have been obtained for a 1-D isentropic flow in the nozzle, coupled with a boundary layer.

The test matrix was obtained by combining

- the three external flow conditions (1,2,3 in part (a) of Table 1) and an additional case with the jet emerging into a quiescent atmosphere with no free-stream flow
- the two geometrical configurations ( $y_1 = 15$  and 30 mm for Configurations 1 and 2, respectively)
- the three jet stagnation pressures  $P_{0j} = 4, 12, 20$  bars and an additional case with the free-stream flow and no jet

The procedure used to measure wall pressures was as follows: the wind tunnel was started, and as soon as the stagnation conditions were correctly stabilized, the model was injected into the test section. This procedure reduced the risk of flow blockage by the model during wind tunnel startup. Furthermore, due to the time needed to measure the pressure, the wall-temperature rise was limited to 10–15 K. This rise made it unnecessary to water-cool the model, which facilitated the integration of the pressure tubes inside the

Table 3. Additional information for SR3 flow conditions

Condition	$P_\infty$ [Pa]	$P_{i2}$ [Pa]	$Re_w$ [ $\text{cm}^{-1}$ ]
1	0.0683	35.92	14.5
2	0.209	107.7	43.7
3	2.115	1145	427

Table 4. Jet exit conditions

$P_{0j}$ [bars]	$M_e$	$P_e$ [Pa]	$T_e$ [K]	$\lambda_e$ [mm]	$q_{mj}$ [g/s]
4	5.288	544	45.5	$5.3 \times 10^{-4}$	0.0327
12	5.532	1245	42.2	$1.78 \times 10^{-4}$	0.0981
20	5.617	1893	41	$1.07 \times 10^{-4}$	0.1635

model. A sting, rigidly attached to the rear portion of the model, provided the connection to a streamlined transverse support mechanism. This support was actuated by a pneumatic elevator to inject and retract the model in and out of the test section.

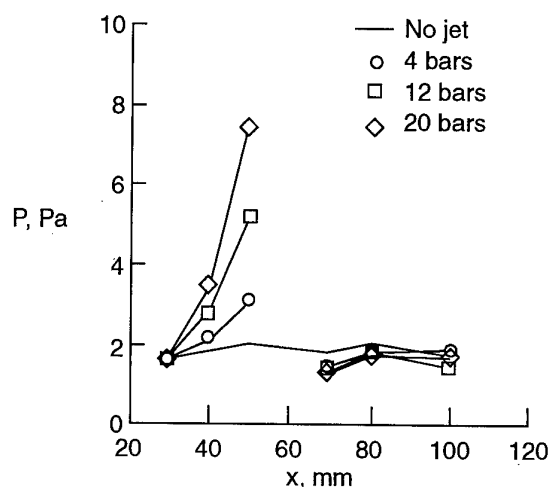
A pressure bench, including 5 Validyne DP 103 pressure transducers, was mounted inside the test chamber at a distance of approximately 400 mm from the model. The transducers have a high sensitivity and can measure pressures as low as 1 Pascal. A Turbovac 50 vacuum turbomolecular pump provided the vacuum (approximately  $10^{-4}$  Pa) used as a reference pressure. Careful outgassing and calibration were made before each series of pressure measurements. Pressure distributions are presented by Allègre<sup>3</sup> et al. in tables and figures and are summarized hereafter.

#### 4.1.2 Results

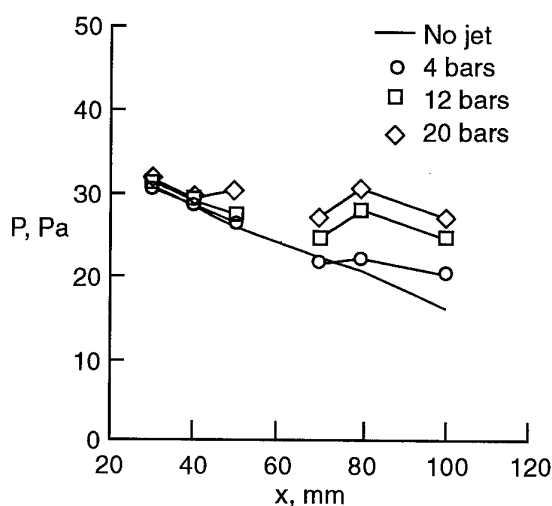
Experiments conducted in a background pressure  $P_\infty$  of about 2 Pa without external flow result in a moderate interaction of the jet with the walls: the wall-to-background pressure ratio varied from 0.69 to 1.19 and 0.50 to 1.44 in Configuration 1 for  $P_{0j}$  equal to 4 and 20 bars, respectively. There was less interaction with Configuration 2.

The pressure distribution along line A is plotted in Fig. 4 (part a) for Condition 1 and Configuration 1. When the jet is on, it acts as a barrier. When compared with the no-jet case, a substantial increase of the pressure on the horizontal plate is observed just ahead of the jet and a decrease is observed behind it. The increase is the largest for the largest flowrate of the jet. Similar results are found for Configuration 2. The same observations are made for Condition 2.

For Condition 3, there is only a small increase of pressure ahead of the jet (Fig. 4, part b) and an increase (rather than a decrease) behind it. The difference in behavior compared with Conditions 1 and 2 is best understood when considering the pressure distributions on the vertical plate. For Condition 1 (Fig. 5, part a), the jet is seen to bend downstream, but does not "touch" the horizontal wall. For Condition 3 (Fig. 5, part b), the jet central line is strongly



(a) Test Condition 1.



(b) Test Condition 3.

Fig. 4 Pressure distribution along line A in Configuration 1.

curved and the jet "touches" the horizontal wall, inducing a pressure increase.

Surface flow visualizations were obtained by oil-film deposit for Conditions 2 and 3 of the external flow and for the highest stagnation pressure of the jet (20 bars). The extent of the jet upstream influence on the wall flow is approximately the same when deduced from the pressure distribution and from the visualization.

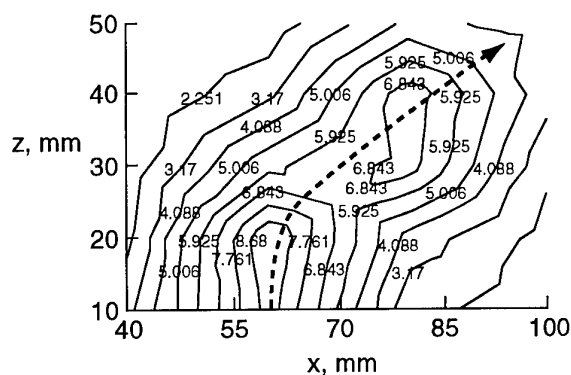
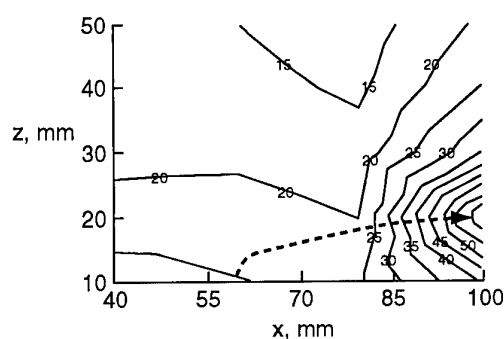
(a) Test Condition 1,  $P_{0j} = 4$  bars.(b) Test Condition 3,  $P_{0j} = 20$  bars.

Fig. 5 Pressure measurements along the vertical plate in Configuration 1.

## 4.2 Computations and Comparisons

Computations have been carried out at Aérospatiale, at NASA Langley, and at the Laboratoire d'Aérodynamique du CNRS.

### 4.2.1 Aérospatiale

The numerical work done at Aérospatiale has been presented by Chauvot<sup>5</sup> et al. They considered Configuration 1 with stagnation pressure  $P_{0j} = 20$  bars for the jet and Condition 1 for the external flow. They used a combined approach with a 3D Navier-Stokes (NS) solver (CEL3DNS) and a 3D DSMC code (JMC3D). The NS calculation included the converging part of the nozzle. It was first carried out in the jet region, with a limited extent into the external flow domain. The authors found that the calculated mass flow rate of the jet was 78% of the inviscid 1D estimation. They considered a boundary surface in the NS flow field and used the flow parameters on this surface to start a DSMC calculation beyond it. In a first simulation, the boundary surface was placed in the nozzle exit plane. In the final simulation, the NS calculation was extended by 20 mm into the dense part of the jet, and the DSMC calculation was extended 0.8 mm into the

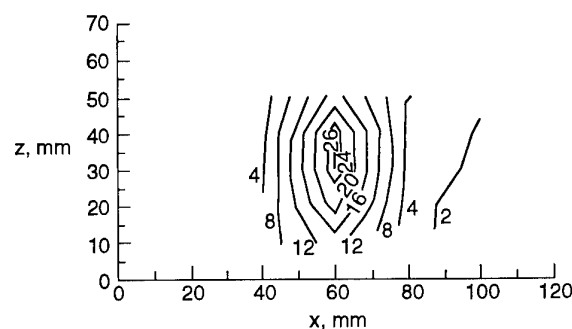
nozzle in order to include the nozzle lip region. The DSMC mesh was refined near the plates and near the injection surface.

Both simulations give similar results. Good agreement was found between experimental and computed wall pressures without the jet. When the jet is on, the main features of the pressure distribution are found (Fig. 6) but the agreement is poor on the downstream part of the plates, where the pressure level is low.

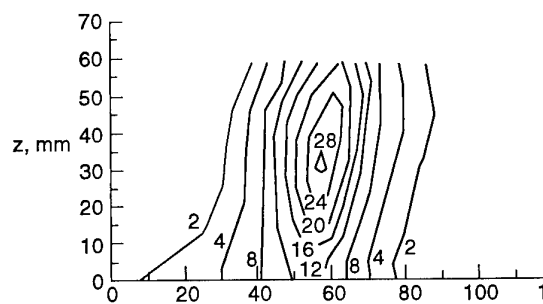
In a previous calculation, a commercial code PHOENICS was used instead of the CEL3DNS code. An empirical adjustment, consisting of limiting the jet flow rate to 60% of its inviscid 1D value, was needed to provide the best agreement between numerical and experimental pressure distributions.

### 4.2.2 CNRS

Hendriadi<sup>6</sup> presents results obtained by DSMC calculations of Configuration 1 in Condition 1 ( $P_{0j}$  equal to 4 and 20 bars) and in Conditions 1 and 2 without the jet. He used the code DISIRAF, developed at the Laboratoire d'Aérodynamique du



(a) Experiment.

(b) Calculated, Chauvot et al.<sup>5</sup>Fig. 6 Pressure measurements and calculations on vertical plate in Configuration 1,  $P_{0j} = 20$  bars.

CNRS, with a rectangular 3D mesh refined near the walls and near the jet exit. The jet was generated by injecting the adequate flow rate of molecules through the horizontal wall, with distribution functions based on a 1D isentropic expansion from the stagnation conditions to the nozzle exit (uniform nominal exit conditions).

For Condition 1, good agreement is found between the experimental and calculated pressures when the jet is off. The agreement is worse for Condition 2. When the jet with  $P_{0j} = 20$  bars is on, the same observations as for Aérospatiale's calculations can be made. For the jet with  $P_{0j} = 4$  bars, the pressures calculated on the horizontal plate agree reasonably well with the experiment. However, the experimental jet appears to bend more strongly than the calculated one, which is clearly visible on the pressure distribution on the vertical plate.

#### 4.2.3 NASA Langley

Tartabini<sup>7</sup> et al. (see also Tartabini<sup>8</sup> et al. for an early version of the paper) present results obtained by a 3D DSMC calculation for Configuration 1 in Condition 1 with a jet characterized by  $P_{0j} = 4$  bars. A no-jet case was also studied for comparison. It reveals a rather good agreement between computed and experimental pressure distributions. A correction for the orifice effect proposed by Potter and Blanchard<sup>13</sup> was applied to the experimental data, which improved the agreement. The jet was simulated by injecting molecules at the adequate location through the horizontal wall. The characteristics of the injection corresponded to the jet flow rate and to the velocity and temperature profiles in the exit plane of the nozzle, as calculated by a Navier-Stokes calculation of the nozzle flow using the VNAP2 code<sup>14</sup>, with the calculation started at the nozzle throat. As for Hendriadi's corresponding calculation, the computed pressures exhibited similar trends to those indicated by the experimental measurements. However, quantitative agreement was not achieved over the whole surface of the plates.

Further calculations relative to the same problem have been carried out by Wilmoth and Tartabini<sup>9</sup>. They examined a number of potential reasons for the discrepancy between experimental and numerical results. By lowering artificially the stagnation pressure of the jet (2.4 bars in place of 4 bars), the jet plume shape was more consistent with the experiment, and gave the best agreement between experimental and calculated pressures. This behavior is consistent with the observation that was made by Chauvot<sup>5</sup> et al.

#### 4.3 Discussion

Comparisons between experimental and calculated pressure distributions for the most rarefied external flow (Condition 1) are presented in Fig. 7 parts (a) and (b) for  $P_{0j} = 4$  and 20 bars, respectively.

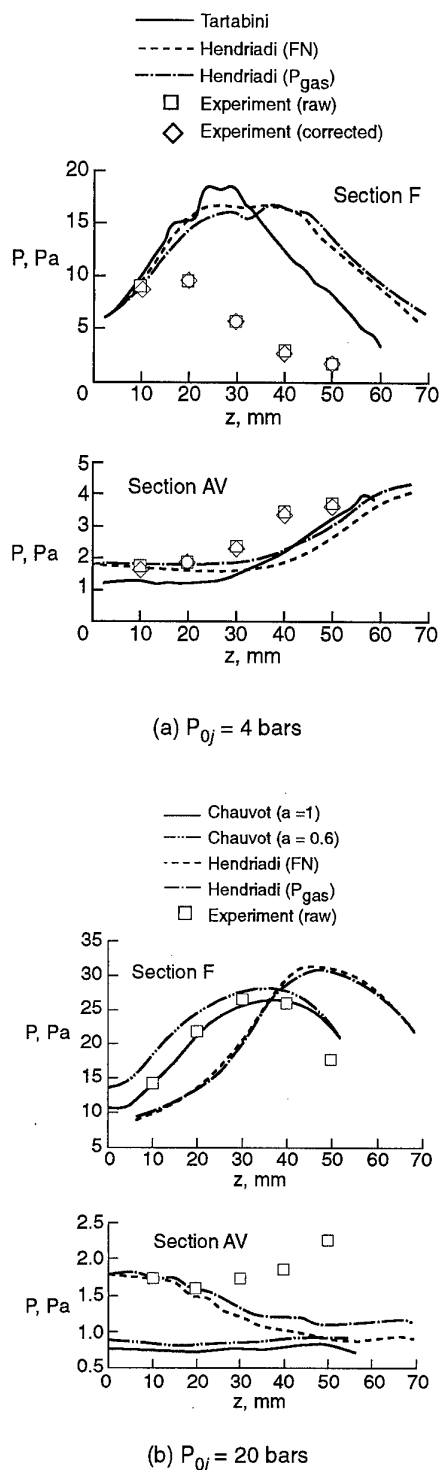


Fig. 7 Pressure profiles on vertical plate for Configuration 1 and test Condition 1.

All numerical calculations performed for the present problem are based on a continuum description of the nozzle flow together with a DSMC calculation of the external flow. They differ by details in their implementation. Although results do not coincide exactly with one another, they exhibit similar trends and the same qualitative discrepancies with the available experimental pressure distributions. Different issues will now be considered to understand these discrepancies.

#### 4.3.1 Discretization in DSMC Calculations

Macroscopic quantities are obtained by averaging information sampled over a cell. Thus, the size of a cell in the direction of a unit vector  $\vec{x}$ ,  $\delta x$ , must be such that  $|\delta \vec{x} \cdot \nabla Q| \ll |Q|$  where  $Q$  is the most rapidly changing flow parameter. In the direction of the gradient, the condition becomes

$$\delta x \ll L = |Q/\nabla Q|. \quad (5)$$

This condition is the same as for any numerical method. If the gradient length scale  $L$  is governed by the collisional process, it results from Eq. 3 that the condition can be very severe

$$\delta x \ll \lambda \quad \text{or} \quad \delta x \ll \lambda \cos(\vec{v}, \nabla Q) \quad (6)$$

whichever is larger. Furthermore, in a DSMC calculation the exact position of molecules within a cell is disregarded for the treatment of collisions. This simplification is valid when the above conditions are satisfied. Introducing subcells and forcing colliding molecules to be selected within the same subcell allows conditions 5 and 6 to be satisfied more "loosely".

For example, the numerical results obtained by Wilmoth and Tartabini<sup>9</sup> are not grid independent, but a parametric study indicates that a further refinement of the grid would not improve the agreement.

Decoupling the processes of moving and colliding molecules with time step  $\delta t$  requires that  $\delta t$  be much smaller than the mean collision time  $1/\nu$  and the probability of a molecule colliding during  $\delta t$  is small:

$$\delta t \times \nu \ll 1. \quad (7)$$

If condition 7 is not satisfied, a bias is introduced when sampling the collision partners; and transport properties are not simulated properly, but conservation laws are still satisfied. As confirmed by Chauvot<sup>5</sup> et al., results are not affected by violating condition 7 in regions where the flow is little dependent on transport properties (inviscid flow regions).

In the extreme situation when  $\nu \delta t \gg 1$ , molecules come to a local equilibrium in the cell before all collisions corresponding to  $\delta t$  take place. To save computing time, Lengrand<sup>15</sup> et al. proposed that computing collisions in a cell be stopped as soon as they do not change the distribution functions. The number of collisions allowed is set equal to some multiple of the number of molecules in the cell. Tartabini<sup>7</sup> et al. use the same technique in the central part of the jet.

Another condition on  $\delta t$  is due to the collisions being calculated at discrete times separated by  $\delta t$  rather than continuously. This condition requires that the variations of macroscopic flow parameters are negligibly small along the distance traveled by molecules during  $\delta t$ . In a locally supersonic flow, this condition is expressed as  $|\delta t \times (\vec{v} \cdot \nabla Q)| \ll |Q|$ . In a locally subsonic flow, it is expressed as  $\delta t \times \bar{c} \ll |Q/\nabla Q|$  or  $\delta t \times \nu \ll |Q/\nabla Q|/\lambda$ . If the local rarefaction parameter  $P$  is introduced, both conditions for supersonic and subsonic flows have the same expression

$$\delta t \times \nu \times P \ll 1. \quad (8)$$

In the dense part of the flow,  $P$  is very small and condition 8 is less severe than condition 7. It must be satisfied even if condition 7 is not. Otherwise flow gradients are "smeared" due to the numerical process.

Calculations where condition 7 is satisfied (Ref. 5 in simulation 1) and calculations where it is not satisfied (the other ones) result in similar discrepancies with the experiment. There is no indication that the discrepancies observed between numerical and experimental results are due mainly to time or space discretization.

#### 4.3.2 Boundary Conditions

None of the calculations include iterative coupling between nozzle flow and corner flow. Rather, the conditions in (or near) the nozzle exit plane are estimated and taken as input boundary conditions for the DSMC calculation.

For the combination of the lowest  $P_{0j}$  with the less rarefied external flow, the jet emerges into the external flow with a pressure that is lower than the stagnation pressure  $P_{i2}$  behind a normal shock wave. Thus, it may not present the usual structure of an underexpanded jet. In all other cases, the jet is underexpanded. The nozzle lip exerts some upstream influence on a distance of a few local mean free paths and this affects the profiles of flow parameters near the lip. For a vacuum expansion, the external part of the jet (typically the backflow region) is also affected, and it is desirable to include

the nozzle lip in the DSMC computational domain. For the present problem, the jet expansion is limited by the external flow and the upstream influence of the nozzle lip can be disregarded. Chauvot<sup>5</sup> et al. found no difference when including it in the DSMC region.

The papers considered for this discussion do not include details on the flow conditions retained along the lateral, upper, and downstream boundaries for the calculations. If the subsonic (or low-supersonic) part of the corner downstream boundary fails to be reproduced, the pressure on a small region near the trailing edge is affected (it extends approximately 20 mm for Condition 1). The failure to reproduce the exact flow conditions along the upper boundary (through which the jet leaves the computational domain) may affect the bending of the jet and the pressure distribution along the vertical plate.

All calculations consider the free-stream conditions in the external flow to be uniform, whereas the actual experimental conditions are not uniform. However, this approximation has little consequence as indicated by the fact that the experimental and calculated pressure distributions are in good agreement when the jet is off.

#### 4.3.3 Physical Modeling

The VHS model used in DSMC calculations cannot reproduce the real transport properties over the whole temperature range encountered. Results are nevertheless acceptable if they are reproduced correctly in regions where they actually govern the flow. This is the case in Tartabini's calculations where the simulated viscosity is correct at 300 K (near the wall), but high by a factor of 2 in the free stream.

The model used for rotational energy exchange also affects the pressure distribution. However, Wilmoth<sup>9</sup> et al. show that changing the model has only a moderate influence on the discrepancy between calculated and experimental results.

The model used for gas-surface interaction also affects the pressure distribution. Diffuse reflection with full accommodation is usually assumed in the calculations. Chauvot<sup>5</sup> et al. found no clear improvement of the calculation by reducing the accommodation from 1 to 0.6.

A potential problem is due to condensation occurring during the experiment, but it is not taken into account in the calculations. A part of the flow field is well within the liquid domain of a ( $P, T$ ) diagram. When designing the SR3 facility, the absence of condensation in the free stream was checked. However, condensation remains possible in the jet.

#### 4.3.4 Experimental Uncertainty

The accuracy of pressure measurements at pressures as low as 1–2 Pa is poor. In particular, the pressure measured is

affected by the temperature of the wall. However, this uncertainty is not sufficient to explain the discrepancies observed at higher pressures.

A more serious cause of experimental error is due to the small size of the nozzle. Any error on its dimensions would affect the flow rate and the exit conditions of the jet, and thus its interaction with the external flow.

The mean free path at  $T_w = 300$  K ranges from 5.5 mm to 0.08 mm when the pressure ranges from 1 to 70 Pa. The pressure taps have a diameter of 1 mm. Thus, the question of the orifice effect on pressure measurements must be considered. This effect is hardly an experimental uncertainty, but rather a real difference between two physically distinct quantities. On one hand the "calculated wall pressure" is the normal stress due to the exchange of normal momentum of molecules striking the wall. Hendriadi<sup>6</sup> shows that there may be a large difference between this quantity and the thermodynamic pressure of the gas at the wall (deduced from the equation of  $P = nkT_{tr}$ , with number density  $n$ , Boltzmann constant  $k$ , and translational temperature  $T_{tr}$ ). This difference is an indication of nonequilibrium. On the other hand, the "experimental pressure" is the equilibrium pressure in a transducer cavity connected to the pressure tap. Previous experience indicates that the experimental pressure is much closer to the normal stress than to the thermodynamic pressure of the gas close to the wall. However, there is no simple relation between them. Orifice corrections (as that applied by Tartabini et al. to the experimental pressure) are attempts to make them coincide, but they cannot be claimed to apply to situations other than those that were used to establish them. However, as can be seen in Fig. 7, discrepancies between experimental and calculated pressures occur even under conditions where nonequilibrium and orifice corrections are small.

## 5 BLUNT-BODY/WAKE-CLOSURE RESULTS

Experiments and computations have been performed for the same forebody configuration: a 70° spherically blunted cone with a nose radius equal to one-half the base radius and the corner or shoulder radius equal to 5 percent of the base radius (Fig. 2). Computations have been made for both wind tunnel and generic flight conditions for the same forebody configuration. Results of experiments performed in each of five hypersonic test facilities are briefly summarized along with some of the findings of the computational studies that have been made for specific test conditions.

The nominal test conditions for the low density wind tunnels participating in the AGARD WG 18 investigation are listed in Table 1. Also included are the test conditions for two impulse facilities that were used to achieve rarefied flow. One test was run in the Large Energy National Shock Tunnel (LENS) facility<sup>16-17</sup> at a low pressure condition to produce Mach 15.6 nitrogen flow. Also, tests<sup>18</sup> were conducted at the highest

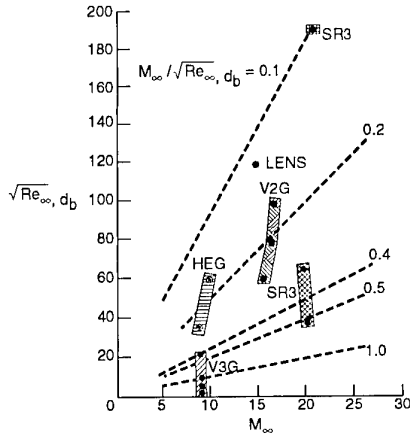


Fig. 8 Experimental test conditions in terms of the rarefaction parameter  $M_\infty / \sqrt{Re_\infty}$ .

enthalpy conditions in the HEG (High Enthalpy Göttingen) free piston shock-tunnel using very small models ( $d_b = 5$  mm). Two of the HEG test conditions are included in Table 1. Fig. 8 displays these test conditions in terms of rarefaction, as indicated by lines of constant  $M_\infty / \sqrt{Re_\infty}$ , where the characteristic dimension is the base diameter. The larger this parameter is, the greater the flow rarefaction.

These test conditions provide a range of flow environments that include both nonreacting and reacting flows. Also, thermal nonequilibrium issues exist for even the lowest enthalpy tests (translational, rotational, etc.) with more internal modes participating for the higher enthalpy flows.

Hence, the conditions include a variety of flow environments that serve as test cases to measure the ability of computational codes to calculate such flows where compression, expansion, and separation are key features. Table 5 lists the organizations that have made one or more computations for the experiments and generic flight test conditions. The significant number of DSMC codes applied to this activity are representative of current capabilities both in terms of solution algorithms and physical modeling. The two Navier-Stokes codes are the Langley aerothermodynamic upwind relaxation algorithm (LAURA) of Gnoffo<sup>19-20</sup> and a code developed at North Carolina State University by Olynick<sup>21-22</sup> et al.

### 5.1 CNRS Tests (SR3)

Allègre<sup>23-24</sup> et al. provide detailed information concerning the experiments conducted by the CNRS at Meudon, France, using the SR3 wind tunnel. The test matrix included three free stream flow conditions (Table 1), the same conditions as for the corner-flow/jet interaction experiments. The free-stream was nitrogen at a nominal Mach number of 20 and Reynolds number, based on model base diameter, ranging from 1,420 to 36,265. Measurements were performed that obtained three sets of data: density flow fields, heating rate

distributions, and aerodynamic forces and moments. Density flow-field measurements were made with the electron beam fluorescence technique for the two more rarefied conditions and for two angles of incidence:  $0^\circ$  and  $10^\circ$ . Heating rate distributions along the forebody, base, and sting, as well as aerodynamic forces, were obtained for angles of incidence between  $0^\circ$  and  $30^\circ$ .

#### 5.1.1 Procedures and Representative Results

Three different models were used according to the type of measurement, each having a 5 cm base diameter and an afterbody sting. For aerodynamic force measurements, the model was made of aluminum and uncooled. The model was directly attached to an external balance mounted around the open-jet test section of the SR3 wind tunnel. The model used for the flow-field density measurements was made of brass, water cooled, and sting supported. For heat-flux measurements, a thin-wall model made of Armco steel elements was used (Fig. 9). Chromel alumel thermocouples were embedded through the wall thickness at nine locations along the forebody, base plane and sting ( $s/R_n = 0.00, 0.52, 1.04, 1.56, 2.68, 3.32, 5.06, 6.50,$  and  $7.94$ ). Additional details concerning the models, test procedures, and tabulated and graphical presentations of results are documented by Allegre and Bisch<sup>23</sup>. Examples of data obtained for heat transfer and aerodynamics are presented in Figs. 10 and 11, respectively. The heating rate distributions as a function of angle of incidence are those for test Condition 2 (Table 1) while the axial ( $C_A$ ) and normal ( $C_N$ ) force coefficients are those for each of the three test Conditions as a function of incidence. Examples of the flow-field density measurements are discussed later.

#### 5.1.2 Computations and Comparisons

Extensive computations have been made for the SR3 test conditions since the test parameters were defined well in advance of the actual experiments. Test Condition 2 (Table 1) was a test case of the 4th European High-Velocity Database Workshop, ESTEC, Noordwijk, The Netherlands, Nov. 1994. Eight DSMC solutions were presented at this workshop, and a summary of those results is given by Coron and Harvey<sup>25</sup>.

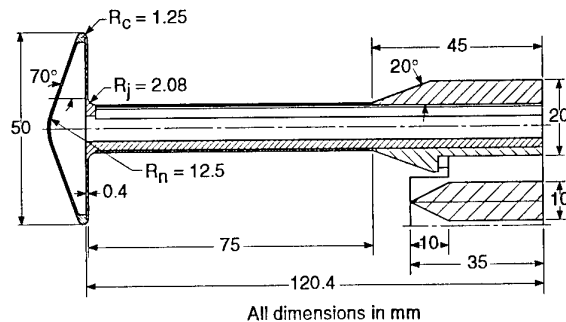


Fig. 9 Model for heat transfer rate measurements in SR3.

Table 5. Computational contributions for blunt-body/wake experimental and generic flight test conditions using direct simulation Monte Carlo (DSMC) and Navier-Stokes (NS) Codes.

Contributors	Low Density Wind Tunnels			Impulse Facilities			Flight	
	SR3	V3G	V2G	HEG	LENS		Earth	Mars
Aerospatiale les Mureaux, France	DSMC <sup>a</sup>							
CNRS Meudon, France	DSMC							
Cornell University, U.S.A.	DSMC				DSMC			
DLR Göttingen, Germany	DSMC		DSMC					
DRA Farnborough, U.K.	DSMC							
Fluid Gravity, Hampshire, U.K.	DSMC							
Imperial College, U.K.	DSMC	DSMC			DSMC		DSMC	DSMC
ITAM, Novosibirsk, Russia	DSMC							
Middle East Tech. Univ., Turkey	DSMC						DSMC <sup>a</sup>	
NASA Langley, U.S.A.	DSMC <sup>a</sup> & NS		DSMC	DSMC	DSMC		DSMC	DSMC
North Carolina State University, U.S.A.	DSMC <sup>a</sup> & NS				NS		NS	
Sandia Albuquerque, U.S.A.	DSMC							

<sup>a</sup>3-D solutions included



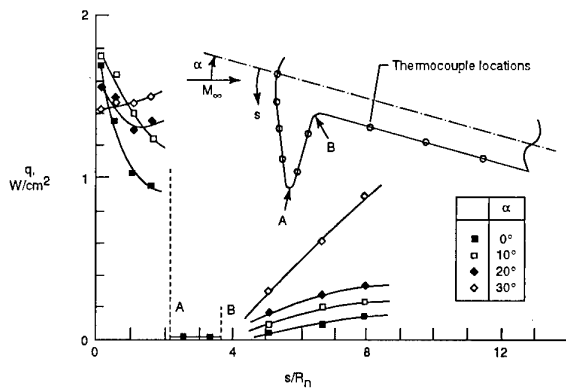
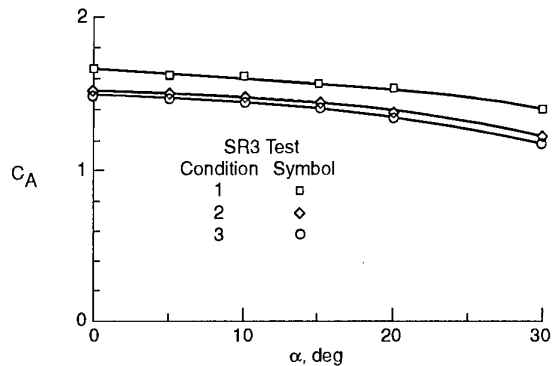
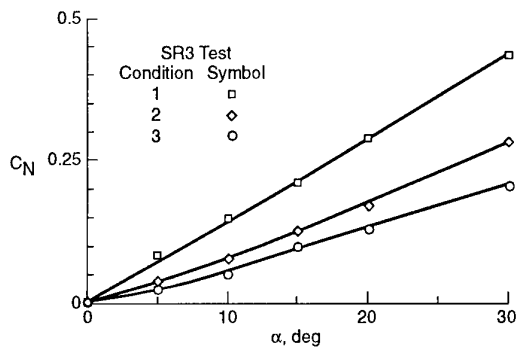


Fig. 10 Measured<sup>23</sup> heating rate distributions for SR3 test Condition 2.



(a) Axial force coefficient.



(b) Normal force coefficient.

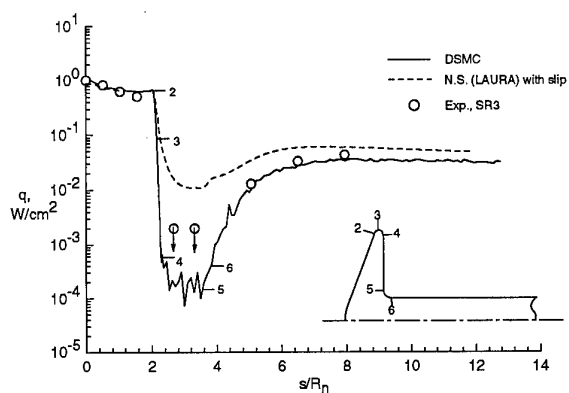
Fig. 11 Measured<sup>23</sup> aerodynamic coefficients for the three SR3 test conditions.

Calculations using both DSMC and Navier-Stokes solvers were made either prior to the experiments (Refs. 25 through 31, for example) or prior to release of the experimental data at the ESTEC Workshop. Moss<sup>31</sup> et al. provide an extensive presentation of information concerning flow-field features and surface quantities (including tabulated surface results) resulting from one set of DSMC calculations. Also reported in Ref. 31 are the results of parametric studies concerning numerics (cell size and time step) and physical modeling (rotational collision number and surface reflection model). Gilmore<sup>29</sup> also examined the effect of varying the surface accommodation coefficient from 0.5 (50 percent specular) to 1.0 (fully diffuse).

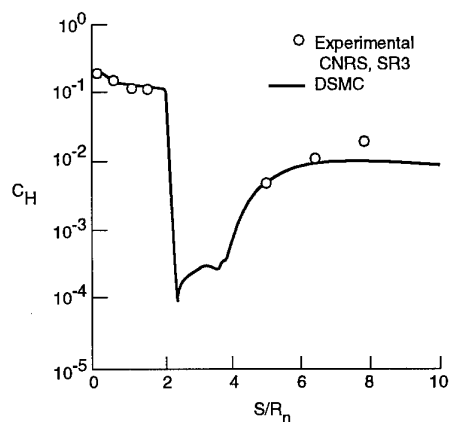
Examples of the calculated and measured results for the SR3 tests are shown in Figs. 12–14. Surface heating distributions at zero incidence are presented in Fig. 12 for each of the three test conditions. As evident by the comparisons, the DSMC solutions<sup>32</sup> show a better agreement with the measured values than do the Navier-Stokes<sup>19–22</sup> methods (with surface slip and temperature jump boundary conditions) along the base plane and sting, regions where rarefaction effects are most significant. The agreement of DSMC predictions and measurements is quite good along the sting and also on the base plane, where measured signal levels for Conditions 1 and 2 were so small that the heating magnitude could only be characterized as being less than 0.002 and 0.004 W/cm<sup>2</sup> for Conditions 1 and 2, respectively (indicated by symbol with downward pointing arrows in Fig. 12).

Along the forebody, the agreement between calculated and measured results is not as good as expected<sup>32</sup>. Along the blunted cone forebody, agreement between calculation and measurement decreases with decreasing rarefaction. This is most evident for Condition 3 where the experimental value at  $s/R_n = 1.56$  is 55 percent of the DSMC value. When the DSMC results along the forebody are compared with the Navier-Stokes solutions<sup>32</sup>, the agreement is 10 percent or better. Currently, the discrepancy observed in measured and computed heat transfer distributions along the forebody remain unresolved. Further experiments should be conducted to resolve this issue.

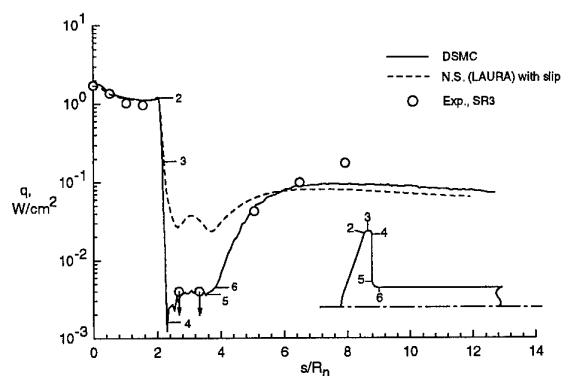
Figure 13 presents the measured and calculated heat transfer distributions for Condition 2 with the model at incident angles of 0°, 10°, and 20°. The data are presented in terms of the heat transfer coefficient defined as  $C_H = 2q/\rho_\infty V_\infty^3$ . The calculated values for both the windward and leeward rays are the 3-D DSMC solutions of Pallegoix<sup>30</sup>. Heat transfer measurements were made only along the windward ray, and agreement between measurements and calculations is very good. Also, Nance<sup>33</sup> et al. obtained fair agreement with the experimental heat transfer measurements for Condition 1 at 10° incidence using two different 3-D DSMC codes, one using a uniform Cartesian grid and one an unstructured tetrahedral grid.



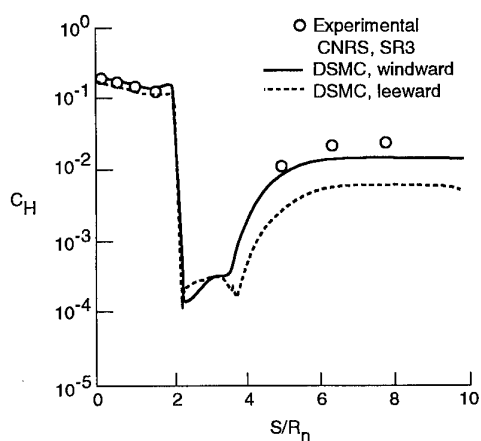
(a) Condition 1.



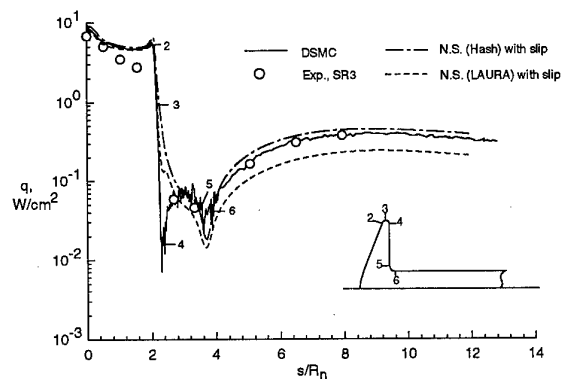
(a) Incidence = 0°.



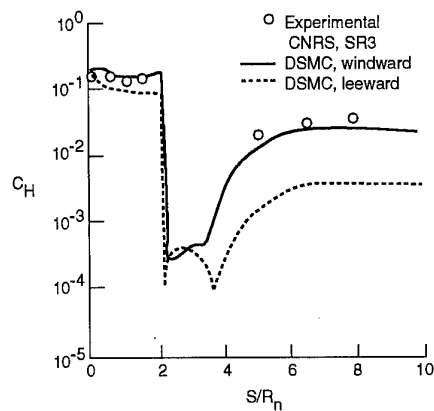
(b) Condition 2.



(b) Incidence = 10°.



(c) Condition 3.



(c) Incidence = 20°.

Fig. 12 Comparison of SR3 experimental<sup>23</sup> and computed<sup>32</sup> heating rate results ( $d = 5.0$  cm).

Fig. 13 Comparison of SR3 experimental<sup>23</sup> and computed<sup>30</sup> heating rate distributions for Condition 2.

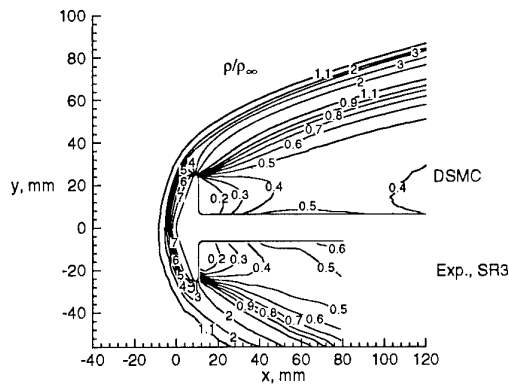


Fig.14 Comparison of measured<sup>23</sup> and calculated<sup>32</sup> density for SR3 test Condition 2.

A number of computational studies have presented graphical results of the forebody and wake flow features, demonstrating the influence of rarefaction on the flow structure. The DSMC calculations of Refs. 26 and 31 yield a wake vortex for each of the three test conditions with the size of the vortex increasing with decreasing rarefaction. Also, the location of maximum heating along the sting is downstream of the location of the free shear layer reattachment, as indicated by the sting shear stress distribution.

Wilmoth<sup>27</sup> et al. computed the flow for the SR3 test conditions without an afterbody sting using both DSMC and Navier-Stokes codes. These computations indicate that a wake vortex does not exist for Condition 1 but is present for the other two conditions, consistent with the finding of an earlier study of Dogra<sup>34</sup> et al. Wilmoth also demonstrated that a zonally decoupled DSMC solution procedure can be used effectively for these flow conditions ( $Kn_\infty$  ranging from 0.01 to 0.0005). That is, the forebody flow is solved separately by using either a DSMC or Navier-Stokes method, and the forebody exit-plane solution is specified as the in-flow condition to the decoupled DSMC solution of the wake region. The zonally decoupled solutions show good agreement with fully coupled DSMC solutions of the wake flow densities and velocities. The combined use of Navier-Stokes for the forebody with a decoupled DSMC solution for the wake provides an efficient method for solving transitional blunt-body flows where the forebody flow is continuum and the wake is rarefied. This approach has been employed in several studies<sup>17,35-37</sup> for much smaller Knudsen number cases than considered herein. The study of Hash and Hassan<sup>37</sup> concluded that the decoupled approach was more advantageous when applied to a small Knudsen number ( $Kn_\infty \approx 10^{-4}$ ) problem than a hybrid coupled DSMC/Navier-Stokes solver.

As mentioned earlier, nonintrusive electron beam fluorescence measurements of flow-field density were

made<sup>23</sup>, and Fig. 14 presents, as an example, a comparison of a DSMC calculation<sup>32</sup> with measured values. (See Ref. 25 for even better agreement of computed and measured results and Ref. 30 for good comparisons at 10° incidence.) The measured results are presented as the ratio of local density with the model installed in the test section of the wind tunnel to free-stream values without the model in the test section since density gradients exist in the undisturbed flow. The calculated results are local values ratioed to the free-stream value (Table 1). The overall quantitative features of the two data sets are similar, with the exception of the expansion of the flow about the outer corner of the model and the sudden up-turn of the 0.5 density contour adjacent to the sting. The calculated density contours in the near wake show a concentrated expansion from the rearward facing portion of the outer corner. This behavior is consistent with other DSMC calculations that have been made for Condition 2, as summarized in Ref. 25, both at 0° and 10° incidence. The measurements show a more diffuse expansion extending down the base of the model. Part of this discrepancy may be due to a measurement resolution issue, since the gradients in density are substantial near the surface and occur in a rather small volume. As suggested in Ref. 25, the up-turn of the measured density contours along the sting are most likely due to an increase in the cross-sectional area of the sting starting 80.4 mm downstream of the forebody stagnation point of the model. The change in the sting configuration was not included in the numerical simulations.

The aerodynamic forces, moments, and center of pressure were also measured for each flow condition at six angles of incidence spanning 0° to 30°. Tabulated results of these measurements are presented in Ref. 23. As reported in Ref. 32, the maximum difference in the measured and DSMC calculated drag coefficients for zero incidence was 6 percent. Reference 30 presents DSMC results for axial, normal, pitching moment, and center of pressure results for test Condition 2 at 0°, 10°, and 20° incidence. The discrepancies with measured values are 11 percent or less.

## 5.2 DLR Tests (V3G, V2G, and HEG)

Blunted cone models with base diameters of 5, 25, and 50 mm were utilized in the DLR Göttingen tests exploring the effects of rarefaction on forebody and wake flows. Three different test facilities were used: the two vacuum wind tunnels V3G and V2G, and the high enthalpy facility HEG. A brief summary of the experiments performed and computations for selected tests follows.

### 5.2.1 V3G Tests and Computations

The experimental measurements made by Legge<sup>18,38</sup> with the V3G free-jet facility concentrated on aerodynamic and heating measurements to provide data for validating theoretical results. The model was a 5 mm base diameter copper model suspended by means of 0.06 mm diameter thermocouple leads. Drag, lift, global aerodynamic heat transfer, and recovery temperature were measured in a Mach 9 nitrogen free-jet flow. These measurements were made at

stagnation temperatures of 300 K and 500 K for various degrees of rarefaction. The wall-to-stagnation temperature ratio was varied between 0.8 and 1.5. The desired wall temperature is established and maintained at a constant value before the flow is started by means of two radiators (Fig. 15). The global aerodynamic heat transfer rate to the blunted cone model was determined by using the model itself (Fig. 16) as a calorimeter. Lift and drag were determined by means of an electromagnetic two-component balance. Angle of attack results were obtained for  $\alpha = 0^\circ$ ,  $20^\circ$ , and  $40^\circ$ . The estimated overall errors for the measurements were  $\pm 8\%$  at  $T_0 = 300$  K and  $\pm 12\%$  at  $T_0 = 500$  K. Additional details concerning the experiments, data reduction, data accuracy, and results are included in Refs. 18 and 38.

The drag coefficient (Fig. 17), along with the other force coefficients, have the usual behavior between continuum and free-molecular flow. That is, there is a smooth transition between the continuum and free-molecular values for complete accommodation. The aerodynamic curves for  $T_0 = 300$  K and 500 K agree well, which means that the Knudsen number,  $Kn_0 = 3.2\mu_0 / (\rho_\infty \sqrt{2\pi RT_0} \cdot d_b)$  is a reasonable correlation parameter when  $T_0$  is changed. This behavior is demonstrated in Fig. 17 where the drag coefficient is plotted for  $T_0 = 300$  K and  $T_0 = 500$  K at  $T_w/T_0 = 1$ . For  $\alpha = 0$ ,  $T_0 = 1100$  K and  $T_w = 300$  K, two numerical results (Dogra<sup>34</sup> et al.) are also included: (1)  $M_\infty = 20.2$ ,  $\rho_\infty = 1.73 \times 10^{-5}$  kg/m<sup>3</sup>,  $C_D = 1.61$ ,  $Kn_0 = 0.11$  and (2)  $M_\infty = 19.7$ ,  $\rho_\infty = 5.19 \times 10^{-5}$  kg/m<sup>3</sup>,  $C_D = 1.54$  and  $Kn_0 = 0.038$ . The smooth transition from continuum to free-molecular values was not observed for the heat transfer and recovery temperature data at the higher wall-to-total temperature ratios. The heat transfer coefficient,  $C_H = 2\dot{Q} / (\rho_\infty U_\infty^3 A \cos \alpha)$  where  $\dot{Q}$  is the global heat transfer rate and the cone reference area is  $A = \pi R_b^2$  follows the same

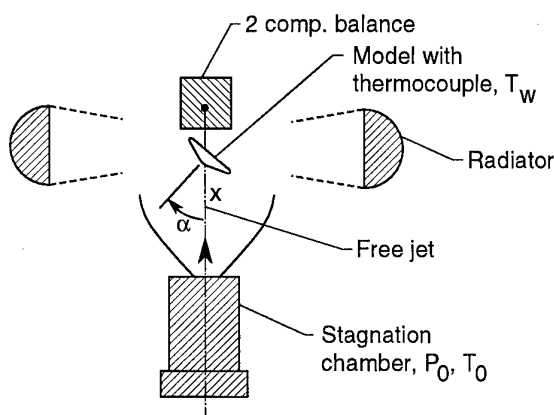


Fig. 15 Schematic of experimental set-up for V3G Götting blunted-cone tests.

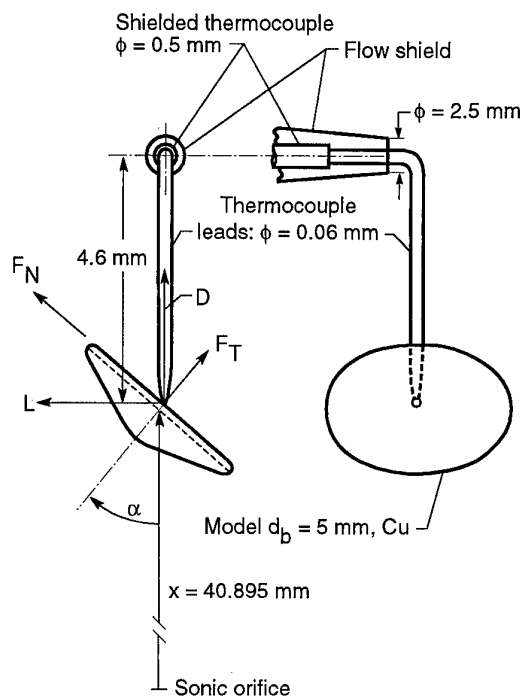


Fig. 16 Suspension of cone model and coordinate system for global heat-transfer rate and force measurements in V3G.

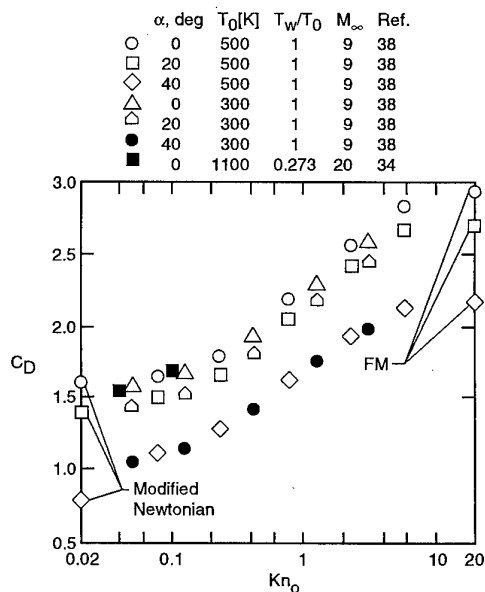
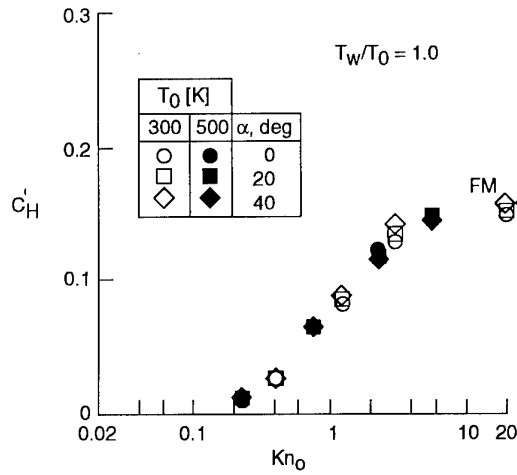
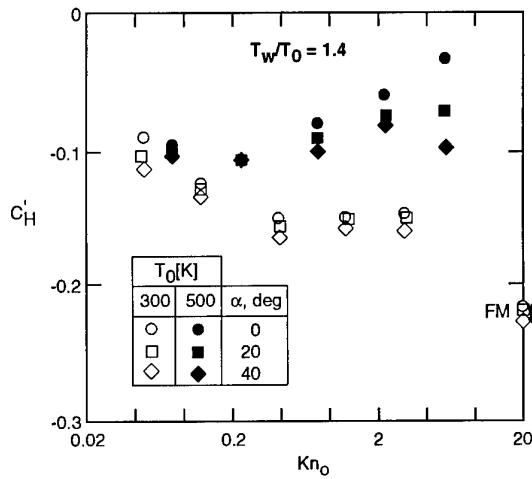


Fig. 17 Drag coefficient as a function of  $Kn_0$  and comparison of DSMC and experimental results for different flow conditions (V3G).

(a)  $T_w/T_0 = 1.0$ .(b)  $T_w/T_0 = 1.4$ .Fig. 18 Heat transfer coefficients  $C'_H$  (based on  $A' = A \cos \alpha$ ) as a function of  $Kn_0$  (V3G).

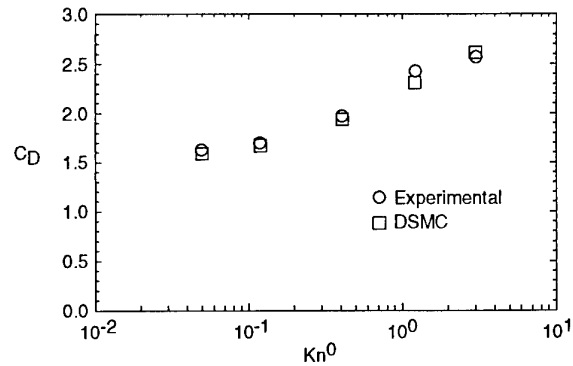
curves for both  $T_0 = 300$  K and  $T_0 = 500$  K at  $T_w/T_0 = 1.0$  as shown in Fig. 18(a). At larger  $T_w/T_0$  values; however, the absolute value of  $C'_H$  becomes smaller for  $T_0 = 500$  K than  $T_0 = 300$  K, indicating that the accommodation coefficients becomes less with increasing  $T_w$ . This behavior is demonstrated in Fig. 18(b) where  $C'_H$  is plotted as a function of  $Kn_0$  and  $T_w/T_0 = 1.4$  for the two total temperature conditions and three angles of attack.

DSMC calculations have been made by Gallis and Harvey<sup>39-40</sup> for the zero incidence test conditions at  $T_w/T_0 = 1.0$  for both  $T_0 = 300$  K and 500 K. The DSMC

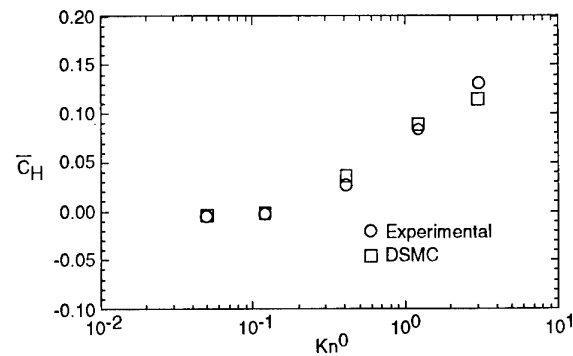
simulation modeled collisions with the variable soft sphere collision model<sup>41</sup> and energy exchange with the Maximum Entropy model<sup>40</sup>. The surface was assumed to be diffusely reflecting with full accommodation. The computational and experimental results are in good agreement for almost all cases simulated as demonstrated in Figs. 19(a) and 19(b) for the  $T_0 = 300$  K results where the drag and global heat transfer coefficient ( $\bar{C}_H = 2\dot{Q}/\rho_\infty v_\infty^3 A$ ) results are presented, respectively. The good agreement between V3G experimental measurements and DSMC calculations has also been evident for other configurations as discussed in Ref. 42 for a disk and in Ref. 43 for a delta wing.

### 5.2.2 V2G Tests and Computations

The vacuum wind tunnel V2G at DLR, Göttingen, has been used extensively to support the blunt body/wake research. Both qualitative and quantitative data have been reported by Legge<sup>18,44,45</sup> for models with and without a sting. The experiments were conducted in rarefied nitrogen flow at a nominal Mach number of 16 (see Table 1). Calibration results for the 15° half angle conical nozzle used to produce the flow is reported in Ref. 46. Reference 44 details many of the



(a) Drag coefficient.



(b) Global heat transfer coefficient.

Fig. 19 Comparison of V3G experimental<sup>38</sup> and DSMC<sup>39</sup> results for blunted at zero incidence.

qualitative results obtained for 50 and 25 mm base diameter models with and without (wire suspension) stings. The data include high frequency glow discharge flow visualization showing the shock shape, oil flow pictures giving surface streamlines, liquid crystal surface temperature visualization providing lines of constant temperature (lines of constant heat transfer under certain restrictions), and pitot pressure measurements in the wake. Data obtained with a 5 mm base diameter model is included in Ref. 18.

DSMC computations by both Danckert<sup>47</sup> and Moss (Appendix A of Ref. 45) were made for the V2G test conditions (Table 1) for the test model without a sting. Both DSMC codes are based on the method of Bird<sup>11</sup>. Comparisons of the V2G measurements with the DSMC results are presented in Ref. 18 where it is stated that excellent agreement is achieved between the calculated and experimental shock shapes (deduced from glow discharge visualization). The experimental shape for the 10 bar condition runs between the calculated iso-density lines (value normalized by free-stream density) of 2 and 3. For the same test condition, it was shown in Ref. 18, that the heating distribution along the sting, inferred from the liquid crystal heat transfer visualization measurements, was in reasonable agreement with the DSMC calculations. As discussed in Ref. 18, the data extraction process used the DSMC heating results at an arbitrary location to infer the quantitative values at other locations along the sting.

Global heat transfer and recovery temperature measurements were also made in V2G by using a 5 mm base diameter model. When the recovery temperature and Stanton number (Fig. 20)

$$St = \frac{\dot{Q}}{\rho_{\infty} U_{\infty} C_p (T_r - T_w) A} \quad (9)$$

results from V2G and V3G are compared, the agreement is generally good. This agreement confirms<sup>18</sup> that  $Kn_0$  is a good

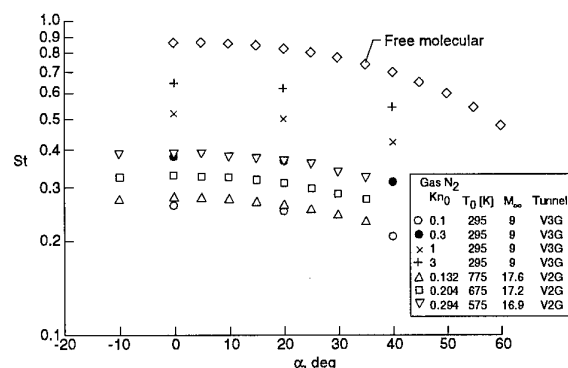


Fig. 20 Global Stanton number as a function of angle of attack and Knudsen number as measured<sup>18</sup> in V3G and V2G.

correlation parameter in the rarefied regime for wind tunnels with  $T_0 < 2000$  K. These data also confirm that good agreement can be achieved between free jet data (V3G) and conical nozzle data (V2G) which has much smaller gradients, provided the reference point for the free-stream conditions is addressed<sup>18</sup> for the free jet flow.

In addition to the wake density measurements made in the SR3 wind tunnel of CNRS, a study was conducted on the wake flow features under rarefied hypersonic flow conditions using the Göttingen V2G wind tunnel. The establishment of a vortex in a highly nonequilibrium flow (non-Maxwellian distribution function of the translational degrees of freedom) was investigated numerically with the DSMC<sup>47</sup> method and experimentally<sup>45</sup> with Patterson probe measurements. This intrusive measurement technique provides detailed information on the molecular number fluxes, hence information on the wake vortex features and how it is influenced by rarefaction.

Details of the experimental setup and flow conditions (three conditions listed in Table 1 for V2G), along with the theoretical aspects of the Patterson probe measurements, are given in Ref. 45. The measurements were made behind a blunted cone model (without sting) with a base diameter of 50 mm while suspended by three thin tungsten wires fixed at the backside. The coordinate system and the Patterson probe geometry are given in Fig. 21, where  $x$  is the distance on the wake centerline from the model nose. The Patterson probe could be moved in  $x$ - and  $y$ -directions and could be turned 360 deg around the slit (not the probe axis), where the slit center was located at  $z_p = 0$ .

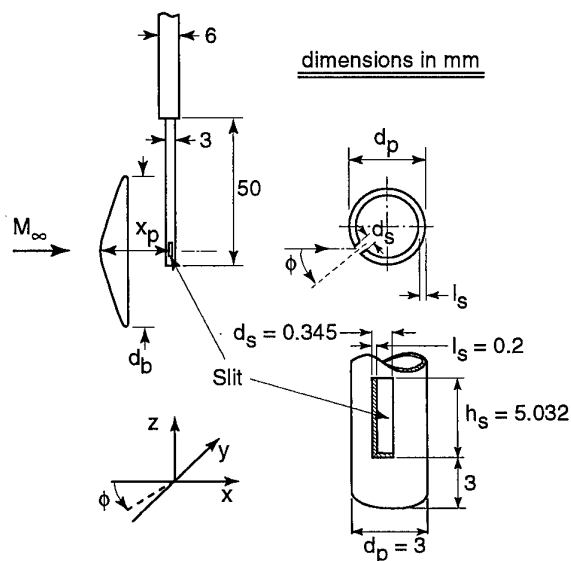


Fig. 21 Model and Patterson probe geometry used in V2G experiments ( $d_b = 50$  mm).

An example of the experimental and numerical results for test Condition 1 ( $p_0 = 2$  bar) is presented in Fig. 22. Shown is the incoming number flux,  $\dot{n}_i$ , at the entrance plane of the Patterson probe slit normalized by the free-stream mass flux as a function of the probe turning angle  $\phi$  (for  $\phi = 0^\circ$ , the slit is facing the negative  $x$ -direction) for various probe locations,  $x_p$ , measured downstream of the cone nose. The value of  $x$  at the cone base plane was 10.4 mm. At  $x_p = 15$  mm, the existence of a vortex is indicated by the fact that  $\dot{n}_i(\phi = 180^\circ) > \dot{n}_i(\phi = 0^\circ)$ , i.e., reverse flow. Also, the measurements show two relative maxima for  $x_p \leq 30$  mm, indicating that more molecules are impacting the probe from the lateral direction. The two maxima cannot<sup>47</sup> be described by a local Maxwellian distribution function, but as shown in Ref. 47, they can be approximated remarkably well with an ellipsoidal distribution function along the flow centerline.

Both measurements and calculations show that a vortex forms for the most rarefied case (Condition 1) and increases in length with decreasing Knudsen number. These findings are consistent with the DSMC calculations<sup>32</sup> for the SR3 test conditions. Figure 23 presents calculated and measured results for test Condition 2 ( $P_0 = 5$  bars), and illustrates good agreement for the wake centerline number flux,  $nu$ , ratioed to the free-stream flux,  $(nV)_\infty$ . The agreement is good in terms of both the extent of separation and the magnitude of the molecular fluxes. An obvious implication<sup>47</sup> is that the assumptions for the experimental data evaluation—no flow disturbance by the probe, free molecular flow about the probe, ratio of transmission probabilities equal to one—are sufficient to build a physical picture of the wake flow that is consistent with the DSMC calculations. The range of validity of these assumptions as well as the sensitivity of the numerical results to different DSMC models and calculation procedures should be investigated in future studies. Three-dimensional

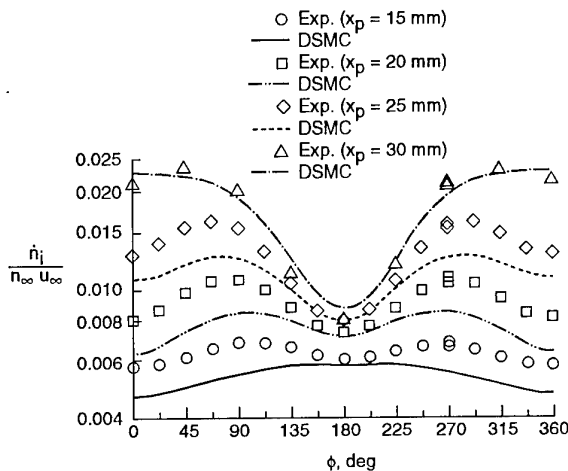


Fig. 22 Measured<sup>45</sup> and calculated<sup>47</sup> Patterson probe incident flux as a function of position and turning angle ( $\phi = 0^\circ$  denotes probe looking at model base plane).

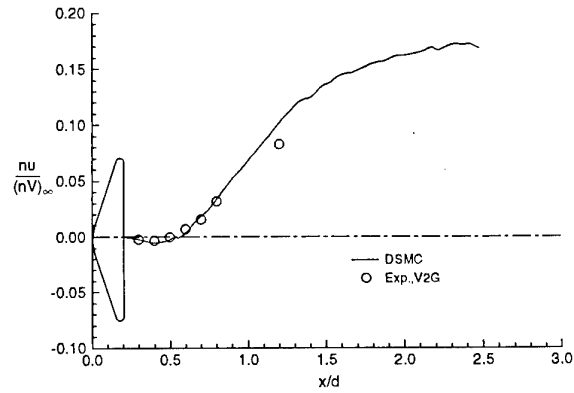


Fig. 23 Measured<sup>45</sup> and calculated<sup>32</sup> number flux along centerline of near wake for V2G test Condition 2.

simulations are essential to clarifying the impact of the probe-induced flow disturbance on the probe measurements.

### 5.2.3 HEG Tests and Computations

The HEG facility is a large free piston shock tunnel<sup>48</sup> that is capable of producing very high enthalpy gases. A series of experiments has been conducted in the HEG at the DLR, Göttingen, with a  $70^\circ$  spherically blunted cone having a base diameter of 15.24 cm. These tests have contributed to the high enthalpy, higher Reynolds number results of the WG 18 activity as discussed in Chapter IV. Legge<sup>18</sup> describes several tests that have been conducted in air with enthalpies of 10 to 23 MJ/kg at free-stream Mach numbers of approximately 10. For some of these tests, an array of four small models, 5 mm in diameter, were tested simultaneously with the larger model. The small models were located off centerline of the nozzle axis, as was the large model. Objectives of the small model tests were to assess different heating rate measurement techniques and obtain heating rate data at two locations along the forebody. Details concerning the experiments, models, and data reduction are given in Refs. 18 and 49. The estimated<sup>18</sup> error of the heat transfer measurements for the small cone tests is  $\pm 25$  percent. The scatter as shown in Ref. 18 is within  $\pm 20$  percent.

Reference 18 presents the free-stream conditions, including the free-stream gas composition as calculated with a one-dimensional nonequilibrium nozzle code for nine test conditions. Table 1 lists the free-stream conditions for two of these tests [shots 132 (Condition 1), and 131 (Condition 2)] for which DSMC calculations<sup>32</sup> have been made. The DSMC calculations were made using a 5-species reacting air gas model. For the lower enthalpy condition (Condition 1), the maximum mole fraction of atomic nitrogen behind the bow shock was of the order of 0.01, while the value for Condition 2 was of the order of 0.2. The calculated heating rate distributions for both cases are presented in Fig. 24 where the surface is assumed to be noncatalytic at a cold wall temperature of 300 K. Also shown are the measured results<sup>18</sup>

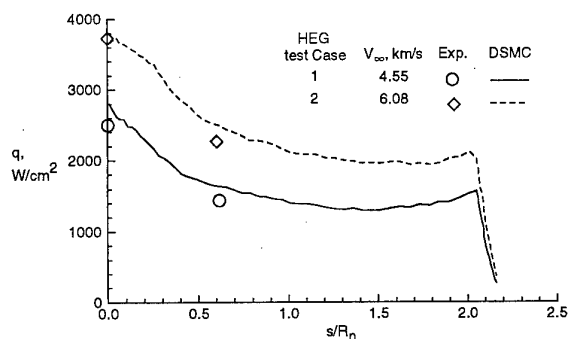


Fig. 24 Measured<sup>18,49</sup> and calculated<sup>32</sup> heating rates for two HEG tests using 5 mm base diameter models.

obtained by using the thin wall technique at the stagnation point and an  $s/R_n$  location 0.6. Good agreement is obtained for both shots concerning the distributions and absolute values.

For the mini cone tests in HEG, the free-stream Knudsen number is rather small, having values of .003 and .009 for the two conditions listed in Table 1; consequently, the effects of rarefaction on forebody heating should be minimal. This result is confirmed by the data analysis of Legge<sup>18</sup> that shows that the stagnation point heat transfer follows essentially a continuum behavior. Also, the heat transfer values at  $s/R_n = 0.6$ , when normalized by the stagnation value for the mini cones, fit well with the measurements of Kastell et al.<sup>50</sup> for the large models ( $d_b = 152.4$  mm).

### 5.3 Calspan Tests (LENS)

Several series of experiments<sup>16-17</sup> have been conducted at Calspan with large ( $d_b = 15.24$  cm) spherically blunted cone models. Tests were made in the Large Entry National Shock (LENS) facility using both nitrogen and air as test gases. Tests at 5 and 10 MJ/kg conditions for a range of reservoir pressure conditions (70 to 500 bars) have been completed where the models were sting-supported at zero incidence. Measurements consisted of surface pressure and heating rates along the forebody, base, and sting. The focus of these tests have been at continuum conditions; however, one test has been made at low pressure conditions where rarefaction effects should be evident in the wake. The specifics of this test condition, normally denoted as LENS test condition B, is listed in Table 1.

#### 5.3.1 LENS Test Condition B and Computations

Details of the instrumentation which was concentrated along the sting are given in Ref. 16. Med-Therm coax gauges were installed on the front face of the model while magnesium fluoride-coated thin film heat transfer gages were employed on the base of the model and sting. The pressure transducers were piezoelectric sensors developed by Calspan. Special requirements for conducting the measurements at the current

test condition along with measurement uncertainties are summarized in Ref. 17.

Results of the experimental measurements for the low pressure test were first presented in Ref. 16 and more recently were included in Ref. 17. DSMC results for this test condition have been reported in Refs. 32, 39, and 51-54. Figures 25 and 26 present comparisons of calculated surface quantities for heating rate and pressure where the calculations were for nonreacting nitrogen. The DSMC results shown are those obtained by Moss<sup>51</sup> et al. using the DSMC method of Bird, while the Navier-Stokes results are those obtained by Hash<sup>32</sup>, using an implicit, 3-temperature Navier-Stokes solver having the features discussed in Ref. 21-22. The slip boundary conditions used are those discussed in Ref. 55. The overall agreement between the DSMC and Navier Stokes calculations is shown to be good, particularly along the sting. Largest differences occur along the base plane. The implication of the present comparison is that a Navier-Stokes solver can provide an adequate prediction of surface quantities for the current test problem ( $Kn_\infty = 0.002$ ).

Also shown in Figs. 25 and 26 are comparisons of measured and calculated values. As evident, there is generally good agreement between the calculations and measurements, both in the separated region and toward the end of the recompression process, indicating<sup>16</sup> that the size of the base flow region is well predicted. The calculations produce slightly higher values for pressure and heat transfer in the recompression region over the sting. The measurements for the forebody are very limited for this particular test in that pressure values initially reported<sup>16</sup> had to be discarded since the range of the pressure sensors was not appropriate for this test condition. With only two heat transfer measurements along the forebody, it is not possible to establish the experimental trend for heat transfer distribution. The DSMC and Navier-Stokes results are in close agreement along the forebody with differences less than 10 percent.

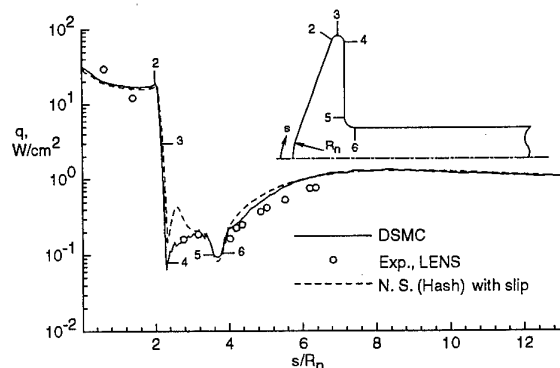


Fig. 25. Measured<sup>16</sup> and calculated<sup>32</sup> heating rate distributions for LENS test Condition 1 (Condition B).



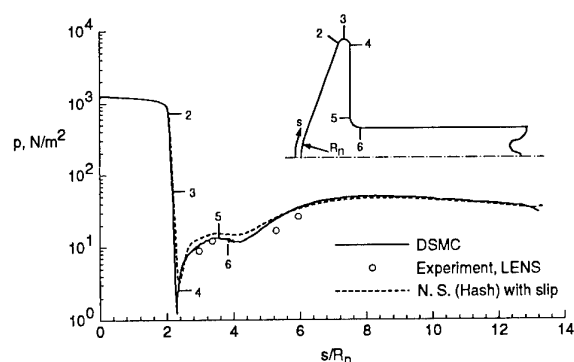


Fig. 26 Measured<sup>16</sup> and calculated<sup>32</sup> pressure distributions for LENS test Condition 1 (Condition B).

A summary of the DSMC<sup>51</sup> results for this test condition is as follows: 1) a wake vortex exists and extends 9 cm ( $s/R_n = 6.0$ ) downstream of the base plane; 2) peak heating on the sting occurs downstream of the near wake stagnation point at  $s/R_n = 8.4$ , having a magnitude of  $1.3 \text{ W/cm}^2$  or 4.2 percent of the forebody stagnation point value; 3) separation occurs on the outer corner before the surface becomes tangent to the base plane (just before location 4 in Fig. 25); 4) minimum values for surface pressure and heating rate occur at or near this location; 5) density in the near wake has a minimum value near the junction of the outer corner and base plane with a magnitude of about 20 percent of the free-stream value; and 6) small values for temperature jump and velocity slip are evident along the sting.

Other DSMC solutions obtained for this test condition are those of Gallis and Harvey<sup>39,53</sup> and Dietrich and Boyd<sup>54</sup>. In general, the agreement among the three DSMC solutions is good for surface quantities.

This test condition provides a valuable complement to the flow conditions that can be produced in low-density wind tunnels in that more energetic flows are produced. For the current condition, high temperature gas effects are present. That is, the nitrogen gas that envelops the test model is in thermal nonequilibrium; yet there is negligible dissociation.

**5.3.2 LENS Test Conditions C and E and Computations**  
During the course of the WG18 activity, results from several DSMC computations have been published for free-stream Knudsen numbers of the order of 0.0001, flows well outside the focus of the present chapter. A few comments are appropriate since DSMC computations have been published for these conditions. A concern was the possible effects of rarefaction as the flow expands about the corner radius into the wake. Test conditions for which DSMC solutions have been reported are LENS conditions C<sup>25,40</sup> and E (Refs. 35 and Boyd in Ref. 17) and one<sup>35</sup> for the HEG series of tests (shot 132, listed as Condition 1 in Table 1) where the test model was the large sting-supported, spherically blunted cone ( $d_b = 15.24 \text{ cm}$ ). Details of the latter two test conditions are

given in Chapter IV. These tests were conducted in air. Test Condition C ( $V_\infty = 3088.7 \text{ m/s}$ ,  $\rho_\infty = 4.247 \times 10^{-3} \text{ kg/m}^3$ ,  $T_\infty = 226.3 \text{ K}$ ,  $M_\infty = 10.23$ ) was included as a rarefied test case in the 4th European High-Velocity Database Workshop, ESTEC, Noordwijk, Nov. 1994. Note that the free-stream density is 32.5 times that listed for LENS B or Condition 1 in Table 1. Therefore, the local mean free path throughout the computational domain for Condition C would be an order of magnitude smaller than that for Condition B. By using a typical engineering workstation, the computational resources are probably excessive to achieve a cell resolution that would ensure accurate heat transfer predictions for Condition C. Experience shows that when the computational cells adjacent to a surface are larger than the local mean free path, the calculated heating rates will be too high. This was the ESTEC Workshop experience where four reacting and one nonreacting DSMC submissions were made. The DSMC forebody heating results were much higher than the measured values and the same was true along the sting. Another concern expressed in Ref. 25 was the lack of convergence, particularly in the wake region, because of the longer time required to achieve steady flow. The best agreement between calculations and measurements was achieved with the one Navier-Stokes solution submitted by Hash<sup>56</sup> et al.

More recent DSMC computations (Refs. 35 and 36 and Boyd in Ref. 17) for these conditions have used a zonally decoupled (forebody solved using Navier-Stokes and the wake using DSMC) approach (discussed earlier for the SR3 test conditions) or a hybrid<sup>37</sup> DSMC/Navier-Stokes approach. Even with these computational approaches, which achieve a substantial reduction in computational cost as compared to a full DSMC simulation, the computational requirements are still substantial. In fact, the solutions of Hash and Hassan<sup>36-37</sup> and Gochberg<sup>35</sup> et al. indicate deficiencies (cells too large or cells not adequately populated). Consequently, a convincing case has not been made that rarefaction effects are significant or that DSMC would enhance the computational results for the blunt body/wake problems where  $Kn_\infty$  is of the order of  $10^{-4}$ .

#### 5.4 Flight Entry Test Conditions

The flight test cases consist of four individual cases to provide code-to-code comparisons for a  $70^\circ$  spherically blunted cone 2 m in diameter and flat along the afterbody. No experimental results are available for these test cases. The test cases are for both Earth and Mars entry using both reacting and nonreacting gas models. The free-stream and surface boundary conditions are specified in Ref. 1 and listed in Table 2. These conditions correspond to altitudes of approximately 85 and 68 km in the Earth and Mars atmospheres, respectively. Consequently, both the model size and entry conditions are representative of current planetary missions. The combination of high velocity and relatively low free-stream Knudsen numbers ( $Kn_\infty \approx 0.003$ ) ensures substantial forebody dissociation. Key interest was the impact of nonequilibrium chemical activity along the forebody and

the combined effects of rarefaction and chemical activity in the near wake.

#### 5.4.1 Earth Reentry

Dogra<sup>57</sup> et al. presented results for both reacting and nonreacting air test cases calculated with the DSMC method of Bird and also reacting air solutions using an axisymmetric 3-temperature, 5-species implicit Navier-Stokes solver described in Refs. 21 and 22. The DSMC and Navier-Stokes results were in close agreement for the wake flow-field quantities. Also, the size of the vortex, as measured from the base of the blunted cone to the wake stagnation point, is identical ( $0.77 d_b$ ) for the two solutions. Both solution methods indicate that the air dissociation is significant for the current flow conditions. Near the forebody surface, essentially all the molecular oxygen and over half of the molecular nitrogen species are dissociated (noncatalytic wall assumption). Species separation among the heavy ( $N_2$ ) and light ( $O$  and  $N$ ) species was evident in the DSMC results as the flow expanded into the wake region. This separation produces some differences in the wake chemical composition where a larger concentration of atomic species was evident in the near wake for the DSMC solution. As for the surface heating results (Fig. 27), both methods are in good agreement along the forebody. Along the base plane, the Navier-Stokes heating values results exceeds the DSMC results by 25 percent or more with a maximum difference of 200 percent aft of the corner expansion.

When the calculation is made assuming nonreacting chemistry, as was done in Ref. 57, then the DSMC results, compared with the reacting air solution, shows much higher surface heating rates—49 percent higher at the forebody stagnation point and about 240 percent higher along the base; a smaller wake vortex ( $0.62 d_b$ ); similar values for the wake density contours; and essentially the same value for drag. If

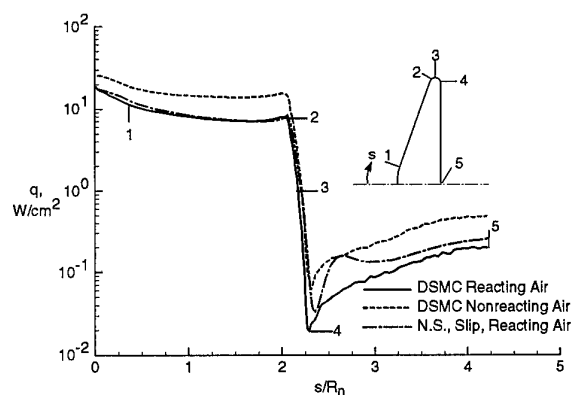


Fig. 27. Calculated<sup>57</sup> heating rate distributions for Earth reentry (Alt = 85 km,  $V_\infty = 7.0$  km/s,  $d_b = 2.0$  m,  $R_n = 0.5$  m).

the reacting gas calculations had been made with a finite or fully catalytic surface boundary condition, then the difference in surface heating would have been less.

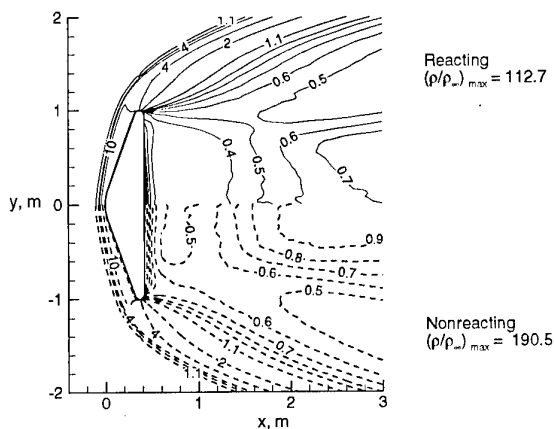
DSMC solutions along the forebody were also reported by Gallis and Harvey<sup>58</sup> for this test case, in which a different model for the nonequilibrium chemistry is used compared to that of Ref. 57. Reacting and nonreacting results are presented showing the effect of the chemistry on stagnation temperature and density profiles, but not on heating rates. The reacting heating rate results are somewhat higher, particularly in the stagnation region, when compared to that of Ref. 57.

Additional DSMC solutions related to this test condition have been reported. Dogra<sup>57</sup> et al. also examined the effect of including two afterbody configurations: (1) a cylindrical afterbody (cylinder diameter =  $0.5 d_b$ ) and 2) a conical frustum (similar to the Mars Pathfinder afterbody). Details of the effect on flow-field features and surface heating are discussed. As was the case for the DSMC calculations made for the SR3 wind tunnel conditions, the presence of an afterbody had no effect on the forebody flow field or surface quantities. Dogra<sup>59</sup> et al. examined the effect of rarefaction on the wake structure by calculating the flows for altitudes of 75, 85, 95, and 105 km at the same free-stream velocity and surface boundary conditions, but for the Mars Pathfinder Probe ( $d_b = 2.65$  m). Three-dimensional DSMC calculations have been presented by Celenligil<sup>60,61</sup> where the only modification was that the free-stream conditions were for an altitude of 90 km; hence a more rarefied condition where  $Kn_\infty \approx 0.0085$ . The calculation used the DSMC method of Bird and a reacting five species air gas model. Results for zero incidence are discussed in Ref. 60, while those for  $10^\circ$ ,  $20^\circ$ , and  $30^\circ$  incidence are presented in Ref. 61. Results show the presence of a wake vortex for all cases considered. Reference 61 presents details of calculated surface, flow field, and aerodynamic results.

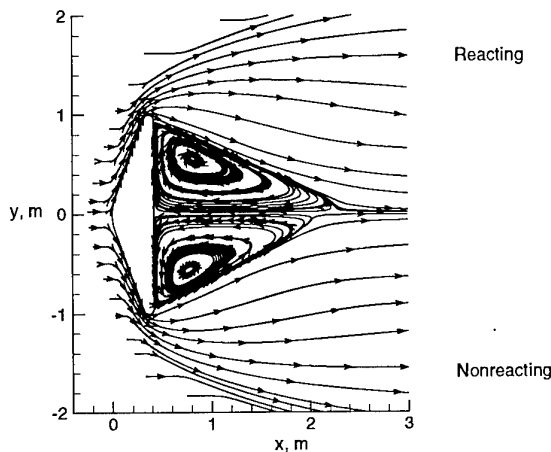
#### 5.4.2 Mars Entry

Previous studies addressing chemical reactions and rarefaction effects for Mars entry are relatively few. DSMC studies by Hash and Hassan<sup>62</sup> and Gallis and Harvey<sup>63</sup> are examples of simulations that address the chemical and fluid relaxation issues associated with blunt body entries where the free stream consists primarily of  $CO_2$ . One contribution<sup>64</sup> has been reported for the Mars test conditions (Table 2) and one closely related contribution<sup>63</sup>. Those of Moss<sup>64</sup> et al. were done for both reacting and nonreacting  $CO_2/N_2$  flows using the DSMC method of Bird<sup>11</sup> with the chemical reaction set (9 species) based on the data of Hash and Hassan<sup>62</sup>. The calculations of Gallis and Harvey used the maximum entropy method for simulating the chemical reactions and energy exchange. The later calculations are only for the forebody and were conducted at a free-stream density equal to 72.7 percent of the test case value.

Examples of the results obtained from the calculations by Moss<sup>64</sup> et al. are presented in Figs. 28 through 29 showing the effect of chemical reactions on flow field and surface results. Several calculations were made to refine the grid to achieve a cell spacing normal to the surface that is less than the local mean free path. Flow-field features as influenced by chemical reactions are presented in Figs. 28(a) and 28(b) where the density contours and particle traces are shown, respectively. As was shown for the Earth reentry results<sup>57</sup>, the flow with reacting chemistry has a larger wake vortex than the nonreacting results. Unlike the Earth entry test case results, there are larger differences in the near wake density contours for the reacting and nonreacting calculations. For the reacting calculation, the gas species adjacent to the surface are



(a) Density contours,  $\rho/\rho_\infty$ , where  $\rho_\infty = 1.187 \times 10^{-5} \text{ kg/m}^3$ .



(b) Particle traces.

Fig. 28 DSMC Calculated<sup>64</sup> effects of nonequilibrium chemistry on flow-field quantities for Mars entry (Alt  $\approx 68$  km,  $V_\infty = 7.0$  km/s,  $d_b = 2.0$  m,  $R_n = 0.5$  m).

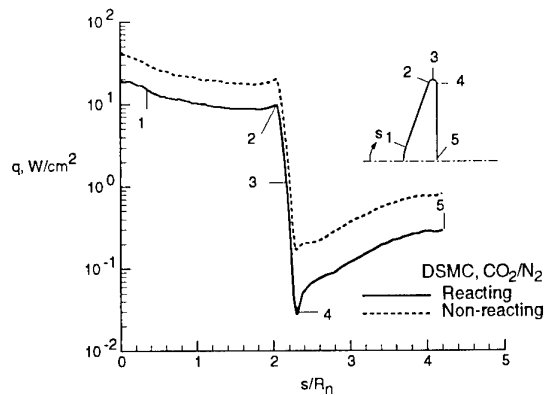


Fig. 29. Calculated<sup>64</sup> heating rate distributions for Mars entry (Alt  $\approx 68$  km,  $V_\infty = 7.0$  km/s,  $d_b = 2.0$  m).

predominantly CO and atomic oxygen. In the near wake, the calculated mole fractions for atomic oxygen and CO are approximately 0.50 and 0.45, respectively.

With essentially all of the  $\text{CO}_2$  being dissociated over the forebody, the surface heating to a noncatalytic wall is substantially less than the nonreacting solution. At the stagnation point, the nonreacting value was 2.1 times the reacting value while along the base plane the nonreacting value was 2.9 times (at  $y = 0.5$  m) the reacting value. As was the case for Earth re-entry, the impact of chemistry on the drag coefficient was insignificant. The calculated drag coefficient was 1.65 for the reacting solution where the pressure contribution to the total drag was 98.8 percent.

Gallis and Harvey<sup>63</sup> presented forebody solutions with and without chemical reactions for the Mars entry conditions except that the free-stream density was less than the test condition. Consequently, their dimensional heating values would be lower than that for the test conditions. However, their calculated heating values are greater by a factor of two or more than the results shown in Fig. 29 for both the reacting and nonreacting cases. Their heating results appear excessively high based on stagnation engineering correlations or viscous-shock-layer results. For the Mars test condition, the stagnation engineering correlation of Sutton and Graves<sup>65</sup> gives a value of  $32 \text{ W/cm}^2$  assuming chemical equilibrium. A 16-species nonequilibrium reacting gas model as implemented in the viscous-shock-layer analysis of Gupta<sup>66</sup> gives a stagnation value of  $22.9 \text{ W/cm}^2$ . The heating results presented in Fig. 29 are believed to be more realistic based on the correlation and viscous-shock-layer results than the results presented in Ref. 63.

Additional calculations are needed for the generic flight test cases, particularly the Mars test case, to assess the differences among solution methods as well as the modeling issues

associated with thermal and chemical nonequilibrium. Solutions, with and without chemical reactions, help to isolate differences that might exist among solutions. A critical discriminator is the surface heating.

## 6 FINDINGS AND RECOMMENDATIONS

### 6.1 Corner-Flow/Jet Interaction Problem

Calculations performed by different workers on the corner flow / jet interaction problem reproduce qualitatively the features of the pressure distributions obtained experimentally. However, quantitative agreement was not achieved. Also small differences between calculated results were observed.

The potential sources of discrepancies between results have been examined. Differences in implementing the numerical methods (e.g., boundary conditions, gas modeling, discretization) can explain small differences but not large ones.

It is suggested that additional experiments be conducted to clarify other potential causes of discrepancies:

- Measure the jet mass flow rate.
- Measure the wall temperature (and examine its influence on measured pressure).
- Confirm the absence (or not) of condensation in the jet.
- Scan or visualize the flow field (e.g., using the electron beam fluorescence technique) to obtain a better understanding of the shape of the jet and of the boundary conditions to use, particularly along the upper boundary.

### 6.2 Blunt-Body/Wake-Closure

A key aspect of the success of this activity has been the experimental contributions from five hypersonic facilities that have fostered a significant number of computational contributions. The experiments have provided heating and aerodynamic data and previously unavailable data as to the features of the wake flow structure and how these quantities are influenced by rarefaction. Application of DSMC and Navier-Stokes methods to many of the test conditions have provided insight and confidence on where the methods can be effectively applied to such problems. The synergy of the computational/experimental activities has produced a significant database that can serve as a valuable aid for validation purposes as well as an aid for aerobraking and planetary probe mission designs. Some of the key contributions or findings of this activity are 1) first experimental measurements of wake density field and number flux for generic Aerassist Space Transfer Vehicle configuration; 2) database involving both quantitative and qualitative information that spans a wide range of conditions (nonreacting to reacting flows) in the transitional regime; 3) demonstrated capability of different DSMC codes to simulate selected test cases (SR3, Condition 2); 4) the

experimental (V2G, Patterson probe) and computational findings which show that a vortex is established when there is a strong non-Maxwellian distribution function in the wake and the size of the wake vortex increases with decreasing Knudsen number; 5) the maximum heating along a sting/afterbody for zero incidence was of the order of five percent of the forebody stagnation value; 6) the location of wake reattachment and maximum sting heating rate are not coincident, and the separation between the two locations diminishes with decreasing rarefaction; 7) inclusion of slip boundary conditions in the Navier-Stokes solvers provided improved agreement with experimental and DSMC results; 8) results from the Navier-Stokes solutions suggest that the overall Knudsen number should be of the order of 0.001 or less before good agreement is achieved between experiment or DSMC for the near wake surface and flow features, and that the Navier-Stokes solutions agree with the DSMC results for quite large overall Knudsen numbers along the forebody; 9) the combined use of Navier-Stokes for the forebody with a decoupled DSMC solution for the wake provides an efficient method for solving transitional blunt-body flows where the forebody flow is continuum and the wake is rarefied; and 10) for the generic flight test cases which involve substantial dissociation, the calculated forebody and afterbody heating for the reacting solutions are substantially less than for the corresponding nonreacting cases.

Additional experiments and computations should be carried out to address discrepancies and areas of uncertainties:

- generation of a more extensive experimental heating rate distribution data base with contributions from multiple facilities using the same test model when possible (wakes with laminar free shear layers including sting reattachment are essential data for computational tool benchmarking)
- parametric DSMC studies demonstrating the sensitivity of flow-field and surface results to the models implemented regarding internal energy exchange and nonequilibrium chemistry for generic flight test conditions
- parametric studies using Navier-Stokes solvers with surface slip and temperature jump boundary conditions to examine the sensitivity of calculated wake flow-field and surface results to grid (both density and alignment) and code dissipation for free-stream Knudsen numbers of the order of  $10^{-3}$
- three-dimensional DSMC simulations to complement the Patterson probe measurements and provide more insight as to potential interference effects of the intrusive measurements

## REFERENCES

1. Hypersonic Experimental and Computational Capability, Improvement and Validation," edited by Saric, W. S., Muylaert, J., and Dujarric, C., AGARD AR-319 Vol.1, May 1996.

2. Allègre, J. and Raffin, M., "Experimental Study on Control Jet Interaction," Laboratoire d'Aérodynamique du CNRS, Report RC 91-11, 1991.
3. Allègre, J. and Raffin, M., "Experimental Study on Control- Jet/Corner-Flow Interaction," Laboratoire d'Aérodynamique du CNRS, Report RC 92-7, 1992.
4. Allègre, J., and Raffin, M., "Control Jets Interacting with Rarefied Hypersonic Flows," 72nd Fluid Dynamics Panel Symposium on Computational and Experimental Assessment of Jets in Cross Flows, Winchester, UK, April 19-22, 1993.
5. Chauvot, J. F., Dumas, L. and Dupuis, D., "Corner flow jet interaction: computation and experiment," *Rarefied Gas Dynamics 19*, edited by J. Harvey and G. Lord, Oxford University Press, 1995, pp. 773-779.
6. Hendriadi, R., "Etude de simulation numérique d'un Écoulement hypersonique de gaz raréfié limité par deux plans perpendiculaires avec jet transversal," Laboratoire d'Aérodynamique du CNRS, rapport de stage RS 93-3 (in French), 1993.
7. Tartabini, P. V., Wilmoth, R. G. and Rault, D. F. G., "Direct Simulation Monte Carlo Calculation of a Jet Interaction Experiment," *Journal of Spacecraft and Rockets*, Vol. 32, No 1, Jan.-Feb., 1995, pp.75-83.
8. Tartabini, P. V., Wilmoth, R. G. and Rault, D. F. G., "A systems approach to a DSMC calculation of a control jet interaction experiment," AIAA Paper 93-2798, 1993.
9. Wilmoth, R. G. and Tartabini P. V., "Three-Dimensional DSMC Calculations of Jet/Corner Flow Interactions," *Rarefied Gas Dynamics 19*, edited by J. Harvey and G. Lord, Oxford University Press, 1995, pp. 1209-1215.
10. Spear, A. J., Freeman, D. C. and Braun, R. D., "Mars Pathfinder Status at Launch," IAF- 96-Q.3.02, 47th International Astronautical Congress, Oct. 1996.
11. Bird, G. A., "Molecular Gas Dynamics and the Direct Simulation of Gas Flows," Clarendon Press, Oxford, 1994.
12. Bird, G. A., "Definition of a Mean Free Path for Real Gases," *Phys. of Fluids*, Vol.26, 1983, pp. 3222-3223.
13. Potter, J. L. and Blanchard, R. C., "Thermomolecular Effect on Pressure Measurements with Orifices in Transitional Flows," *Rarefied Gas Dynamics*, edited by A.E. Beylich, VCH, 1991, pp. 1459-1465.
14. Cline, M. C., "VNAP2: A Computer Program for Computation of Two-Dimensional, Time-Dependent, Compressible, Turbulent Flow," Los Alamos Scientific Laboratory, LA-8872, Los Alamos, NM, Aug. 1981.
15. Lengrand, J.C., Raffin, M. and Allègre, J., "1981 Monte Carlo Simulation Method Applied to Jet-Wall Interactions under Continuum Flow Conditions," *Rarefied Gas Dynamics*, Sam.S.Fisher ed., Progress in Astronautics and Aeronautics, Vol.74, 1981, pp.994-1006.
16. Holden, M., Kolly, J. and Chadwick, K., "Calibration, Validation, and Evaluation Studies in the LENS Facility," AIAA Paper 95-0291, Jan. 1995.
17. Holden, M., Harvey, J., Boyd, I., George, J., and Horvath, T., "Experimental and Computational Studies of the Flow Over a Sting Mounted Planetary Probe Configuration," AIAA Paper 97-0768, Jan. 1997.
18. Legge, H., "Experiments on a 70 Degree Blunted Cone in Rarefied Hypersonic Wind Tunnel Flow," AIAA Paper 95-2140, June 1995.
19. Gnoffo, P. A., "An Upwind-Biased, Point-Implicit Relaxation Algorithm for Viscous Compressible Perfect-Gas Flows," NASA TP-2953, February 1990.
20. Gnoffo, P. A., Gupta, R. N. and Shinn, J. L., "Conservation Equations and Physical Models for Hypersonic Air Flows in Thermal and Chemical Nonequilibrium," NASA TP-2867, Feb. 1989.
21. Olynick, D. R. and Hassan, H. A., "New Two-Temperature Dissociation Model for Reacting Flows," *Journal of Thermophysics and Heat Transfer*, Vol. 7, No. 4, Oct.-Dec. 1993, pp. 687-696.
22. Olynick, D. R., Taylor, J. C. and Hassan, H. A., "Comparisons Between DSMC and the Navier-Stokes Equations for Reentry Flows," AIAA Paper 93-2810, July 1993.
23. Allègre, J. and Bisch, D., "Blunted Cone at Rarefied Hypersonic Conditions—Experimental Density Flow-fields, Heating Rates, and Aerodynamic Forces," CNRS Report RC 95-2, September 1995.
24. Allègre, J., Bisch, D. and Lengrand, J.C., "A 70° Blunted Cone at Rarefied Hypersonic Conditions," submitted to *Journal of Spacecraft and Rockets*, 1997.
25. Coron, F. and Harvey, J. K., "Synopsis for Test Case 6—Rarefied 70° Spherically Blunted Cone," 4th European High-Velocity Database Workshop, ESTEC, Noordwijk, The Netherlands, Nov. 1994.
26. Moss, J. N., Mitcheltree, R. A., Dogra, V. K. and Wilmoth, R. G., "Direct Simulation Monte Carlo and Navier-Stokes Simulations of Blunt Body Wake Flows,"

- AIAA Journal*, Vol. 32, No. 7, 1994, pp. 1399–1406; also AIAA Paper 93-2807, July 1993.
27. Wilmoth, R. G., Mitcheltree, R. A., Moss, J. N. and Dogra, V. K., "Zonally Decoupled Direct Simulation Monte Carlo Solutions of Hypersonic Blunt-Body Wake Flows," *Journal of Spacecraft and Rockets*, Vol. 31, No. 6, Nov. – Dec. 1994, pp. 971–979; also AIAA Paper 93-2808, July 1993.
  28. Marriott, R. M. and Bartel, T. J., "Comparison of DSMC Flow Field Predictions using Different Models for Energy Exchange and Chemical Reaction Probability," *Rarefied Gas Dynamics 19*, edited by J. Harvey and G. Lord, Oxford University Press, 1995, pp. 413–419.
  29. Gilmore, M. R., "Rarefied Flow Over a Blunt Body," DRA/DWS/WX7/TR 95 189, February 1995.
  30. Pallegoix, J. F., "Workshop ESTEC—Test Case No. 6—Rarefied Spherically Blunted Cone," Paper presented at 4th European High-Velocity Database Workshop, ESTEC, Noordwijk, The Netherlands, Nov. 1994.
  31. Moss, J. N., Dogra, V. K. and Wilmoth, R. G., "DSMC Simulations of Mach 20 Nitrogen Flows about a 70° Blunted Cone and its Wake," NASA TM-107762, August 1993.
  32. Moss, J. N., Dogra, V. K., Price, J. M. and Hash, D. B., "Comparison of DSMC and Experimental Results for Hypersonic External Flows," AIAA Paper 95-2028, June 1995.
  33. Nance, R. P., Wilmoth, R. G., and Hassan, H. A., "A Comparison of Grid-Definition Schemes for DSMC," AIAA Paper 96-0604, Jan. 1996.
  34. Dogra, V. K., Moss, J. N., and Price, J. M., "Near Wake Structure for a Generic ASTV Configuration," *Journal of Spacecraft and Rockets*, Vol. 31, No. 6, Nov.-Dec. 1994, pp. 953-959; also AIAA Paper 93-0271, Jan. 1993.
  35. Gochberg, L. A., Allen, G. A., Gallis, M. A., and Deiwert, G. S., "Comparison of Computations and Experiments for Nonequilibrium Flow Expansions Around a Blunted Cone," AIAA Paper 96-0231, Jan. 1996.
  36. Hash, D. B., and Hassan, H. A., "A Decoupled DSMC/Navier-Stokes Analysis of a Transitional Flow Experiment," AIAA Paper 96-0353, Jan. 1996.
  37. Hash, D. B., and Hassan, H. A., "Two-Dimensional Coupling Issues of Hybrid DSMC/Navier-Stokes Solvers," submitted for publication, *Journal of Thermophysics and Heat Transfer*, 1997.
  38. Legge, H., "Heat Transfer and Forces on a Blunted 70 Deg. Half Angle Cone Measured in Hypersonic Free Jet Flow," DLR Report IB 222-93 A 33, November 1993.
  39. Gallis, M. A. and Harvey, J. K., "Validation of DSMC Computations for the Flow-field Around a 70° Blunted Cone," *Rarefied Gas Dynamics 19*, edited by J. Harvey and G. Lord, Oxford University Press, 1995, pp. 1284–1290.
  40. Gallis, M. A. and Harvey, J. K., "Comparison of the Maximum Entropy DSMC Code with Flow-field Measurements," AIAA Paper 95-0413, Jan. 1995.
  41. Koura K. and Matsumoto H., Variable Soft Sphere Molecular Model for Inverse-Power-Law or Lennard Jones Potentials, *Physics of Fluids A*, Vol. 3, No. 10, pp. 2459–2465.
  42. Legge, H., Nanbu, K. and Igarishi, S., "Force and Heat Transfer on a Disc in Rarefied Flow," *Rarefied Gas Dynamics*, edited by A. E. Beylich, VCH, 1991, pp. 679–686.
  43. Celenligil, M. C. and Moss, J. N., "Hypersonic Rarefied Flow About a Delta Wing—Direct Simulation and Comparison with Experiment," *AIAA Journal*, Vol. 30, No. 8, August 1992, pp. 2017–2023.
  44. Legge, H., "Flow Visualization and Pitot Probe Measurements in Hypersonic Rarefied Flow Around a 70 Deg. Half Angle Cone," DLR Report IB 223-95 A 01, February 1995.
  45. Legge, H., "Patterson Probe Measurements in the Wake of a 70 Deg. Half Angle Cone in Hypersonic Rarefied Flow," DLR Report-IB 223-94 A 15, December 1994.
  46. Legge, H., von Roden, G., Klotzbach, A. and Rammenzweig, D., "Calibration Data of V2G with a Conical Ma  $\approx$  15 Nozzle," DLR IB 223-94A 11, 1994.
  47. Danckert, A. and Legge, H., "Experimental and Computational Wake Structure Study for a Wide-Angle Cone," *Journal of Spacecraft and Rockets*, Vol. 33, No. 4, 1996, pp. 476–482; also AIAA Paper 95-2141, June 1995.
  48. Eitelberg, G., McIntyre, T., Beck, W., and Lacey, J., "The High Enthalpy Shock Tunnel in Göttingen," AIAA Paper 92-3942, 1992.
  49. Legge, H., Rammenzweig, D. and Klotzbach, A., "Heat Transfer Measurements on a Blunted 70 Deg Half Angle Cone in High Enthalpy Small Reynolds Number Flow," DLR Report IB 223-95 A 22, March 1996.

50. Kastell, D., Horvath, T. J., and Eitelberg, G., "Nonequilibrium Flow Expansion Experiment Around a Blunted Cone," Paper presented at the 2nd European Symposium on Aerothermodynamics for Space Vehicles," Noordwijk, Netherlands, November 1994.
51. Moss, J. N., Price, J. M. and Dogra, V. K., "DSMC Calculations for a 70° Blunted Cone at 3.2 km/s in Nitrogen," NASA TM-109181, January 1995.
52. Moss, J. N. and Price, J. M., "Review of Blunt Body Wake Flows at Hypersonic Low Density Conditions," AIAA Paper 96-1803, June 1996.
53. Gallis, M. A. and Harvey, J. K., "Comparison of the Maximum Entropy DSMC Code with Flow-field Measurements," AIAA Paper 95-0413, Jan. 1995.
54. Dietrich, S. and Boyd, I. D., "Scalar and Parallel Optimized Implementation of the Direct Simulation Monte Carlo Method," *Journal of Computational Physics* 126, Vol. 126, 1996, pp. 328-342.
55. Gupta, R. N., Scott, C. D. and Moss, J. N., "Slip-Boundary Equations for Multicomponent Nonequilibrium Airflow," NASA TP-2452, Nov. 1985.
56. Hash, D. B., Hassan, H. A., Dogra, V. K. and Price, J. M., "Navier-Stokes Calculations for a Spherically Blunted Cone-LENS Condition," Fourth European High-Velocity Database Workshop, ESTEC, Noordwijk, Nov. 1994.
57. Dogra, V. K., Moss, J. N., Wilmoth, R. G., Taylor, J. C., and Hassan, H. A., "Effects of Chemistry on Blunt-Body Wake Structure," *AIAA Journal*, Vol. 33, No. 3, 1995.
58. Gallis, M. A. and Harvey, J. K., "Implementation of a Maximum Entropy Method in Monte Carlo Direct Simulations," AIAA Paper 95-2094, June 1994.
59. Dogra, V. K., Moss, J. N., Wilmoth, R. G., Taylor, J. C., and Hassan, H. A., "Blunt Body Rarefied Wakes for Earth Entry," *Journal of Thermophysics and Heat Transfer*, Vol. 9, No. 3, July-Sept., 1995, pp. 464-470; also AIAA Paper 93-0271, Jan. 1993.
60. Celenligil, M. C., "Three-Dimensional Wake Flow Simulations for a 70-deg Blunted Cone During Re-Entry," *Rarefied Gas Dynamics 19*, edited by J. Harvey and G. Lord, Oxford University Press 1995, pp. 1140-1146.
61. Celenligil, M. C., "Rarefied Wake Flow Simulation for a 70-deg Blunted Cone at Incidence," 20th International Symposium on Rarefied Gas Dynamics, Beijing, China, August 1996.
62. Hash, D. B. and Hassan, H. A., "Monte Carlo Simulation of Entry in the Martian Atmosphere," *Journal of Thermophysics and Heat Transfer*, Vol. 7, No. 2, April-June 1993, pp. 228-232.
63. Gallis, M. A. and Harvey, J. K., "Analysis of Non-Equilibrium in Mars Atmosphere Entry Flows," AIAA Paper 95-2095, June 1995.
64. Moss, J. N., Wilmoth, R. G. and Price, J. M., "DSMC Simulations of Blunt Body Flows for Mars Entries," AIAA Paper 97-2508, June 1997.
65. Sutton, K. and Graves, R. A., "A General Stagnation-Point Convective-Heating Equation for Arbitrary Gas Mixtures," NASA TR-376, Nov. 1971.
66. Gupta, R. N., Lee, K. P. and Scott, C. D., "Aerothermal Study of Mars Pathfinder Aeroshell," *Journal of Spacecraft and Rockets*, Vol. 33, No. 1, Jan.-Feb. 1996, pp. 61-69.

# Real Gas / Blunt Cone Phase II Report

George S. Deiwert

Georg Eitelberg

## 1. INTRODUCTION

In this chapter recent activity in real-gas database definition and code validation will be summarized. In the Phase I report of the Working Group (WG) 18<sup>1</sup>, aerothermodynamic problems were classified, for purpose of discussion, into seven types: aerodynamic parameters, viscous/shock interaction, boundary-layer transition, forebody-heating/heat-transfer, radiation and ablation, lee and base-region flow, and low-density flow. Several of these problem types were the subject of various chapters of the Phase 1 report describing real-gas effects and ground test facility issues.

In this chapter some background and objectives outlined in the real-Gas effects Chapter V of the Phase 1 report will be reviewed. The results of the blunt cone test campaign developed under the auspices of the WG18 activity to study real-gas phenomena will be summarized, including the experimental and computational programs, issues and questions, and recommendations. Further, recent progress in other real-gas areas beyond the blunt cone test campaign will be discussed. Finally, a summary in which the present status of our understanding of real-gas issues will be presented.

## 2. BACKGROUND/OBJECTIVES

Real-gas effects are important in hypersonic flows both in terms of their influence on aerodynamic performance and their effect on aerothermodynamic heating. It is recognized that high-

enthalpy, ground-based test facilities cannot fully simulate flight conditions and that they exhibit unique real-gas behavior themselves. Hence, the process for developing validated analysis tools is one in which real-gas CFD is involved in all aspects of a real-gas ground-test program. CFD is used to design and define the experiment, to define the ground-facility test conditions, and to simulate the ground-test experiment itself. The ground-test data, in turn, are used to validate, or calibrate, the CFD simulations. Only in this manner can sufficient confidence be gained and real-gas analysis tools be validated.

In the Phase I report<sup>1</sup> the issues of real-gas effects on aerodynamic coefficients, forebody heating/heat transfer, and lee and base flows were discussed in the chapter on real-gas effects, chapter V. Viscous interactions were discussed in Chapter II, transition to turbulence in Chapter III and low density in Chapter IV. Radiation and ablation were not specifically treated.

Ground-facilities required to provide meaningful data for the real-gas issues were discussed in Chapter V, in VI regarding calibration requirements, and in Chapter VIII regarding future needs.

The development of validated analysis tools for hypersonic flows was described and involves a process in which real-gas CFD development and application and experimental testing are performed hand-in-hand, synergistically, until the validation is complete. Hypersonic flows inherently involve real-gas phenomena. The validation of CFD tools requires considerations asso-



ciated with perfect-gas CFD validation *plus* consideration of additional complexities associated with real-gas phenomena. These real-gas complexities include thermal and chemical time scales, multiple gas species, internal-energy flow variables and properties, and coupled fluid/chemical processes.

An effort was made to identify existing real-gas databases for the subject hypersonic flow problems. These included published studies involving the flow field about building block configurations including hemispheres, cylinders, and blunt cones as simulated in ground-based test facilities, and flight data obtained on the spherically blunted cone in the RAMC flight test program.

Additional building block experiments involving bluff and slender cones were identified, and new studies were recommended to augment the existing database for both compressive and expanding flows.

In this regard a blunt-body base-flow test configuration was developed as part of the WG18 activity. The results of this activity are the subject of the next section of this report.

Configuration studies on the shuttle orbiter configuration and the orbiter-like configuration Halis were also considered in the WG18 activity and were described in some detail in Ref. 1 and Chapter V of the present report.

In the following section, a detailed report of the blunt cone test campaign will be presented.

### 3. BLUNT CONE TEST CAMPAIGN

The blunt-body/wake closure problem was selected to help identify real-gas effects, including thermal non-equilibrium and rarefaction. Experimental and computational investigations have been made for low-density conditions reproduc-

ible in rarefied gas wind tunnel experiments<sup>2-7</sup> and high-enthalpy conditions reproducible in impulse shock tunnel facilities<sup>8-10</sup>. Several participants committed to perform tests on simple configurations, the most often-used one being the 70-degree half-angle blunt cone, either sting-mounted or free-flying (see Fig. 1). This geometry is the same forebody as used in the NASA Viking missions, and the geometry for the Mars Pathfinder probe.

Initially, a series of overlapping tests was proposed for three experimental facilities: the 16-inch shock tunnel at the NASA Ames Research center, Moffett Field, CA, the HEG piston-driven shock tunnel at the DLR-Göttingen, Germany, and the Large Energy National Shock Tunnel (LENS) at CALSPAN, Buffalo, NY. All three facilities were to examine a flow expanded through a nozzle of area ratio approximately 1600:1 to provide essentially equivalent free-stream conditions. The common test condition is based on the driver stagnation enthalpy and pressure conditions for this flow expansion, namely 10 MJ/kg, and 500 bar.

Each facility was to be operated at the same enthalpy and the same Mach and Reynolds number ( $H_0 = 10$  MJ/kg,  $M = 7$ , and  $\rho_0 = 500$  bar). In addition, tests in the Ames facility were planned at total enthalpies of 5 and 14 MJ/kg at total pressures of 100 bar, in the DLR HEG facility at enthalpies of 20 MJ/kg and total pressures of 500 and 1000 bar, and in the LENS at enthalpy 5 MJ/kg and pressures of 500 and 2000 bar.

The lower enthalpy levels produce only modest levels of dissociated oxygen and no dissociated nitrogen. At 10 MJ/kg there will be substantial oxygen dissociation and negligible nitrogen dissociation. At 20 MJ/kg there will be substantial dissociation of both oxygen and nitrogen. Nitrous

oxide (NO) will be produced under all test conditions.

The main motivation for these tests was to provide data for numerical code validation, but the tests were also designed to give further information on facility behavior and quantification<sup>1</sup>. The code validation portion of the tests was designed to quantify the shear layer separation point, its turning angle and wake closure in the presence of flows exhibiting real-gas effects. The unsteady character of the near wake would also be documented, if possible. Body surface instruments would provide calibration/validation data for computational fluid dynamic (CFD) simulations. Both sting-mounted and free-flight models would be necessary to assess and quantify the influence of the sting in the instrumented model. Issues in the facility behavior context included shock standoff distance and shape, information about which can help characterize dissociation effects behind the bow shock. Also of facility behavior interest is the extent of the expansion wave over the shoulder of the blunt body. This data would help obtain global information about the properties of the free stream.

Several different experiments and computations have been completed for a variety of conditions<sup>2-10</sup>. Here, we concentrate on the hypersonic, high enthalpy conditions where real-gas effects must be considered. Experimental data for the high enthalpy flow conditions for this series have been reported by Kastell et al.<sup>9</sup> from HEG, and by Holden et al.<sup>10</sup> from LENS. The tests planned for the 10-inch shock tunnel at NASA Ames have not yet been performed.

Described herein are numerical simulations of the flow fields from the HEG and LENS high enthalpy experiments at the common test condition of 10 MJ/kg and 500 bar using both NS and DSMC solvers. The results from each code are

compared not only to the experimental data, but to each other as well. Thermal non-equilibrium is examined using both codes, and representations of rarefaction effects are studied using the DSMC results. The ability of CFD to accurately simulate these high enthalpy flows is evaluated in terms of both computational accuracy and comparison to experimental data.

### 1.1. Computational Methods

The NEQ2D<sup>11</sup> code (also referred to in the literature as NASCAND or GIANTS) is used for all continuum flow-field computations in this paper. It uses the two-dimensional axisymmetric Navier-Stokes equations and expands them to allow for the presence of multiple species and Park's two-temperature model<sup>13</sup> (translational/rotational and vibrational/electronic temperatures). The equations are solved by a fully implicit, flux-split, Gauss-Seidel relaxation numerical technique. A five species air model is used (N<sub>2</sub>, O<sub>2</sub>, N, O, NO) in the solutions. The computational mesh (see Fig. 2a) is generated by the HYPGEN code<sup>14</sup> and is constructed so that all grid lines intersect the model body orthogonally. Exponential stretching is used where grid spacing changes are required normal to the model surface. Changes in step size along the surface of the model are smoothed to assure a clean computational grid. Zero wall velocity and room temperature boundary conditions are used in the computations. Since the wall temperatures are low, non-catalytic boundary layers are assumed.

The DSMC code is used an axisymmetric particle solver by Gallis and Harvey<sup>4</sup>, which uses the Variable Soft Sphere (VSS) model from Koura and Matsumoto<sup>15</sup>. The code uses a multi-regional mesh (see Fig. 2b) to achieve the best possible distribution of cells in the computational

domain. Weighting factors are used in the radial direction to reduce the number of particles required in the simulation. The code simulates translational, rotational, vibrational, and electronic energy modes. The vibrational and the electronic modes are treated in quantum states. All other properties are treated as continuous distributions. A modification of the Maximum Entropy method of Levine and Bernstein<sup>16</sup> is used for the simulation of chemical reactions and energy exchange. The wall boundary conditions are fully accommodating, diffusely reflective, and noncatalytic.

The DSMC code described by Gallis and Harvey<sup>4</sup> is not modified for use in this work, but it uses results from NS forebody computations as its startline condition for computing the wake flow. However, the NS code, NEQ2D, is adapted for this work from previous versions of the code. First, the original FORTRAN code is converted to run as a C code for this study. Second, the original NEQ2D code uses both a second order differencing scheme and a first order upwind differencing scheme. The upwind differencing is intended only for use in near and through shock waves (it is unstable otherwise). The trigger for deciding which of the two differencing schemes is used monitors when the pressure gradient exceeds a critical value. The original gradient algorithm is only one-dimensional in the streamwise direction. The code is revised to use a two-dimensional gradient in both the streamwise and orthogonal directions. This removes some mesh-sensitivities in the stagnation point region, which were seen with the original code formulation. Finally, the code is changed to use thermal and vibrational energy as boundary conditions rather than temperature. This technique enhances low temperature (near 300 K) solution stability near the walls.

## 1.2. Shock Tunnel Facilities

The three shock tunnel facilities, which have been used to perform experiments with blunt cone models, are the 42-inch combustion-driven shock tunnel, located at the NASA Ames Research Center, the high-enthalpy free piston-driven shock tunnel (HEG) at DLR-Göttingen, and the Large Energy National Shock Tunnel (LENS) at CALSPAN. Though the facilities have differing operating characteristics, all three shock tunnels are or were capable of simulating high-pressure, and/or high-enthalpy conditions required to study hypersonic flows with real-gas effects.

A schematic of a generic shock tunnel facility is shown in Fig. 4. The NASA Ames facility has been decommissioned and is not available for further testing. It was 30.0 m in total length and consisted of a 7.66 m driver tube (diameter of 68.6 cm), a 12.2 m shock tube (diameter of 15.8 cm), and a 2.74 m, 10 degree half-angle conical supersonic nozzle segment at the end of the driven tube. The nozzle exit diameter was 1.1 meters. An open jet test section was located at the end of the nozzle. In this shock tunnel, the driver section of the shock tunnel was filled with a light combustible mixture, and the driven section (shock tube) was filled with the test gas. When the main diaphragm ruptured after ignition of the driver gas, a shock propagated towards the end of the driven tube. A secondary diaphragm located at the nozzle entrance was used to accurately control the driven tube fill pressure. The reflected shock burst the secondary diaphragm and initiated the nozzle flow. The test time for this facility was designated as the length of time (for the experimental conditions used in this paper, on the order of several milliseconds) during which quasi-steady nozzle stagnation conditions were achieved before the driver gas

arrived at the test section<sup>17</sup>. The test models in this facility (and in the other two shock tunnels as well) were situated in the test chamber at the nozzle exit.

The HEG facility produces flows similar to the NASA 42-inch shock tunnel. The driver compression is supplied by a moving piston, rather than from combustion, and its scale is larger. It is 60.0 m in total length, with a 33.0 m driver tube (diameter of 55.0 cm), a 17.0 m shock tube (diameter of 15.0 cm), and a 3.75 m supersonic contoured nozzle. The diameter at the nozzle exit is 0.88 meters. Test times are several milliseconds long for high enthalpy operating conditions<sup>18</sup>.

The LENS facility is similar in size to the HEG facility, but the operation differs slightly. The driver tube is pressurized and can be heated prior to the diaphragm rupture, rather than using a combustion or free-piston driver. A double-diaphragm configuration vents pressure in an intermediate chamber to fire the tunnel. The facility is 44.0 m in total length, with a 7.9 m driver tube (diameter of 29.2 cm), a 17.5 m shock tube (diameter of 20.3 cm), and a 6.2 m nozzle. The nozzle exit diameter is 1.22 m. The test times are also several milliseconds long under high enthalpy operating conditions<sup>19</sup>.

### 1.3. Shock Tunnel Flows and Numerical Simulations

The reservoir conditions driving the nozzle expansion are the flow properties behind the reflected shock at the end of the driven tube (shock tube). Those stagnation conditions are usually calculated from the measured initial pressure in the driven tube and the measured incident shock speed. The most commonly used computer code for estimating shock tunnel reservoir conditions is called ESTC<sup>20</sup>. For a "tai-

lored" shock tunnel operating condition, the gas left behind the reflected shock near the driven tube end wall has a zero flow velocity. The gas is assumed to be in chemical equilibrium since the pressure and temperature are high, and the flow is nearly stagnant.

The flow in the facility nozzle is calculated using quasi-1D and/or 2D/axisymmetric formulations capable of capturing the non-equilibrium effects. Several numerical methods and computational tools have been used to solve the Navier-Stokes equations for this application. In order of increasing complexity as well as accuracy, some of the recently used codes implemented for these applications are NENZF<sup>21</sup>, LSENS<sup>22</sup>, STUBE<sup>23</sup> (all three of these codes assume inviscid flow and quasi-1D equilibrium chemistry from the reservoir to the nozzle throat and thermal/chemical non-equilibrium from just downstream of the throat to the nozzle exit), a 3D Euler/NS solver by Hannemann<sup>24,25</sup>, and GASP<sup>26</sup> (the last two being viscous, multidimensional Navier-Stokes codes with full thermochemical non-equilibrium). The multidimensional computations have been recently validated with shock tunnel experimental pitot pressure data by Hannemann<sup>24,25</sup> and Papadopoulos et al.<sup>27</sup>.

The expanded driven gas enters the test section of the shock tunnel at the nozzle exit and washes over the model. After a quasi-steady flow is established (as determined by pressure and heat flux measurements during the run time of the facility), the actual usable test time begins. The test time is terminated when the driver gas reaches the test section and significantly changes the flow field around the model. Hence, the quoted free-stream conditions in the test section of the facility are determined by a combination of experimental and computational methods. The free-stream conditions for the experi-

mental data examined in this paper are summarized in Table 1. These values are used as the input to the NS code used in this study.

Table 1: HEG, LENS and NASA 42-inch test conditions<sup>8,9,12</sup>

	HEG Run 132	HEG Run 133	LENS Case E	NASA 42-inch
$P_0$ (Mpa)		55	49.11	28.98
$H_0$ (MJ/kg)	11.48	11.97	11.03	9.3
$T_0$ (K)	6712.9	6564.9	6483.3	-
$M_\infty$	10.12	9.99	8.53	14.9
$V_\infty$ (m/s)	4539.5	4470.7	4430.3	4150
$T_\infty$ (K)	489.9	488.1	673.1	190
$P_\infty$	588.4	575.5	692.1	18.24
$\rho_\infty$ (kg/m <sup>3</sup> )	0.00409	0.00402	0.0035	0.00031
Molecular wt.	28.3	28.32	28.4	28.86
$N_2$ (mol.cond.)	0.7279	0.7289	0.7363	0.785
$O_2$ (mol.cond.)	0.1475	0.1493	0.157	0.215
$N$ (mol.cond.)	4.80E-07	4.50e-07	0.0091	1.00E-08
$O$ (mol.cond.)	0.0478	0.0446	0.0387	1.00E-08
$NO$ (mol.cond.)	0.067	0.0675	0.0589	1.00E-08

The subscripts 0 and  $\infty$  refer to reservoir stagnation and free-stream conditions, respectively. Conditions as determined by experimental calibration data, by the shock tube code ESTC<sup>20</sup> for air, and by STUBE<sup>23</sup> for HEG<sup>8,29</sup>, GASP<sup>26</sup>, for LENS<sup>9</sup> and Refs. 17 and 28 for the 42-inch tunnel.

#### 1.4. Results

The blunt cone geometry has been the object of both experimental and computational scrutiny for several years<sup>2-9</sup>. Much of the work has been concentrated on the lower density cases, in which the NS codes break down and would not be expected to yield accurate results. DSMC codes have been used for many of those inves-

tigations, and that work has yielded good comparisons between computations and experiments. At the higher enthalpy flow conditions in this investigation, the densities are expected to be at levels where NS codes stand a better chance of producing reasonable accuracy. At the same time, the DSMA codes will have difficulty dealing with the higher densities and the large density gradients seen over the computational domain.

#### 1.5. Navier-Stokes Forebody solutions

The NEQ2D code has been used previously in computations for a 70-degree blunt cone model forebody by Stewart and Chen<sup>12</sup>. In that work, the geometry in the shoulder region of the body differed slightly from the AGARD WG18 test model. A separate grid (not pictured) is generated to run this case for code validation purposes since changes have been made to the NEQ2D code for this study.

The computational and experimental results for the Stewart and Chen work can be seen in Fig. 4, where the heat flux is plotted along the body surface. There is a difference between those results and the runs with the updated version of NEQ2D. Some of these differences can be attributed to changes in the boundary conditions used in the newer version of the code, which eliminated some numerical problems when simulating room temperature walls<sup>30</sup>. Also, the older version of the code contained eigenvalue limiters, which were adjusted when comparing the CFD results to the experimental data<sup>31</sup>. The newer version of NEQ2D has had the limiters removed so the results cannot be "tuned" to fit to an experimental database. Additionally, the change in the algorithm for computing gradients in the stagnation region resulted in grid independent solutions for the forebody computations

in this paper. The previous version of the code produced mesh-dependent stagnation point fluxes and was the reason for implementing the previously discussed modifications to the NEQ2d code.

The match of the present NS results to the experimental data is similar to that reported by Stewart and Chen. The normalized heat fluxes match significantly better in this study, but the actual heat fluxes are underpredicted by 23% at the nose. The Chen CFD overpredicts the stagnation point heat flux data by only 6.5%, but eigenvalue limiters were used with the code, and the results remained somewhat mesh-sensitive in the nose region<sup>31</sup>. Stewart reported a 10% uncertainty in the data, which is indicated by the error bars in Fig. 4. However, issues of heat flux uncertainties in light of new data analysis methods for coaxial thermocouples are currently being investigated<sup>9,32,33</sup>. This work may eventually account for some of the differences in the absolute values of these heat flux data.

Forebody data are also available from Kastell et al.<sup>9</sup> and Holden et al.<sup>10</sup>. HEG Run 132 results can be seen in Fig. 5, where the normalized computed and experimental heat fluxes are within approximately 15% of each other. The shape of the heat flux profile around the shoulder of the body is well simulated, but the shape of the forebody heat flux curve is somewhat different. Also, the magnitudes of the stagnation point heat fluxes differ by 37% (the stagnation point heat flux value of approximately  $500 \text{ W/cm}^2$  was extrapolated from data presented by Legge<sup>34</sup>). Here the questions concerning the coaxial thermocouples were eliminated by using the same material for the model (chromel) as one of the thermocouple materials. It should be noted that absolute errors for the HEG experimental data have not yet been reported in the available lit-

erature, though they are expected to be in the 10% range<sup>32</sup>. Results for LENS Case E show an underprediction of the both normalized and actual heat fluxes compared to experimentals, but the data in the forebody are very limited. The LENS experimental stagnation heat flux value was extrapolated from the limited data to allow for comparative evaluations. The value used,  $380 \text{ W/cm}^2$ , was not available experimentally.

## 1.6. Navier-Stokes Wake Solutions

NS wake computations have been completed for HEG Runs 132, 133 and LENS Case E. The results can be seen in Figs. 6-9. Since all of these runs showed similar behavior, only one case, HEG Run 132, will be shown as representative of the three runs. Where significant differences appear, they will be noted individually.

Fig. 6 shows the density field (in  $\text{kg/m}^3$ ) for HEG Run 132. The wake region is clearly defined by the locations of the shock and the free stream. The white area in front of the blunt body contains higher density gas flow than is indicated by the contour levels in the figure. This region was excluded from the contour plot to allow visualization of the bow shock and not to wash out all flow features in the wake. The results show the expected region of low density immediately behind the blunt body in the recirculation zone. The density begins to increase at the point where the shear layer impinges on the sting. A weak compression region can also be seen above the sting at about 1.5 nose radii from the corner where the sting mated with the blunt body. This weak compression contour appears at an angle of approximately 15 degrees to the sting.

Traces of the particle paths are shown in Fig. 7. The main recirculation zone is clearly defined, and a smaller zone is seen in the corner where

the sting joins with the blunt body. A final small recirculation zone is located just behind the point of separation along the back of the blunt body near the shoulder. A plot of Mach number contours in Fig. 8 identifies the two smaller recirculation zones as subsonic, but inside the main recirculation cell exist two separate regions where the Mach number exceeds one slightly (approximately Mach 1.5). These supersonic recirculation flows have also been seen by Anagnost<sup>35</sup> and Haas<sup>36</sup> in similar NS blunt body computations without a sting.

The wake can be examined for thermal non-equilibrium by looking at the normalized difference between vibrational and translational-rotational temperatures  $((T_{t,r}-T_v)/T_{t,r})$  in the two-temperature model. Fig. 9 shows that there exist regions near the backside of the body and along the sting where the vibrational temperature is still out of thermal equilibrium. This is due to the low densities in those regions, the speed of the flow, and the cooling of the gas due to heat transfer to the sting. There is an insufficient amount of time (i.e., number of molecular collisions in these regions) for the vibrational energies to equilibrate. The frozen, non-equilibrium expanding flow in the far wake, behind the blunt body and above the sting, is also clearly seen in Fig. 9.

Fig. 10 shows the heat flux on the sting for the NS results and the corresponding experimental data for HEB Run 132 and LENS Case E. For HEG Run 132, the location of the local heat flux maximum on the sting is similar for both the experimental data and NS computations (between  $S/R_n$  values of 7 and 8). However, the magnitudes of the normalized heat flux differ by a factor of 3.4, and the actual heat fluxes differ by a factor of 5.4. In contrast, the LENS Case E computations and experiments show excellent agreement in the magnitude of the local heat flux

maximum on the sting, at approximately 6.5% of the stagnation point value (actual heat fluxes differ by approximately 26%). But, the experimental data indicate the maximum is farther down on the sting near an  $S/R_n$  of 10.5. Fig. 11 shows a combination of Figs. 5 and 10 on a single log plot. In this way, one can better see the global matching of the heat fluxes from computations and experiments. In some regions, the match appears reasonably visually, but due to the log nature of the plot, absolute errors are hard to read and the reader must refer to the original linear plots or numerical values.

One possible explanation for the disagreement in the LENS and HEG experiments is the existence of a turbulent shear layer in the HEG wake flow. As a quick investigation into this possibility, the computational viscosity was arbitrarily increased (as a crude model for turbulence) significantly in the wake region on a test run for the HEG Run 132 condition. The heat flux along the sting showed that a threefold increase before numerical instabilities near the rear corner where the sting mates with the blunt body forced the computation to stop. Though this is no definitive indicator of any answer to the differences in the experimental data, it certainly indicates that an investigation of the state of the shear layer could be a worthy avenue of pursuit both computationally and experimentally. Another recent study (Holden et al.<sup>37</sup>) also indicates that turbulence might be the cause for the differences in the experimental data between HEG Run 132 and LENS Case E. Studies are in progress to experimentally study the state of the shear layer in the wake behind this blunt body at NASA Langley Research Center in perfect gas nitrogen flows to help demonstrate the onset of turbulence in these wake flows<sup>32</sup>.

Another possibility for the differences in experimental data is that the flow in either or both experimental facilities may not be fully established in the wake. Measurements for both pressure and heat flux in LENS indicate that the flow has been established<sup>10</sup>, but Kastell et al.<sup>9</sup> and Horvath<sup>32</sup> have examined HEG heat flux data using the method of Holden et al.<sup>10</sup>, as well as their own method, giving ambiguous results on the existence of an established flow. If the flow indeed is unsteady, this could be from a lack of test time for flow establishment or the result of an inherent unsteadiness in the flow field. This kind of unsteadiness has been demonstrated computationally by Anagnost<sup>35</sup> using a 3D unsteady code for flow over a 70 degree blunt cone without a sting.

### 1.7. DSMC Wake Solutions

Although the high densities in front of the body preclude the use of a particle code in that region, the rapid expansion of the flow around the shoulder of the body drops the density significantly so that DSMC codes can be used. Previous simulations of the LENS Cases B and C, using DSMC codes, have shown that the code was spending most of the time calculating the flow field in front of the body<sup>2,4</sup>. There, the density rises up to 90 times the free-stream density. To simulate these high-density regions, most of the particles are concentrated in the compression region, while the rarefied wake area is left with only a few particles, thereby deteriorating the statistics of the simulation in this region.

On the other hand, the ability of the NS solvers to provide physically correct solutions in rapidly expanding low-density flows, such as the one behind the shoulder of the body, has been questioned. Recent studies into the breakdown of the continuum assumption<sup>37</sup> may be accelerated due

to numerical diffusion introduced by the continuum solver or due to non-equilibrium chemical relaxation phenomena. To address this problem and the problem of a more balanced distribution of the particles in this study, solutions have been sought that include the use of two different calculations for the wake and the forebody regions. The code to be used for the forebody is the aforementioned NEQ2D code<sup>11</sup>. The results of the NS solver for the forebody will be used to provide the input conditions for the DSMC code to calculate the flow in the wake. For the purposes of this study, the coupling of the two codes (NS to DSMC) was made along a straight line parallel to the vertical axis, starting from the shoulder of the body (where the normal to the surface is in the vertical direction). This coupling section has been used before by Moss et al.<sup>2</sup> for the same geometry. The DSMC code is started with the assumption of vacuum in the wake, while the input boundary is set to reproduce the conditions calculated by the NS code along the startline.

Two cases were calculated, the LENS Case E and HEG Run 132. The grid used for these calculations is shown in Figure 2b. It is multi-block structured grid with 18,000 cells, in which 300,000 particles were used. Experience has shown that the heat flux is a sensitive indicator of code convergence. When no significant changes in heat fluxes were seen in DSMC data samples, the solution was considered converged.

Fig. 12 presents the density profile (in  $\text{kg/m}^3$ ) for this case. The flow comes from left to right. The shock wave expands over the shoulder of the body into the wake region. The rapid expansion around the shoulder causes the density and the temperature to drop in the wake. The diffuse recompression wave (also seen in the NS re-



sults) that starts from the shoulder causes a localized density rise along the sting where the density rises to 70% of the free-stream density (60% in LENS Case E). The impact of the recompression wave on the sting is followed by an increase of the heat transfer and pressure in the same area. The angle of the compression from the sting is similar to the NS code results (approximately 15 degrees).

Fig. 13 shows particle traces for HEG Run 132. A single vortex is seen in the wake region. The smaller recirculation zones are not visible due to the low densities in that region, coupled with a low number of particles in these cells. Finer grid resolution, as well as more particles, would result in better statistics in these cells, and the more flow structure might be seen. The particle paths are seen to impact the body surface in the corner where the sting mates with the blunt body. This is also a direct consequence of the insufficient resolution of the DSMC computation in that region. The LENS Case E results show traces of a second vortex near the tip of the body. The grid resolution at the back of the body, though, did not allow a better representation of the flow.

Fig. 14 shows a Mach number contour for HEG Run 132 from the DSMC computations. Some similarities are seen in comparison to the NS results in Fig. 8, especially in the far field flow. Even with the lack of resolution in the corner, small pockets of supersonic flow are seen in the DSMC, as was also seen in the NS code results. Fig. 15 shows the normalized differences between the vibrational and translational-rotational temperatures  $((T_{t-r} - T_v)/T_{t-r})$  used in the DSMC work. This gives an indication of the non-equilibrium in the flow-field. Equilibrium (value of 0) is only met in the free-stream while most of the wake, and in particular, the recirculation area

behind the body are in thermal non-equilibrium. It is worth noting that equilibrium is hardly achieved along the sting of the body in the boundary layer. This non-equilibrium flow must be attributed to the cooling of the gas that impacts on the room temperature sting. This result is very similar to the NS code results seen in Fig. 9. However, the majority of the flow-field shows differences between the NS and DSMC work for the normalized vibrational temperatures. The DSMC results for both cases show no differences in the translational and rotational temperatures, validating the use of the two-temperature model in the NS code.

Figs. 10 and 11 present DSMC and NS surface heat fluxes in the wake region for the HEG Run 132 and LENS Case E experiments. The peak heat fluxes for both DSMC results occur with almost identical locations ( $S/R_n$  values of approximately 10.5) and normalized magnitudes (18% of the stagnation point value). But these computed normalized values are distinctly different from either experimental data set, and the actual magnitudes of the two DSMC peak heat fluxes differ by 30%. Also, the DSMC normalized heat flux for the HEG Run 132 is 18% below the experimental data point, but for LENS Case E, the DSMC normalized heat flux is a factor of 2.8 higher than the data. Thus the DSMC and NS codes are only partially successful in matching the experimental measurements of heat flux on the body in the wake.

### 1.8. Flow Visualization

An experimental interferogram for HEG Run 133 (a very similar condition to Run 132) has also been reported<sup>9</sup>. The NS output for the HEG Run 133 condition was used to generate a computational interferogram using the CISS (Constructing Interferograms, Schlieren, and Shadows-

graphs) code<sup>38</sup>. The experimental and computed interferograms can be seen in Fig. 16. The top portion of the figure is the experimental data, and the bottom portion is the mirror image of the computed result. The agreement is excellent, and fringe-shift measurements show the difference in the location of the bow shock in the forebody to be less than 10%.

### 1.9. Discussion

There are many similarities seen in the NS and DSMC wake flow computations for HEG Run 132 and LENS Case E. However, there are also many significant differences. It has been noted that the current DSMC work appears to have insufficient resolution and statistical representation of the flow in the near wake immediately behind the blunt body near the sting. However, we have no good indicators so far as to the quality of the NS computations, outside of their convergence criterion and the mesh-insensitivity of the results. An examination of the DSMA results using the Bird breakdown parameter can shed some light on the accuracy of the NS code in this application.

The Bird breakdown parameter,  $P$ , is defined as<sup>39</sup>

$$P = \frac{u}{\rho v} \left| \frac{dp}{ds} \right| = \frac{\lambda u}{\rho v_s} \left| \frac{dp}{ds} \right|$$

where  $u$  = velocity

• = density

• = collision frequency

$s$  = distance along a streamline

• = mean free path

$v_s$  = average molecular speed

In Bird's analysis, the onset of rarefaction effects was seen at 0.02, which is similar to the usual

critical Knudsen number (mean free path divided by a characteristic length) of 0.01. In a recent study by Gilmore and Gallis<sup>40</sup>, an entropy formulation of the onset of continuum breakdown in expanding flows indicated an even earlier onset than would be indicated by the parameter  $P$ . Fig. 17 shows a calculation of the  $P$  from the HEG Run 142 DSMC results. It is seen that near the shoulder of the body,  $P$  is in excess of 0.05. Even if the DSMC results have less than the desired statistical accuracy in the corner where the body and sting mate, one can conclude from this plot that near the separation point on the shoulder, the NS computation is being pushed beyond its limits. In this region, the DSMC has sufficient resolution and numbers of particles.

Even under conditions where the NS code may be exhibiting breakdown, there are strong similarities seen in some aspects of the NS and DSMC code computations (density, Mach contours particle paths, etc.). However, caution must be exercised in interpreting NS code results for these test conditions and those at lower densities, such as LENS Cases B and C. In addition of a slip boundary condition on the body might enable the NS codes to more accurately represent flow fields such as these and the other test cases that have been studied. Also, continued DSMC modeling efforts using finer grids in the near wake regions, and more particles overall will prove beneficial. This will surely require massively parallel computing machines or significant advances in computing architectures to achieve results quickly.

### 1.10. Conclusions

Improvements have been made in the NEQ2D code that have produced mesh-independent Navier-Stokes computational results for a 70-degree blunt cone model. The results for the

forebody region were significantly different from previous efforts by Stewart and Chen, who used an older version of the code. Both aforementioned forebody computations show a reasonable agreement with each other, but the current work shows a significant improvement in matching the shape of the normalized heat flux. However, there is a 23% difference in the stagnation point heat flux for the present work, in comparison with NASA Ames 41-inch shock tunnel data. Also the new results underpredict the forebody heat flux, which was the reverse of the previous work.

The Navier-Stokes code NEQ2D was also used to make comparisons with experimental data from the LENS and HEG shock tunnels for the sting-mounted AGARD 70-degree blunt cone model. Normalized computational heat fluxes showed reasonable agreement with the experimental data in the forebody. However, the dimensional computed heat flux values in the forebody showed a 37% difference at the stagnation point, compared to data from the HEG facility. Results for the LENS forebody heat flux data showed the same type of underprediction as in the case of the NASA Ames data. The Navier-Stokes code was also used to generate a computational interferogram for comparison to experimental results from HEG Run 133. The agreement for this comparison was excellent, and the location of the bow shock differed less than 10% with experiments.

Navier-Stokes computations were also presented for the wake region along the sting and compared to data from HEG and LENS. Here, the two sets of experimental heat flux data differed dramatically. The location of the computed heat flux maximum on the sting compared well with the HEG data, but the magnitude was underpredicted by almost a factor of 4. The reverse

was the case for the LENS data, where the magnitude of the computed heat flux matched the LENS data, but the experimental heat flux maximum was located further down the sting. One possible explanation for this difference could be the existence of a turbulent shear layer in the wake. The turbulent shear layer would increase the surface heat transfer due to increased mixing and would also affect the turning angle of the wake flow and the shear layer impingement point on the sting (location of local heating maximum).

The DSMC and Navier-Stokes computations showed many areas of agreement with each other, as well as areas where they differed significantly. Density and Mach number contours show reasonable global agreement with supersonic regions immediately behind the blunt body. Additionally, both codes predicted the main recirculation zone, but the Navier-Stokes codes showed two smaller recirculation zones, which did not appear in the HEG Run 132 case. However, traces of the small recirculation zone near the shoulder of the body did appear in the LENS Case E DSMC results. Thermal non-equilibrium was indicated by both codes along the sting near the blunt body, but the normalized vibrational temperatures differed significantly over most of the flow-field. The DSMC code exhibited a difficulty in accurately computing the flow in the corner where the sting meets the rear of the blunt body. The difficulty is due to insufficient grid resolution, and too few particles in cells for that region.

The DSMC heat flux result showed almost an opposite behavior in comparison to the Navier-Stokes computations. The magnitude of the DSMC heat fluxes for the HEG Run 132 case was only 18% below the experimental data. However, the DSMC heat flux for LENS Case E

was overpredicted by a factor of 2.8. Also, the location of the peak heating along the sting moved farther from the body compared to the Navier-Stokes results, showing a better correlation to the peak heating in the LENS Case E data. Both of these results are opposite from the Navier-stokes computational results.

The DSMC results also indicated that the degree of rarefaction is high enough in portions of the near-wake region, especially at the shoulder, near the separation point. The Bird breakdown parameter exceeds 0.6 at that point, well in excess of any commonly used indicator of breakdown in Navier-Stokes computations. Hence, care must be exercised in the interpretation of any Navier-Stokes code results for this application. Further work using slip boundary conditions for the Navier-Stokes code and more refined grids for the DSMA codes may give improved results. For the DSMC work, this will probably require massively parallel machines in order to achieve results in a reasonable amount of time.

Unsteadiness is another issue, which could affect the interpretation of the flow-field data and computations. There is some ambiguity in the analysis of the shock tunnel data, which makes it unclear whether the impulse facility flow has been established or not. Additionally, there is computational evidence to show that the three-dimensional wake flow is inherently unsteady. Issues of three-dimensionality, turbulence, and unsteadiness will all have to be addressed, both computationally and experimentally, before a complete understanding of the blunt body flow-field in impulse shock tunnel facilities is possible.

#### 4. PROGRESS IN OTHER REAL-GAS AREAS

In addition to the major blunt cone activities, a number of related topics have been pursued in

the real gas aerodynamic community. As closest to the blunt cone blunt side activity the work by Wen and Hornung<sup>42</sup> on the shock standoff distance off a sphere should be reported.

Wen and Hornung analyzed the standoff distance in terms of two similarity parameters, the free stream energy parameter

$$\mu = \frac{U_\infty^2 M}{\Theta_d \mathfrak{R}} \quad \text{and}$$

the reaction rate parameter

$$\Omega = \left( \frac{d\alpha}{dt} \right)_{sh} \frac{R_{Body}}{U_\infty}$$

Here  $U_\infty$  is the uniform free stream velocity,  $\Theta_d$  the characteristic temperature for dissociation of a diatomic gas,  $\mathfrak{R}$  the universal gas constant,  $M$  the molecular weight of the gas,  $\alpha$  the mass fraction of the atomic component of the gas and  $R_{Body}$  the radius of the sphere. The index sh refers to the value directly behind the shock wave.

The free stream energy parameter  $\mu$  determines whether the dissociation reaction in the flow has to be accounted for, and is essentially the same as the one used to characterize the HEG in its form  $h_0/h_{N_2}$  in many references about the HEG, e.g.<sup>18,25</sup>.

The reaction rate parameter,  $\Omega$ , is a measure of the deviation from equilibrium of the gas behind the shock.  $\Omega \rightarrow 0$  represents the frozen limit,  $\Omega \rightarrow \infty$  the equilibrium limit. Between these limits the gas between the shock and the blunt body is in chemical non-equilibrium.

A significant effect that results from chemical reactions in the flow is the change of gas density behind the bow shock wave. The shock wave standoff distance is inversely proportional to the average density on the stagnation streamline in the shock layer. While in the case of a non-reacting flow and an infinitely fast reacting flow the density along the stagnation streamline stays

approximately constant, for non-equilibrium flows this is not the case.

Figure 18, which has been taken from Wen and Hornung<sup>42</sup> shows a typical calculated plot for density profiles in the shock layer along stagnation streamlines for different values of the reaction rate parameter  $\Omega$ . The free-stream condition, and hence  $\mu$ , was kept constant here, while the body radius and hence  $\Omega$  was varied. Also, the influence of the boundary layer was neglected here. It can be seen that for the non-equilibrium case the density increases from the frozen value directly at the shock wave approximately linearly until it reaches the value at the body or the equilibrium value. In the above work this approximation was used to develop an analytical method which predicts the dimensionless shock wave standoff distance as a function of a reaction rate parameter. The result of the application of this analysis is shown in Fig. 19 for free-stream condition 1 in HEG in pure nitrogen, where the reaction rate parameter can be easily calculated and the blunt model used was a cylinder rather than a sphere. Although it has been shown that the analysis of the shock layer confirms that non-equilibrium effects are produced in the free piston driven shock tunnels, quantitative discrepancies between experiment and calculations remain just like in the blunt cone activities<sup>43</sup>.

## 5. SUMMARY

The objective of the real-gas element of the WG18 activity was to identify the status of our simulation capability of the hypervelocity flight environment of aerospace vehicles. Such capability will be necessary for the design optimization of future aerospace transportation systems for access to space and space exploration where

the requirements of reliability, reusability, performance, and cost are important considerations. Such missions will include, but are not limited to, future manned missions to Mars and a permanent presence of man in cis-lunar space. Additional applications will be found in unmanned applications where improved performance and cost benefits are important, such a repeated transportation of material in cis-lunar space or the transportation of large mass in the near solar system.

An attempt to identify current capability and shortcomings has been made, and an approach to address the shortcomings has been proposed. Specifically, current ground test simulation capability for hypervelocity flight in air has been described, and the corresponding capability of real-gas CFD simulation has been illustrated.

In our real-gas ground test facilities, there is a critical need to accurately describe the flow quality and to calibrate the facility in regards to reacting flow phenomena. Such a need is clearly manifested when one attempts to compare test results from one facility with another or when test results from a facility are used to verify, or to develop, CFD simulation tools. A critical element of the solution to this shortcoming is the development and application of state-of-the-art instrumentation and diagnostics.

Of course there are several limitations in our capability to simulate flight conditions with our current ground test facilities, particularly regarding physical scale, test time, and reproduction of actual flight environment, but these issues are discussed in another section of this report.

In the area of real-gas CFD all of the accomplishments and shortcomings of the perfect gas capability are apparent, including success and the lack thereof in the areas of turbulence and

transition and grid structure and resolution. Additional capability associated with real-gas phenomena indicates success in modeling reacting air in a compressive flow environment but shows less success where the flow is expanding and rarefaction, freezing, and non-equilibrium three-body atomic collision effects are important. Additionally, difficulties modeling turbulence and transition are compounded, and treatment of boundary conditions can require special attention. Also, unsteady phenomena in a real-gas environment are not adequately treated due to limitations in computing resources.

The recommended approach to developing an adequate simulation capability for hypervelocity flight is identified in the following critical steps:

1. Continue development of state-of-the-art instrumentation and diagnostics for high enthalpy real-gas flows in our ground facilities. Emphasis should be on non-intrusive optical diagnostics capable of accessing thermodynamic state of the gas and of providing quantitative data and qualitative imaging necessary in the description and understanding of the flow and for developing and verifying CFD models and tools.
2. Synergistic application and development of real-gas ground test and real-gas CFD is imperative! The CFD must be used in the definition of ground test experiments and in the interpretation of test results. Conversely, the ground test data must be used to verify the CFD models and simulation results. CFD simulations must include simulation of the flow environment produced in the ground test facility.
3. The approach illustrated with the WG18 blunt cone activity, in which a common model is tested in a variety of real-gas facili-

ties, with common instrumentation, is recommended whenever possible.

4. Maintain a steady development of CFD tools with emphasis on reacting flow model enhancement and verification for non-equilibrium conditions, particularly for expanding flows, and emphasis on improvement in numerical issues involving discretization errors and boundary condition. Issues with turbulence modeling and transition in high enthalpy compressible flows are not easily tractable and demand a sustained and focused program over the long term.
5. To finalize the development of simulation capability verification with flight data will be ultimately required. This requirement should be considered in developing ground test campaigns and in developing and applying CFD methods.

## 6. ACKNOWLEDGEMENTS

The contributions of Drs. L. Gochberg and G. Allen<sup>41</sup> comprise a large part of this work and are gratefully acknowledged.

## 7. REFERENCES

- 1 "Hypersonic Experimental and Computational Capability, Improvement and Validation", edited by Saric, W.S., Muylaert, J., and Dujarric, C., AGARD-AR-319 Vol. 1, May 1996.
- 2 Moss, J.N., Mitcheltree, R.A., Dogra, V.K., and Wilmouth, R.G., "Direct Simulation Monte Carlo and Navier-Stokes Simulations of Blunt Body Wake Flows", AIAA Journal, 32 (7) 1399-1406 (1994).
- 3 Allègre, J., and Bisch, D. "Experimental Study of a Blunted Cone at Rarefied Hyper-

- sonic Conditions", Laboratoire D'Aerothermique RC 94-7, Centre National de la Recherche Scientifique (1994).
- 4 Gallis, M.A. and Harvey, J.K., "Comparison of the Maximum Entropy DSMC Code with Flowfield Measurements", AIAA Paper 95-0413 (1995).
  - 5 Legge, H., "Heat Transfer and Forces on a Blunted 70 Degree Half Angle Cone Measured in Hypersonic Free Jet Flow", IB 222-93 A33, Institut für Experimentelle Strömungsmechanik, DLR, Göttingen (1994).
  - 6 Gilmore, M., "Test Case 6 – Rarefied Flow Over a Blunt Body", 4<sup>th</sup> European High Velocity Database Workshop ESTEC, Noordwijk, The Netherlands (1994).
  - 7 Pallegoix, J.-F., "Workshop ESTEC – Test Case No. 6 – Rarefied Spherically Blunted Cone", 4<sup>th</sup> European High Velocity Database Workshop ESTEC, Noordwijk, The Netherlands (1994).
  - 8 Hash, D.B., Hassan, H.A., Dogra, V.K., and Price, J.M., "Navier-Stokes Calculations for a Spherically Blunted Cone (LENS Condition)", 4<sup>th</sup> European High Velocity Database Workshop ESTEC, Noordwijk, The Netherlands (1994).
  - 9 Kastell, D., Horvath, T.J., and Eitelberg, G., "Non-equilibrium Flow Expansion Experiment Around a Blunted Cone", 4<sup>th</sup> European High Velocity Database Workshop ESTEC, Noordwijk, The Netherlands (1994).
  - 10 Holden, M., Kolly, J., and Chadwick, K., "Calibration Validation and Evaluation Studies in the LENS Facility", 33<sup>rd</sup> Aerospace Sciences Meeting, AIAA Paper 95-0291 (1995).
  - 11 Candler, G.V. and McCormack, R.W., "Computation of Weakly Ionized Hypersonic Flows in Thermochemical Non-equilibrium", Journal of Thermophysics and Heat Transfer, 5 (3) 226-273 (1991).
  - 12 Stewart, D.A., and Chen, Y.K., "Hypersonic Convection Heat Transfer over 140 Degree Blunt Cones in Different Gases", Journal of Spacecraft and Rockets, 31 (5) 735-743 (1994).
  - 13 Park, C., "Assessment of Two-temperature Kinetic Model for Ionizing Air", Journal of Thermophysics and Heat Transfer, 3 (3) 233-244 (1989).
  - 14 Chan, W.M., Chiu, I.-T., and Buning, P.G., "User's Manual for the HYPGEN Hyperbolic Grid Generator and the HGUI Graphical User Interface", NASA TM 108791 (October, 1993).
  - 15 Koura, K., and Matsumoto, H., "Variable Soft Sphere Molecular Model for Air Species", Physics of Fluids A, 4 (5) 1083-1085 (1991).
  - 16 Leving, R.D., and Bernstein, R.B., "Molecular Reaction Dynamics and Chemical Reactivity", Oxford University Press (1987).
  - 17 Loubsky, W.J., Hiers, R.S., and Stewart, D.A., "Performance of a Combustion-Driven Shock Tunnel with Application to the Tailored-Interface Operating Conditions", Proceedings of the 3<sup>rd</sup> Conference on Performance of High Temperature Systems, Paper 30, p. 547-559 (1964).

- 18 Eitelberg, G., McIntyre, T.J., Beck, W.H., and Lacey, J., "The High Enthalpy Shock Tunnel in Göttingen", AIAA Paper 92-3942 (July, 1992).
- 19 Holden, M.S., "Large Energy National Shock Tunnel (LENS) Description and Capabilities", CALSPAN-UB Research Center, Buffalo, NY (February 1991).
- 20 McIntosh, M.K., "Computer Program for the Numerical Calculation of Frozen and Equilibrium Conditions in Shock Tunnels", Department of Physics, Australian National University, Canberra (December, 1968).
- 21 Lordi, J.A., Mates, R.E. and Moselle, J.R., "Computer Program for the Numerical Solution of Non-equilibrium Expansions of Reacting Gas Mixtures", NASA CR-472 (May, 1966).
- 22 Radhakrishnan, K., and Bittker, A.D., "LSENS, A General Chemical Kinetics and Sensitivity Analysis Code for Gas-Phase Reactions: User's Guide", NASA TM-105851 (January, 1993).
- 23 Vardavas, I.M., "Modelling Reactive Gas Flows Within Shock Tunnels", Australian Journal of Physics, 37 (2) 157-177 (1984).
- 24 Hannemann, K., and Brenner, G., "Numerical Simulation of Reacting Flows Related to the HEG", Proceedings of the 19<sup>th</sup> International Symposium on Shock Waves, Marseilles (July, 1995).
- 25 Eitelberg, G., "First Results of Calibration and Use of the HEG", AIAA Paper 94-2525 (June, 1994).
- 26 McGrory, W.D., Slack, D.C., Applebaum, M.P., and Walters, R.W., "The General Aerodynamic Simulation Program", GASP Version 2.2, User's Manual, Aerosoft Inc. (1993).
- 27 Papadopoulos, P., Tokarcik-Polsky, S., Venkatapathy, E., and Deiwert, G.S., "The NASA Ames 16-Inch Shock Tunnel Nozzle Simulations and Experimental Comparison", AIAA Paper 95-6038, 6<sup>th</sup> International AIAA Aerospace Plane and Hypersonic Technologies Conference (April, 1995).
- 28 Kastell, D., private communication (1995).
- 29 Heirs, R.S. Jr., and Reller, J.O. Jr., "Analysis of Non-equilibrium Air Conditions in the Ames 1-Foot Shock Tunnel", NASA TN-D 4985 (1969).
- 30 Candler, G.V., private communication (1995).
- 31 Chen, Y.K., private communication (1995).
- 32 Horvath, T.J., private communication (1995).
- 33 Kidd, C.T., Nelson, C.G., and Scott, W.T., "Extraneous Thermocouple EMF Effects Resulting From the Press-Fit Installation of Coaxial Thermocouples in Metal Models", Proceedings of the ISA 40<sup>th</sup> International Instrumentation Symposium, Paper No. 94-1022, p. 317-335 (1994).
- 34 Legge, H., "Experiments on a 70 Degree Blunted Cone in Rarefied Hypersonic Wind Tunnel Flow", AIAA Paper 95-2140 (June, 1995).



- 35 Anagnost, A.J., "Time Accurate Simulation of Hypervelocity Base Flows on Massively Parallel Computers", Ph. D. Dissertation, Department of Aeronautics and Astronautics, Stanford University, SUDAAR 653 (1994).
- 36 Haas, B.L., "Mars Pathfinder Computations Including Base-Heating Prediction", AIAA Paper 95-2086 (June, 1995).
- 37 Holden, M.S., Chadwick, K.M., Gallis, M.A., and Harvey, J.K., "Comparison Between Shock Tunnel Measurements on a Planetary Probe Configuration and DSMC Predictions", Proceedings of the 20<sup>th</sup> International Symposium on Shock Waves, Pasadena (July 1993).
- 38 Yates, L.A., "Images Constructed From Computed Flowfields", AIAA Journal, 31 (10) 1877-1884 (1993).
- 39 Bird, G.A., Molecular Gas Dynamics and the Direct Simulation of Gas Flows", Clarendon Press, Oxford (1994).
- 40 Gilmore, M.R. and Gallis, M.A., "Breakdown of Continuum Solvers in Rapidly Expanding Flows", AIAA Paper 95-2134 (June 1995).
- 41 Gochberg, L.A., Allen, G.A. Jr., Gallis, M.A., and Deiwert, G.S., "Comparison of Computations and Experiments for Non-equilibrium Flow Expansions Around a Blunted Cone", AIAA Paper 96-0231 (January 1996).
- 42 Wen, C.-H., and Hornung, H., "Non-equilibrium Dissociating Flow Over Spheres", J Fluid Mech 199; 389-405 (1995).
- 43 Kastell, D., Carl, M., and Eitelberg, G. "Phase Step Holographic Interferometry Applied to Hypervelocity, Non-equilibrium Cylinder Flow", Experiments in Fluids 22; 67-66 (1996).

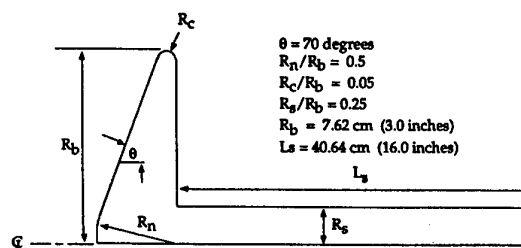


Fig. 1 Geometry for the 70° blunt cone test model

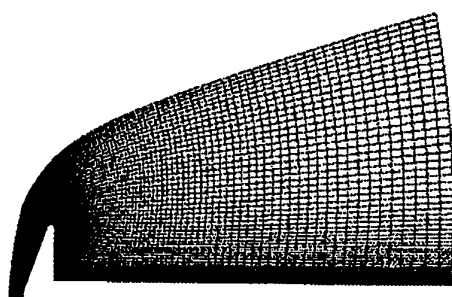


Fig. 2a Mesh from NS code simulation of blunt body flow

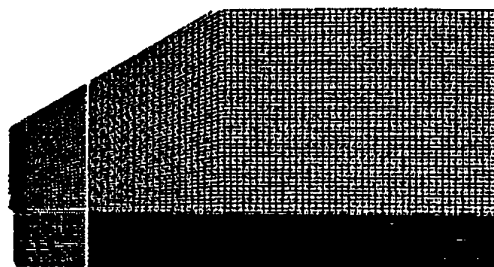


Fig. 2b Mesh used for DSMC code simulation of blunt body flow

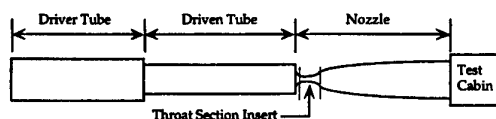


Fig. 3 Schematic of a generic shock tunnel facility (not to scale)

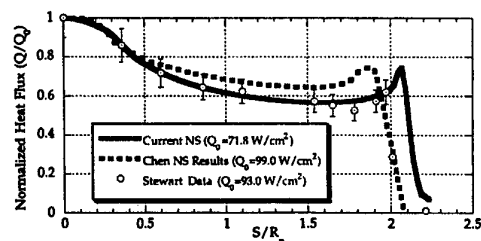


Fig. 4 Normalized forebody heat fluxes from NS computations, and Chen and Stewart data and computations

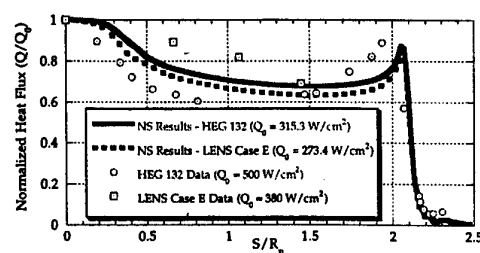


Fig. 5 Normalized forebody heat fluxes from NS computations, HEG run 132 data, and LENS case E data

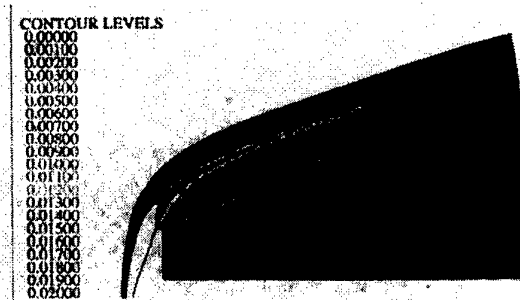


Fig. 6 HEG run 132 density contours from NS computations



Fig. 7 HEG run 132 particle paths from NS computations

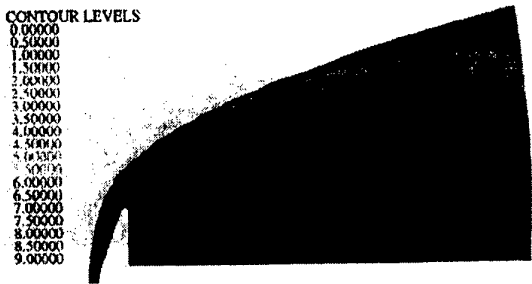


Fig. 8 HEG run 132 Mach number contours from NS computations

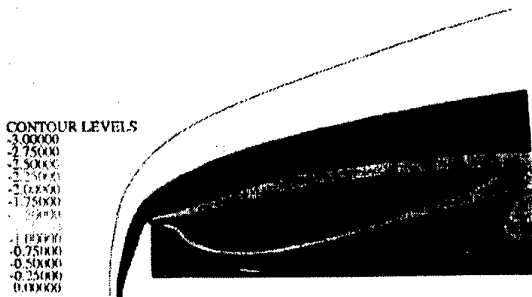


Fig. 9 HEG run 132 normalized vibrational temperature from NS computations

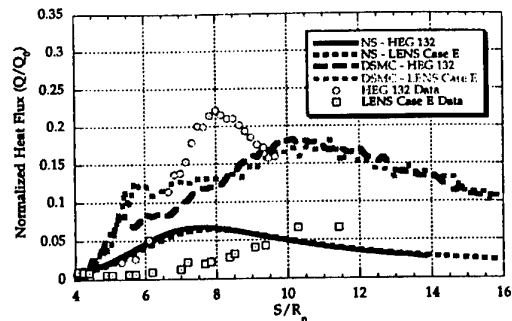


Fig. 10 Normalized heat fluxes from wake flow NS and DSMC computations compared to experimental data

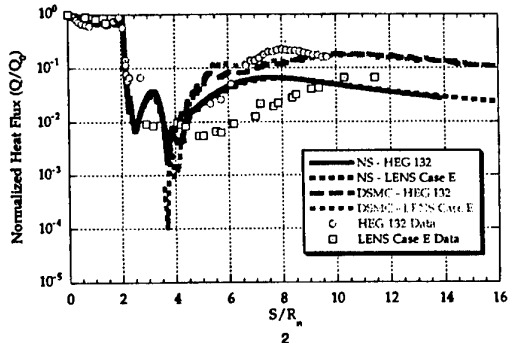


Fig. 11 Normalized heat fluxes from NS and DSMC computations compared to experimental data for entire flow field

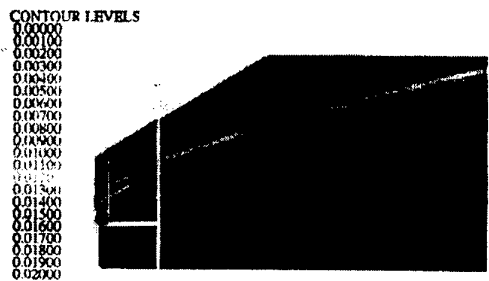


Fig. 12 HEG run 132 density contours from DSMC computations



Fig. 13 HEG run 132 particle paths from DSMC computations

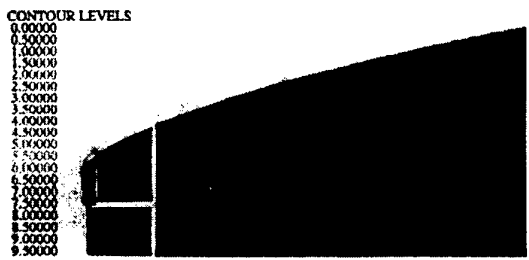


Fig. 14 HEG run 132 Mach number contours from DSMC computations

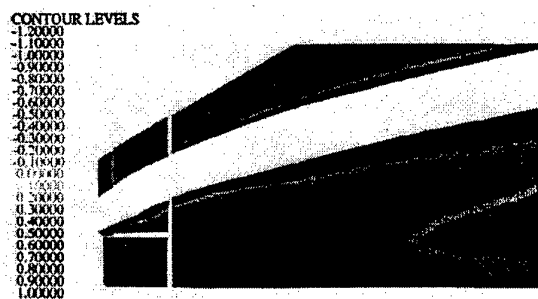


Fig. 15 HEG run 132 normalized vibrational temperature from DSMC computations

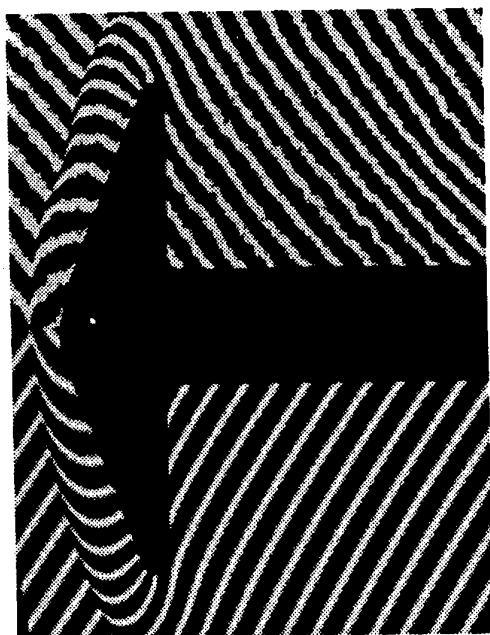


Fig. 16 Experimental and computational interferograms from HEG run 132

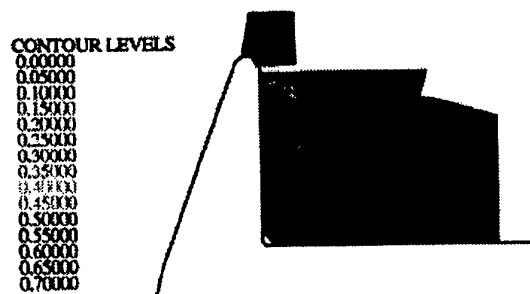


Fig. 17 Bird breakdown parameter from HEG run 132 DSMC computations

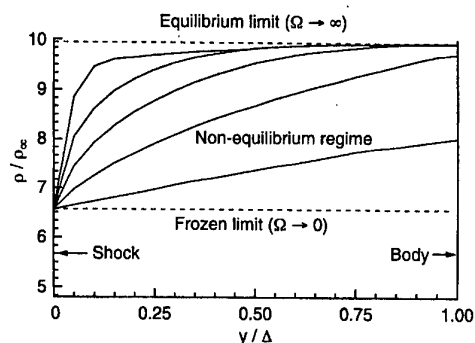


Fig. 18 Pilot of density profiles on stagnation streamlines of spheres for equilibrium, frozen and non-equilibrium flows. The five intermediate density profiles represent flow over spheres of five different radii of 0.025, 0.25, 1, 3 and 60 inch with the same free stream conditions ( $U_\infty = 5.2$  m/s,  $\rho_\infty = 0.043$  kg/m<sup>3</sup>,  $T_\infty = 2300$  K and  $\alpha_\infty = 0.0156$ ) (Wen and Hornung)<sup>42</sup>

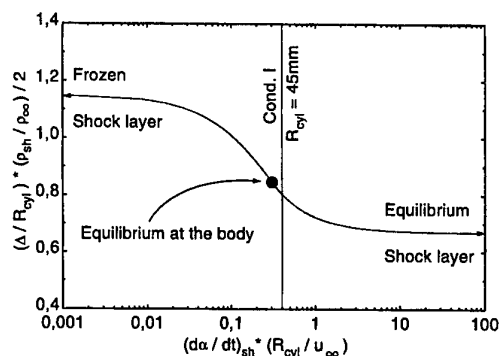


Fig. 19 Dimensionless shock wave standoff distance over reaction rate parameter obtain using Wen and Hornung's analytical method for pure nitrogen at HEG condition 1

# EXTRAPOLATION FROM WIND TUNNEL TO FLIGHT: SHUTTLE ORBITER AERODYNAMICS

J. Muylaert, L. Walpot - ESA-ESTEC, The Netherlands

P. Rostand, M. Rapuc - Dassault Aviation, France

G. Brauckmann, J. Paulson, D. Trockmorton, K. Weilmuenster -  
NASA LaRC, USA

## ABSTRACT

The paper reviews a combined numerical and experimental activity on the Shuttle Orbiter, first performed at NASA Langley within the Orbiter Experiment (OEX) and subsequently at ESA, as part of the AGARD FDP WG 18 activities. The study at Langley was undertaken to resolve the pitch up anomaly observed during the entry of the first flight of the Shuttle Orbiter. The present paper will focus on real gas effects on aerodynamics and not on heating. The facilities used at NASA Langley were the 15-in. Mach 6, the 20-in. Mach 6, the 31-in. Mach 10 and the 20-in. Mach 6 CF4 facility. The paper focuses on the high Mach, high altitude portion of the first entry of the Shuttle where the vehicle exhibited a nose-up pitching moment relative to pre-flight prediction of  $(\Delta C_m) = 0.03$ . In order to study the relative contribution of compressibility, viscous interaction and real gas effects on basic body pitching moment and flap efficiency, an experimental study was undertaken to examine the effects of Mach, Reynolds and ratio of specific heats at NASA. At high Mach, a decrease of gamma occurs in the shock layer due to high temperature effects. The primary effect of this lower specific heat ratio is a decrease of the pressure on the aft windward expansion surface of the Orbiter causing the nose-up pitching moment. Testing in the heavy gas, Mach 6 CF4 tunnel, gave a good simulation of high temperature effects.

The facilities used at ESA were the 1m Mach 10 at ONERA Modane, the 0.7 m hot shot F4 at ONERA Le Fauga and the 0.88 m piston driven shock tube HEG at DLR Goettingen. Encouraging good force measurements were obtained in the F4 facility on the Orbiter configuration. Testing of the same model in the perfect gas Mach 10 S4 Modane facility was performed so as to have "reference" conditions. When one compares the F4 and S4 test results, the data suggests that the Orbiter "pitch up" is due to real gas effects. In addition, pressure measurements, performed on the aft portion of the windward side of the Halis configuration in HEG and F4, confirm that the pitch up is mainly attributed to a reduction

of pressure due to a local decrease in gamma.

## 1 Introduction

During the high Mach number, high altitude segment of the first entry of the Space Shuttle Orbiter, with laminar, continuum flow over the windward surface, the vehicle exhibited a nose-up pitching-moment increment ( $\Delta C_m$ ) relative to pre-flight prediction of approximately 0.03. This caused the body-flap to deflect twice the amount thought necessary to achieve trimmed flight. This so-called "pitch-up anomaly" has been investigated over the years with explanations ranging from compressibility, to viscous, to real-gas (high temperature) effects on basic-body pitching moment and/or body-flap effectiveness. Compressibility and viscous effects, while affecting basic aerodynamics, also govern the behavior of flow separation ahead of deflected control surfaces. Low values of Reynolds number, such as occur in flight at high altitudes, may cause the flap to lose effectiveness by submerging it in a thick boundary layer such that the flap does not encounter the inviscid flow. In addition, high viscous shear of the cross flow in the nose region has been postulated as the mechanism to induce nose-up pitching moments. High-temperature effects occur when the free stream gas crosses the strong bow shock of the vehicle in hypersonic flight. The main consequences relative to perfect gas as far as aerodynamics are concerned are an increase in the shock density ratio, hence decrease in shock detachment distance and altering of the inviscid flow field, and a lowering of the flow field specific heat ratio.

In order to clarify and substantiate the causes of the flight-to-preflight discrepancies, a systematic study was undertaken to examine the effects of Mach number, Reynolds number, and real gas effects on basic-body pitching moment and body-flap effectiveness.

At NASA, two approaches were used by Brauckmann, Paulson, and Weilmuenster (1995). First, conventional hypersonic wind tunnels, all with instrumentation upgrades and most with new nozzles

that provide better flow uniformity, were used to examine the effects of Mach number and Reynolds number on configuration aerodynamics and control effectiveness. Effects due to specific-heat ratio were examined in the 20-Inch Mach 6  $CF_4$  tunnel, where testing in a heavy gas simulates the higher normal shock density ratio and lower specific heat ratio characteristic of that experienced in flight. Second, a Navier-Stokes computer code utilizing finite-rate chemistry was used to predict the flow field over the entire orbiter windward geometry, including the deflected body-flap, for both wind tunnel and flight conditions ((Weilmuenster, Gnoffo, and Greere 1993)). Comparisons are made between the present experimental results, computational predictions, the preflight aerodynamic data book released in 1980 and aerodynamic coefficients derived from the Space Shuttle Orbiter flights specially that of STS-1. The results of this study are expected to help define the optimum approach for the design of the next generation space transportation system.

At ESA, the orbiter model was used for a study by Perrier, Rapuc, P.Rostand, Sagnier, Verant, Eitelberg, Bogstad, and Muylaert (1996) on hypersonic wind tunnel to flight extrapolation. The objective of the study presented here is to investigate the extent to which the use of high enthalpy facilities can contribute to the validation of such a ground to flight extrapolation, and more specifically to the validation of "real gas effects". Such high enthalpy facilities, where both forces and heat fluxes can be measured, have been developed recently in Europe, and preliminary encouraging results have been obtained on simple shapes such as Electre model, which is a blunt cone and a hyperboloid flare ((Muylaert, Walpot, and Durand 1993)). A methodology to validate the ground to flight extrapolation of re-entry aircraft aerodynamics is proposed and implemented in the case of the Orbiter, based on the utilization of European high enthalpy facilities, and theoretical rebuilding of the flow fields in these facilities and in flight. It is shown that uncertainties on the real gas effect on aerodynamic forces, and in particular on pitching moment, could be reduced through this procedure.

## 2 Experimental methods

### 2.1 NASA Facilities

Three models were used for this study. Two were scale models of the full Shuttle Orbiter configuration, with scales of .004 and .0075. Body-flap deflections tested were 0.0, 12.5, and 16.3 deg for the smaller model and 0.0, 16.0, and 20.0 deg for the larger model. The third model was a .0075 scale modified Orbiter geometry, referred to as Halis,

which accurately represented the windward surface, including the body-flap, but used elliptical cross-sections to create the upper surface. All models were numerically machined from stainless steel. A verification check of the aerolines was performed prior to testing, and both larger models represented the shuttle windward surface aerolines within  $\pm .003$  in. Five blow-down hypersonic wind tunnels were used in this study. They were the 15-Inch Mach 6 Hi-Temperature Air Tunnel, 20-Inch Mach 6 Tunnel, 31-Inch Mach 10 Tunnel, 22-Inch Mach 20 Helium Tunnel, and the 20-Inch Mach 6  $CF_4$  Tunnel at NASA Langley. (See table 2)

All data are presented about a moment reference center of 65 % of reference body length.

### 2.2 European Facilities

In Europe, 2 Orbiter models and 3 hypersonic facilities were used for the present study as seen from table 2. The 3 facilities are the ONERA S4, The ONERA F4 and the DLR HEG.

The ONERA S4 facility is a Mach=10 perfect gas blow down tunnel. It is considered as the European reference perfect gas Mach 10 facility. It was decided to run it at its lowest Re number corresponding to a reservoir pressure of 25 Bar so as to avoid boundary layer transition in separated shear layers in front of deflected flaps.

The ONERA F4 hot shot, is a high enthalpy facility which enables force and moment measurements. The F4 facility covers enthalpy levels corresponding to the dissociation of oxygen. Typical reservoir conditions are 500 bar with 250 reduced enthalpy ( $Hi/RTo$ ,  $R = 288.2$  J/kg/K for air,  $To = 273.15$  K), i.e 19.7 MJ/kg. The lowest total conditions are about 200 Bar and  $Hi/RTo = 30$ . (i.e. 23.61 MJ/kg) High pressure and low enthalpy levels can also be obtained such as  $Pi = 750$  Bar and  $Hi/RTo = 30$ , (i.e. 23.61 MJ/kg). The test gas used is synthetic air or  $N_2$ .

The DLR HEG free piston driven shock tunnel allows both oxygen and nitrogen dissociation and presents higher enthalpy levels and Reynolds numbers than F4. Typical reservoir pressure conditions are 1000 Bar combined with a reservoir enthalpy which can vary between 10 MJ/kg up to 25 MJ/kg.

## 3 Computational Methods

The NASA results presented were obtained with the LAURA code (Langley Aerothermodynamic Upwind Relaxation Algorithm) ((Gnoffo 1990)) was used in this study to solve the thin-layer Navier-Stokes equations. The inviscid first-order flux is constructed us-

ing Roe's flux-difference-splitting ((Roe 1983)) and Harten's entropy fix with second-order corrections based on Yee's symmetric total variation diminishing scheme ((Harten 1983)). A seven species ( $N$ ,  $O$ ,  $N_2$ ,  $O_2$ ,  $NO$ ,  $NO^+$ , and  $e^-$ ) chemical reaction model is used for the non-equilibrium computations. The usual no-slip boundary conditions for viscous flow is applied at the wall while freestream conditions are set at points on the outer boundary of the computational domain. The exit plane is set such that the inviscid outer flow is supersonic. The computations presented account for a variable wall temperature. These values are based on the radiation equilibrium temperature at the wall, and were determined from computed heating rates. A catalytic wall boundary condition was used based on Scott's recombination rates for nitrogen and Zoby's rates for oxygen ((Scott 1981; Zoby, Gupta, and Simmons 1985)). A multi-block solution strategy is applied in two stages. The first stage may be regarded as a space marching solution, like the Parabolized Navier-Stokes (PNS) methods, except three-dimensional data blocks are employed rather than two-dimensional data planes. The second stage is a conventional, global relaxation which uses the first stage solution as an initial condition. The computational results presented herein are discussed further, and with more detail about the code and solution procedure in papers by (Weilmuenster, Gnoffo, and Greere 1993).

In Europe, Dassault Aviation used an Euler and boundary layer approach rather than a Navier Stokes approach, in order to perform a large number of simulations at a reasonable cost.

The Euler code used is the EUGENI code of Dassault Aviation, which solves the compressible fluid equations discretized on an unstructured mesh, for a perfect gas or a reacting mixture, either in equilibrium or in chemical or thermochemical non-equilibrium. Implicit time integration to the steady state is used; convergence requires 100 to 500 iterations, depending on cases and accuracy requirements. The solver is based on a Galerkin finite volume method, in which inviscid fluxes are upwinded using a generalized version of Osher's Riemann solver. Second order accuracy is achieved using the MUSCL method, extended to unstructured meshes.

The finite rate dissociation of air is modeled with 5 species ( $O_2$ ,  $O$ ,  $N_2$ ,  $N$  and  $NO$ ) and 34 reactions. The rates are taken from Park's model. The finite rate thermal relaxation is modeled with two vibrational temperatures and one translational and rotational temperature.

The boundary layer code used is the COUL code of Dassault Aviation, which is a package containing different boundary layer solvers, ranging in complexity from integral method based codes to finite difference

defect correction based ones, and able to take into account finite rate chemistry. The solver used here is the finite difference defect correction one, with finite rate chemistry and second order matching with the inviscid flow field (for velocity, temperature and concentrations).

## 4 NASA Results and Discussion

### 4.1 Ideal Gas Results at Mach 6 and 10 in Air

For the low-to-mid hypersonic Mach numbers the flight-to-preflight aerodynamic discrepancy is small. Post-flight analysis of heating data indicate that the orbiter windward surface boundary layer is everywhere turbulent. Experimental results at Mach 6 are presented showing the effect of Reynolds number on  $C_N$  and  $C_m$  for the baseline (zero control surface deflections) in Figures 1 and 2, respectively. The experimental data show only a slight effect of Reynolds number.  $C_N$  is decreased, and  $C_m$  is slightly nose-down with increasing Reynolds number; however, it should be noted that most of this is within the accuracy of the data, especially for the lower Reynolds numbers (and hence dynamic pressure). Results for a body-flap deflection of 16.0 deg are shown in Figures 3 and 4.  $C_N$  is approximately the same for all Reynolds numbers, indicating an increase relative to the baseline configuration. Pitching moment shows a marked nose-down increment with increasing Reynolds number, indicating a more effective body-flap as Reynolds number increases. The cause of these effects can be traced to changes in the location of boundary layer separation and re-attachment in front of and on the body flap. Surface-streamline patterns (oil flows) on the windward surface in the vicinity of the body-flap are shown in Figures 5 to 8. The model is at an angle of attack of 40 deg with a body-flap deflection of 16.0 deg. As Reynolds number increases, the separation region decreases. While the forward separation line moves rearward a small amount, the main effect is the forward motion of the re-attachment line on the flap itself. The separation is not as well defined at a length Reynolds number of  $1.6 \times 10^6$ ; the oil appearing somewhat smeared or "runny". Several repeat runs were made which verified this pattern. It is postulated that the flow is, or is near, transitional; at the next Reynolds number tested,  $Re_\infty = 3.2 \times 10^6$ , the flow overcomes the pressure gradient due to the deflected flap and remains attached on the whole lower surface, and the oil flow appears clear and sharp again. Similar aerodynamic and oil-flow results were observed at Mach 10. The data and oil flow photographs can be found in Brauckmann, Paulson, and Weilmuenster (1996). At  $M_\infty = 10$ , no limiting case

of flap effectiveness was obtained, as at  $M_\infty = 6$ , presumably due to insufficient Reynolds number variation to achieve transitional flow. Comparisons of the current  $M_\infty = 6$  and  $M_\infty = 10$  results to the preflight prediction (ADDB) and to STS-1 mission flight-derived data points are made in Figures 9 and 10. The highest Reynolds number experimental data are used. All data are interpolated at flight values of  $\alpha$ , referenced to a center-of-gravity location of 0.65L, and the flight derived data points have been adjusted to zero-control surface deflection using the ADDB effectiveness values. The agreement of the current values of  $C_N$  with the data book is very good. Both the current data and the preflight prediction overestimate the flight  $C_N$  by a slight amount. The agreement in pitching moment is not as good, especially at Mach 10. Values from the ADDB are in-between the current data and flight. The discrepancy between the current wind tunnel data and flight represents a movement in center of pressure location of 7.7 inches, or 0.6 % of the body length. It is probable that non-ideal gas effects are present. Also, recall that the flight data were corrected using ADDB control surface effectiveness values. Body-flap effectiveness,  $\Delta C_m$ , at  $M_\infty = 6$  and 10 is compared to the preflight prediction in Figure 11. Reynolds number plays a small role on basic-body pitching moment at these Mach numbers, primarily affecting body-flap effectiveness. As just shown, predicted body-flap effectiveness is bounded; i.e the current data at Mach=6 and 10 are in general less than ADDB. While not duplicating the preflight data book, the current tests are in line with the results. Conventional hypersonic wind tunnels (non-impulse) are therefore able to accurately describe the aerodynamics of this class of entry vehicles at these low to mid hypersonic Mach numbers. Proper determination of flight control surface effectiveness requires proper simulation of the state of the boundary layer (i.e. laminar, transitional, or turbulent).

## 5 Computational Predictions

Computational fluid dynamics (CFD) were used to examine differences between ideal gas and real-gas flow fields. Ideal gas flow fields can be duplicated in the wind tunnel, whereas in this study real-gas effects were only simulated. Solutions for the modified orbiter geometry corresponding to wind tunnel and flight conditions were obtained at angles of attack of 35, 40, 45 deg for body-flap deflections of 0, 5, 10, 15, and 20 deg. The data were interpolated for body-flap deflections of 16.0 and 16.3 deg, to compare with data presented from the wind tunnel tests. A more complete discussion of these results can be found in a paper by Weilmuenster ((Weilmuenster, Gnoffo, and Greere 1993)). The predictions were in good quali-

tative agreement, although the code over-predicted  $C_N$  by about 2.5 %. Differences in  $C_m$  amounted to 1 % error in center of pressure location. In order to examine the differences in the flow field that occur in flight, computations were carried out using finite-rate chemistry on the modified orbiter geometry at flight conditions. As shown in Figure 12, the occurrence of high temperatures associated with this flight condition dissociates the flow within the shock layer such that the ratio of specific heats,  $\gamma$ , defined here as  $h/e$ , is reduced from 1.4 in the freestream, to 1.3 immediately behind the shock to about 1.14 near the body. In the nose region,  $\gamma$  is reduced to about 1.12. The major effect of this change in  $\gamma$  is a lowering of the surface pressure on the last 20 % of the vehicle. A plot of computed center-line surface pressure for wind tunnel and flight conditions is given in Figure 13. Included are results from Weilmuenster, Gnoffo, and Greere (1993) a solution at a Mach number of 24 using an ideal gas value for  $\gamma$  of 1.4. There is a small difference due to Mach number alone, but the largest difference is due to the lower  $\gamma$ . The lower  $\gamma$  results in the expansion on the aft end occurring to a greater degree, lowering the pressure over a large area of the vehicle. It should be noted that the Orbiter geometry has a large influence on the magnitude of the real-gas effects. The Orbiter has an expansion that starts at approximately 0.8L, which coincides with the largest planform area, and thus the greater expansion of the flow, relative to ideal gas flow, lowers the pressure over a large area. The impact of this reduced pressure on the aerodynamic coefficients is shown in Figures 9 and 17. The lower pressure on the aft end causes a reduction in normal force and a nose up pitching-moment increment. The computed increment in  $C_N$  between tunnel and flight conditions is .062 and .048 for  $\delta_{BF} = 0.0$  deg and 16.3 deg, respectively. This agrees well with the delta found in flight,  $\Delta C_N = .059$  (preflight ADDB-to-flight, STS-1). The increment in  $C_m$  for  $\delta_{BF} = 0.0$  deg is 0.040, which is larger than the increment found between flight and pre-flight prediction. For the 16.3 deg flap case however, the delta is 0.028, which is very close to that found between the preflight ADDB and flight. The difference in the two increments can be traced to greater flap effectiveness at flight conditions. There are two reasons for the greater calculated flap effectiveness. The predicted separation region in front of and on the flap is smaller in flight than in the wind tunnel, for the same length Reynolds number. Calculated streamline patterns in the region of the body-flap at both tunnel and flight conditions for two flap deflections are shown in Figures 14 and 15. The much smaller separation region for flight conditions is evident. In addition, as discussed by Weilmuenster the pressure rise on the flap was higher in flight than in the wind tunnel, but this was due to a combination of Mach



and  $\gamma$  effects. In fact, the lower  $\gamma$  tends to reduce the pressure rise, but the higher Mach number in the shock layer in flight overcomes this. A solution at  $M_\infty = 24$  (flight) but with  $\gamma = 1.4$  (ideal gas) was not obtained on the deflected flap configuration, thus a separation of these effects cannot be made. An analysis of control-surface effectiveness was performed after the first few flights of the Shuttle Orbiter. Both an elevon and a body-flap pulse maneuver were analyzed in terms of center-of-pressure location for predicted and flight performance. While the results were biased from the perfect correlation line, the conclusion was reached that flap effectiveness, as presented in the preflight ADDB, was predicted correctly. More analysis of this discrepancy is needed.

## 6 High Mach Number Simulation

Two facilities at Langley were used to examine the high Mach number flight regime, the 22-Inch Mach 20 Helium Tunnel and the 20-Inch Mach 6  $CF_4$  Tunnel. The 22-Inch Helium Tunnel uses purified helium which behaves as an ideal gas with a  $\gamma$  of 1.667. There are a number of advantages to testing with helium, the primary one being that very high values of  $Re_L$  may be generated at high Mach numbers without having to heat the gas to prevent liquefaction. For this study, the facility provided a close match of flight Mach and Reynolds numbers. However, the flow field  $\gamma$  remained at  $\gamma = 1.667$ . The results from the helium tunnel tests showed a significant nose-down pitching moment compared to flight, which can be explained by  $\gamma$  being higher rather than lower than ideal air. In addition, body flap effectiveness was reduced. Thus, testing in helium is inappropriate for the simulation of real-gas effects. The  $CF_4$  tunnel uses a heavy gas which has a  $\gamma$  lower than ideal air to simulate this aspect of real-gas flows such as occurs in flight. The value of  $\gamma$  in the  $CF_4$  tunnel, around 1.15 in the shock layer, is close to that determined to occur in flight. A comparison of aerodynamic coefficients obtained in air and  $CF_4$  at identical values of Reynolds number and Mach number is given in Figures 18 and 19. As can be seen, testing in a heavy gas decreases the normal force coefficient and causes a nose-up pitch increment, when compared with results in air. At 40 degree of incidence, the decrease in  $C_N$  is 0.046 for  $\delta_{BF} = 0.0$  deg and .077 for  $\delta_{BF} = 16.3$  deg. This decrement is approximately the same as the flight decrement and that determined by the CFD analysis. The change in  $C_m$  is .029 for  $\delta_{BF} = 0.0$  deg and .027 for  $\delta_{BF} = 16.3$  deg. This increment is the same as the flight-to-preflight increment. The increment is the same for both the undeflected and deflected body-flap configurations as seen experimentally in figure

18. For this configuration then, with an expansion region on the windward surface, the real-gas effects are closely approximated by testing in a heavy gas such as  $CF_4$ .

## 7 ESA results and discussion

### 7.1 Methodology

The process of ground to flight extrapolation is the following :

1. Definition of reference conditions in perfect gas hypersonic facilities.
2. Reduction of aerodynamic uncertainties for these reference conditions through comparisons with results from different sources, both experimental and computational and analysis of all possible sources of errors ( shape inaccuracies in wind tunnel or CFD model, inadequate flow modeling, biased instrumentation.. ).
3. Transposition to flight : utilization of the same prediction method for the reference and flight conditions.
4. Analysis of the differences in terms of flow physics between wind tunnel and flight and derivation of the uncertainties in the process of transposition.
5. Establishment of the preflight uncertainties in the predictions for flight conditions, as the sum of the uncertainties for the reference conditions and those due to the transposition process.

The purpose here is to investigate to what extent the use of high enthalpy facilities can contribute to the validation of the real gas effects in this process of ground to flight extrapolation. The F4 and HEG facilities represent two intermediate steps between the S4 perfect gas conditions and the flight conditions, on which CFD results can be cross-checked in the process of extrapolation to flight.

The real gas effects which can be expected in each of these impulse facilities are presented in figures 21 and 22, in the form of dissociation level, equivalent  $\gamma$  and Damkholer number versus enthalpy, for flight and wind tunnel conditions, behind a normal shock wave (representing the stagnation point) and behind a 40 degree shock wave (representing the aft part of forebody) , assuming thermochemical equilibrium. The conditions are those following a typical Orbiter trajectory. Figure 20 shows the preflight to flight discrepancy for STS 5. The flight data is for the Orbiter flying at a trim condition, hence a zero pitching moment. The predicted results are those based

on the preflight aerodynamic database and for the flight aerodynamic control settings. It can be seen from figure 20 that the  $\gamma$  effect appears for relatively moderate enthalpies, corresponding to flight Mach numbers of about 10. Indeed the analysis of flight results shows that, when the Mach numbers increases, the pitch-up appears at Mach=10 and stabilizes at Mach=16. The two high enthalpy facilities are in the range of enthalpies representative of this *gamma* effect, and so should be quite representative of the pitch-up effect expected. This *gamma* effect, since it is a function of the derivative of the equation of state ( $C^2 = \partial P / \partial \rho$ ), appears as soon as deviation from perfect gas occurs, i.e. as soon as vibrational energy appears, which for oxygen is around 2000 K.

Equilibrium dissociation levels are also significant in the ground facilities for oxygen; however for nitrogen only HEG can give a limited dissociation, and only in the stagnation area. It must be recalled however that actual dissociation levels in the ground facilities could be much smaller due to the very low Damkohler numbers. This means that finite rate effects can be expected to be significantly different between ground and flight conditions.

The base line flight point chosen is the following:

STS-2, time: 75620s

Mach number: 24.3

Altitude: 72.3 km

Angle of attack: 39.40 degrees

Elevon deflection: 1.70 degrees

Body flap deflection: 14.90 degrees

Computations and wind tunnel tests are performed for the following configuration:

Angle of attack: 40 degrees

Elevon deflection: 0 degrees

Body flap deflection: 0 and 15 degrees

Corrections for the slightly different angle of attack and deflections are introduced in the comparisons.

For the purpose of analysis, the real gas effect is subdivided in three elements:

- the equilibrium chemistry effect, defined as the difference between results with equilibrium chemistry assumption and those with perfect gas,  $\gamma=1.4$  assumption.
- the effect of finite rate chemistry, defined as the difference between results with finite rate chemistry and those with equilibrium chemistry.
- the effect of finite rate thermal relaxation defined as the difference between results with finite rate chemistry and thermal relaxation and those with finite rate chemistry only.

For comparison between flight and ground facility results, the effect of Mach number must be defined also, as the difference between results obtained at flight and ground facility Mach numbers, using the perfect gas,  $\gamma=1.4$  assumption.

Computations have been performed with the corresponding modeling for the four conditions investigated here (S4 "blow down", F4 "hot shot", HEG "shock tube" and flight). The conditions are summarized in the table 2.

## 7.2 High Enthalpy Simulation

This chapter will cover both results from the numerical computations carried out on the Orbiter as well results from high enthalpy testing. The shape of both the Orbiter and Halis are described by CAD files provided by NASA. The geometry of the Orbiter includes accurate representations of all items except windshield and elevon gaps. The aircraft surface is represented with an unstructured triangular mesh made of 7000 nodes in the case of the Orbiter and 6000 in the case of Halis. The volume mesh is built by an advancing front method from the skin mesh, and is made of tetrahedras. Its unstructured nature facilitates the clustering of the mesh points in the shock layer. The volume mesh of the Orbiter contains 130000 nodes and that of Halis 113 000 nodes. In order to compute the flow field around models in high enthalpy facilities, it is necessary to first rebuild the flow in the facilities' nozzle, since complex phenomena are expected in these nozzles, and significant uncertainties exist in their prediction. The flow field is rebuilt using CFD, in which unknown parameters, such as transition point of the boundary layer, are tuned in order to match measurements made at the nozzle wall and exit. The computed nozzle exit plane is then used as inflow conditions for the computations of the flow around the model.

The computed pitching moment of the US Orbiter is represented in figures 23 to 26, and compared to experimental data. It is given for the flight center of gravity, angle of attack and elevon deflection, as defined in previous paragraph, and for 0 degrees and 15 body-flap deflection. Ground facility and flight conditions are referenced in these figures by total enthalpy, which is the primary parameter controlling the chemistry effects; however other parameters, such as pressure or Mach number also play a role, so that the data presented should not be interpreted as a direct pitch(enthalpy) function, but rather as a pitch(real gas effect) one, the scale for the real gas effect being qualitative. In figure 23 the pitching moment for the Orbiter with no flap deflection is presented for S4, F4 and flight conditions, from computations with four different gas models (perfect gas, equilibrium chemistry, finite rate chem-

istry, finite rate chemistry and thermal relaxation), and from experiment. In figure 24 the same data is presented collapsed to its S4 value, which is the reference point. The S4 computations were subtracted from the computations corresponding to higher enthalpy; the S4 experimental data were subtracted from those of F4. The difference between the S4 experiments and computations can be reduced by approximately half if special attention is given to grid refinements and base correction. In addition the force and moment measurements were performed on the "Orbiter model" whereas the computations on the HALIS configuration which contains a simplification of the leeward side. Consequently figure 24 illustrates best the transposition to flight of the pitching moment for the Orbiter with no flap deflection. It is seen that for flight conditions the major part of the real gas effect can be accounted for using equilibrium chemistry, finite rate chemistry effect being much smaller, and finite rate thermal relaxation playing no role. The effect shown for the F4 enthalpy conditions is essentially the same as for the flight conditions. At the F4 condition, the experimental results falls roughly midway between the calculated results assuming equilibrium and nonequilibrium. However, the equilibrium solution produces the big change with respect to the perfect gas solution as it did for the flight condition. Then the nonequilibrium calculation produces a significant but more modest correction to the equilibrium results. It is seen also that the computational and experimental results agree best on the S4 to F4 transposition if the flow is assumed to be in equilibrium.

In figures 24 to 26 the comparison of results for different conditions, and transposition to flight, are presented for the case with 15 degrees body flap deflection and for the body-flap efficiency, using the same method as for the 0 degree case. In figure 26, again, the same data as from figure 24 are shown but collapsed to its S4 value.

It must be recalled however that the computations have been performed with an Euler code, and that although a viscous correction, derived from previous studies ((Perrier, Rapuc, P.Rostand, Sagnier, Verant, Eitelberg, Bogstad, and Muylaert 1996)), has been introduced, the objective here is not to predict the control surface efficiency itself but the effect of air dissociation on this efficiency.

It is seen on figures 25 and 26 that the pitching moment for HEG conditions is lower than for F4 conditions, i.e. that the "real gas effect" on pitch in HEG is lower than in F4; this is somewhat surprising but could be explained by the evolution of the "equivalent  $\gamma$ " with enthalpy, figure 22, which is not monotonic. More numerical analysis is needed to understand why the calculated pitching moment for

HEG conditions are lower than those obtained in F4 conditions. Figure 26 shows the body flap efficiency defined as the ratio of the pitching moment difference between bodyflap 15 degree and 0 degrees with the corresponding difference as obtained in the reference S4 conditions. It can be seen that the flap efficiency is much higher in flight than in F4, suggesting that not just Reynolds but also  $\gamma$  and local Mach number play a role. In addition, the analysis need to be completed with a discussion of wall temperature effects on boundary layer development and resulting pitching moment. Indeed we should not forget that in high enthalpy short duration facilities like F4 and HEG, wall temperature are ambient temperature whereas in flight radiative equilibrium wall temperatures are obtained.

Pressure coefficient distribution along the windward centerline are presented in figure 28 for S4, F4 and HEG conditions and for the non deflected body-flap configuration. These distributions confirm the pitch up described in the previous chapter since one can notice between S4 and F4 a small pressure coefficient increase at the nose and larger decrease at the rear. Less difference are visible between S4 and HEG, indicating that the pitch up would be smaller.

The pressure distributions obtained for the four conditions investigated are presented in figures 29 to 32, and compared to experimental data in figures 33 to 35. The real gas effect is very local, and occurs mainly in the expansion and secondary compression areas, i.e. in front of the body flap and at the leading edges / corners of the fuselage and wing, so that only the pitching moment is significantly affected by the real gas effect (lift and drag changes are small).

## 7.3 Ground to flight transposition

### 7.3.1 Reference "cold" uncertainties

The rebuilding of the cold reference point is an important part of the ground to flight extrapolation process, as presented in the introduction. In order to reduce the uncertainties to a minimum, it is necessary, in the framework of a design study, to perform mesh refinement studies, and to compare the results coming from a large number of sources. Also all differences and inaccuracies in the shape must be tracked and accounted for.

Such a study, which is quite lengthy, has been performed for Hermes ((Perrier, Rapuc, P.Rostand, Sagnier, Verant, Eitelberg, Bogstad, and Muylaert 1996)); here our main effort is on the transposition process, and the uncertainties on the predictions for the reference point, although reasonable, could be further reduced: the discrepancy between CFD and experimental results in terms of pitching moment is equivalent to a 3 degree deflection of the body-flap;

on the body-flap efficiency it is 6 %; The wind tunnel results are in good agreement with the computations, in terms of pitching moment, so that the remaining discrepancies between CFD and experiment are due to insufficient gridding or more probably to small inaccuracies in the CFD shape.

### 7.3.2 Influence of real gas effects

For the flight point chosen the real gas effects can be decomposed in the following way ( 0 body flap deflection ):

- Effect of Mach number : + 0.0045
- Total real gas effect: 0.0332
  - Effect of equilibrium chemistry : + 0.038
  - Effect of finite rate chemistry : - 0.0055
  - Effect of finite rate thermal relaxation : + 0.0007

On the control surface efficiency, the real gas effect can be decomposed similarly (excluding coupling between chemistry and viscous interactions):

- Effect of Mach number : - 1%
- Total real gas effect: + 22%
  - Effect of equilibrium chemistry : + 26%
  - Effect of finite rate chemistry : - 4%

### 7.3.3 Assessment of uncertainties

The effect of equilibrium chemistry on pitching moment is of the same order of magnitude in F4 and flight conditions; also better agreement is obtained between CFD and experiment in F4 if equilibrium flow is assumed. The effect of finite rate chemistry and thermal relaxation is not validated at this stage. However in flight these elements only contribute to 15 % of the real gas effects; consequently the uncertainties they induce are quite small. In the present example , the dispersion on real gas effect on pitching moment between experimental results and CFD results obtained with equilibrium chemistry is 8 % for the case with no body flap deflection and 13 % for the case with 15 degree body flap deflection. ( This latter number includes dispersion due to approximate representation of viscous interactions) If the uncertainty of the effect of finite rate is taken arbitrarily to be 50 % , then the total uncertainty on the real gas effect can be estimated as follows in table 1. The total uncertainty is the sum of an 8 % ( 13 % for the case with 15 degree deflection) dispersion for equilibrium chemistry applied on the 115 % of the total real gas effect and a 50 % dispersion

Nature	Contribution to real gas effect, %	Intrinsic uncertainty, %	Contribution to global uncertainty
Equilibrium chemistry	115%	8%	9.2%
Finite rate	-15%	50%	7.5%
Total	100%		16.7%

Table 1: Total uncertainty on the real gas effect

applied on 15 % of the total real gas effect, and so is globally 17 % ( 22 % for the 15 degree body flap case).

The figures above for dispersion can be reduced through the use of Navier Stokes equations due to improved representation of viscous interaction effects.

The mentioned 17 % uncertainty on the orbiter pitching moment is equivalent to a 1.9 degree body flap deflection, which is coherent with a discrepancy between flight data and prediction equivalent to a 1.3 degree deflection.

## 8 SYNTHESIS AND CONCLUSION.

A study was undertaken at the NASA Langley Research Center to resolve the cause of the "pitch-up anomaly" observed during entry of the first flight of the Shuttle Orbiter. At high Mach flight conditions a reduction in specific heat ratio occurs due to high temperature effects. The primary effect of this lower specific heat ratio within the flow field of the Orbiter is lower pressures on the aft windward expansion surface of the Orbiter, relative to those deduced from hypersonic wind tunnel tests with ideal or near ideal gas test flows, and thus a corresponding nose-up pitching moment. Computationally, good agreement with the flight aerodynamic coefficients was obtained with the flap deflected to approximately 16 deg. Testing in a heavy gas in the 20-Inch Mach 6  $CF_4$  Tunnel gave a good simulation of high temperature effects as the aerodynamic increments and flap effectiveness were in good agreement with flight results. The overall agreement between flight, computational solutions at flight conditions (laminar boundary layer, continuum flow regime), and measurements made in the  $CF_4$  tunnel was quite good. This study has demonstrated a preferred approach to test high fidelity models in conventional facilities to provide base-line data for design; combined with the use of the heavy gas facility for the simulation of the high temperature effects. Complementary CFD to be used for substantiating these results as well as to provide information at flight conditions.

AT ESA, through Dassault Aviation, a procedure to validate ground to flight extrapolation of re-entry spacecraft aerodynamics has been proposed and im-

plemented in the case of the Orbiter, using European high enthalpy facilities. Encouraging results have been obtained for force coefficients, leading to a possible method to significantly reduce the uncertainties in the transposition to flight and in particular the uncertainties associated with real gas effects.

*Aeroassisted Orbital Transfer Vehicles* 96, 445-465.

## REFERENCES

- Brauckmann, G., J. Paulson, and K. Weilmuenster (1995, September). Experimental and computational analysis of the space shuttle orbiter hypersonic pitch-up anomaly. *AIAA Journal of Spacecraft and Rockets* 32(5), 758-764.
- Brauckmann, G., J. Paulson, and K. Weilmuenster (1996, January). Experimental and computational analysis of the space shuttle orbiter hypersonic 'pitch-up anomaly'. In *AIAA Conference*, Reno, USA. AIAA paper 94-0632.
- Gnoffo, P. (1990). An upwind point implicit relaxation algorithm for viscous compressible perfect-gas flows. Technical Report TP 2953, NASA.
- Harten, A. (1983). High resolution schemes for hyperbolic conservation laws. *Journal of Computational Physics* 49, 357-393.
- Muylaert, J., L. Walpot, and G. Durand (1993, 6-9 July). Computational analysis on generic forms in european hypersonic facilities: standard model Electre and hyperboloid flare. In *19th International Symposium on Shock Waves (ISSW19)*, Marseille.
- Perrier, P., M. Rapuc, P. Rostand, P. Sagnier, J. Verant, G. Eitelberg, M. Bogstad, and J. Muylaert (1996, June). Ground to flight extrapolation of reentry aircraft aerodynamics: an experimental and computational approach. In *AIAA 14th Applied Aerodynamics Conference*, New Orleans, USA. AIAA paper 96-2434.
- Roe, P. (1983). Approximate Riemann solvers, parameters vectors and difference schemes. In *Journal of Computational Physics*, Volume 43, pp. 357-372.
- Scott, C. (1981). Catalytic recombination of oxygen and nitrogen in high temperatures surface insulation. *Aerothermodynamics and Planetary Entry*. 77, 192-212.
- Weilmuenster, K., A. Gnoffo, and A. Greere (1993, 6-9 July). Navier-stokes simulations of the shuttle orbiter aerodynamic characteristics with emphasis on pitch trim and body flap. In *AIAA 28th Thermophysics Conference*, Orlando, FL.
- Zoby, E., R. Gupta, and A. Simmons (1985). Temperature dependant reaction rate expressions for oxygen recombination. *Thermal Design of*

TUNNEL	Mach no.	Scale	$Re_{\infty,L}, 10^6$	$\gamma_{\infty}$	Pt (Psia)	Tt( $^{\circ}F$ )
15-in. Mach 6	6.0	0.004	0.2	1.4	45	780
			1.7		240	470
20-in. Mach 6	6.0	0.0075	0.4	1.4	30	400
			0.8		60	425
			1.6		125	450
			3.2		250	475
			6.1		475	475
31-in. Mach 10	10.0	0.0075	0.4	1.4	350	1350
			0.9		720	1350
			1.8		1450	1350
20-in. Mach 6 $CF_4$	6.0	0.004	0.2	1.22	1600	800

Table 2: NASA LaRC facilities for Orbiter testing

FACILITIES	ONERA S4 MA	ONERA F4	DLR HEG	FLIGHT
TYPE	BLOW DOWN	HOT SHOT	SHOCK TUBE	
MODEL SCALE	1/90	1/90	1/90	1/1
MACH NUMBER	10	8	10	24
Hi/RT	14	160	280	330
Res.PRESSURE(bar)	25	280	450	
ALTITUDE(km)				72
REYNOLDS( $10^{-5}$ )	6.	0.3	1.2	10
PL/V $10^6$	3.6	0.044	0.12	0.28
MEASUREMENTS	FORCES	FORCES		
	PRESSURE	PRESSURE	PRESSURE	
	HEAT FLUX	HEAT FLUX	HEAT FLUX	

Table 3: ESA facilities for Orbiter testing

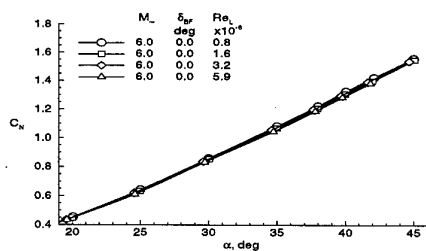


Figure 1: Effect of Re-number on Shuttle Orbiter on  $C_N$  for body flap 0 degrees

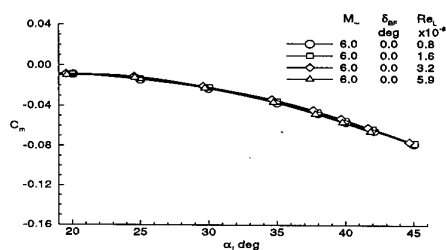


Figure 2: Effect of Re-number on Shuttle Orbiter on  $C_m$  for body flap 0 degrees

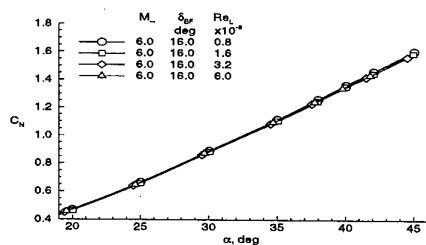


Figure 3: Effect of Re-number on Shuttle Orbiter on  $C_N$  for body flap 16 degrees

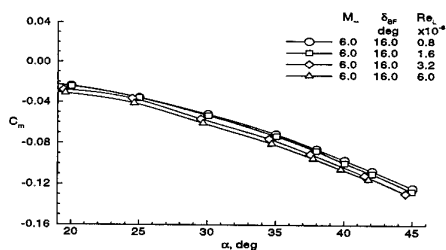


Figure 4: Effect of Re-number on Shuttle Orbiter on  $C_m$  for body flap 16 degrees

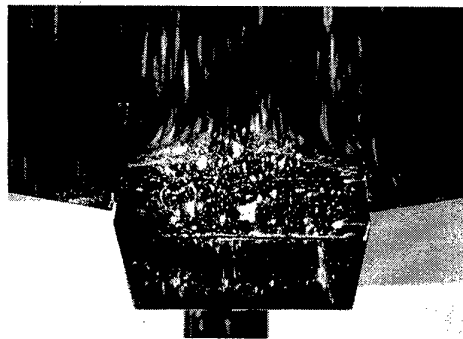


Figure 5: Oil flow for  $Re_L = 0.4 \times 10^6$

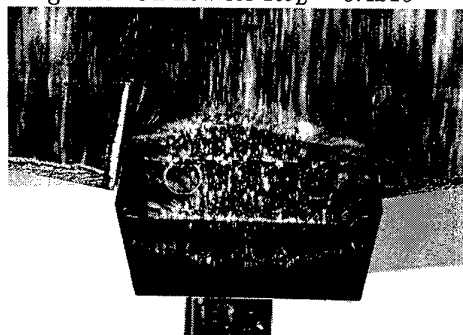


Figure 6: Oil flow for  $Re_L = 0.8 \times 10^6$

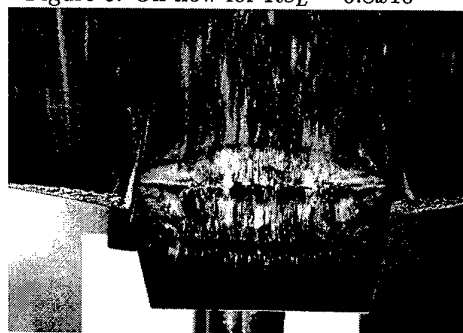


Figure 7: Oil flow for  $Re_L = 1.6 \times 10^6$

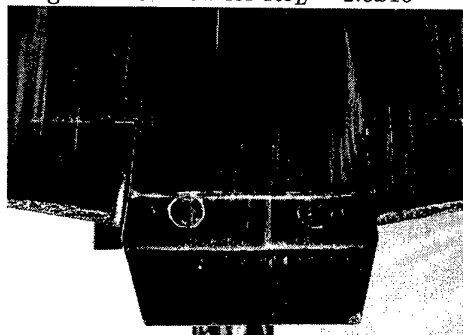


Figure 8: Oil flow for  $Re_L = 3.2 \times 10^6$

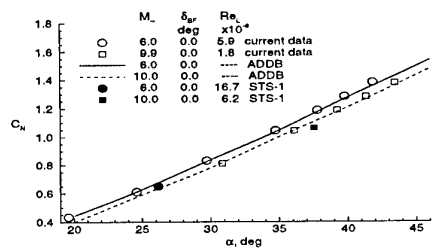


Figure 9: Comparison of  $C_N$  for current experimental data with ADDB and flight

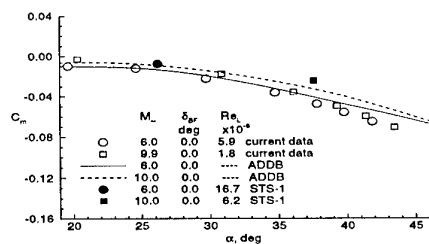


Figure 10: Comparison of  $C_m$  for current experimental data with ADDB and flight

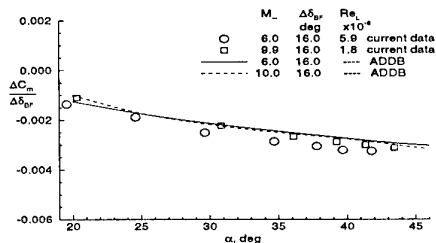


Figure 11: Comparison of flap efficiency for current experimental data with ADDB and flight

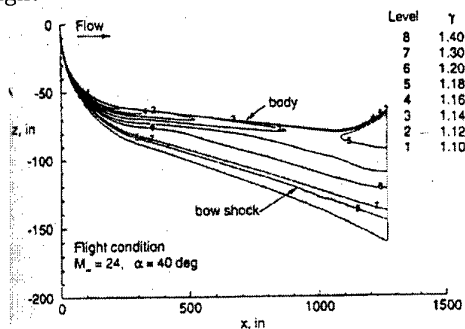


Figure 12: Computed variation of  $\gamma$  in windward flow field of modified Orbiter

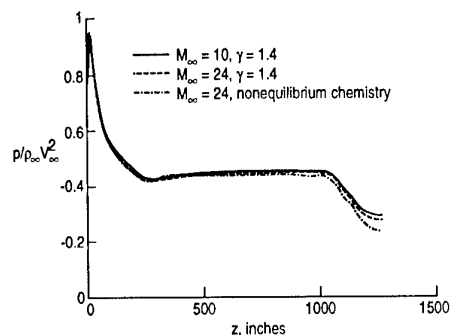


Figure 13: Computed centerline surface pressure for modified Orbiter,  $\alpha = 40^\circ$

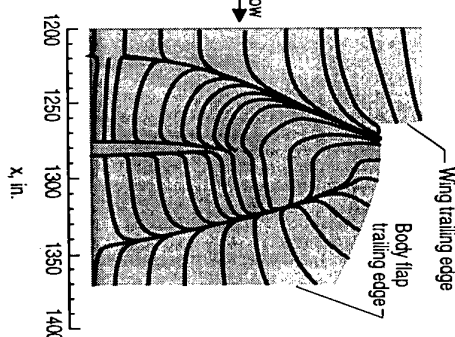


Figure 14: Calculated surface streamline patterns in vicinity of body flap at wind tunnel conditions

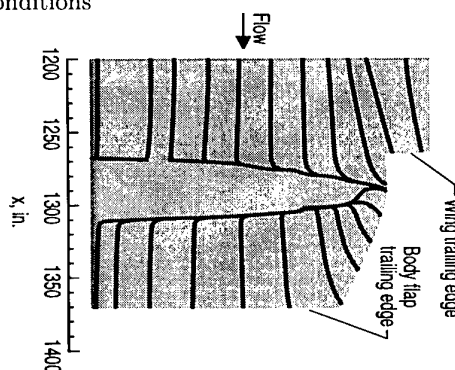


Figure 15: Calculated surface streamline patterns in vicinity of body flap at flight conditions

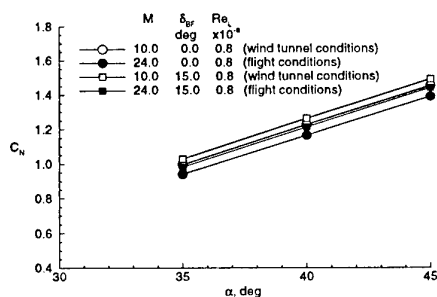


Figure 16: Comparison of computed modified Orbiter  $C_N$  at wind tunnel and flight conditions



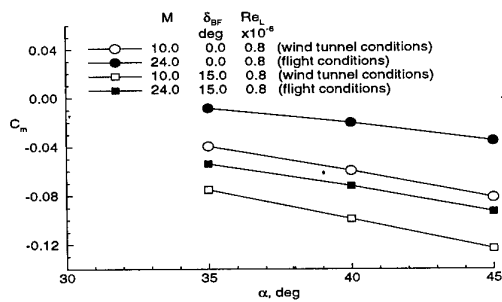


Figure 17: Comparison of computed modified Orbiter  $C_m$  at wind tunnel and flight conditions

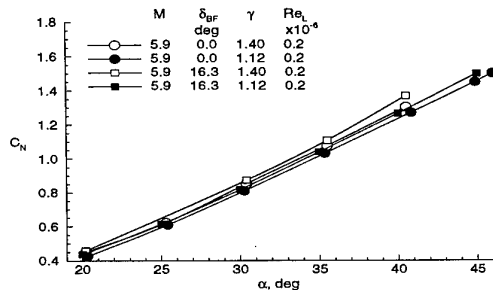


Figure 18: Comparison of Shuttle Orbiter aerodynamics in air and  $CF_4$

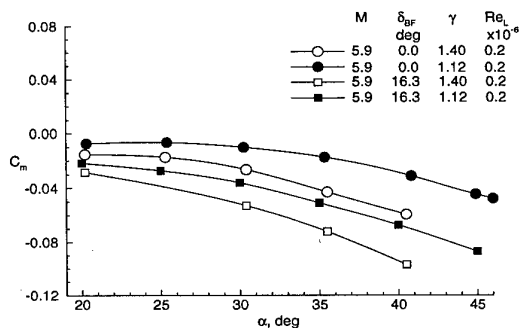


Figure 19: Comparison of Shuttle Orbiter aerodynamics in air and  $CF_4$ : wind tunnel data

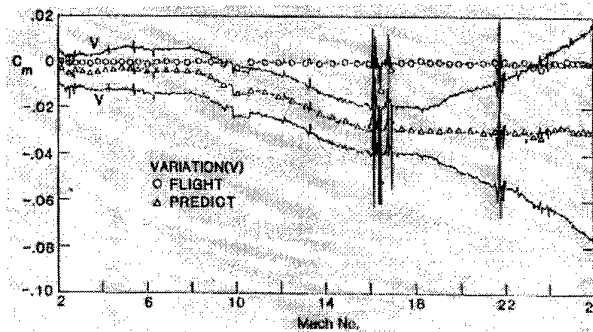


Figure 20: Pre-flight to flight discrepancy for STS-5

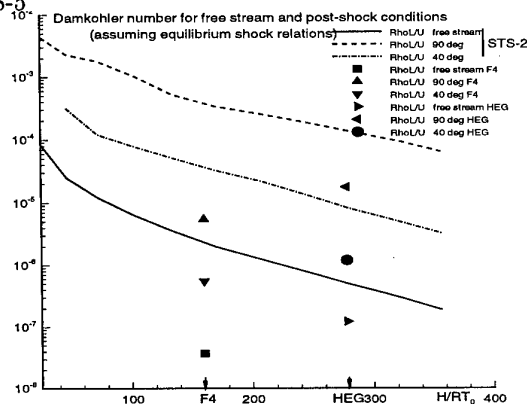


Figure 21: Damkohler number in terms of  $\rho L/V$  for free stream and post-shock conditions assuming equilibrium flow, plotted versus reduced enthalpy following STS2 trajectory or for F4, HEG wind tunnel conditions.

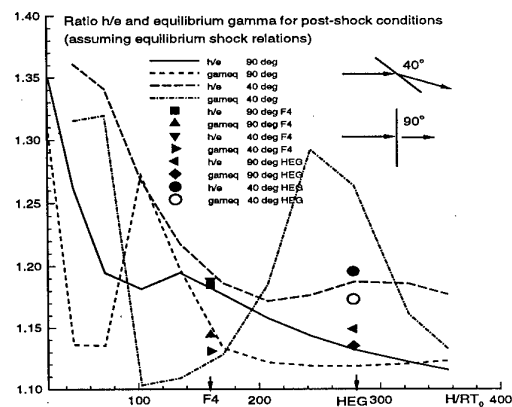


Figure 22: Equivalent  $\gamma$ 's behind a 40 or 90 degree shock wave assuming equilibrium flow, plotted versus reduced enthalpy following STS2 trajectory or for F4, HEG wind tunnel conditions.

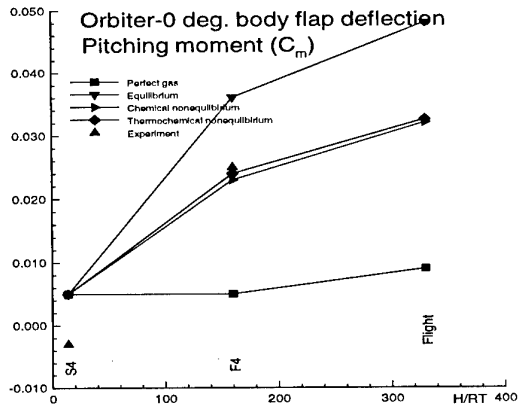


Figure 23: Pitching moment of the Shuttle Orbiter with 0 degrees body flap deflection;  $C_m$  pitching moment versus reduced enthalpy.

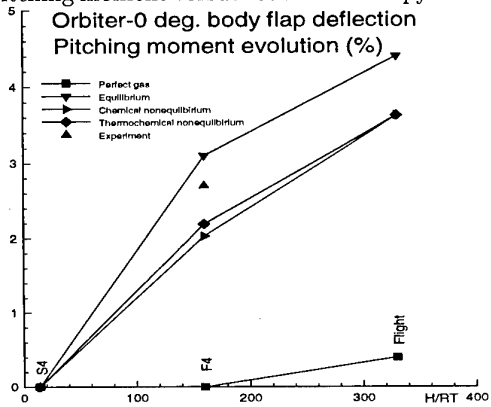


Figure 24: Pitching moment evolution of the Shuttle Orbiter with 0 degrees body flap deflection; % pitching moment referenced to S4 results.

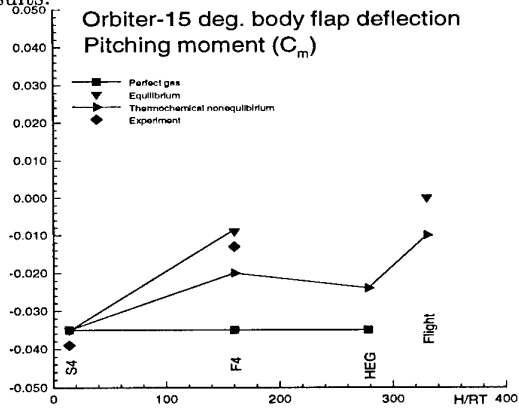


Figure 25: Pitching moment of the Shuttle Orbiter with 15 degrees body flap deflection;  $C_m$  pitching moment versus reduced enthalpy.

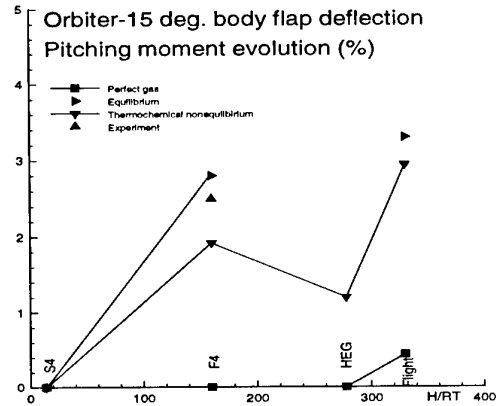


Figure 26: Pitching moment evolution of the Shuttle Orbiter with 15 degrees body flap deflection; % pitching moment referenced to S4 results.

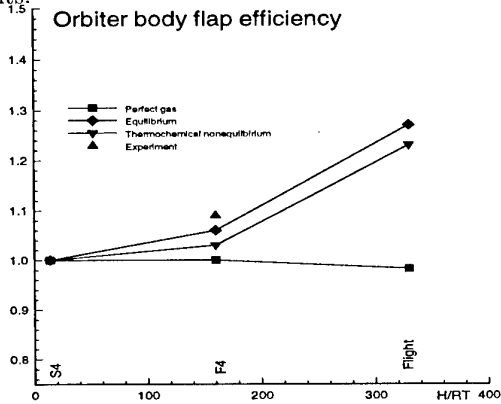


Figure 27: Flap efficiency of the Shuttle Orbiter.

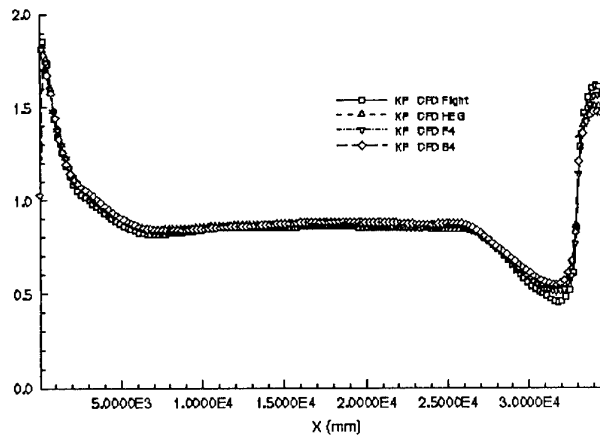


Figure 28: Centerline pressure coefficient distribution on HALIS.

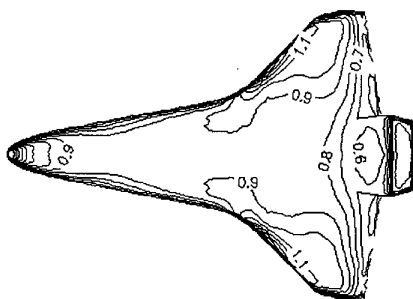


Figure 29: Pressure coefficient distribution for S4 conditions.

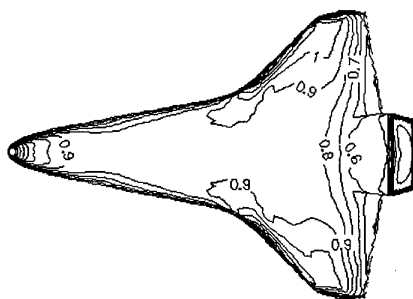


Figure 30: Pressure coefficient distribution for F4 conditions.

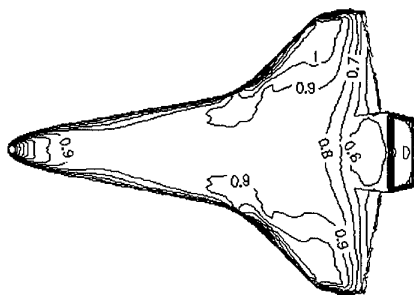


Figure 31: Pressure coefficient distribution for HEG conditions.

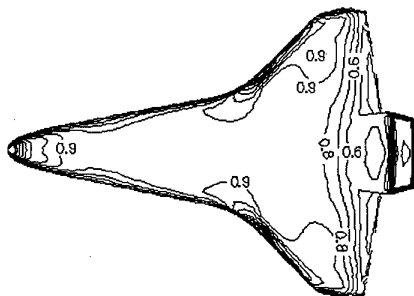


Figure 32: Pressure coefficient distribution for flight conditions.

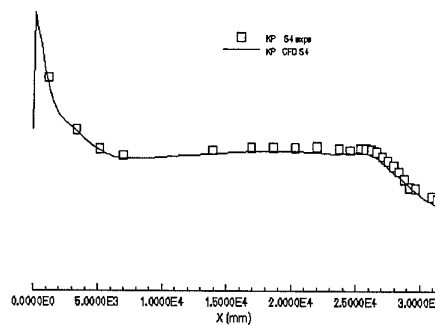


Figure 33: Pressure distribution on the symmetry line of HALIS, compared to experimental data, at S4 conditions.

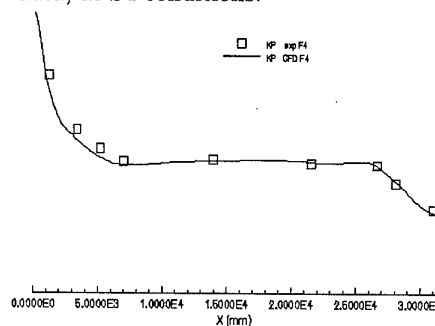


Figure 34: Pressure distribution on the symmetry line of HALIS, compared to experimental data, at F4 conditions.

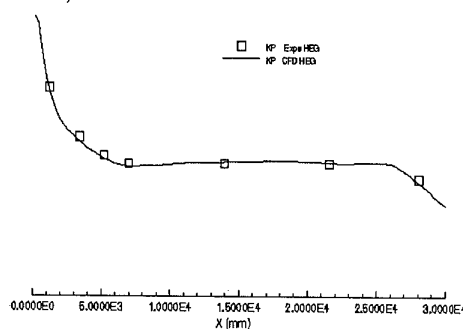


Figure 35: Pressure distribution on the symmetry line of HALIS, compared to experimental data, at HEG conditions.



# REAL-GAS AEROTHERMODYNAMICS TEST FACILITIES

**James O. Arnold**

Space Technology Division  
MS: 229-3  
NASA Ames Research Center  
Moffett Field, California 94035-1000  
USA

**George L. Seibert**

Wright Laboratory  
WL/FIMD Bldg. 246  
2145 5th St., Suite 1  
Wright-Patterson AFB, OH 45433-7005  
USA

and

**John F. Wendt**

von Kármán Institute  
Chaussée de Waterloo 72  
B-1640 Rhode Saint Genèse  
BELGIUM

## CONTENTS

1	INTRODUCTION	1xx	7	FUTURE FACILITY NEEDS AND FACILITIES UNDER DEVELOPMENT	1xx
2	MISSION NEEDS	1xx	7.1	Results of U.S. Studies	1xx
3	MODERN APPROACH TO AEROTHERMODYNAMICS	1xx	7.2	Results of European Studies	1xx
4	EXISTING FACILITIES	1xx	8	RECOMMENDATIONS ON POSSIBLE AREAS OF COOPERATION AND POTENTIAL BENEFITS	1xx
4.1	U.S. Facilities	1xx	9	SUMMARY	1xx
4.2	European Facilities	1xx		ACKNOWLEDGMENTS	1xx
4.3	Russian Facilities	1xx		REFERENCES	1xx
5	ASSESSMENT OF FACILITIES	1xx		APPENDIX	1xx
5.1	LENS			FIGURES	1xx
5.2	GALCIT T5 Facility		1	INTRODUCTION	
5.3	HEG Facility			This chapter provides an overview of the current ground-based aerothermodynamic testing capabilities in Western Europe and the United States. The focus is on facilities capable of producing real-gas effects (dissociation, ionization, and thermochemical nonequilibrium) pertinent to the study of atmospheric flight in the Mach number range of $5 < M < 50$ . Perceived mission needs of interest to	
5.4	F4 ONERA				
6	ASSESSMENT OF INSTRUMENTATION	1xx			
6.1	Requirements				
6.2	Status				

the Americans and Western Europeans are described where such real-gas flows are important.

The role of Computational Fluid Dynamics (CFD) in modern ground testing is discussed, and the capabilities of selected American and European real-gas facilities are described. An update on the current instrumentation in aerothermodynamic testing is also outlined.

Comments are made regarding the use of new facilities which have been brought on line during the past 3-5 years. Finally, future needs for aerothermodynamic testing, including instrumentation, are discussed and recommendations for implementation are reported.

## 2 MISSION NEEDS

Figure 1 (adopted from Howe 1990) is an altitude-velocity map of past missions and representative missions of future interest to the aerothermodynamics community in the United States and Western Europe. For reference, the reentry corridor of the Space Shuttle Orbiter is depicted by the line labeled Space Transportation System (STS). The black dot on the curve represents the peak heating point for the STS trajectory as do those for other trajectories to be discussed below. The higher-density ascent flight envelope for the National Aerospace Plane (NASP) type scramjet-propelled vehicle is shown by the shaded bar. Both trajectories asymptote at speeds of about 6.7 km/s to meet their mission objectives of access to Low Earth Orbit (LEO).

The Apollo lunar-return trajectory is also shown for reference in Figure 1 with its entry speed of 11 km/s. This trajectory involved landing and is called a "direct" entry as contrasted to aerocapture type maneuvers to be discussed below. The NASP Program was canceled, and American efforts to replace the Space Shuttle are now embodied in the Reusable Launch Vehicle X-33 and X-34 programs. Missions of interest to the American community involving space beyond Low Earth Orbit include new return missions into the Earth's atmosphere from the Moon, Mars, and comets. In some cases, aerocapture maneuvers will be used to decelerate vehicles by dipping into the atmosphere and exiting the atmosphere into a prescribed, lower energy orbit. The flight envelope for the aerocapture maneuver for return from bodies other than the Moon are not shown. They are similar to the lunar-return case except with higher entry speeds. Also plotted in Figure 1 is the aerocapture trajectory that was planned for the canceled American Aeroassist Flight Experiment which was to have been launched from the Shuttle Orbiter. Future piloted Mars missions must account for abort scenarios with entry speeds of up to 15 km/s as depicted by the Mars abort trajectory with a direct entry to the Earth's surface.

The Magellan spacecraft used aerobraking (Haas and Schmitt 1993) to circularize its orbit about Venus by making many high-altitude "dips" in the atmosphere. While this mission did not exhibit aerobraking where significant aeroheating occurred, it does illustrate the viability of such maneuvers.

Additional missions of interest to the Americans include a 1997 planetary entry into the atmosphere of Mars by the Mars/Pathfinder probe vehicle which is a precursor to the landing of a network of surface stations in a proposed new program called Micromet. A new Discovery class mission

called Stardust will collect ejecta at a distance of 60 miles from Comet Wild-2 in 2003 and return to the Earth's atmosphere at 13.5 Km/sec in 2006. Entry technology will be involved in numerous U.S. missions in the coming decade.

Huygens-Cassini, a joint European-American program, will send a sampling probe into the atmosphere of Titan, one of Saturn's moons. This will entail an entry speed of about 6 km/s.

Figure 1 indicates regions of important real-gas flow phenomenon which must be adequately accounted for at increasing speeds. Boundaries are shown in the figure where dissociation of  $O_2$  and  $N_2$  occur and where ionization effects become important. These boundaries are for normal shock/stagnation regions of the flow. At altitudes below about 45 km, flow simulations can be made assuming equilibrium thermochemistry on moderately sized blunt bodies within the Navier-Stokes approximations. On small bodies or sharp leading edges, these approximations may not be valid. At altitudes above about 45 km, finite-rate chemistry must be taken into account. In many instances single-temperature CFD models break down requiring more complicated treatments such as the two-temperature, nonthermochemical models (Park 1990). At higher altitudes, the Navier-Stokes approximations break down, requiring treatments for rarefied flows (Lumpkin and Chapman 1991).

European human mission needs are first focused on the independent access capability to space. The initial mission of the European vehicles is to perform the servicing of manned or man-tended space stations, either in the frame of an international cooperation, or possibly later in full autonomy. The planned duration of the stay in orbit varies from a week to several months, depending on the operational scenario. The vehicles considered have to take into account particular geographic and geopolitical constraints, namely a launch capability from Kourou (French Guyana) and a return capability on European countries. These constraints include a preference for medium-or high-inclination orbits but imply the need for a maneuverable vehicle with significant cross range in case this vehicle is to be operated regularly. The European vehicles, as they are envisaged today, should rely on medium-level technology and yield performance capacities which are unique and complementary to those of the USA and Russia. The aerodynamic shapes under study provide a good lift-to-drag ratio (0.6 to 1) and a positive aerodynamic control in hypersonics but do not allow a conventional landing as an airplane. Other landing modes are under study, ranging from conventional parachutes to guided paragliders.

The fulfillment of these ambitions implies a large effort in Europe in the field of aerothermodynamics in which both computational and experimental design tools are developed. The creation of this new center of competence in Europe is of a nature, through the dialogue between scientists, to speed up scientific progress within NATO in hypersonic aerodynamics.

In the longer term, Europe also considers participating in human space exploration, most probably in the frame of an extended cooperation. However, the present tight-budget restrictions do not allow us to start conceptual studies for the time being. Finally, The Europeans are putting together a technology program to prepare the development of future

reusable launchers. For the time being, both single-stage-to-orbit and two-stage-to-orbit concepts are considered, and both airbreathing and advanced rocket options are studied. A technology effort is made in aerothermodynamics, propulsion, and other relevant technologies.

In addition to the European programs described above, some national programs are also underway.

The German Hypersonics Technology programme terminated at the end of 1995. In its last phase (Phase Ic), emphasis was put on the RAM propulsion technology for the lower stage of the two-stage-to-orbit reference concept SÄNGER. The program is continued now in the Future European Space Transportation Investigations program (FESTIP) of ESA. SÄNGER is one of the concepts studied there. The "Sonderforschungsbereiche (centers of excellence)" of the Universities Aachen, München, and Stuttgart on Advanced Space Transportation Technology are still active. Working groups consisting of members of industry and universities are presently formed in order to keep the old contacts alive.

The French PREPHA program (Programme de Recherche et Technologie sur la Propulsion Hypersonique Avancée) is funded jointly by the DGA (Ministry of Defence), CNES, and the Ministry of Research and Technology. The PREPHA program started in 1992 with the following objectives:

- to investigate and perform ground testing of a scramjet and to study a vehicle which could validate such an engine in flight
- to maintain and improve the advance of French research in the field of technologies specific to the hypersonic regime

The program is now in its final plan and many results have been obtained, both from the theoretical (modeling of physical phenomena and improvement of CFD tools) and experimental (scramjet tests performed at Mach 6 in the Aérospatiale, Bourges, Subdray facility) points of view.

The activities performed covered aerodynamics (external and internal) propulsion, materials and structures, as well as system studies of a generic vehicle.

Finally, we note that two recent discoveries that are leading to renewed interest in solar system exploration: 1) meteors thought to have come from Mars contain suggestions of extraterrestrial life, and 2) the Galileo Spacecraft's photographs suggest the possibility of warm, life giving, liquid water on Europa. Since solar system exploration involves hypervelocity, atmospheric flight, this interest is likely to rejuvenate waning interest in hypersonic facilities worldwide.

### 3. MODERN APPROACH TO AEROTHERMODYNAMICS

The traditional aerodynamic design tools for aeronautics and space projects, i.e., wind tunnels, semiempirical codes, and flight testing, have been supplemented by CFD due to rapid advances in computer power and algorithm developments.

As with all design tools, the CFD codes must be validated; i.e., they must be checked against a range of experiments and experimental conditions spanning the range of involved flow physics and chemistry before they can be considered as serious design tools.

There currently is a dearth of archival quality, benchmark experimental data suitable for CFD code validation and calibration. What defines a benchmark experiment is still open to question and debate. One version of the structure that sorts and classifies the types of testing is shown in Table 1. Included is a statement on the necessary acceptance criteria for the data, the facilities that cover the range of testing required, desirable acceptance criteria and data completeness and accuracy requirements.

TABLE 1

CLASS	PURPOSE	EXAMPLES
1. Phenomenological data	Understand flow physics	Studies of large-scale structures
2. Unit problem data	Assess a model incorporated in a CFD code	Simple shear-layer data
3. Component data	Assess code's ability to analyze comp. of overall flow field	Rotor blade in wind tunnel
4. Performance data data/complete flow field	Assess if code predicts eng. parameters	Nozzle thrust
5. Full or subscale	Assess code ability to analyze specific flow parameters	Blunt body heating

#### Necessary Acceptance Criteria:

1. Baseline applicability ( $M > 3$ )
2. Simplicity
3. Specific applicability
4. Well-defined experimental boundary conditions
5. Well-defined experimental error bounds
6. Consistency criterion
7. Adequate documentation of data
8. Adequate spatial resolution of data

#### Facilities Required:

- conventional hypersonic wind tunnels
- high enthalpy or real-gas facilities
- rarefied facilities
- airbreathing propulsion testing
- materials testing

Table 2 shows another set of criteria for an ideal benchmark experiment for CFD validation as reported from the Antibes meeting on CFD code validation.

TABLE 2

CRITERIA FOR AN IDEAL BENCHMARK  
EXPERIMENT FOR CFD VALIDATION

1. Appropriate For CFD Validation:
  - a. Simple enough for economical CFD treatment.
  - b. Universal enough for applicability to numerous real world problems.
2. Model Flow field Adequately Characterized:
  - a. Boundary conditions defined:  $T_w$ ,  $\sqrt{\rho ck}$ ,  $m$ , catalytic effects, etc.
  - b. Boundary-layer surveys made (laminar or turbulent state defined)
  - c. Force, pressure, and heat data available as appropriate.
  - d. Shock locations measured (Optically or by other means)
  - e. Model attitude accurately measured ( $\leq 0.1^\circ$ )
  - f. Base pressure measured.
3. Model Fidelity Sufficient:
  - a. Sharpness/bluntness accurately manufactured, maintained, and defined.
  - b. Surface conditions quantified.
  - c. Model shape faithful to the defined configuration.
4. External Flow field Characterized:
  - a. Mach and Reynolds numbers,  $T_0$ ,  $T_\infty$ ,  $T_{\text{vib}}$ ,  $P_\infty$ , and time accurately defined.
  - b. Chemical/energy states of test gas defined (frozen, nonequilibrium, etc.)
  - c. Gradients of pressure, temperature, velocity defined in terms of the primary variables.
  - d. Contamination levels measured; potential effects noted.
  - e. Flow angularity measured in the test area.
5. Variables Identified and Controlled:
  - a. External flow-field variables varied in an orderly and rational manner.
  - b. Model variables varied in an orderly and rational manner.
6. Facility and Instrumentation Adequately Described:
  - a. Principles of operation as they affect data.
  - b. Limitations.
7. Data Uncertainties Defined For All Measurements:
  - a. Defined by standard methods and convention.
  - b. Repeatability demonstrated.

CFD clearly can be an essential design tool for hypersonic vehicles because wind tunnels do not provide full simulation at velocities above about 3 km/s (or Mach number above 5 - 10). This raises the question of how to extrapolate wind tunnel results to flight, addressed in chapter V. Semiempirical codes are inadequate and flight tests are exceedingly expensive. Moreover, CFD can directly assist in the improvement of wind-tunnel designs and in the efficient use of wind tunnels. Examples of methods already in use are

1. Hypersonic nozzles are validated and even designed with CFD methods, using available models for transition and turbulence.

2. Decisions on the relative importance of a given flow parameter for vehicle design are made by performing sensitivity studies using CFD.
3. Estimations of the allowable uncertainty for a given measurement technique are made by performing sensitivity studies with CFD.

However, CFD has the potential to play an even more important role in the future. CFD codes could replace the role of empirical design codes when new facility concepts are considered. For example, CFD can be used to predict the time-dependent operation of a new facility concept by simulating the influence of diaphragms, valve ports, shock propagation and reflection, etc. on the overall flow development. In other words, the entire aerodynamic design of a proposed new facility could be carried out with CFD. Optimization of the design may also be envisaged.

This process would permit the construction of a pilot tunnel with enhanced confidence; the pilot tunnel, in turn, would serve to validate the codes whose improved versions could then be employed to design the full-scale facility. A caveat: a pilot tunnel implies different physical scaling which may alter the relative importance of certain physical phenomena!

Clearly, the procedure can be continued to predict the gasdynamic state of the flow in the test section and even the flow nonuniformities. Such knowledge is the first step leading to the elimination of nonuniformities and will improve the credibility of wind-tunnel testing and in the long run will reduce the number of wind-tunnel tests required for a given design effort.

This philosophy is already producing results. In one example, Wilson et al. (1993) have published time-dependent simulations of reflected-shock/boundary-layer interactions in a cold-flow model of the NASA Ames Electric Arc Shock Tube called the E.A.S.T. Facility. The results on the mixing of driver/driven gas are in qualitative agreement with experiments and have shed new light on the effect of this phenomenon on the prediction of reservoir conditions. In another example, Bakos et al. (1996) have used CFD to aid in the design, calibration, and analysis of a tunnel mode of operation of the NASA Hypulse Facility with excellent results. At present, these computations are very CPU intensive, but if past experience is a guide, continued increases in computer power and algorithm efficiency will reduce this limitation.

It can be concluded that the pacing item in the use of CFD for facility design and flow characterization is code validation carried out through the use of building-block experiments. Only when facility designers have confidence in CFD codes will these codes be used for the design of major facilities. The promise to aerothermodynamics held out by this modern approach is so large as to fully justify the important investments that will be necessary to bring it to fruition.

#### 4 EXISTING FACILITIES

This section begins with a broad overview of the simulation capabilities of various types of wind tunnels designed to study hypersonic flows and to simulate aspects of hypersonic flight. Then a brief summary of the characteristics of the major real-gas, high-Reynolds



number, and rarefied facilities for aerodynamic research will follow.

Above Mach numbers of 8 to 10, *duplication* of flight conditions cannot be attained in most existing ground-based facilities with models of realistic size, even for entry from LEO; the upper limit is even lower if scramjet vehicles or entry from lunar or higher energy orbits are considered. Thus, *simulation*, which is the duplication of the essential dimensionless parameters characterizing the specific flow problem of interest, is the only methodology generally available at present. (It must be emphasized that if nonequilibrium chemical reactions are present, full simulation cannot be achieved in the most general case. Only full-scale testing at real flight conditions will suffice). As a general rule, blunt bodies require Mach-number, binary-gas-number ( $\rho L$ ), and  $T_0/T_w$  simulation; slender bodies require Reynolds-number simulation as well. If surface radiation effects are important, then absolute wall temperature must be duplicated which leads to the so-called "hot-model" technique (Hirschel 1991).

Figure 2 summarizes the Reynolds-Mach capabilities of European and American facilities; an overlay of two mission trajectories is shown for comparison. Figure 2(a) is adopted from Holden et al. (1995) and 2(b) is from Wendt (1992). A clear need for high-Reynolds-number tunnels is evident if the mission is to be a single-stage-to-orbit (SSTO), air-breathing vehicle. Figure 3 shows the situation with regard to the simulation of  $\rho L$  for the European facilities. The newest European and American facilities (F4, HEG, T5, LENS etc.) were designed with this phenomenon in mind.

Figure 4 summarizes the capabilities of existing facility types in terms of stagnation temperatures they can produce as a function of run time. The figure shows that shock tubes are useful in simulating gasdynamics and kinetics where the duration of chemical processes are the same or greater than that for which the flow persists ( $1\mu s$  to  $10\mu s$ ). For example, nonequilibrium radiation behind normal shocks. The next realm from  $10\mu s$  to  $10 ms$  can be studied by shock tubes, shock tunnels, and ballistic ranges. Gasdynamics and kinetics can be studied at the lower range of the time scale. At the upper end of the time scale, the researcher can study aerodynamics and flow field definition in the hypersonic regime where real-gas effects are important. Shock tunnels are generally driven with a free-piston driver or a shock tube. Flow quality and chemical cleanliness are of concern to these facilities. Ballistic ranges generally launch into a quiescent gas and contamination is not a concern. However, current ballistic-range-model scales are quite small. The realm of simulation from  $10 ms$  to  $2 s$  of flow can be explored with hot-shot and long-shot tunnels and high-performance blowdown tunnels. Here, the flow duration is sufficiently long to observe controlled motion of the test article, enabling detailed studies of aerodynamics. Finally, conventional blowdown tunnels can provide long-duration flows of up to minutes, but these facilities cannot usually produce real-gas flows. Most arc-jet facilities can provide long-duration, real-gas flows. An arc jet is basically a wind tunnel in which energy is added to the flow with a high-power arc discharge. Arc jets generally do not have aerodynamic quality flows and are used to study heat shield materials. This chapter will not consider further conventional blowdown tunnels or arc jet facilities.

Thus, a given mission and flight vehicle will define the relative importance of the various dimensionless parameters whose values must be matched in the facility. In addition to the fluid dynamic parameters, it is clear that such elements as cleanliness (freedom from solid particles) and flow uniformity (spatial and temporal, including wind-tunnel-generated pressure fields) must be quantified. It should be noted that some types of measurements may be carried out to an acceptable degree of precision in spite of the presence of noise, dirt, fluctuations, etc.; however, other important phenomena may be totally obscured by some of these effects. (The well-known influence of nozzle-wall turbulent boundary layers on the location and character of boundary-layer transition is a classic example).

An accurate knowledge of facility characteristics is obviously essential if tests of high quality are to be undertaken. High-enthalpy facilities are, however, particularly difficult to characterize due to their short running times, the presence of particles, nonequilibrium conditions, etc. Therefore, the need for sophisticated instrumentation techniques, which is summarized in Section 6 of this chapter, is of paramount importance.

## 4.1 United States Facilities

### 4.1.1 NASA Ames 16-Inch Shock Tunnel

The 16-Inch Shock Tunnel is being currently in a standby mode. Until recently, it was used for scramjet propulsion testing in support of the NASP program and the NASA Hypersonics Research Programs. The description below is a contraction of information contained in Cavolowsky et al. (1992).

A schematic of the 16-Inch Shock Tunnel is shown in Figure 5. The driver section consists of a tube 21 m long with an inside diameter of 432 mm. The driven section is 26 m long with an inside diameter of 305 mm. The shock tunnel received its name from the 16-inch naval rifles used to construct its driver section. The shock tunnel is rated at 680 atm maximum driver pressure. The contoured Mach 7 nozzle is 5.8 m long and has an exit diameter of 990 mm. Interchangeable throat sections are used to vary the nozzle area ratio. Results have been obtained for area ratios of 190, and a minimum of 95 as attainable without sacrificing test time or ideal shock tube end wall behavior. The test cabin is a 1.82 m long by 1.37 m square cross-section box located immediately downstream of the nozzle exit. Flow simulations equivalent for Mach 12, 14, and 16 have been achieved in the tunnel. Uncontaminated flow times of 3-5 ms are routinely seen in the 16-Inch Shock Tunnel.

It is important to note that although its recent efforts were directed toward propulsion testing and research studies, the 16-Inch Shock Tunnel is not restricted to this use. It could be valuable to experimental and computational research involving real-gas, blunt-body aerothermodynamics. This includes flight trajectories for spacecraft that will be studied as part of the Mars mission program and NASA's efforts to return to the lunar surface. Future plans will include calibration of test conditions required for these and other flight programs.

#### **4.1.2 Large Energy National Shock Tunnel (LENS)**

The LENS facility described by Holden, et al. (1995) is a reflected shock tunnel, and its basic components are shown in Figure 6. The driver/driven configuration consists of a chambered shock tube with an area ratio (driver/driven) of two. The 292 mm internal diameter driver is 7.6 m long and is externally heated by a resistance heater to 2270 K. The driven tube has an internal diameter of 203 mm and is 15.2 m long. The test section has a diameter of 2.43 m. Two nozzles are employed to cover the Mach number range from 6 to 18. A contoured nozzle is used for the Mach 6 to 9 range, and its exit plane diameter is 1.06 m. A conical nozzle is used for the Mach 10 to 18 range, and its exit diameter is 1.22 m. The nozzles employ replaceable throat inserts of different diameters so that, with a particular nozzle, the test Mach number can be varied. Both nozzles are calibrated using pitot pressure survey rakes over the Mach number ranges indicated. This facility can produce flow velocities from 0.91 to 4.9 km/sec. Test times vary from 4 milliseconds at the higher velocities to 20 milliseconds at the lower velocities for reservoir pressures up to 2,040 atmospheres. Figure 7 shows the altitude/velocity performance map for the LENS facility and compares its capability to Shuttle entry trajectory and to those of other U.S. facilities.

Aerothermodynamic instrumentation associated with the LENS facility permits surface measurements of heat transfer, pressure, and skin friction. Force and moment instrumentation is available as are schlieren, holographic interferometry, cine and video, total pressure, heat transfer and temperature gages for flow field measurements. Non-intrusive instrumentation includes electron beam, laser diode, PLIF, LIF, spectroscopy, and microwave interferometry. Extensive instrumentation is available for evaluation of the aerothermal and aero-optical performance of hypervelocity missile interceptors.

#### **4.1.3 Boeing Hypersonic Shock Tunnel**

The Boeing Hypersonic Shock Tunnel HST was built in the early 1960's and was brought on-line to support the development of the X-20 program. It was deactivated in 1981 and restored in 1987.

The major components of the HST are a 4 m long, 76 mm diameter combustion heated driver, a 7.6 m long, 76 mm diameter driven tube, contoured nozzles (305 mm and 762 mm exit diameter), a test section/dump tank, and a high-speed data recording system. Ignition of the driver gases (hydrogen and oxygen in helium) is initiated by 21 spark plugs placed in a spiral pattern along the length of the driver.

The HST uses a double diaphragm arrangement and operates as a reflected-wave shock tunnel. The Mach 5 to 8 range is covered with the 305 mm diameter nozzle while the 762 mm diameter nozzle is used for the Mach 8 to 20 range. Test times range from 2.5 to 5 ms, depending upon the total temperature being run. Reservoir conditions to 8000 K and 400 atm are available for high-enthalpy simulations.

The primary measurements made in the tunnel are surface pressure and aerodynamic heating rates using either platinum thin-film gauges or coaxial thermocouples.

Free-stream velocity has been measured using an exploding wire and a photo diode array. Instrumentation also includes high-speed cameras, shadowgraph and Planar Laser-Induced Fluorescence (PLIF).

#### **4.1.4 Northrup Grumman Research Detonation Shock Tunnel**

The Northrup Grumman Research detonation shock tunnel has been used for over 25 years to simulate high-temperature gas flows for programs including the Shuttle Orbiter and the National Aerospace Plane.

The tunnel consists of a 19.8 m long, 127 mm ID sectional tube assembly exiting through a nozzle into a 1.83 m diameter by 3.7 m long vacuum chamber. The nozzle has a rectangular cross section with a nearly square throat 38 mm in height, varying to a 38 x 114 mm exit plane.

The shock tunnel operates by first rupturing its primary diaphragm, allowing pressurized helium from the 6.1 m long driver to propagate into the driven tube. The driven gas for combustion simulation studies consists of a detonable mixture of nitrogen, oxygen, hydrogen, and argon. The driven section is isolated from the vacuum chamber by a secondary mylar diaphragm at the entry to the facility nozzle. Test times of 2-3 milliseconds are achievable with this facility.

Total enthalpy conditions corresponding to free-stream Mach numbers between 8 and 12 are produced by varying the composition of the driven gas and the pressure of the helium driver gas.

Instrumentation consists of wall pressure, heat flux, and optical systems. The optical systems consist of holographic interferometry; laser extinction and absorption; UV and visible OMA and photometers; and infrared (IR) radiometers, arrays and cameras.

#### **4.1.5 GALCIT T5 Shock Tunnel**

The T5 facility is a free-piston, reflected-shock tunnel located at the Graduate Aeronautical Laboratory of California Institute of Technology. The tunnel became operational in December 1990. Hornung (1992) describes the facility and its performance. T5 has been used for graduate research and industrial testing in over 1200 runs as of spring 1996.

The compression tube is 30 m in length and is 300 mm in diameter, while the driven tube is 12 m in length and is 90 mm in diameter. The nozzle has a throat diameter of 31 mm, an exit diameter of 310 mm and a length of 1 m. The driver gas is helium or a helium/argon mixture, and the maximum burst pressure is 1,300 atm. The facility test times range from 0.2 to 5 ms, depending upon operating conditions. The tunnel is equipped with a hydrogen injection system with speeds up to 5 km/s. Instrumentation consists of wall pressure, heat flux, and optical systems: schlieren, interferometry, and differential interferometry.

#### 4.1.6 NASA's HYPULSE Facility at GASL

The HYPULSE Facility is an expansion tube/tunnel which was originally built at NASA Langley in the 1960's, decommissioned in 1983, transferred to GASL, Ronkonkoma, New York, in 1987, refurbished, and recommissioned in 1989. Erdos et al. (1994) have recently described the GASL facility and its expanded operational envelope.

Figure 8 shows a wave diagram describing the basic operation of an expansion tube. This figure assumes a not-yet funded free-piston driver is being used. Typically, about two-thirds of the total enthalpy and total pressure is generated through the unsteady expansion fan and occurs in the test section mainly in the form of velocity. The tunnel mode of operation uses a divergent (throat-less) nozzle at the end of the tube to increase the Mach number and size of the test section.

The HYPULSE Facility components consist of a 2.44 m long, 165 mm ID, driver tube rated for an operating pressure of 1360 atm, a 2.44 m long, 152 mm ID intermediate tube rated for 1000 atm, and a combination of intermediate and acceleration tubes of 152 mm ID, totaling 19.66 m long, rated for 525 atm. The test section/dump tank is 11 m long with a 1.2 m ID. In a typical configuration, the intermediate tube is 7.5 m long, and the acceleration tube is 14.6 m long. The lengths of these two sections are variable. An additional two sections of acceleration tube, each 2.29 m long, are available but not installed, as is a divergent nozzle having an exit diameter of 635 mm. The driver can be operated with either room-temperature helium, helium-hydrogen, or helium-nitrogen mixtures or with detonatively heated hydrogen-oxygen-helium mixtures.

The test section conditions are varied by varying the driver conditions and the fill pressures of the intermediate and acceleration tubes. The facility has been used extensively at a total enthalpy of 15.2 MJ/kg for hypervelocity aerothermodynamic studies. This condition is achieved with room-temperature driver gas and provides a free stream velocity of 5.33 km/s, a static temperature and static pressure of 1200 K and 1.8 kPa, respectively, a unit Reynolds number of  $6.6 \times 10^5 \text{ m}^{-1}$ , and a total pressure of 163 MPa. The test time at this condition is 0.3 ms. The facility has also been calibrated and operated at total enthalpies from 7.5 to 17.3 MJ/kg, primarily for supersonic/hypersonic combustion studies. At these conditions, the free-stream velocities vary from 3.5 to 5.7 km/s; the static temperatures vary from 1100 to 2400 K; the static pressures vary from 1.5 to 150 kPa; and the total pressures vary from 60 to 400 MPa. The total test time available for flow establishment and data collection/averaging varies from 0.3 to 0.8 ms. The quoted conditions are all for air as the test gas. The facility has also been calibrated and operated over a similar range of hypervelocity conditions using pure gases, including nitrogen, oxygen, helium, and carbon dioxide as test media.

Instrumentation available at HYPULSE includes pressure and heat flux (up to 160 channels sampled at up to 1 MHz with 12-bit resolution) and various optical devices: laser holographic interferometry, schlieren, shadowgraph, various types of spectroscopy, and time-averaged Mie scattering imagery.

Supporting systems for studies involving gas injection include two Ludweig tubes and a shock tube (installed inside the dump tank) for delivering room-temperature or shock-heated gases to a model in synchronization with start-up of the primary test gas flow.

Instrumentation available for testing include laser holographic interferometry, emission measurements, spontaneous Raman spectroscopy (vibrational and rotational temperature measurements), and UV absorption spectroscopy (NO and O concentration measurements).

#### 4.1.7 NASA AMES Electric Arc Shock Tube

NASA Ames's electric arc-driven shock tube facility has been in existence since the 1960's. This facility is currently in standby mode. The operating characteristics of the facility are described in Sharma and Park (1990). A photograph of the facility is shown in Figure 9. The facility consists of one driver system and two parallel driven tubes. One is a 100 mm ID tube 12 m in length, and the other is a 600 mm ID tube 21 m in length. The driver can be operated in two configurations: (1) a 177 mm conical drive configuration with a 101.6 mm exit (driver volume = 0.632  $\ell$ ), and (2) a variable length (340-1370 mm) 100 mm ID cylindrical configuration (driver volume = 2.7 to 10.7  $\ell$ ). The length of the cylindrical drivers can be varied by using a Lexan filler plug.

Energy to the driver is supplied by a 1.24 MJ, 40 kV capacitor energy storage system. By using the two different driven tubes, varying the driver/driven gas combination, driver charge pressure and preset capacitor bank voltages; normal shock velocities in the range of 3.0 - 50.0 km/s, with unshocked test gas pressures at the higher velocities in the range of several tenths to several torr, have been obtained. In order to minimize the level of impurities, contact of the test gas with steel and any material containing carbon or hydrocarbons has been minimized. Past experience shows that the spectra of the test gas, which was in contact with steel wall and carbon (burned mylar diaphragm), were overwhelmed by spurious emission spectral lines of iron and CN-violet (Sharma and Park 1990). For this reason, aluminum diaphragms and an aluminum 100 mm ID driven tube are used. Instrumentation consists of laser holographic interferometry, emission measurements, spontaneous Raman spectroscopy (vibrational and rotational temperature measurements), and UV absorption spectroscopy (NO and O concentration measurements).

#### 4.1.8 NSWC Hypervelocity Tunnel Number 9

The Hypervelocity Wind Tunnel 9, located at the Naval Surface Warfare Center in White Oak, Maryland, is a blow-down facility which currently operates at Mach numbers of 7, 8, 10, 14, and 16.5. Tunnel 9 provides a high Mach-number and Reynolds number testing environment with usable test times up to 15 seconds and a 1.5 meter diameter test section.

A schematic of Tunnel 9 is shown in Figure 10. A vertical heater vessel is used to pressurize and heat a fixed volume of nitrogen to a predetermined operating pressure and temperature. The test section and vacuum sphere are evacuated and separated from the heater by a pair of metal

diaphragms. When the nitrogen in the heater reaches the desired temperature and pressure, the diaphragms are ruptured. The gas flows from the top of the heater, expanding through the contoured nozzle into the test section at the desired test conditions. As the hot gas exits the top of the heater, fast-acting valves are opened allowing cooler nitrogen from four pressurized driver vessels to enter the heater base and maintain a constant heater pressure. The cold gas drives the hot gas out of the heater in a "fluid piston" fashion while maintaining constant conditions in the test section during the run.

Tunnel performance characteristics are given below:

Contoured Nozzle [Mach]	Supply Pressure [MPa]	Supply Temp- erature [K]	Reynolds Number [10 <sup>6</sup> m <sup>-1</sup> ]	Usable Test [sec]
7	13 - 90	1920	6 - 55	1 - 6
8	13 - 83	920	28 - 183	0.2 - 0.75
10	3.5 - 97	1005	3 - 72	0.2 - 15
14	0.7 - 131	1755	02. - 20	0.7 - 15
16.5	131 - 145	1810	9 - 11	3

Tunnel 9 Capabilities are under continuous development. In 1995, a new facility leg with full-flight duplication at Mach 7 for providing a thermal/structural test environment was brought on line. This capability matches the true temperature and pressure at flight altitudes as low as 15 km with run times up to 6 seconds. Future developments will allow this test leg to duplicate flight altitudes down to 10 km. Ragsdale et al. (1993) and Lafferty et al. (1996) have discussed the capabilities of NSWC Tunnel 9.

#### 4.1.9 Ballistic Ranges

With its clean test-gas environment, the ballistic range provides correct thermochemistry at true-flight enthalpy. The enthalpy comes from the use of light-gas guns which can launch projectiles at speeds in the 3 to 9 km/s range. However, the model scale is currently very small and there is concern that the test capability is inadequate. A very detailed AGARD Report (AGARDograph 138), primarily discussing the NASA Ames ballistic ranges of the 1970 time frame, details the methodology of the ballistic range, including the use of a shock tunnel to provide a counterflow, enabling the simulation of lunar return (11 km/s) entry of the Apollo vehicles. With the advent of CFD, the role of the ballistic range has changed to become more of a validation tool.

Below is a synopsis of ballistic ranges in the U. S. as in the 1996 time frame, based on a more detailed review by Chapman (1992).

##### NASA Ames Research Center

Ames has four two-stage light gas launchers ranging in size from 7.1 mm to 38.1 mm diameter. These launchers were designed to provide low-acceleration (soft) launching. Ames has two facilities which use these launchers: the Hypervelocity Free-Flight Aerodynamic and Radiation Facilities. The aerodynamic facility uses the 16-Inch Shock Tunnel discussed above as its counterflow source, but the facility has not been operated in this mode for over 20 years. The facility has a 25 m long test section with 16 orthogonal shadowgraph stations. The test section was

sized to the capability of the shock tunnel to provide a slug of moving test gas of this length. It is capable of conducting aerodynamic testing at hypervelocities and can yield good quality flow visualization and aerodynamic coefficients for simply-shaped vehicles. The aerodynamic range is currently operated as an impact facility, while the 16-Inch Shock Tunnel is in standby status. The radiation facility is configured solely for gun development and impact testing.

Arnold Engineering and Development Center: AEDC has several launchers. The largest is 62.5 mm in diameter, and there is one being designed and built which is 82 mm in diameter. All of these launchers have been optimized with operational experience for low acceleration launch loads. The new launcher has been optimized from the design stage. There are two long variable pressure ranges, the longest being 300 m in length. This range is also designed for either free-flight launches or launching onto a rail. The rail launch system also allows for recovery of models. Besides the conventional range instrumentation, this range is currently instrumented with spectrometers for wake-flow diagnostics. There is also ongoing work to develop planar laser induced fluorescence (PLIF). This facility has the best set of diagnostics equipment of any in the United States at the present time.

University of Alabama, Huntsville: This range was previously located at the Delco facility in Santa Barbara, CA. It has a 62.5 mm diameter launcher that has been extensively optimized to minimize launch accelerations. The range is over 300 m long with variable pressure capability. This facility has the radiometric instrumentation that was at Delco. This instrumentation needs to be updated if it is to be useful for detailed flow-field studies and CFD code validation.

Wright Laboratory Armament Directorate at Eglin Air Force Base: This is a sea-level atmospheric pressure range of over 200 meters in length. The launcher room is small, and hence the light-gas launcher is small and not optimized for soft launches. It also has an optical system that cannot reject optical radiation from the model and hence is limited to 3 to 4 km/s. However, in this speed range it has the best developed aerodynamic determination system in operation at the present time. There are plans to replace all of the conventional cameras with electronic cameras and to fully automate the aerodynamic data-reduction procedure to provide rapid determination of aerodynamic parameters.

Lawrence Livermore National Laboratory: LLNL has developed a 100 mm two-stage light-gas launcher for potential application as a space launcher. This launcher has two novel features. First, the driver tube (1st stage) and the launch tube (2nd stage) are at right angles; hence the launch tube can be elevated for firing without altering the driver. This could be a useful feature for saving space in a constrained area. It also presents an opportunity for using the pump tube (first stage) as a free-piston driver for a shock tunnel without significant interference with the ballistic-range portion of the facility. The second feature is that it uses methane-oxygen combustion as the driver for the first stage piston rather than the conventionally used gunpowder. This launcher with the extensive advanced instrumentation base that exists at LLNL could be the nucleus of an aerothermodynamic testing capability. What is missing is a variable pressure test range. A total of about

30 shots have been fired as of fall 1995. Some were in support of scramjet testing. These shots were with 5 kg models with launch speeds of about 3 km/sec. Whether this facility contributes to the aerothermodynamic testing capability remains to be seen.

#### 4.1.10 UC-Berkeley Rarefied Gas Wind Tunnel

The configuration and instrumentation of the University of California at Berkeley rarefied-gas wind tunnel have changed greatly from their state in the 1960's and 1970's (see Figure 11 for schematic of present facility Gochberg (1993)). Currently, the electron-beam fluorescence technique is used as the primary experimental diagnostic tool, measuring density and rotational and vibrational temperatures in the hypersonic, low-density flows generated using free-jet expansions. A ceramic resistance heater with a maximum operating temperature of 2000 K functions as the flow reservoir and can be operated with virtually any gas, including oxygen. The facility is capable of producing shock Mach numbers for nitrogen in excess of 20 at the highest stagnation temperature available. The shock barrel is 65 mm long with a Mach disk diameter of 55 mm for this condition.

#### 4.1.11 AEDC Free-Piston Shock Tunnel

A new concept for a very high pressure free-piston shock tunnel being developed at AEDC has been described in Maus et al. (1992). Figure 12 depicts the evolution of this concept from the conventional free-piston, light-gas gun. In the light-gas gun, the disposable piston is driven by gunpowder, compressing hydrogen to a high pressure. The diaphragm bursts at a prescribed pressure and the projectile is accelerated through the launch tube into free flight.

In the disposable free-piston shock tunnel, the piston propellant is moderate-to-high-pressure air, and the compression gas is helium. The diaphragm bursts and drives the rest of the facility as a conventional shock tunnel. Conventional free-piston shock tunnels are limited to about 2000 atm stagnation pressures to avoid damage to their reusable pistons and gas leakage. In the light-gas-gun operation, the deformable piston seals the gases by extruding the piston into a tapered section. Pressures in excess of  $10^4$  atm are routinely achieved in this manner. Maus et al. (1992) state that this concept for a disposable free-piston shock tunnel has the potential of attaining stagnation pressures as high as  $10^4$  atm with enthalpies over 20 MJ/kg. Their paper discusses pilot experiments for this concept and makes comparisons against theory. Blanks (1996) reported that the facility has been constructed and low pressure (up to 650 bar) calibration data have been obtained for enthalpy of 12.5 MJ/Kg. The facility has a 27.5 m compression tube whose ID is 203 mm. The length of the shock tube is 12.2 m and its diameter is 7.62 cm. The conical nozzle has throat diameter that vary from 9.5 - 19 mm. The 8 degree conical nozzle exit diameter is 45.7 cm. Flow times are about 1 -2 milliseconds at the aforementioned low pressure test condition. It is also reported that good comparison with CFD modeling of the facility has been obtained. It was reported that a copper liner was effective in preventing reservoir erosion. It was noted by Blanks that the attainment of nozzle stagnation pressures in excess of 2000 bar will require solution of the erosion problems.

## 4.2 European Facilities

### 4.2.1 HEG Shock Tunnel (Germany)

The HEG Göttingen facility is a free-piston-driven shock tunnel (Fig. 13). The tunnel is 60m long with an internal diameter of 20 cm and has a test section diameter of 1.2 m. The maximum reservoir pressure achievable is 1000 bar which allows a maximum binary scaling parameter,  $\text{Rho-L}$  (or  $\rho L$ ), of  $1/1000 \text{ kg/m}^2$  (Fig. 14). This parameter represents the number of molecular collisions. The total temperature can reach 10,000 K. The speed reached in the test section varies from 4.5 to 7 km/s. The core of parallel flow has been estimated to be 0.55 m with a static temperature of 1000-2000 K. The flow is frozen non-equilibrium in the undisturbed free stream. This nonequilibrium occurs because of the low density which is reached in the expansion through the nozzle. The nozzle exit Mach number is approximately equal to 10. The testing time is currently about 2 ms. Forces and balances are not currently worked on. The instrumentation consists of pitot tubes and static pressure transducers to measure the pressure and Mach number. Heat transfer measurements are also performed with coax thermocouples and laser-induced fluorescence to measure density and possibly temperature to get the flow velocity. For flow visualization, a 2-D holographic interferometer is used, from which the density can also be computed. A laser-schlieren flow visualization setup is also used in the facility.

### 4.2.2 ONERA F4 WIND TUNNEL

The F4 depicted in Figure 15 is the ONERA's high-enthalpy hypersonic testing facility. It is an intermittent blowdown (impulse) "hot-shot" type of wind tunnel. It has three different steel and fiberglass contoured nozzles with different exit diameters, the largest measuring 0.67 m with a length of 3.9 m. The electric power needed to operate it is 150 MW. This arc-heated facility can attain a stagnation pressure of 2000 atm. The flow velocity can reach 5.5 km/s, and the binary scaling parameter  $\rho L$  goes from  $10^{-3} \text{ kg/m}^2$  at a velocity of 5.5 km/s to  $10^{-2} \text{ kg/m}^2$  at a velocity of about 3 km/s (see Figure 14). The testing time is between 50 and 150 ms. The Mach number range of the facility is 7 to 18. The main area of interest is at a Mach number of about 16 and a unit Reynolds number of about  $3 \times 10^6 \text{ m}^{-1}$ . A typical model size is about 0.3 m in length. With the relatively long testing time, accurate force and moment measurements can be performed. The instrumentation includes balances, heat transfer gauges, and pressure transducers.

### 4.2.3 RWTH Aachen Shock Tunnel (Germany)

The RWTH Aachen facility TH2 is a high-enthalpy shock tunnel (Fig. 16) driven by a resistance-heated helium driver. In the reflected mode, the shock tunnel has a driver section of 6 m, a driven section of 16 m, and conical nozzles with exit diameter of 0.57 m, 1 m and 2 m. A contoured nozzle with an exit diameter of 0.57 m is also available. The inner diameter of the driver, as well as driven section, amounts to 140 mm. The tunnel can simulate Mach (6 to 15) and Reynolds (12 million/m) numbers, duplicate the flight velocity up to 4km/s, and

simulate real-gas effects. Measurements include pressure and heat transfer. To meet the requirements of the shock tunnel operation, a special 6-component balance has been developed which allows force and moment measurements for flow duration of at least 2ms. Flow visualization is achieved by color schlieren and shadow optics, and interferometry. The maximum total pressure is 1500 atm, and the maximum total temperature is 5000 K; the maximum testing time is 10 ms. Currently the shock tunnel is calibrated for 11 different flow conditions with a Mach number ranging from 6.1 to 12.1 and for total temperatures ranging from 1500K to 4700K. To improve the performance of the tunnel, a detonation driver has been built which is currently in the testing phase. With this new driver in the tailored interface mode, the total maximum pressure will be 2800 atm and the maximum total temperature 7500K.

#### **4.2.4 LRBA C2 Reflected Shock Tunnel (France)**

The LRBA C2 is a classic shock tunnel with stagnation conditions to 2400 K and 350 bar; test times are 10 to 20 ms. The main feature of this tunnel is the large nozzle exit diameter of 1.2 m. Mach numbers can be varied from 8 to 16 using conical nozzles; however, a contoured nozzle for Mach 16 is generally employed.

#### **4.2.5 VKI Longshot (Belgium)**

The von Karman Institute's Longshot is a free-piston tunnel (Fig. 17). It has one contoured nozzle with a 0.43 m exit diameter and a 6 degree conical nozzle with a 0.355 m exit diameter. The total pressure can reach 4000 bar, and the total temperature about 2500K. For the calibrated flow conditions with the contoured and conical nozzles, the Mach number range is 11 to 15; the Reynolds number ranges between 4 and 14 million/m and the useful running time is about 10 to 20 ms. With the contoured nozzle, the tunnel is operated with nitrogen; with the conical nozzle it can also be operated with carbon dioxide. Four operating points (two for N<sub>2</sub> and two for CO<sub>2</sub>) are calibrated with the conical nozzle so that the effect of variation of the specific heat ratio  $\gamma$  at constant viscous interaction parameter can be studied. The models are mounted on a high precision incidence mechanism for pitch, yaw, and roll. Instrumentation includes a 6 component strain gauge balance with accelerometers to account for impulse forces; infrared photography, thin-film gauges, and coaxial thermocouples for heat transfer measurements; piezo-electric pressure gauges; a 64 channel acquisition system with integrated amplifiers and filters and a schlieren system for flow visualization. The research conducted includes support to the development and validation of the physical modeling used in the numerical codes and investigations of the aerothermodynamics of reentry vehicles.

#### **4.2.6 CNRS SR-3 Low-Density Tunnel (France)**

The SR-3 wind tunnel (Figure 18) of the National Center of Scientific Research can achieve Mach numbers from 2 to 20. Its flow is of low density, and the maximum Reynolds number obtainable is  $7.3 \times 10^4$  at Mach 30. The gas used in the tests is nitrogen. The nozzle exit diameter goes from 0.15 m to 0.40 m. The tunnel flow is continuous and the flow regimes can be from near-free-molecular to continuum.

The instrumentation includes electron-beam probes for low-density measurements, pressure transducers, devices for heat-flow measurements, i.e., thin-wall technique and infrared thermography, hot-wire probes, and aerodynamic balances. Flow visualization is obtained by sweeping the electron beam by glow discharge. The research conducted includes plume interaction studies (launcher stage separation, spacecraft control) and low-density aerothermodynamics.

#### **4.2.7 VG Low-Reynolds-Number Tunnels (Germany)**

The V1G and V2G facilities at the DLR Göttingen are resistance-heated continuous tunnels which were designed for hypersonic low-Reynolds number (low-density) flow research. V1G and V2G have nozzle exit diameters of 0.25 m and 0.4 m, respectively. Because they are low Reynolds-number facilities, the useful cores are much smaller than the geometric cores: from 0.05 m to 0.3 m, depending on selected conditions. Reservoir temperatures can reach 1500 K. Force balances, electron-beams, thin-wall heat transfer techniques, and flow visualization by glow discharge are just some of the instrumentation methods which have been developed over many years.

#### **4.2.8 Facilities in Development ISL-RAMAC (France)**

Ram-accelerator research has been under way at ISL (French-German Research Institute of Saint Louis) since 1988. The largest facility now operational is RAMAC 90, consisting of a ram accelerator tube of 90 mm in diameter and a conventional powder gun as pre-accelerator. The length of the accelerator tube is at present 16.2 m (180 calibers). Extension to about a 30 m length is planned within the next years. The facility is located in a 120 m long ballistic range already existing in ISL since 1958.

The first ram acceleration was attained in March 1992. A recent result has been increasing the velocity of a 1.340 kg body from 1335 m/s to about 2000 m/s within the tube of 16.2 m length. The main future objective of this facility is the acceleration of important masses to velocities up to 3 km/s.

A smaller facility is RAMAC 30, which consists of a ram accelerator tube of 30 mm in diameter of up to 12 m using a conventional powder gun as the pre-accelerator. Stepwise extension up to about 40 m is planned for the next years.

The facility is built for basic research mainly in the superdetonative flight mode. The objectives are to achieve velocities beyond 4 km/s and to identify and overcome possible limiting factors such as aerodynamic heating which may lead to ablation and unstart phenomena; i.e., a detonation wave moves in front of the projectile and ends the acceleration phase.

Two versions of ram tubes have been used: (1) a rail tube and (2) a circular bore tube. With the rail tube, cylindrical aluminum projectiles of 130 g could be accelerated with up to  $90,000 \text{ m/s}^2$ . In this case, ablation problems were not as dominant as in the circular bore experiments using fin guided projectiles. Here heating and ablation caused a

strong erosion especially on the projectile's fins, resulting in a projectile canting followed by an unstart.

### 4.3 Russian Facilities

The first version of this chapter edited by Saric, et al. (1996) included a section by W. Calarese, based on his visits to Russia. A publication by Czajkowski (1994) contains excellent descriptions and photographs of the Russian facilities. This publication can now take the place of the section in our previous AGARDOGRAPH.

## 5 ASSESSMENT OF FACILITIES

As shown in Figures 2, 3, and 4, no facility can reproduce all the conditions required for complete reentry or ascent simulation. Consequently, each class of facilities has aimed at reproducing some of the required conditions, and all classes can be seen as complementary to one another. Depending on the problem to be investigated, certain characteristics of a given class may range from very undesirable to acceptable; e.g., contamination may strongly influence combustion processes but have negligible influence on force measurements.

All the facilities discussed above which are more than five years old can be said to be useful contributors to our experimental database within their specific limitations and advantages.

We also comment here on the progress being made with the newer facilities: LENS, T5, HEG, and F4 which now have one to several years of regular calibration, operation, and practical testing. They all represent very valuable additions to our testing capabilities and, in particular, to our code validation capabilities.

### 5.1 LENS

The LENS facility has become an important asset for the measurement of aero-optic and aerothermodynamic effects as well as scramjet propulsion testing. The calibration of the facility is described by Holden et al. (1995). LENS is capable of producing critical design data in turbulent, non-equilibrium hypervelocity gas flows over large, well-instrumented models. Recent major use of the facility has been to evaluate the aerothermal and aero-optical performance of full-scale interceptor configurations, including seeker head geometries. Importantly, the actual aerothermal environment encountered in flight and its effect on optics can be demonstrated. Tests of large-scale scramjet engines in the facility have demonstrated its use for ground testing and development of engines in the range of velocities from 1.8 to 4.6 km/sec. The long test times and clean airflow generated in the LENS tunnel under conditions where nonequilibrium real-gas effects are important enable study of vehicles of interest to Earth reentry and planetary entry as well. Fundamental studies in high-enthalpy flows also provide an excellent opportunity for code validation and the models of turbulence, vibrational relaxation and dissociation, which are employed in Navier-Stokes and Direct-Simulation Monte Carlo computational schemes. Initial results of these studies are described by Holden et al. (1995) and by Holden, Chadwick, Gallis, and Harvey (1995).

### 5.2 GARCIT T5 Facility

As mentioned in section 4.1.5, the GARCIT T5 facility at the California Institute of Technology has been used in over 1200 runs in the time frame from December 1990 through the spring of 1996. Clearly, this facility is serving as an important focal point for the advancement of understanding real-gas, hypervelocity flows. This advancement is occurring because faculty, students, and researchers from a wide range of institutions (academia, industry, and government) with both computational and experimental interests are focusing their attention on the capabilities of T5. Part of the focus is on the prediction of tunnel mechanisms, operations, and flow quality, e.g., the behavior of free pistons using CFD as described by Belanger and Hornung (1994); improvements in diaphragm manufacture and nozzle throat materials; and in corroboration of the predicted free-stream flow conditions of the tunnel. As described by Candler, Dimotakis, Hornung, Leonard, Meiron, McKoy, Pullin, and Sturtevant (1995), excellent progress is being made by an interdisciplinary effort by computational fluid dynamists, experimentalists, and computational chemists in understanding the interactions of chemistry, turbulence, and shock waves in hypervelocity flows. Results of this work to date include a clear understanding of two important parameters that define hypervelocity flow over spheres. This reference also discusses detailed experimental and theoretical studies which show that real-gas effects do not further enhance heat flux in type IV shock-shock interactions as compared to ideal-gas flows. These shock-shock interaction studies resulted in the first high-resolution interferograms of such flows, and these also established a good measure of the flow quality in T5. Candler et al. (1995) also report on an important computational discovery of a flow field that is sensitive to vibration-dissociation coupling, which suggests an important shock tunnel measurement that could lead to improved real-gas CFD modeling. Finally, this reference shows how computational chemists are providing reliable information on real-gas properties via first-principles quantum mechanical calculations on collision cross sections of electronic excitations of OH, NO, and CO<sub>2</sub>, important in weakly ionized flows.

### 5.3 HEG Facility

The HEG (High-Enthalpy Göttingen) facility has demonstrated its ability to produce hypervelocity flows characterized by nondimensional binary scaling parameters identical to those experienced in the high-velocity regime of reentry from Earth orbit. At present (late 1996), 350 shots, of which the first (50) were part of a commissioning process, have been made. The facility was commissioned in July 1993. Since then, it has been used mainly for European Space Agency programs which the major efforts have been devoted to the calibration and understanding of the flow. Since the number of measured parameters is limited by the experimental capabilities, all calibration efforts are performed concurrently with numerical calculations (e.g., Hannerman et al., 1995).

As a result, a realization grew that the HEG contoured nozzle does not always produce sufficient flow quality, due to centre line perturbations/focusing. Therefore a new conical nozzle was installed, providing a more uniform central core flow. However, for many experiments, the flow produced by the contoured nozzle was of sufficient quality for studying real gas effects. These effects are measurable with conventional measurement techniques adapted to the HEG flow characteristic (Eitelberg 1996). The studies of on-going interest are

- Flows over blunt or blunted objects. These can be spheres (Eitelberg et al., 1996), missile-shaped objects (ELECTRE), or blunt coned (70° case, ref. Ch. 4). In all cases, shock shapes and shock stand-off-distances provide significant fluid dynamics/real gas effect data for code validation. In all these blunt cases the existence of a non-equilibrium (neither frozen nor equilibrium) shock layer has been shown to be present. The influence of nonequilibrium flow on the configuration of flow features is demonstrated unequivocally. The determination of its influence on surface quantities (pressure and heat transfer) is complicated, and this stage is not always unequivocal.
- Shock/shock interaction serves as a test case for code validation. Here again the geometry dependence on flow-field shape upon high-enthalpy is easy to demonstrate. The high-enthalpy effects lead to changes in the characteristics of peak heat loads.
- Capsules and flight configurations (Halis, HERMES). Here data have been provided in the framework of ESA projects.

In order to obtain good quality data, a large effort has been dedicated to instrumentation development. In particular, for the study of real gases, spectroscopic methods have been developed. The LIF technology has been applied for visualization of changes in species concentrations and thereby the flow-field shape (Beck et al., 1996) and temperature profiles (Rosenhauer 1994). Work towards fully quantitative measurements ( $T$ ,  $C_i$ ) is continuing. Also under development is a laser disk absorption technique to determine free-stream temperatures and velocities. Flow visualisation with schlieren and interferometry is mature and reliable (Kastell, Eitelberg 1995). There is good experience with pressure and heat transfer measurements.

It is important to note that all current experimental programs have been accompanied by numerical analyses (e.g., Hanneman 1995). Further numerical analysis into the shock tube behaviour and nozzle flow starting process is ongoing.

#### 5.4 F4 ONERA

The ONERA F4 wind tunnel (Figure 15) was built in the early 1990s to simulate the atmospheric re-entry of hypersonic vehicles. It is a hot-shot type, meaning that the settling conditions are obtained by heating the test gas with an electric arc in an arc chamber. The energy is delivered by an impulse generator, at a power of up to 150 MW for several tens of milliseconds. The settling-chamber pressure can be as high as 500 bar and the reduced total enthalpy  $H/RT_0$  can be as high as 250 (about 20 MJ/kg).

After the arc-chamber conditions reach the desired levels, the arc is stopped and the nozzle throat is opened by igniting a pyrotechnic plug to initiate the nozzle flow. The blowdown is interrupted by firing a pyrotechnic valve in the arc chamber, quickly evacuating the remaining gas into a dump tank. Run duration of up to 400 ms can be achieved, but with reservoir conditions decreasing with time. Reservoir pressure and enthalpy decays are slow enough (1%/ms) to allow force measurements to be performed. The useful run period is established after a perturbed period of 30 ms because of the throat-plug-expelling phase. Synthetic air and pure nitrogen are used as test gases. F4 can be equipped with four different contoured nozzles with area ratios varying from 1850 to 32,000. Nozzle 2 with an area ratio of 4490, a length of 3.4 m, and an exit diameter of 0.7 m, was used for most of the aerothermal testing. Figure 14 shows the range of the binary scaling factor versus velocity.

Measurement techniques comprise forces and moments with six-component balances and inertia compensation, model pressure and heat transfer, infrared thermography either with the scanning line technique (2500 Hz) or with the 2D high rate ONERA camera (400 Hz), emission spectroscopy, absorption spectroscopy and velocity (Doppler effect) with Diode Laser infrared Absorption Spectroscopy (DLAS) on NO, H<sub>2</sub>O, and spectroscopy with Electron Beam Fluorescence (EBF) on NO, N<sub>2</sub>. Recently, free stream velocity has been measured with a time-of-flight technique using a pseudospark electron gun.

## 6 ASSESSMENT OF INSTRUMENTATION

### 6.1 Requirements

Experimental testing in hypervelocity flows must consider four basic parameters (Seibert et al. 1992):

- (1) The total temperature or enthalpy determines the maximum velocity attainable.
- (2) The total pressure determines the test pressure and, therefore, the altitude to be simulated, and it has a profound effect on the nature of the test gas.
- (3) The size of the facility determines the largest model scale that can be used.
- (4) Test duration determines the type of instrumentation that can be used, the ability to "soak" structures in the hot flow, and the relationship of the chemical relaxation times.

The following fluid properties need to be measured: pressure,  $P$ , density,  $\rho$ , temperature,  $T$ , the components of velocity,  $u$ ,  $v$ ,  $w$ , the stream or global velocity,  $U$ , and the sound speed in the flowing medium,  $a$ . Flow profiles of chemical species,  $X_i$ , ionization, and the transport properties: viscosity,  $\mu$ , thermal conductivity,  $k$ , and diffusion,  $D_{ij}$ , must be measured or determined.

In order to provide the physical interpretation of the experiment, the following topics must be characterized.

**Flow Patterns:** Shock Shape, shock locations, boundary-layer transition locations, reattachment, boundary-layer thickness and profiles, and vortex patterns all significantly affect the determination of flight performance and ultimately the design of the flight vehicle.



**Turbulence:** Fluctuations in pressure,  $P'$ , density,  $\rho'$ , temperature,  $T'$ , and velocities  $u'$ ,  $v'$ ,  $w'$ , as well as frequency spectra and power spectral densities, must be measured or determined. Since the determination of these parameters depends heavily on statistical analyses, extreme care must be taken in their measurement, estimation, or calculation.

**Thermodynamic States:** Spectroscopic techniques must be employed to measure the state of the gases in conditions where physical probing is not feasible or would so adversely affect the measurement that the data could not be adequately corrected. Measurements include, but are not limited to, rotational lines, vibrational bands, luminescence, induced fluorescence, Rayleigh scattering, excited electronic states (electronic excitation), net charge, currents, and electron beam fields.

These measurements may be made in conjunction with or separately from forces and moments and heat transfer rates. In addition, combustion requirements and effects must be considered if propulsive studies are to be made. All this must include measuring the parameters that describe performance in flight and those that describe deviations or departure from the flight conditions.

One of the driving forces behind the research and development of diagnostic techniques for hypersonic flows is the need to validate CFD codes (Marvin 1988). This matter is discussed in some detail in Section 3.

## 6.2 Status - January, 1994

AGARD-CD-514, Theoretical and Experimental Methods in Hypersonic Flows, published in April 1993, extensively categorized the state-of-the-art in hypersonic diagnostics. A hypersonics mini-symposium, held at Wright-Patterson AFB in May 1993 was the forum for update discussions on some of the technologies presented and discussed one year earlier at the AGARD meeting. This report, therefore, will concentrate on updating the activities that have occurred in the U.S. since the AGARD meeting.

Diagnostic developments in hypersonic flow measurements in the United States, since that symposium, have reached, essentially, an evolutionary phase in their progress. Direct measurement of skin friction and heat transfer in rough and smooth surfaces was made in the Mach 6, high-Reynolds-number facility at WPAFB Wagner (1993). The direct use of skin-friction and heat-flow sensors gave performance levels of  $\pm 6.0\%$  in the conventional heat-transfer coefficient and  $\pm 0.2\%$  full scale (nonlinearity and hysteresis) in shear-stress measurement.

Also at Wright Laboratory, LDV measurements were accomplished at  $M = 6$  and  $M = 12$  in the cold-gas facilities in the Flight Dynamics Directorate (Maurice 1993; Schmisser and Maurice 1994). 2-LDV measurements were made in a Mach 6 flow over and through a generic hypersonic inlet model where the flow had been calculated using a Navier-Stokes code. Particle response through oblique shocks was corrected for particle lag, and comparisons were made with the CFD solutions showing good agreement where there was no shock-wave/boundary-layer interaction, but a significant discrepancy existed internally in the nozzle where the shock-wave pattern was complex. Pressure distributions on the cowl and ramp

matched the CFD solution, indicating the danger of just matching pressure distributions with the CFD solution.

Additional measurements in the 20-inch Mach 12 tunnel were made in the shear layer at the nozzle exit in the free stream and behind the shock on a cylinder model injected into the flow. CFD solutions of the nozzle flow field were made using a full N-S solution in the throat region, a PNS code in the expansion section, and an Euler scheme in the free-jet portion of the test section. A notable result of the work showed that the alumina seed, regardless of size, never reached the theoretical free-stream velocity, even though it had three meters of nozzle length within which to equilibrate.

Other particle techniques that have emerged include an LV system proposed by Smeets which is being developed at NSWC for their hypervelocity facilities. This technique allows the use of submicron size particles, and since it incorporates a spectrometer with a one-microsecond response, the measurement of highly turbulent flow is possible.

A technique proposed for propulsion testing in HYPULSE at GASL involves seeding the  $H_2$  plenum chamber with Silane and some  $O_2$ , which then spontaneously burns, creating  $SiO_2$  as a by-product in the submicron size range. A long-pulsed, flash-lamp, pumped-dye laser with a 50  $\mu s$  pulse width, giving 150 mm of flow passing through the sheet, is used to track the flow using Mie scattering. This process gives the opportunity to observe mixing and also relate concentrations to intensity to get time averaged measurements of the  $H_2$  mass fraction. CFD calculations are also being made. Standard video cameras are being used to prove the concept before going to higher resolution optics. A practical problem is the vaporization of the  $SiO_2$  at very high temperatures, causing data dropout.

Efforts at AEDC include PLIF imaging in the Mach 8-14 impulse facility, imaging NO to determine concentration and temperature and also doing nonabsorptive Rayleigh scattering to determine He arrival. Dual pulse LIF is planned for the next fiscal year. Work will also be done in Tunnel B at Mach 8 measuring jet-interaction phenomena using LIF of NO looking at parts/trillion.

Later this year, a dual line LIF system using  $O_2$  in the H2 facility measuring temperature and density and LIF velocity measurement using atomic copper also in H2 will be attempted. Plans also included the use of a pulsed e-beam in H2 to measure densities. AEDC has also looked at flow fields in shuttle engines using naturally occurring sodium in the hydrogen, where the sodium is vaporized in the hot hydrogen and imaged. One can scan the laser and then measure temperature, density, and pressure.

Boeing is continuing to pursue PLIF measurements in their shock tunnel by looking at large NO concentrations (1% or more) to enhance signal levels. Quantitative measurements of temperature and density are being sought. Coaxial thermocouple heat transfer gauges are being used instead of thin-film gauges due to reliability. Iron-constantan gauges are used in steel models, or plugs are used in aluminum models.

The LENS facility at CALSPAN is using an advanced version of pulsed e-beam and LIF technologies to probe the flow field for measurements of temperature and density.

NASA Ames is continuing development of optical techniques in their 16-Inch Shock Tunnel, including an optical-probe layout in a scramjet model looking at the Raman scatter of nitrogen (Cavolowsky et al. 1993). NASA Ames is also looking at two classes of laser systems that are being developed and applied to absorption measurements of the critical species  $O_2$ , OH, and  $H_2O$  in hypersonic reacting flow. An Argon-ion pumped tunable ring-dye UV laser system at 306 nm probing OH has been tested.

Also under development are two laser-diode systems: one for the measurement of  $O_2$  in the near IR at about 760 nm and the other for the measurement of  $H_2O$ , also in the IR at about 1385 nm. These systems have great potential for flight-vehicle application since they are small and rugged. The systems have all been validated in shock tube experiments simulating pressures, temperatures, and velocities applicable to hypersonic simulations. OH mole and temperature were measured in an expanding nozzle flow in the 16-Inch Shock Tunnel at a simulated flight Mach number of 14.

Flow-visualization techniques included double-pulsed laser holographic interferometry in the Ballistic Range Facility at a Mach number of 14.4 (Tam et al. 1991). "Synthetic" infinite fringe interferograms are also calculated to examine the intensity pattern of the experimental finite fringe interferogram. These results show flow features in the wake region not found on the experimental interferograms.

Work is ongoing for the development of Resonant Holographic Interferometry Spectroscopy Tomography (RHIST) flow diagnostics of hypersonic flows and combustion. RHIST will be used to quantitatively measure OH concentration in combustor flows.

NASA Langley is continuing to pursue the CARS technique for the measurement of temperature and species in scramjet flow.

NASA Langley is also testing the use of modulation absorption spectroscopy for their 8-foot High-Temperature Hypersonic Tunnel to perform scramjet thrust tests, measuring gaseous concentration and temperatures. Both amplitude modulation spectroscopy and wavelength modulation are being tested. Infrared absorption spectra of constituent gases by using diode lasers is measured. Test-cell results measure changes in oxygen concentration of 0.1% using the  $X^3\Sigma_g^- \rightarrow b^1\Sigma_g^+$  transition. Raleigh imaging is being used at Langley to look at condensate fog in the  $M = 6$  realm where velocity can be measured.

In Europe, work continues in the application of spectroscopic diagnostic techniques to studies on HEG in Göttingen (Beck et al. 1993). LIF measurements have been carried out in the vacuum wind tunnel V2G in Göttingen, the arc-heated tunnel LBK in Cologne, and on the shock tunnel TH2 in Aachen in preparation for measurements in HEG. Emission spectra over the range of 200-850 nm from the hot gases behind a model bow shock has been carried out. NO excitation spectra were measured in V2G and LBK

with temperature and NO concentration being measured in the free stream in LBK.

Free-stream temperature and NO concentration were also measured in TH2 using a single-shot, two-line measurement. Early emission spectra in HEG shots with nitrogen reevaluated that a major limiting species was atomic iron (Fe) requiring the introduction of a copper liner in HEG to prevent the ablating wall effect.

Other work in Göttingen using LIF with an ArF excimer laser (192.8-193.8 nm) in V2G using 90% He + 10% NO and 90%  $N_2$  + 10% NO revealed the rotational temperatures of NO and  $O_2$  at low densities (Grundlach and Hirai 1993). Rotational-temperature measurements were made near a hot copper model of the reflected NO molecules coming back from the surface at nearly free-molecular conditions. Results show a significant deviation from total accommodation at surface temperatures  $T_w > 600$  K where the results indicate that the gas surfaces can be studied by LIF spectroscopy.

A study has been conducted at the von Kármán Institute looking at the application of Particle Image Velocimetry (PIV) in hypersonic facilities (Moraitis and Simeonides 1993). Mie scattering calculations indicate that very small particles, with a diameter of 50 nm or smaller can be detected with readily available lasers and films. Problems from flow contamination by foreign particles would have to be investigated.

ONERA has conducted tests on a heat-flux measurement technique based on a luminescence coating in their R3CL Hypersonic Blowdown Wind tunnel at Mach 10 (LeSant and Edy 1993). Tests were performed at a stagnation pressure of 12.5 MPa and a stagnation temperature of 1050 K. Work was done using a model made of insulating material since the coating has insulating thermal properties. The technique must be proven on metal models to allow for standard temperature measurements.

Work at Caltech in the shock tubes/shock tunnels is being done with PLIF techniques using multiple lines in the same shot to look at more complex flows. Measurements are being made to study chemical effects on boundary-layer stability, boundary-layer transition, and on nonequilibrium flows. Resonant Holography is being used to take holograms of flows that are resonating in some species like  $O_2$  or NO and capturing shock structures.

Rayleigh imaging is being considered by several researchers, but whether it works in the low densities of hypersonic facilities is questioned. One approach is to use multiple-reflecting-mirror sets where one passes the laser beam time and again through the flow and then rasters down to take an image. This way one increases laser power by 10 or 20 to compensate for low-signal levels. This approach, combined with filtered Rayleigh scattering, can eliminate the background scattering from windows and walls.

Another technique getting another look is sodium laser induced fluorescence, previously called Resonant Doppler Velocimetry. In heated facilities, which have sodium and copper, one can look at laser induced fluorescence from these species and get good images of the flow structure. One can look at flows with sodium in the parts per billion range.

Many other diagnostic concepts and variations of existing techniques are under development or testing in various centers around the world. The evolutionary process for diagnostic development continues in all speed regimes; whether it continues to expand in hypersonic facilities will be dictated by rapidly changing events.

## 6.2 Status - January, 1997

Since the last report, activities in hypersonic studies in the U.S. have moderated and are being compromised by continuing budget cuts and restrictions.

Work at Wright Laboratory has been on hold since the hypersonic facilities have been put on a standby status. Work is being completed on tests made in the Mach 6 facility using Rayleigh Scattering to measure density profiles, with mixed results due to scattering effects from condensing water vapor and carbon dioxide, which form nuclei around which oxygen and nitrogen can condense at low degrees of supersaturation. Holographic Interferometry detection of "rope-like" structures in the boundary layer of a cone at Mach 6 are being analyzed to determine stability characteristics and to examine the validity of linear stability theory for these flows. All other activity is on hold with no new testing scheduled for the near term and no new programs being considered.

Progress is continuing on the Radiatively Driven Hypersonic Wind Tunnel Program (RDHWT) which as a facility is discussed elsewhere in this report. Instrumentation and diagnostics development to measure the relevant flow parameters involved with adding megawatts of energy to air at pressure of 700 to 1000 atm is ongoing. The current focus is to implement CO<sub>2</sub> Enhanced Filtered Rayleigh Scattering flow visualization and sodium Laser induced Fluorescence for the measurement of injection and mixing in the Mach 8 tunnel at the Princeton Gasdynamic Laboratory. The latter technique has the potential for direct application to mixing and combustion tests that would be conducted in the RDHWT. In addition, sodium seeded flows have been suggested as a medium for studying radiative energy addition processes to support development of the facility. Additional, related work includes the continued development of a pulse burst Laser system which includes a 1 Megahertz pulsed Nd:Yag laser coupled to a 1 Megahertz framing rate camera which allows for 30 frames to be captured at 1 microsec intervals, synchronized with the pulsed laser. Sequential images of a Mach 2.5 wind tunnel boundary layer have been taken, including a shock wave interaction, qualitatively capturing the boundary layer growth and development in the flow and the shock wave fluctuation previously not seen.

Since the Phase I report, Purdue University researchers have made fully operational a Mach 4 Ludwig Tube and are currently developing new flow diagnostics to measure high-speed laminar to turbulent transition in very quiet flow. Currently they have developed a laser perturber, a glow-perturber, hot-film, hot-wire, and differential-interferometer techniques to measure the transition mechanisms using elliptic cross-section cones. These techniques have been sufficiently developed and could be implemented into larger, higher Mach number facilities.

In the NASA Ames 20MW Arcjet facility, where the test gas was a mixture of argon and air, emission measurements within a blunt shock layer were made using a CCD camera attached to a spectrograph. Spatially resolved emission spectra over a 200-890 nm wavelength were obtained to determine line-of-sight averaged thermodynamic properties, including rotational temperature of the free stream and rotational, vibrational, electronic temperatures and species number density in the shock layer.  $T_r$ ,  $T_v$  and  $T_e$  measured in the shock layer agreed within their uncertainties for two positions closest to the model.  $T_r$  was measured in the free stream using five different NO bands, and the value from each band system was in the estimated error bound from the other band systems.

NASA Ames is also using Laser Induced Fluorescence (LIF) in its arc-jet facility to measure velocity, temperature and species concentration in the very high temperature arc jet flow. NASA Ames is looking at two photon excitation of N<sub>2</sub> and single photon excitation of NO.

The Lens Facility at CALSPAN continues to develop advanced electron beam technology to measure the rotational temperature of N<sub>2</sub>, to obtain the N<sub>2</sub> number density and vibrational populations, as well as to detect unknown gases and atomic species in the flow. USC has developed a Pulsed Electron Beam (PEB) which can operate at potentials of order 40 KeV with currents of 500 - 2000 A with a 10 nSec rise time. This technique delays serious complications of collisional quenching to higher densities up to  $10^{18}/\text{cm}^3$ . Also, due to high currents, a high density of excited states are produced, providing a strong signal relative to the high background levels. The plan is to use this device in the LENS Facility following the success of the continuous wave electron beam. Also in LENS, a tunable semiconductor diode laser, pioneered by Hanson at Stanford, was used to measure temperature, velocity and water partial pressure. This measurement was accomplished by using a hardened probe installed directly into the flow field. Spectrographic techniques are also being employed to determine the species concentrations. Advances in thin film and coaxial gauge instrumentation continue to be accomplished in LENS, where DSMC and Navier-Stokes codes are used to compare experiment and computation. Results indicate good agreement using DSMC in the low-density regions around a planetary probe model, although the computed rates did not exhibit similar characteristics as the measurements did.

The HYPULSE Facility at GASL is conducting fuel plume imaging measurements using monodisperse, one micron SiO<sub>2</sub> particles which are illuminated using a Laser light sheet from an Alexandrite solid-state Laser with a 100 micro-sec pulse width. From a time-averaged image of the density of the particles, one can track the H<sub>2</sub> accurately and back out the H<sub>2</sub> concentration. This method replaces the silane technique which was not successful due to the unknown size of the particles from agglomeration during a run. Also, a water vapor measuring technique, similar to the one being used at CALSPAN, using a tunable diode laser where a beam splitter sends three parallel beams across the combustion field to detectors in a heterodyning fashion, is being employed. However the technique does not give concentration or temperature, so a variation using two water bands is being developed.

In T5 at the California Institute of Technology, to supplement the diagnostic systems currently in place and reported elsewhere, consideration is being given to the use of Particle-Image Velocimetry to measure profiles of transitional and turbulent boundary layers in the presence of dissociation and weak ionization. Recently in T5, a simple duct device was used to detect driver gas arrival at the test section. The technique measures the pressure rise in the duct detector which is affected by the arrival of the driver gas for very carefully designed detectors. Initial results showed good consistency over a wide range of enthalpies and suggest the duct detector will be a useful tool to determine test time for these type facilities.

At AEDC in their Impulse Facility, a dual PLIF system has been installed to measure the temperature and density of NO<sub>2</sub> in the flow, both in the free stream and inside a shock layer around a conical model. CFD calculations were compared with the PLIF measurements showing temperatures lower by 400-500 °K than the theoretical values. The PLIF data are complicated by laser absorption and spectral hole burning in the free stream. Ablation contamination of the flow is considered to be the leading candidate as the source of the temperature discrepancy.

In Europe, spectroscopic work at DLR in Göttingen, Germany in the HEG Facility is being used to measure quantitative, absolute temperature. LIF tests were conducted in HEG at enthalpies of 21 MJ/Kg and pressures of 39 Mpa. Two counterpropagating ArF excimer laser beams at 193 nm are tuned to two different transitions of NO<sub>2</sub> and excite fluorescence from the free stream, behind shocks and in wakes. The short tunnel test times (1-4 msec) require a single-shot technique, making the quantification of the flow parameters difficult. Results to date indicate that the technique must be refined to reduce the uncertainty in the data. The tunable diode laser absorption technique has also been tried in HEG, attempting to detect absorption from an excited state of O so a kinetic temperature (from the absorption bandwidth) and a flow velocity (from the Doppler shift) could be measured. First attempts could not detect the O atom absorption and the sensitivity of the technique is being examined.

Onera, in France at their various research facilities, has, for several years, been pursuing advanced diagnostic techniques for hypersonic and hypervelocity flows. Their preferred methods for high enthalpy facilities include diode laser absorption spectroscopy for free-stream measurement of velocity and static temperature; CARS for point measurement of rotational and vibrational temperatures, and N<sub>2</sub> density with velocity a possibility and Electron Beam Fluorescence and LIF for qualitative imaging and visualization. Work is planned for their R2Ch wind tunnel at Chalais-Maudon using CARS for measuring temperature. They hope to expand the capability for use in their high enthalpy, short duration tunnel, F4.

## 7 FUTURE FACILITY NEEDS AND FACILITIES IN DEVELOPMENT

### 7.1 Results of American Studies

Potential future missions planned by the Americans involving hypersonic flight (air-breathing access to orbit/hypersonic cruise/planetary and earth entry/aeroassist) will require ground-test capabilities for aerothermodynamics testing which cannot be met with simple modifications to existing facilities. Further, some of the required technologies and methodologies for new facilities which can meet the requirements are not in place. This shortfall has led to advocacy within the United States for substantial investments in "facilities research" which will ensure the efficient design/construction/operation of the next generation of U.S. hypersonic facilities.

The following is a synopsis from the aerothermodynamics section of the December 1992 United States Department of Defense/NASA Hypersonics Test Investment Plan (HTIP). This plan is for U.S. Government use only, but the following synopsis has been approved for inclusion in this AGARD document by the HTIP Co-Chairs K. Richey (USAF) and Wayne McKinney (NASA). According to the HTIP report, facilities filling the anticipated needs for aerothermodynamics in the near, mid, and far term are specified below:

**Near Term:** Research should be done to enable the implementation of a large-scale, advanced expansion-tube/shock-tunnel to be used for study in the true-enthalpy flight regime of Mach 16 - 20+. Real-gas effects could be studied in air and planetary atmospheres. The facility would employ the double-diaphragm, shock-tube approach where energy is added to the moving stream as depicted in Figure 8. Arbitrary test gases can be used and, ideally, low dissociation will be experienced in the free stream because the flow is not stagnated. In full scale, this facility would use a 610 mm diameter free-piston driver, a 1.52 m diameter test section, and would have test times of approximately 2 ms. Early research for this facility would include analysis of driver options as well as issues of losses/disturbances and unwanted dissociation effects associated with the secondary diaphragm. The research will include CFD and experimental studies in existing small expansion tubes such as the NASA Langley GASL Facility.

**Mid term:** Studies are advocated to proceed preconstruction of a large facility with several second flow duration at Mach 16+ equivalent enthalpies in a 1.52 m test section. These flows would be driven by a reservoir with temperatures and pressures of 8000 K and 14000 atm, respectively. Facility research would focus early on exploring an extension of the Russian approach to increasing flow time in impulse facilities by using the type of driver depicted in Figure 19. This driver, called a Piston Gasdynamics Unit (PGU), is operational at the TSNIMASH research center (Anfimov 1992; Anfimov and Kislykh 1990) and uses special valves between a piston and the stagnation chamber to subject the test gas to multiple shock passage/heating cycles. Early research on this facility would include analysis of nozzles which minimize reservoir dissociation products (O and NO) in the test section as well as studies of materials which can withstand formidable heat transfer to the accumulators, valves, stagnation chamber, and nozzle throats.

**Far term:** Research includes work on a large ballistic range which would employ large (up to 300 mm diameter) models up to 15 km/s with advanced onboard and nonintrusive instrumentation. A major research issue here is a model launcher. Possible solutions are the University of

Washington's "Ram accelerator" and the Russian TSNIMASH approach with an evacuated tube and timed explosives on walls to accelerate the model (Figure 20 from D. Wilson at the University of Texas at Austin). Advantages of ballistic ranges for aerothermodynamics are well documented in Witcofski et al. (1991).

Finally, the general feeling in the U.S., documented in the HTTP report, is that new, innovative ideas for hypersonic facilities should be nurtured. An example is the high-pressure, cryogenic arc concept as described by Rizkalla et al. (1992).

The United States Air Force Scientific Advisory Board SAB (May 1989) document also is available only to U. S. Government Agencies. The recommendations listed therein are consistent with those discussed in the HTTP report outlined above. The SAB report recommended that research on large arc jet wind tunnels be conducted at the NASA Ames Research Center and at the Arnold Engineering and Development Center, and this is being done, albeit at low levels.

As of August 1996, it is noted that no monies have been made available for using a piston driver for expansion tubes within the United States. However, innovative work at GASL Bakos, et al. 1996) is showing that new test capabilities may be obtained in expansion tubes by drivers employing shock-induced detonation waves. Further, the only research potentially taking advantage of the Russian piston gasdynamic units in the U.S. appears to be within the new studies of a radiatively driven wind tunnel discussed in the next section.

### 7.1.1 Radiatively Driven Hypersonic Wind Tunnel RDHWT

A novel concept is currently being studied (Miles et al., 1994 and Macheret et al., 1995) in the US to circumvent the well-known limitations of providing long-duration, ground aerothermodynamic test flows with true flight simulation for Mach number in excess of about 10. The limitation is that conventional isentropic expansion wind tunnels require that high-temperature air must be contained in a plenum and then flow through a small throat before expansion in the nozzle. This limitation limits one to the lower Mach number regime for long-duration flows or to short (milliseconds) test section flows, possibly contaminated throat material and/or NO created by the high temperatures in the plenum.

Work on the RDHWT has been ongoing for about two years. The approach is to take advantage of Russian Technology discussed above for piston gasdynamic units (PGU's) to provide low-temperature, ultra-high pressure air in a plenum. The concept is that the PGU provides cold, high-density flow through the throat, possibly circumventing both the production of NO in the plenum and the throat-erosion problem. After an initial supersonic expansion, additional energy is added by coupling to either optical or microwave sources. Figure 21 from Miles et al. (1994) shows a schematic comparison of the two approaches.

As discussed by Miles, the ultra-high pressure in the plenum is such that the air cannot be treated as an ideal gas. They believe that the real-gas effects can lead to much

higher kinetic energy passing through the throat at Mach 1 than would be possible for an ideal gas.

Considerable effort and thought is being focused on this activity, including study of energy addition and thermalization of the flow as discussed by Marcheret et al., 1995.

## 7.2 Results of European Studies

An ESA study was initiated in the early 1980's to assess the level of European competence in hypersonic facilities and computational tools required for the design of specific two-stage launchers to LEO. Recommendations were made which concentrated on bringing back into useful operation a series of tunnels that had been constructed in the 1960's. Many of the recommendations were put into effect as the Hermes program developed. However, to the author's European knowledge (J. F. W.), no more recent ESA study looking toward an entire series of missions involving hypersonic flight has been commissioned.

Except for two thermal protection testing facilities called Sirocco and Plasmatron, which are under construction, no new facility is currently planned in Europe for high-enthalpy aerodynamic studies. The efforts will be devoted in the short term to get fully in line the HEG and F4 wind tunnels and to develop appropriate flow diagnostic methods.

The time is not well chosen to consider the possible development in the longer term of new facilities. There is certainly no money available in the foreseeable future for new developments of large size, and there is not even enough activity to keep the present facilities busy. As far as facilities are open for industrial testing, any new duplication should certainly be avoided within NATO in order not to decrease further the workload of each facility.

However, one should keep in mind, when looking at the technical needs, that the development of such facilities takes 5 years if on a national basis, and up to 15 years if in the frame of an international agreement. Therefore, it is still time for AGARD to think about technical needs for future hypersonic aerodynamics facilities, as far as really new needs are identified or new opportunities appear to fulfill unsatisfied needs. Selected authors have expressed their personal views (Muylaert et al. 1992; Wendt 1992; Kuczera and Weingartner 1993; Hirschel 1993).

The long-term objective should be seen as full-flight simulation with clean equilibrium flows to Mach 16-18 and constant conditions for at least some tens of ms. It is clear that much effort must be expended in the interim on such areas as

1. specially designed code validation tunnels (e.g., the iodine vapor facility of Pham-Van-Diep et al. 1992)
2. the "hot-model" technique for radiation dominated flows
3. transition triggering mechanisms, so that a rational decision concerning the need for a "quiet" hypersonic tunnel can be made
4. instrumentation to reliably measure all appropriate temperatures and constituent concentrations with sub-ms response times in the harsh environment of real facilities

5. techniques to add energy to a flowing gas, e.g. by lasers, to avoid the need of stagnating the flow
6. large-scale ballistic ranges and associated instrumentation; e.g., the ram accelerator method

### 7.2.1 *Plasmatron*

A Plasmatron is an induction-heated wind tunnel in which a jet of air (or other gases), heated at temperatures from 6000 K to 10,000 K to a plasma state, is directed onto a target, primarily for the purpose of testing the resistance of thermal protection systems. Figure 22 shows the working elements of the facility.

In 1992, facilities of this kind were found to exist in Russia, where they have been extensively used for the testing and optimization of the ceramic composites used as thermal protection tiles for space reentry objects such as the soviet capsules and the shuttle Buran.

The European Space Agency, recognizing the advantages offered by such facilities in terms of chemical purity of plasma, compared to the arc-jet facilities traditionally used in the western world for the same purpose, decided to sponsor together with the Belgian Federal Office for Scientific, Technical and Cultural Affairs, the construction of a 1.2 MW Plasmatron at the von Karman Institute.

Two interchangeable torches of 80 mm and 160 mm diameter will allow the generation of subsonic and supersonic plasma flows with stagnation pressures ranging from 5 to 175 mbar, producing (catalytic cold wall) stagnation heat fluxes of 350 to 1200 kW/m<sup>2</sup>. The facility will feature segmented water-cooled cold cages in the torches and a solid-state thyristor rectifier and MOS-inverter oscillator. The control system will allow fully automatic operation of the facility from warm-up to complete stop, with varying test parameters to simulate re-entry trajectories.

Intrusive and nonintrusive measurement techniques will be used, including emission spectroscopy and LIF.

The planned completion of the Plasmatron is scheduled for October 1997.

### 7.2.2 *SCIROCCO*

During studies on the HERMES Spaceplane Programme, the European Space Agency (ESA) identified the need to have a large, high-enthalpy plasma wind tunnel to test and qualify real-scale parts of the spacecraft. SCIROCCO is a 70-MW arc-heated free-jet wind tunnel. This facility would be called an arcjet in the U.S. It is now (late 1996) in its realization phase and will be fully operational at CIRA in Capua by early 1999. This facility is cofunded by ESA and the Italian Ministry of University, Scientific and Technological Research (MURST).

## 8 RECOMMENDATIONS ON POSSIBLE AREAS OF COOPERATION AND POTENTIAL BENEFITS

The benefits of collaboration will be more pronounced if a specific joint project(s) can be defined; at the present time,

only Huygens/Cassini is firm, and collaboration on the aerothermodynamic issues is not part of the accord.

However, members of the AGARD WG 18 hope that the future will bring one or more joint projects involving Earth or planetary entry. Obvious candidates are the robotic and human exploration of Mars and exploration of one of Jupiter's moons, Europa. These possibilities arise because of the very recent discoveries of possible evidence of life in Mars meteorites reported by U.S. and British scientists and images from the Galileo spacecraft showing apparent ice covers on Europa. These images suggest the possibility of warm water beneath the ice where life could exist. The use of aerocapture (the use of atmospheric drag forces rather than retropropulsion) for orbit capture and high-speed entry to planetary surfaces from interplanetary trajectories will be important for the transportation systems for these missions. Cost sharing for the aerothermodynamic testing and development of such space transportation systems could hasten the day when humankind will know the answers to these very profound questions. Prior to this time, a certain number of actions will be very useful as precursors to an eventual joint project.

Based on the perspective of the space transportation and space vehicle programs considered by Europe in the near and far future, ESA should initiate a comprehensive study on Europe's needs for new facilities; the study should take into account opportunities offered by CFD to supplement experimental tools. It should also take into account the facilities existing worldwide and the effective possibility to use them for development purposes. The results of this study should be confronted within AGARD in a manner similar to the studies performed in the U.S. The role of flight testing in design tool validation should be analyzed together with the AGARD community. The result of these studies should bring near-term, mid-term, and long-term recommendations and may bring forward a basis for a possible collaborative effort on an international scale.

Within the limited travel funds available, AGARD-FDP-sponsored Symposia, workshops, professional visits, etc. should focus on real-gas hypersonics. Stress should be put on experiences with testing techniques in the recently developed real-gas facilities such as T5, LENS, HEG, F4, etc.

Exchanges of experience with Russian hypersonic facilities to understand their potential should be undertaken in cooperation among Russia, Western Europe, and America. This cooperative effort will serve to ensure that critical decisions at a later date concerning the possible construction of new facilities in the West versus the use of existing Russian facilities can be made with full background knowledge and confidence.

## 9 SUMMARY

Missions of current and future interest to the United States and Europe which involve hypersonic flight within or entry into the atmosphere of the Earth or other planets have been summarized. Aerothermodynamic issues such as heating and chemical reaction rates which arise because of the high-flight velocities have been discussed.

The problems posed for the simulation of these effects in ground-based facilities can be summarized as follows. It should be clear that presently a wide variety of facility

types is required to simulate, even partially, the expected effects. As a result, Computational Fluid Dynamics is an essential tool in the regime, assuming that the codes can be fully validated by means of appropriate experiments on the ground and in flight.

A number of new facilities have been developed in recent years for the express purpose of addressing the crucial aerothermochemistry problems posed by hypervelocity flight. These facilities are now in the "production" phase, as are the nonintrusive instrumentation techniques which have been introduced. Together, they are providing a clearer understanding of hypersonic flows.

Recommendations for the near and mid-term are

Collaborative and cost-effective efforts on projects of benefit to humankind should be encouraged, e.g., robotic and human exploration of the solar system.

Various agencies in the United States have conducted individual or joint studies on future facility needs; a similar study should be undertaken by the European Space Agency.

AGARD symposia, workshops, lecture series, etc. will also serve as a mechanism to bring researchers interested in hypersonic flight together for an exchange of ideas and experiences. Members of the AGARD WG 18 will be an important part of this activity.

A continuing effort should be made to understand Russian Facilities and their methodology of testing and design. This activity should be a cooperative one between Western Europeans, Americans, and the Russians.

## ACKNOWLEDGMENTS

The following persons have made important contributions to this chapter: W. Calarese of WPAFB and P. Vancamberg of Dassault. Acknowledgment to G.S. Deiwert of NASA Ames, and J. M. Charbonnier of VKI, M. Holden of Calspan, Hans Hournung of CALTECH, and J. Erdos of GASL is given for useful discussions and assistance in writing this chapter.

## REFERENCES

- AGARD-AR-319, 1996, Vol. 1, Hypersonic Experimental and Computational Capability, Improvement and Validation. Ed. William S. Saric, Jean Muylaert and Christian Dujarric.
- AGARDograph 138 1970 Ballistic Range Technology. Ed. Thomas N. Canning, Alvin Seiff, and Carlton S. James.
- Anfimov, N. 1992 TSNIMASH Capabilities for Aerogasdynamical and Thermal Testing of Hypersonic Vehicles. *AIAA Paper 92-3962*.
- Anfimov, N. A. and Kislykh, V. V. 1990 Multi-Cascade Compression Effective Means to Obtain High Temperature Dense Gas in Piston Gas Dynamic Units (PGU). In *Current Topics in Shock Waves. Proc. 17th Intl. Symp. on Shock Waves and Shock Tubes*.
- Bakos, R. J., Calleja, J.F., Erdos, J. I., Sussman, M. A. and Wilson, G. J. 1996 An Experimental and Computational Study Leading to New Test Capabilities for the HYPULSE Facility with a Detonation Driver. *AIAA paper 96-2193*.
- Bakos, R. J., Calleja J.F., Erdos, J. I., Anslender, A. H., Sussman, M. A. and Wilson, G. J. 1996 Design, Calibration and Analysis of a Tunnel Mode of Operations for the HYPULSE Facility. *AIAA Paper 96-2194*.
- Blanks, James R. 1996 Initial Calibration of the AEDC Impulse Tunnel. *AEDC-TR-95-36*.
- Beck, W. H., Miller, M., and Wollenhampt, M. 1993 Application of Spectroscopy Diagnostic Techniques to studies on HEG; Preparatory LIF Work and Emission Spectroscopy Results. *ICIASF '93 Record*, ISL, France.
- Beck, W. H., Wollenhaupt, M., Rosenhauer, M., Müller, T., Jourdan J. 1996 Status of the Development and Implementation of Optical Spectroscopic Techniques on the DLR High Enthalpy Shock Tunnel HEG. *AIAA paper No. 96-221, Proc. 19th AIAA Advanced Measurement and Ground Testing Tech. Conference*, New Orleans, USA.
- Belanger, J and Hornung, H. 1994 Numerical Predictions and Actual Behavior of the Free Piston Shock Tunnel T5. *AIAA Paper 94-2527*, 18th AIAA Aerospace Ground Testing Conference.
- Candler, G. V., Dimotakis, P. E., Hornung, H. G., Leonard, A., Meiron, D. I., McKoy, B. V., Pullin, D. I. and Sturtevant, B. 1995 Interaction of Chemistry, Turbulence and Shock Waves in Hypervelocity Flow, *GALCIT Report FM 95-2 Graduate Aeronautical Laboratories*, California Institute of Technology, Pasadena, CA.
- Cavolowsky, et al 1992 Flow Characterization in the NASA Ames 16 Inch Shock Tunnel. *AIAA Paper No. 92-3810*.
- Cavolowsky, J. A.; Newfield, M. E., Loomis, M. P. 1993 Laser Absorption Measurement of OH Concentration and Temperature in Pulsed Facilities. *AIAA Journal*, Vol. 31, No. 3, pp. 491-498.
- Chapman, Gary T. 1992 The Ballistic Range-Its Role and Future in Aerothermodynamic Testing. *AIAA Paper No. 92-3996*.
- Czajkowski, E. 1994 Russian Aeronautical Test Facilities ANSER Center for International Aerospace Cooperation, Suite 800 1215 Jefferson Davis Highway, Arlington, VA 22202-3251.
- Eitelberg, G. 1996 Application of Standard Measurement Techniques in a High Enthalpy Impulse Facility. *AIAA paper No. 96-0034, Proc. 34th Aerospace Sciences Meeting and Exhibit*, Reno, Nevada/USA.
- Eitelberg, G., Krek R., Beck W. H. 1996 Stagnation Point Heat Transfer Testing in non-Equilibrium Flow Produced by the HEG. *AIAA Paper No. 96-4504, Proc. 7th International Space Planes and Hypersonic Systems and Technologies Conference*, Norfolk, Virginia/USA.
- Erdos, J. I., Calleja, J. F., and Tamagno, J. 1994 *AIAA paper No. 94-2524*.
- Gochberg, L. A. 1993 *Rotational Nonequilibrium in Low Density Heated Free Jet Expansions of Nitrogen. Ph.D. Dissertation*, University of California, Berkeley.
- Grundlach, G., Hirai, E. 1993 Rotational Temperature on NO and O<sub>2</sub> in Hypersonic Free Test Flows Near a Hot Model Surface Measured by LIF. *ICIASF's 93 record ISL, France*.

- Guest, J., Williams, G., and Bogdonoff, S. 1994 *AIAA Paper 94-2472*.
- Hannemann, K., Brück, S., Bremer G., Springer 1995 Numerical Simulation of Reacting Flows Related to the HEG. *Proc. 19th Int. Symp. on Shock Waves, Marseille/F*, 1993.
- Haas, Brian L., and Schmitt, Durwin A. 1993 Simulated Rarefied Aerodynamics of the Magellan Spacecraft During Aerobraking. *AIAA Paper No. 93-3676*.
- Hirschel E. H., Deutsche Aerospace Munchen 1993 Hypersonic Aerodynamics. 2nd Space Course on Low Earth Orbit Transportation. Munich Univ. of Technology.
- Hirschel, E. H. 1991 Aerothermodynamic Challenges of the Sanger Space Transportation System. *ESA Paper No. SP-318*.
- Holden M. S., Kolly, J. and Chadwick, K. 1995 Hypervelocity Studies in the LENS Facility. *AIAA Paper No. 95-0291*.
- Holden, M. S., Chadwick, K. M., Gallis, M. A. and Harvey, J. K. 1995 Comparison between Shock Tunnel Measurements on a Planetary Probe Configuration and DSMC Predictions. *20th International Symposium on Shock Waves*, California Institute of Technology.
- Hornung, H. 1992 Performance Data on the New GALCIT Free Piston Shock Tunnel. *AIAA Paper 92-3943*.
- Hornung, H. and Sturtevant G. 1996 Research in Hypervelocity Gasdynamics. Final Technical Report, AFOSR Grant F49610-92-J-0110. Graduate Aeronautical Laboratories, California Institute of Technology, Pasadena, CA.
- Kastel, D., Eitelberg, G. 1995 A Combined Holographic Interferometer and Laser-Schlieren System Applied to High Temperature, High Velocity Flows. *Proc. ICIASF, Dayton, Ohio/USA*.
- Howe, John T. 1990 Hypervelocity Atmospheric Flight: Real Gas Flows. *NASA Reference Publication 1249*.
- Kuczera H., Weingartner S., Deutsche Aerospace Munchen 1993 Guidelines for the Selection and the Design of Future Space Transportation Systems. *2nd Space Course on Low Earth Orbit Transportation*. Munich Univ. of Technology.
- Lafferty John F., Marren Dan E. 1996 Hypervelocity Wind Tunnel 9 Mach 7 Thermal Structural Facility Verification and Calibration. *Technical Report NAVSWC TR 91-616*, Naval Surface Warfare Center, Silver Spring, MD 20903.
- LeSant, Y., Edy, J. L. 1993 Phosphor Thermography Technique in Hypersonic Wind Tunnels; First Results. *ICIASF '93 record, ISL, France*.
- Lumpkin, Forrest E. III and Chapman, Dean R. 1991 Accuracy of the Burnett Equations for Hypersonic Real Gas Flows. *AIAA Paper No. 91-0771*.
- Macheret, S., Williams, G., Comas, G. Meinerken, C., Lempert, W. I and Miles, R. 1995 *AIAA Paper 95-2142*
- Marvin, J. C. 1988 Accuracy Requirements and Benchmark Experiments for CFD Validation. *AGARD CP-437*.
- Maurice, M. S. 1993 Quantitative Laser Velocimetry Measurements in the Hypersonic Regime by the Integration of Experimental and Computational Analysis. *AIAA Paper No. 93-0089*.
- Maus, J. R., Laster, M. L., and Hornung, H. G. 1992 A High Performance Free Piston Shock Tunnel. *AIAA Paper No. 92-3946*.
- Miles, R., Brown, G. Lempert, W., Natelson, D., Yetter, R., Moraitis, C. S., Simeonides, G. A. 1993 Application of Particle Image Velocimetry to Hypersonic Flows; Perspectives and Impedimenta. *ICIASF '93 Record, ISL, France*.
- Moraitis, C.S., Simeonidis, G.A., Application of Particle Image Velocimetry to Hypersonic Flows: Perspectives and Impedimenta, 15<sup>th</sup> International Congress on Instrumentation in Aerospace Simulation Facilities, *IEEE 93CH3199-7*, pp. 41.1-41.5
- Muylart J., Voiron R., Sagnier P., Lourme D., Papirnyk O., Hannemann K., Butefisch K., Koppenwallner G. 1991 Review of the European Hypersonic Wind Tunnel Performance and Simulation Requirements. *ESA Paper No. SP-318*.
- Park, C. 1990 *Nonequilibrium Hypersonic Aerothermodynamics*. John Wiley & Sons.
- Pham-Van-Diep, G. C. Muntz, E. P., et al. 1992 An Iodine Hypersonic Wind Tunnel for the Study of Nonequilibrium Reacting Flows. *AIAA Paper No. 92-0566*
- Ragsdale, William C. and Boyd, Christopher F. *Hypervelocity Wind Tunnel 9 Facility Handbook*, Third Edition. Technical Report NAVSWC TR 91-616, Naval Surface Warfare Center, Silver Spring, MD 20903, July 1993
- Rizkalla, O.; Chinitz, W.; Witherspoon, F. D. and Briton, R. 1992 High Pressure Hypervelocity Electrothermal Wind Tunnel-Performance Study and Subscale Tests. *AIAA Paper No. 92-0329*.
- Rosenhauer, M., Wollenhaupt, M., Müller, T., Beck, W. H., 1994 *LIF Measurements in the Wake of a Blunt Body*. Proc. 2nd Symposium on Aerothermodynamics for Space Vehicles, ESTEC, Noordwijk/NL.
- Schmisser, J. D., Maurice, M. S. 1994 An Investigation of Laser Velocimetry Particle Behavior within Flow Structures at Mach 12. *AIAA Paper No. 94-0668*.
- Seibert, G. L., Miles R., Van Kuren, J., Heath, W. 1992 Optical Measurement Techniques for Hypervelocity Flows. *AIAA Professional Studies Series Notes*.
- Sharma, S. P. and Park, Chul 1990 A Survey of Simulation and Diagnostic Techniques for Hypersonic Nonequilibrium Flows. *J. Thermophysics and Heat Trans. Vol. 4, No. 2*, pp. 129-142.
- Tam, T. C., Brook, N. J, Cavolowsky, J. A., Yates, L. A. 1991 Holographic Interferometry at the NASA Ames Hypervelocity Free-Flight Aerodynamic Facility. *AIAA Paper No. 91-0568*.
- Wagner, M. 1993 Skin Friction and Heat Transfer Measurements in Mach 6 High Reynolds Number Flows. *ICIASF '93 Record, ISL, France*.
- Wendt J.F. 1992 A Review of European Hypersonic Facilities. *Proc. of Wind Tunnels and Wind Tunnel Test Techniques*, Southampton, U.K.
- Wilson G., Sharma, S. P., Gillespie W. D. 1993 Time-Dependent Simulations of reflected-Shock/Boundary Layer Interaction. *AIAA Paper No. 93-0480*.
- Witcofski, R.; Scallion, W.; Carter, D., Jr., and Courter, R. 1991 An advanced Hypervelocity Aerophysics Facility: A Ground-Based Flight-Test Range. *AIAA Paper No 91-0296*.



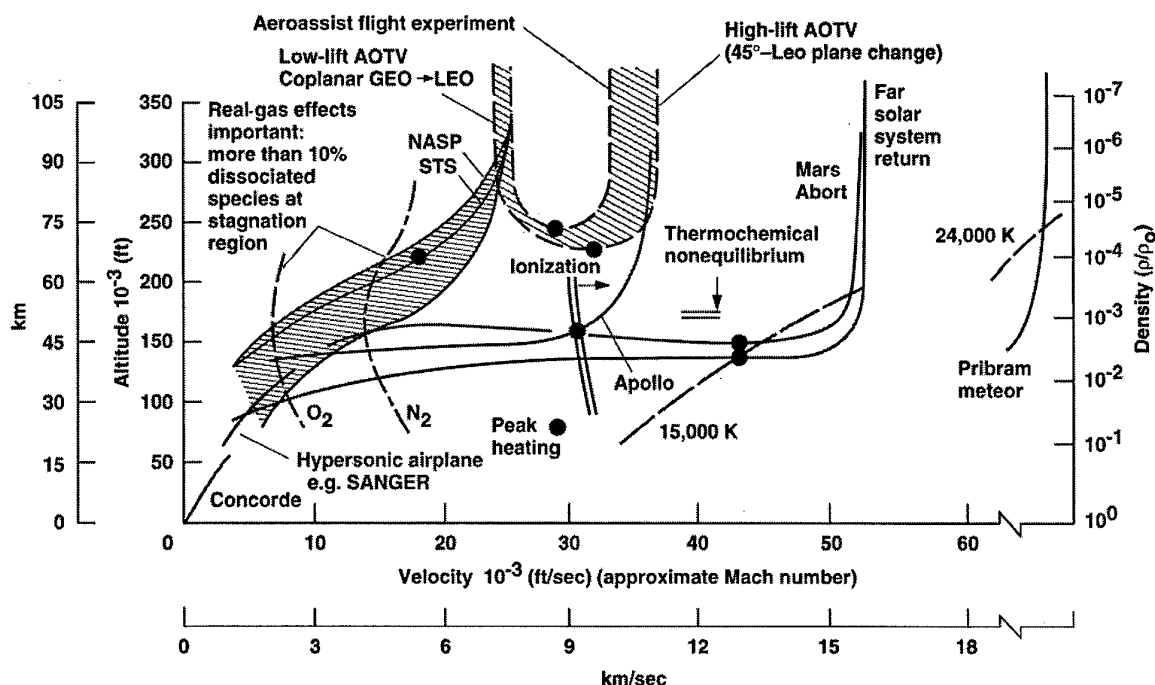


Figure 1. Comparison of vehicle flight regimes in the Earth's atmosphere of interest to the United States and Western European aerothermodynamics community.

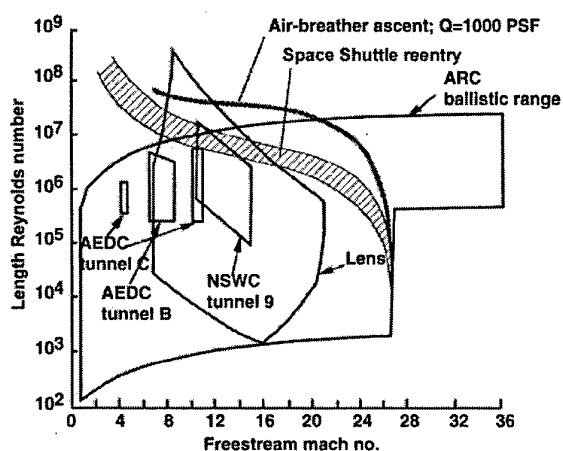


Figure 2(a). Reynolds number versus Mach number plot for American facilities with representative vehicle trajectories.

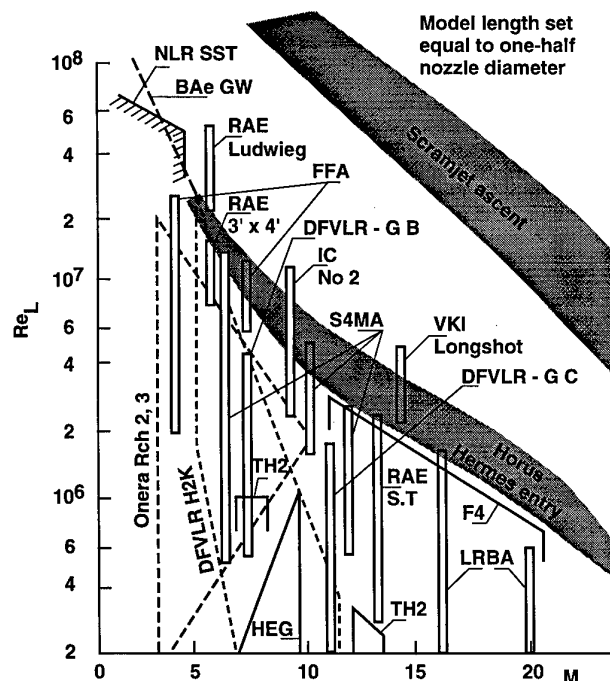


Figure 2(b). Reynolds number versus Mach number plot for European facilities with representative vehicle trajectories.

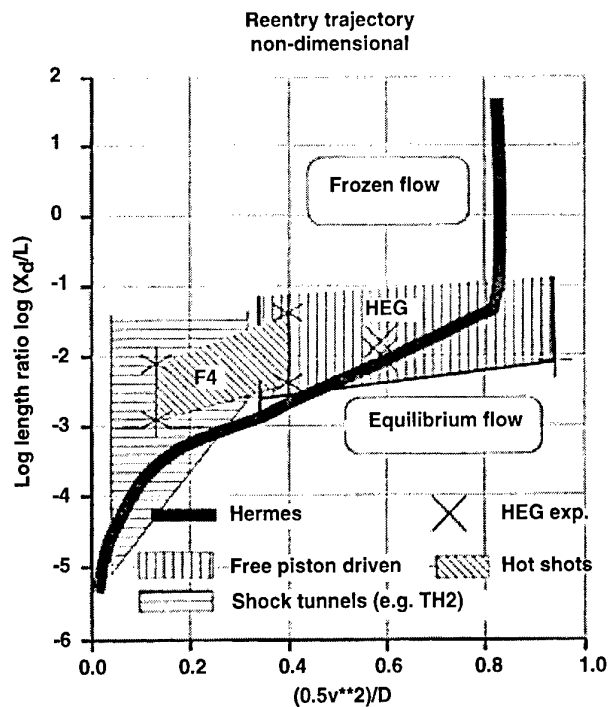


Figure 3. Simulation capabilities with respect to gas dissociation.

Here,  $X_D$  is the dissociation length for a strong shock;

$D$  is the dissociation energy of nitrogen;

$L$  is the length of the reentry vehicle;

$v$  is the free-stream velocity

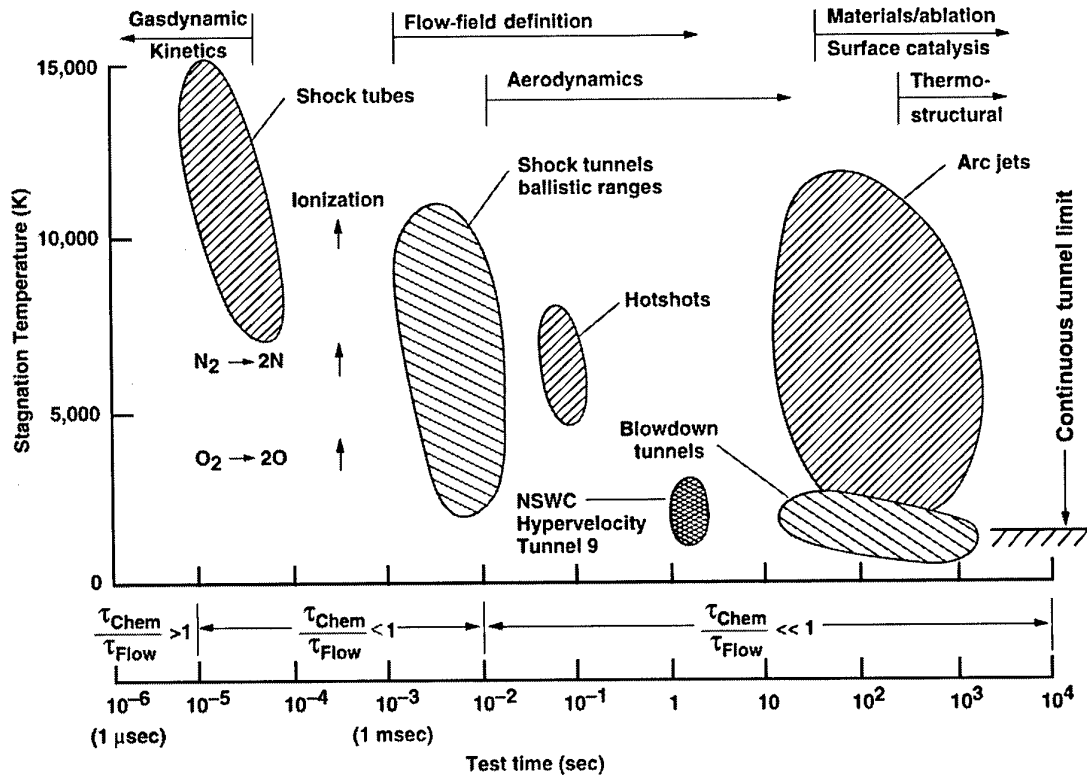
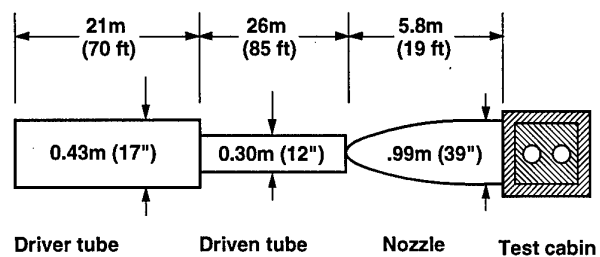


Figure 4. Stagnation point temperatures and flow duration domains for hypersonic simulation facilities.



Note: not to scale

Figure 5. Schematic of NASA Ames 16-Inch Shock Tunnel.

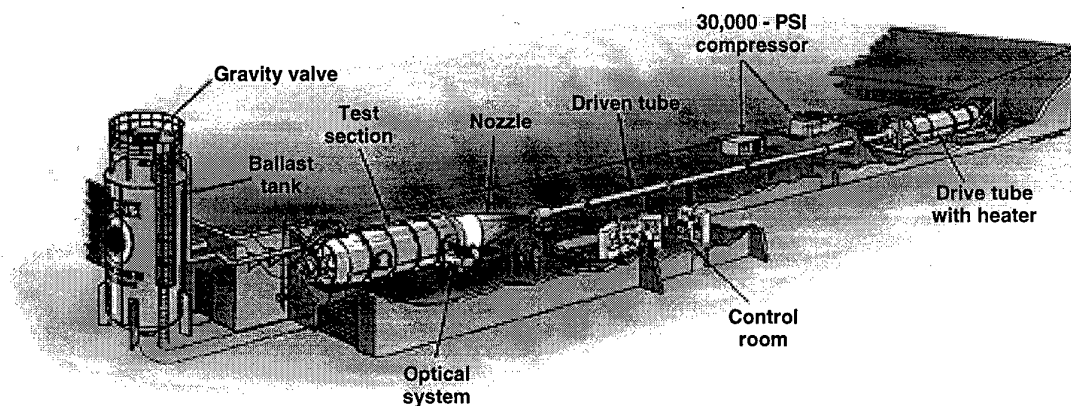


Figure 6. Calspan Large Enthalpy Shock Tunnel LENS.

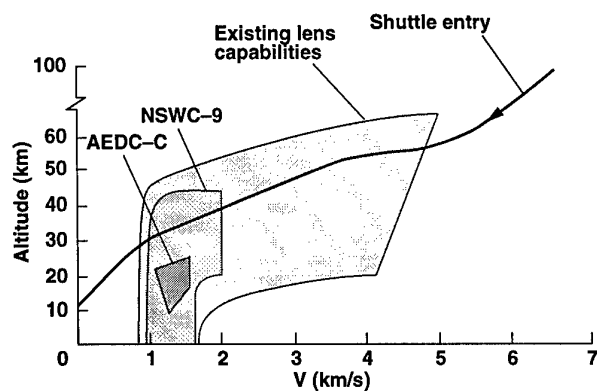


Figure 7. Performance range of Calspan LENS Facility.

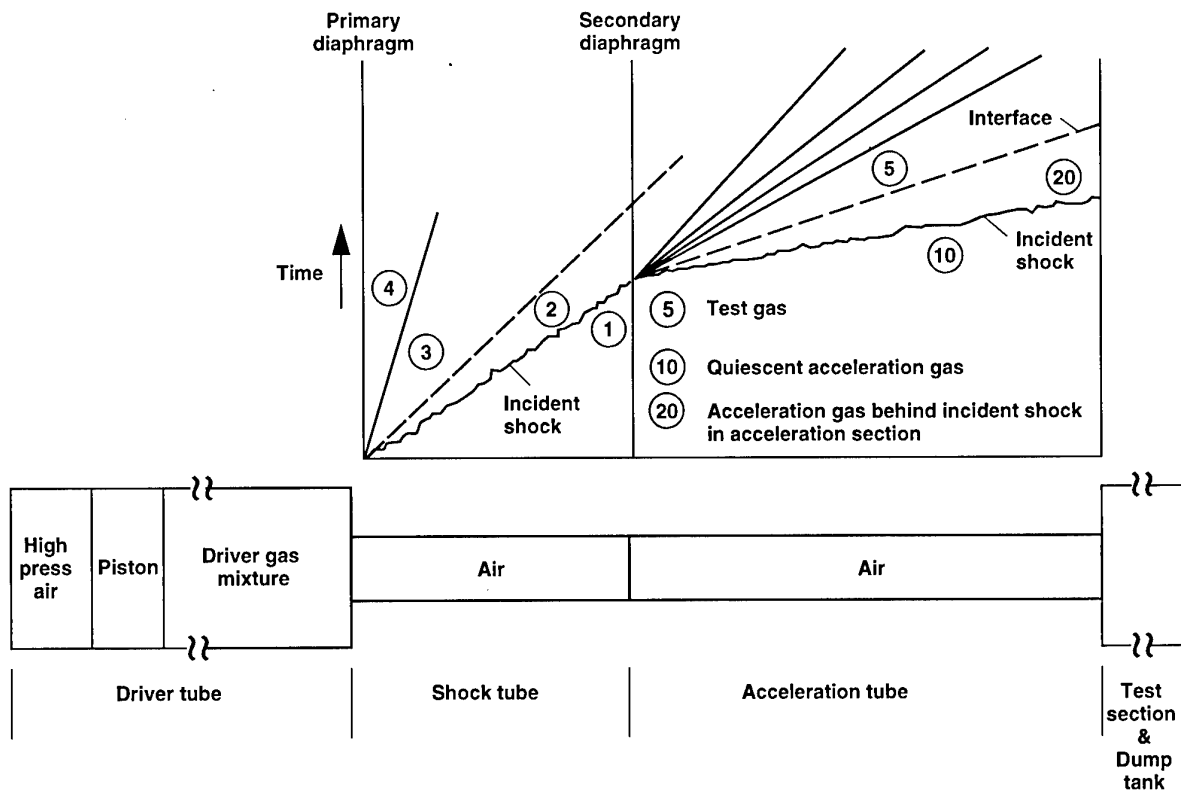


Figure 8. Operation of Expansion Tunnel with free piston driver.

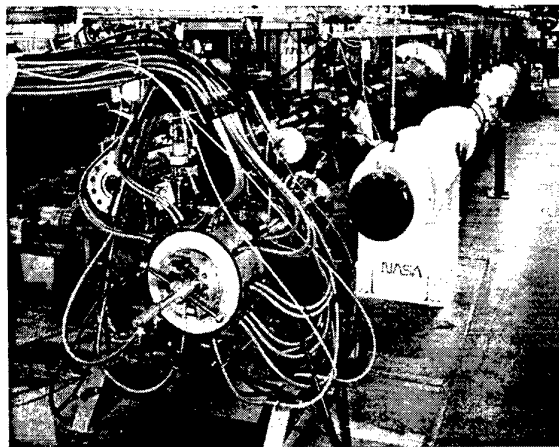


Figure 9. NASA Ames Electric Arc Shock Tube.

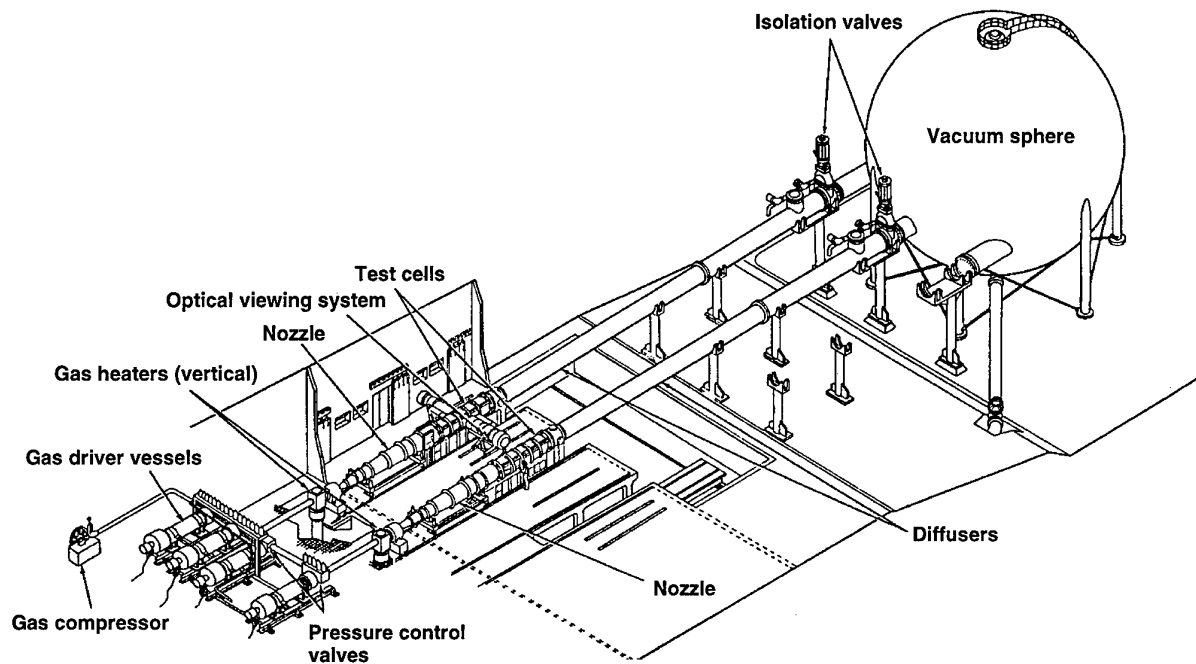


Figure 10. Naval Surface Warfare Center Hypervelocity Tunnel Number 9.

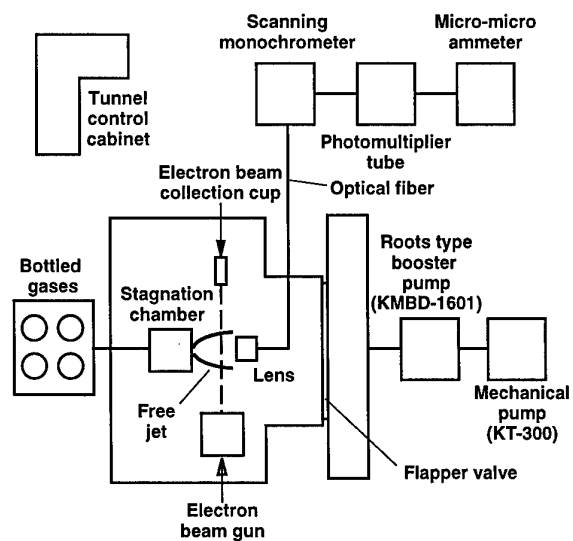
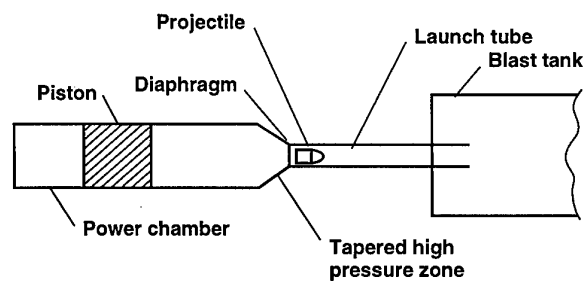
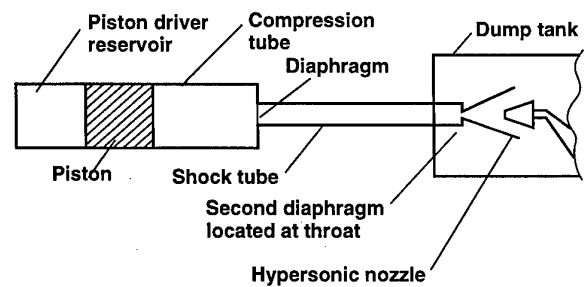


Figure 11. Schematic for University of California at Berkeley Low Density Wind Tunnel.



Impact Facility Launcher



Free Piston Shock Tunnel

Figure 12. Comparison of light-gas gun and AEDC Concept for disposable-piston, High Performance Shock Tunnel.

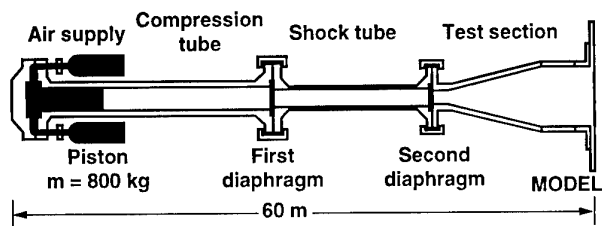


Figure 13. Sketch of the HEG DLR Free Piston Shock Tunnel in Göttingen.

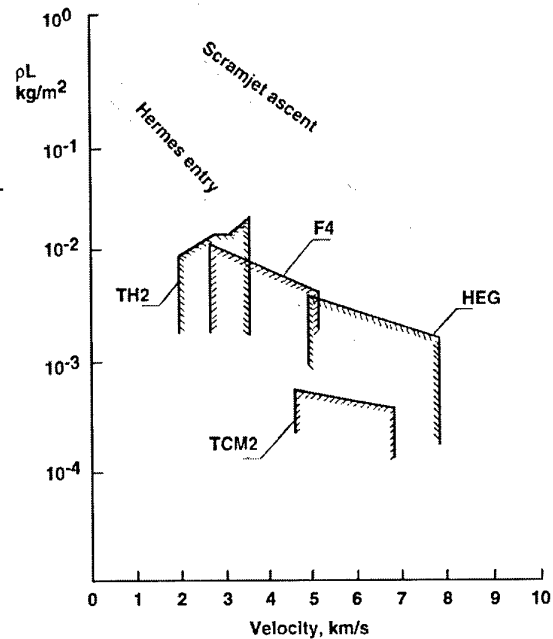


Figure 14. HEG performance and HERMES reentry trajectory.

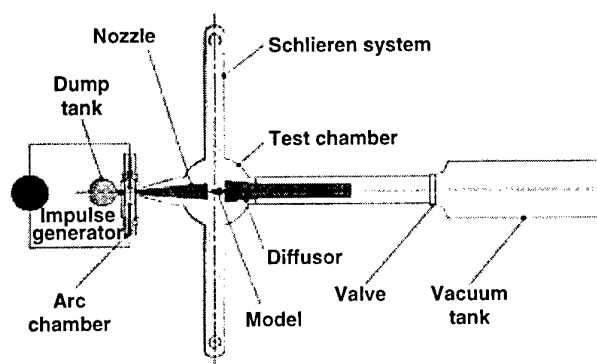


Figure 15. The ONERA High Enthalpy Wind Tunnel F4.

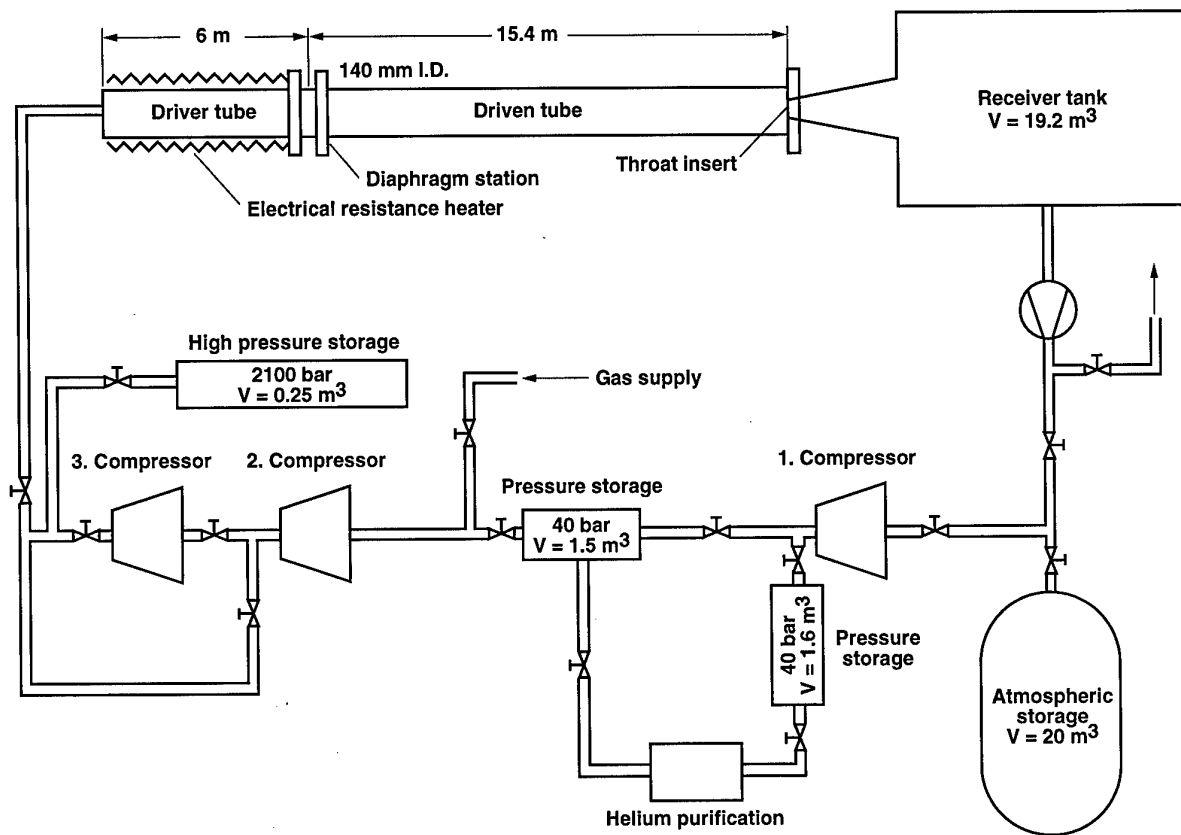


Figure 16. Basic components of the Aachen Shock Tunnel TH2.

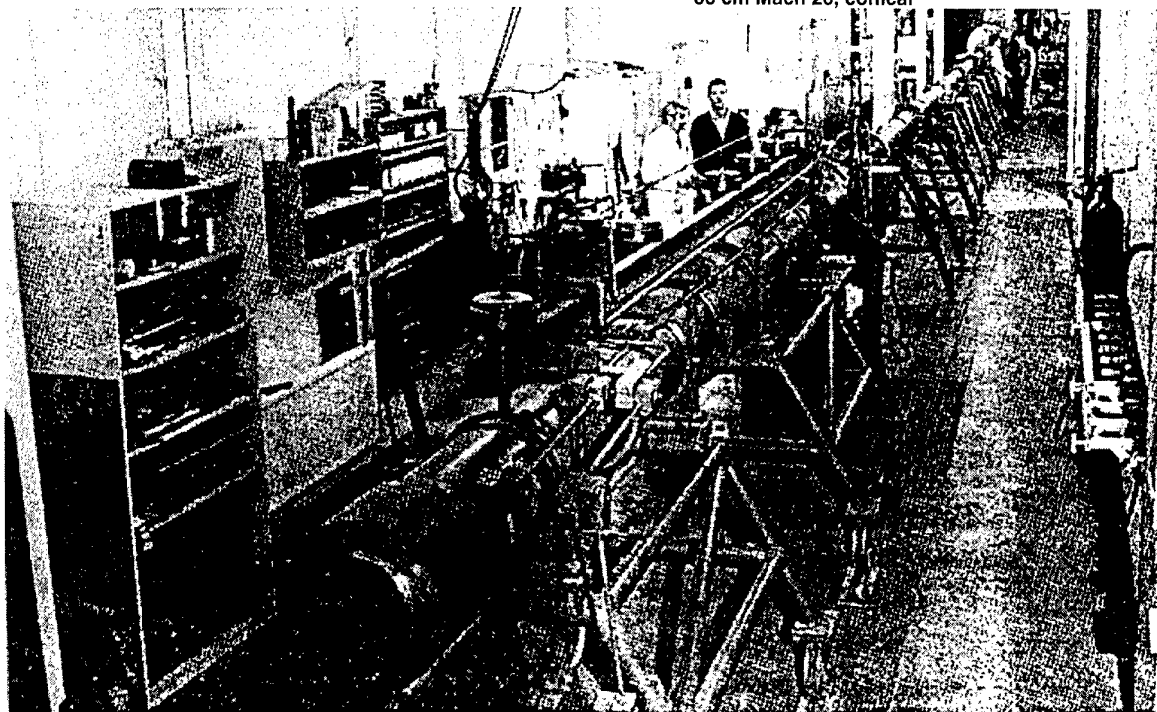
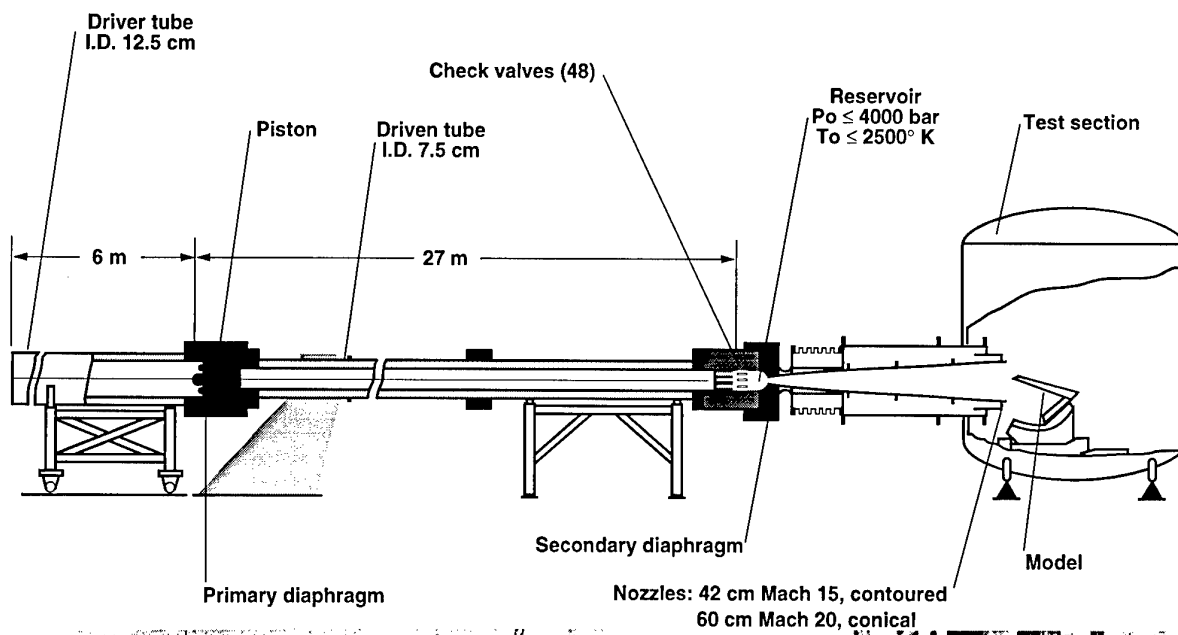


Figure 17. The VKI Longshot Shock Tunnel.



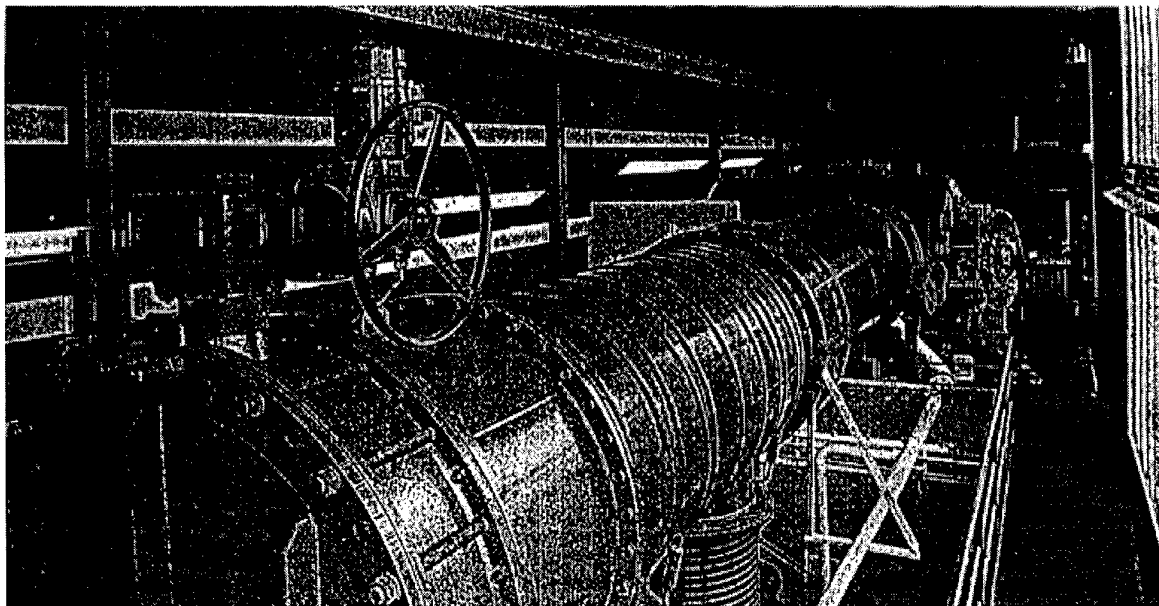


Figure 18. Photograph of the SR-3 Wind Tunnel at the CNRS (France).

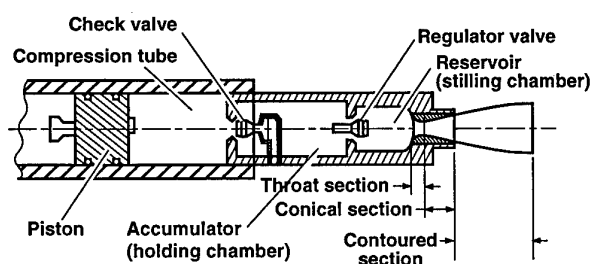


Figure 19. General Arrangement of PGU Compression Cascade.

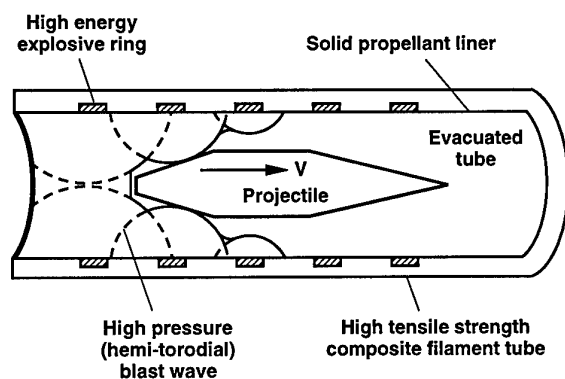
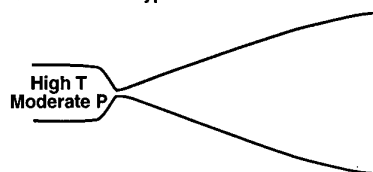


Figure 20. Oblique detonation wave driver.

Conventional hypersonic tunnel



Radiation driven hypersonic tunnel

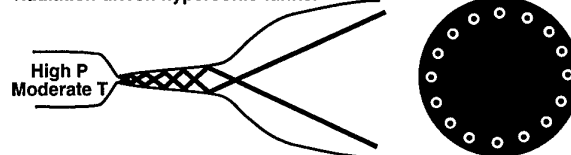


Figure 21. Conventional and radiation-driven wind tunnel philosophies.

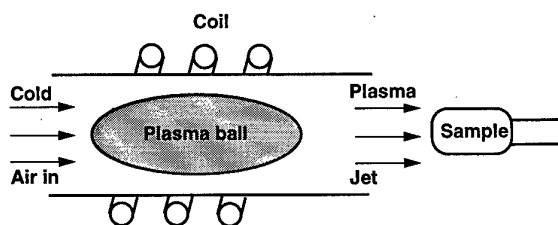


Figure 22. Schematic of VKI Plasmatron.



## CONCLUSIONS/RECOMMENDATIONS

Working Group 18, "Hypersonic Experimental and Computational Capability, Improvement and Validation", was composed of a circle of senior managers and researchers from the United States and Western Europe; its four-year study, summarised herein, has led to a sharing of experiences and the development of trust through well-defined cooperative projects.

Conducting experiments on standard test models in a wide range of hypersonic facilities provided a unique opportunity for facility and code validation. An important contribution was made by the Working Group to the success of the initial calibration and "shake-out" of four new real-gas facilities on both side of the Atlantic.

The studies performed by the various teams have resulted in a better identification of the risks involved in hypersonic vehicle design and have led to a wide range of recommendations to reduce these risks. In broad terms, Working Group 18 urges that resources be allocated within the NATO nations to:

- resolve facility, computational, and modeling deficiencies with targeted research efforts.
- accelerate the multiple facility/multiple computation strategy with standard models

Only in this way will we be ready to meet the inevitable challenges that will arise. In conclusion, the need for sustained hypersonic flight has been expressed by a number of NATO member states. Working Group 18 and other AGARD activities have demonstrated that many member states possess not only the intellectual and physical resources necessary to accomplish this goal, but have shown their ability and readiness to collaborate efficiently at the R & D level. Let us capitalise on these facts and move ahead by supporting the above recommendations and by defining specific NATO wide projects which will serve as drivers for increased collaboration in the future.



## REPORT DOCUMENTATION PAGE

<b>1. Recipient's Reference</b>	<b>2. Originator's Reference</b> AGARD-AR-319 Vol. II	<b>3. Further Reference</b> ISBN 92-836-1078-4	<b>4. Security Classification of Document</b> UNCLASSIFIED/ UNLIMITED														
<b>5. Originator</b>	Advisory Group for Aerospace Research and Development North Atlantic Treaty Organization BP 25, 7 rue Ancelle, F-92201 Neuilly-sur-Seine Cedex, France																
<b>6. Title</b>	Hypersonic Experimental and Computational Capability, Improvement and Validation																
<b>7. Presented at/sponsored by</b>	This Advisory Report was prepared at the request of the Fluid Dynamics Panel.																
<b>8. Author(s)/Editor(s)</b> Multiple	<b>9. Date</b> December 1998																
<b>10. Author's/Editor's Address</b> Multiple	<b>11. Pages</b> 172																
<b>12. Distribution Statement</b>	There are no restrictions on the distribution of this document. Information about the availability of this and other AGARD unclassified publications is given on the back cover.																
<b>13. Keywords/Descriptors</b>	<table><tr><td>Experimentation</td><td>Shock waves</td></tr><tr><td>Research projects</td><td>Hypersonic vehicles</td></tr><tr><td>Hypersonic flow</td><td>Boundary layer transition</td></tr><tr><td>Test facilities</td><td>Transition flow</td></tr><tr><td>Computational fluid dynamics</td><td>Launch vehicles</td></tr><tr><td>Aerothermodynamics</td><td>Real gas effects</td></tr><tr><td>Rarefied gas dynamics</td><td></td></tr></table>			Experimentation	Shock waves	Research projects	Hypersonic vehicles	Hypersonic flow	Boundary layer transition	Test facilities	Transition flow	Computational fluid dynamics	Launch vehicles	Aerothermodynamics	Real gas effects	Rarefied gas dynamics	
Experimentation	Shock waves																
Research projects	Hypersonic vehicles																
Hypersonic flow	Boundary layer transition																
Test facilities	Transition flow																
Computational fluid dynamics	Launch vehicles																
Aerothermodynamics	Real gas effects																
Rarefied gas dynamics																	
<b>14. Abstract</b>	<p>The results of the phase II effort conducted under AGARD Working Group 18 on Hypersonic Experimental and Computational Capability, Improvement and Validation are presented in this report. The first volume, published in May 1996, mainly focused on the design methodology, plans and some initial results of experiments that had been conducted to serve as validation benchmarks. The current volume presents the detailed experimental and computational data base developed during this effort.</p>																



L'AGARD détient un stock limité de certaines de ses publications récentes. Celles-ci pourront éventuellement être obtenus sous forme de copie papier. Pour de plus amples renseignements concernant l'achat de ces ouvrages, adressez-vous à l'AGARD par lettre ou par télécopie à l'adresse indiquée ci-dessus. *Veuillez ne pas téléphoner.*

Des exemplaires supplémentaires peuvent parfois être obtenus auprès des centres de diffusion nationaux indiqués ci-dessous. Si vous souhaitez recevoir toutes les publications de l'AGARD, ou simplement celles qui concernent certains Panels, vous pouvez demander d'être inclus sur la liste d'envoi de l'un de ces centres.

Les publications de l'AGARD sont en vente auprès des agences de vente indiquées ci-dessous, sous forme de photocopie ou de microfiche. Certains originaux peuvent également être obtenus auprès de CASI.

#### CENTRES DE DIFFUSION NATIONAUX

##### ALLEMAGNE

Fachinformationszentrum Karlsruhe  
D-76344 Eggenstein-Leopoldshafen 2

##### BELGIQUE

Coordonnateur AGARD - VSL  
Etat-major de la Force aérienne  
Quartier Reine Elisabeth  
Rue d'Evere, B-1140 Bruxelles

##### CANADA

Directeur - Gestion de l'information  
(Recherche et développement) - DRDGI 3  
Ministère de la Défense nationale  
Ottawa, Ontario K1A 0K2

##### DANEMARK

Danish Defence Research Establishment  
Ryvangs Allé 1  
P.O. Box 2715  
DK-2100 Copenhagen Ø

##### ESPAGNE

INTA (AGARD Publications)  
Carretera de Torrejón a Ajalvir, Pk.4  
28850 Torrejón de Ardoz - Madrid

##### ETATS-UNIS

NASA Center for AeroSpace Information (CASI)  
Parkway Center, 7121 Standard Drive  
Hanover, MD 21076-1320

##### FRANCE

O.N.E.R.A. (Direction)  
29, Avenue de la Division Leclerc  
92322 Châtillon Cedex

##### GRECE

Hellenic Air Force  
Air War College  
Scientific and Technical Library  
Dekelia Air Force Base  
Dekelia, Athens TGA 1010

##### ISLANDE

Director of Aviation  
c/o Flugrad  
Reykjavik

##### ITALIE

Aeronautica Militare  
Ufficio Stralcio AGARD  
Aeroporto Pratica di Mare  
00040 Pomezia (Roma)

##### LUXEMBOURG

Voir Belgique

##### NORVEGE

Norwegian Defence Research Establishment  
Attn: Biblioteket  
P.O. Box 25  
N-2007 Kjeller

##### PAYS-BAS

NDRCC  
DGM/DWOO  
P.O. Box 20701  
2500 ES Den Haag

##### PORTUGAL

Estado Maior da Força Aérea  
SDFA - Centro de Documentação  
Alfragide  
P-2720 Amadora

##### ROYAUME-UNI

Defence Research Information Centre  
Kentigern House  
65 Brown Street  
Glasgow G2 8EX

##### TURQUIE

Millî Savunma Başkanlığı (MSB)  
ARGE Dairesi Başkanlığı (MSB)  
06650 Bakanlıklar - Ankara

#### AGENCES DE VENTE

##### NASA Center for AeroSpace Information (CASI)

Parkway Center, 7121 Standard Drive  
Hanover, MD 21076-1320  
Etats-Unis

##### The British Library Document Supply Division

Boston Spa, Wetherby  
West Yorkshire LS23 7BQ  
Royaume-Uni

Les demandes de microfiches ou de photocopies de documents AGARD (y compris les demandes faites auprès du CASI) doivent comporter la dénomination AGARD, ainsi que le numéro de série d'AGARD (par exemple AGARD-AG-315). Des informations analogues, telles que le titre et la date de publication sont souhaitables. Veuillez noter qu'il y a lieu de spécifier AGARD-R-nnn et AGARD-AR-nnn lors de la commande des rapports AGARD et des rapports consultatifs AGARD respectivement. Des références bibliographiques complètes ainsi que des résumés des publications AGARD figurent dans les journaux suivants:

##### Scientific and Technical Aerospace Reports (STAR)

STAR peut être consulté en ligne au localisateur de ressources uniformes (URL) suivant:

<http://www.sti.nasa.gov/Pubs/star/Star.html>

STAR est édité par CASI dans le cadre du programme

NASA d'information scientifique et technique (STI)

STI Program Office, MS 157A

NASA Langley Research Center

Hampton, Virginia 23681-0001

Etats-Unis

##### Government Reports Announcements & Index (GRA&I)

publié par le National Technical Information Service

Springfield

Virginia 2216

Etats-Unis

(accessible également en mode interactif dans la base de données bibliographiques en ligne du NTIS, et sur CD-ROM)



Imprimé par le Groupe Communication Canada Inc.

(membre de la Corporation St-Joseph)

45, boul. Sacré-Cœur, Hull (Québec), Canada K1A 0S7

AGARD holds limited quantities of some of its recent publications, and these may be available for purchase in hard copy form. For more information, write or send a telefax to the address given above. *Please do not telephone.*

Further copies are sometimes available from the National Distribution Centres listed below. If you wish to receive all AGARD publications, or just those relating to one or more specific AGARD Panels, they may be willing to include you (or your organisation) in their distribution.

AGARD publications may be purchased from the Sales Agencies listed below, in photocopy or microfiche form. Original copies of some publications may be available from CASI.

## NATIONAL DISTRIBUTION CENTRES

## BELGIUM

Coordonnateur AGARD - VSL  
Etat-major de la Force aérienne  
Quartier Reine Elisabeth  
Rue d'Evere, B-1140 Bruxelles

## CANADA

Director Research & Development  
Information Management - DRDIM 3  
Dept of National Defence  
Ottawa, Ontario K1A 0K2

## DENMARK

Danish Defence Research Establishment  
Ryvangs Allé 1  
P.O. Box 2715  
DK-2100 Copenhagen Ø

## FRANCE

O.N.E.R.A. (Direction)  
29 Avenue de la Division Leclerc  
92322 Châtillon Cedex

## GERMANY

Fachinformationszentrum Karlsruhe  
D-76344 Eggenstein-Leopoldshafen 2

## GREECE

Hellenic Air Force  
Air War College  
Scientific and Technical Library  
Dekelia Air Force Base  
Dekelia, Athens TGA 1010

## ICELAND

Director of Aviation  
c/o Flugrad  
Reykjavik

## ITALY

Aeronautica Militare  
Ufficio Stralcio AGARD  
Aeroporto Pratica di Mare  
00040 Pomezia (Roma)

## LUXEMBOURG

See Belgium

## NETHERLANDS

NDRCC  
DGM/DWOO  
P.O. Box 20701  
2500 ES Den Haag

## NORWAY

Norwegian Defence Research Establishment  
Attn: Biblioteket  
P.O. Box 25  
N-2007 Kjeller

## PORTUGAL

Estado Maior da Força Aérea  
SDFA - Centro de Documentação  
Alfragide  
P-2720 Amadora

## SPAIN

INTA (AGARD Publications)  
Carretera de Torrejón a Ajalvir, Pk.4  
28850 Torrejón de Ardoz - Madrid

## TURKEY

Millî Savunma Başkanlığı (MSB)  
ARGE Dairesi Başkanlığı (MSB)  
06650 Bakanlıklar - Ankara

## UNITED KINGDOM

Defence Research Information Centre  
Kentigern House  
65 Brown Street  
Glasgow G2 8EX

## UNITED STATES

NASA Center for AeroSpace Information (CASI)  
Parkway Center, 7121 Standard Drive  
Hanover, MD 21076-1320

## SALES AGENCIES

## NASA Center for AeroSpace Information (CASI)

Parkway Center, 7121 Standard Drive  
Hanover, MD 21076-1320  
United States

## The British Library Document Supply Centre

Boston Spa, Wetherby  
West Yorkshire LS23 7BQ  
United Kingdom

Requests for microfiches or photocopies of AGARD documents (including requests to CASI) should include the word 'AGARD' and the AGARD serial number (for example AGARD-AG-315). Collateral information such as title and publication date is desirable. Note that AGARD Reports and Advisory Reports should be specified as AGARD-R-nnn and AGARD-AR-nnn, respectively. Full bibliographical references and abstracts of AGARD publications are given in the following journals:

## Scientific and Technical Aerospace Reports (STAR)

STAR is available on-line at the following uniform resource locator:

<http://www.sti.nasa.gov/Pubs/star/Star.html>

STAR is published by CASI for the NASA Scientific and Technical Information (STI) Program  
STI Program Office, MS 157A  
NASA Langley Research Center  
Hampton, Virginia 23681-0001  
United States

## Government Reports Announcements &amp; Index (GRA&amp;I)

published by the National Technical Information Service  
Springfield  
Virginia 22161  
United States  
(also available online in the NTIS Bibliographic Database or on CD-ROM)



Printed by Canada Communication Group Inc.  
(A St. Joseph Corporation Company)  
45 Sacré-Cœur Blvd., Hull (Québec), Canada K1A 0S7